Preparation and characterization of templated borophosphates and metalloborophosphates

Dissertation

zur Erlangung des akademischen Grades

Doctor rerum naturalium

(Dr. rer. nat.)

vorgelegt

der Fakultät Mathematik und Naturwissenschaften

der Technischen Universität Dresden

von

Ya-Xi Huang

geboren am 01. Nov. 1975 in Fujian, V. R. China

Gutachter:	Prof. Dr. Rüdiger Kniep
	Prof. Dr. Michael Ruck
	Prof. Dr. Erwin Parthé

Eingereicht:	21.07.2004
Tag der Verteidigung:	19.10.2004

To my daughter

Acknowledgement

Publications

1. S.-Y. Mao, Y.-X. Huang, Z.-B. Wei, J.-X. Mi, Z.-L. Huang, and J.-T. Zhao
   Hydrothermal Synthesis, Crystal Structure, and Characterization of Tetrasodium Tricobalt(II)-bis-Phosphate-bis-Hydrogenophosphate Octahydrate, $Na_4Co_3H_2(PO_4)_4 \cdot 8H_2O$, with a new structure type
   J. Solid State Chem. **2000**, *149*, 292-297

2. J.-X. Mi, J.-T. Zhao, S.-Y. Mao, Y.-X. Huang, H. Engelhardt, and R. Kniep
   Crystal structure of dichromium monoborotriphosphate, $Cr_2[BP_3O_{12}]$
   Z. Kristallogr. NCS, **2000**, *215*, 201-202.

3. Y.-X. Huang, S.-Y. Mao, J.-X. Mi, Z.-B. Wei, J.-T. Zhao, and R. Kniep
   Crystal structure of sodium gallium [monohydrogenmonophosphate-dihydrogen-monoborate-monophosphate], $NaGa[BP_2O_7(OH)_3]$
   Z. Kristallogr. NCS, **2001**, *216*, 15-16.

4. J.-X. Mi, Y.-X. Huang, S.-Y. Mao, X.-D. Huang, Z.-B. Wei, Z.-L. Huang, and J.-T. Zhao
   Hydrothermal Synthesis and Crystal Structure of $Na_2In_2[PO_3(OH)]_4 \cdot H_2O$ with a New Structure Type
   J. Solid State Chem. **2001**, *157*, 213-219.

5. Y.-X. Huang, G. Schäfer, W. Carrillo-Cabrera, R. Cardoso, W. Schnelle, J.-T. Zhao, and R. Kniep
   Open-Framework Borophosphates:$(NH_4)_{0.4}Fe^{II}_{0.55}Fe^{III}_{0.5}(H_2O)_2[BP_2O_8] \cdot 0.6H_2O$ and $NH_4Fe^{III}[BPO_2O_8(OH)]$
   Chem. Mater. **2001**, *13*, 4348-4354.

6. S.-Y. Mao, M.-R. Li, Y.-X. Huang, J.-X. Mi, H.-H. Chen, Z.-B. Wei, and J.-T. Zhao
   Hydrothermal Synthesis and Crystal Structure of the First Ammonium Indium(III) Phosphate $NH_4In(OH)PO_4$ with Spiral Chains of $InO_4(OH)_2$
   J. Solid State Chem. **2002**, *165*, 209-213

7. S.-Y. Mao, M.-R. Li, Y.-X. Huang, J.-X. Mi, Z.-B. Wei, J.-T. Zhao and R. Kniep
   Crystal structure of potassium indium (monophosphate-hydrogenmonoborate-monophosphate), $KIn[BP_2O_8(OH)]$
   Z. Kristallogr. NCS, **2002**, *217*, 3-4.

8. J.-X. Mi, M.-R. Li, S.-Y. Mao, Y.-X. Huang, Z.-B. Wei, J.-T. Zhao and R. Kniep
   Crystal structure of ammonium indium (monophosphate-hydrogenmonoborate-monophosphate), $(NH_4)In[BP_2O_8(OH)]$
   Z. Kristallogr. NCS, **2002**, *217*, 5-6.

9. Y.-X. Huang, J.-X. Mi, S.-Y Mao, Z. -B. Wei, J.-T. Zhao, and R. Kniep
   Crystal structure of sodium indium (monohydrogenmonophosphate-dihydrogen-monoborate-monophosphate), $NaIn[BP_2O_7(OH)_3)]$
   Z. Kristallogr. NCS, **2002**, *217*, 7-8.

10. Y.-X. Huang, J.-T. Zhao, J.-X. Mi, H. Borrmann, and R. Kniep
    Crystal structure of rubidium indium (monophosphate-hydrogenmonoborate-mono-phosphate), $RbIn[BP_2O_8(OH)]$
    Z. Kristallogr. NCS, **2002**, *217*, 163-164.

11. M.-R. Li, S.-Y. Mao, Y.-X. Huang, J.-X. Mi, Z.-B. Wei, J.-T. Zhao and R. Kniep
    Crystal structure of ammonium gallium (monophosphate-hydrogenmonoborate-monophosphate), $(NH_4)Ga[BP_2O_8(OH)]$
    Z. Kristallogr. NCS, **2002**, *217*, 165-166.

12. J.-X. Mi, Y.-X. Huang, S.-Y. Mao, H. Borrmann, J.-T. Zhao, and R. Kniep
    Crystal structure of potassium gallium (monophosphate-hydrogenmonoborate-monophosphate), $KGa[BP_2O_7(OH)_3]$
    Z. Kristallogr. NCS, **2002**, *217*, 167-168.

13. J.-X. Mi, Y.-X. Huang, J.-F. Deng, H. Borrmann, J.-T. Zhao, and R. Kniep
    Crystal structure of caesium aluminum *catena*-[monohydrogen-monoborate-bis (monophosphate)], $CsAl[BP_2O_8(OH)]$
    Z. Kristallogr. NCS, **2002**, *217*, 169-170.

14. J.-X. Mi, J.-T. Zhao, Y.-X. Huang, J.-F. Deng, H. Borrmann, and R. Kniep
Crystal structure of rubidium aluminum *catena*-[monohydrogen-monoborate-bis (monophosphate)], $RbAl[BP_2O_8(OH)]$
Z. Kristallogr. NCS, **2002**, *217*, 171-172.

15. J.-X. Mi, Y.-X. Huang, J.-F. Deng, H. Borrmann, J.-T. Zhao, and R. Kniep
Crystal structure of ammonium aluminum *catena*-[monohydrogen-monoborate-bis (monophosphate)], $(NH_4)Al[BP_2O_8(OH)]$
Z. Kristallogr. NCS, **2002**, *217*, 305-306.

16. J.-X. Mi, H. Borrmann, S.-Y. Mao, Y.-X. Huang, H. Zhang, J.-T. Zhao, and R. Kniep
Crystal structure of rubidium gallium *catena*-[monohydrogen-monoborate-bis(mono-phosphate)], $RbGa[BP_2O_8(OH)]$, from a twinned crystal
Z. Kristallogr. NCS, **2003**, *218*, 17-18.

17. M.-H. Ge, J.-X. Mi, Y.-X. Huang, J.-T. Zhao, and R. Kniep
Crystal structure of sodium cadmium diaqua *catena*-[monoboro-diphosphate]-hydrate, $NaCd(H_2O)_2[BP_2O_8] \cdot 0.8H_2O$
Z. Kristallogr. NCS, **2003**, *218*, 165-166.

18. J.-X. Mi, H. Borrmann, Y.-X. Huang, J.-T. Zhao and R. Kniep
Crystal structure of the α-modification of caesium gallium(III) monohydrogen triphosphate, α-$CsGaHP_3O_{10}$
Z. Kristallogr. NCS, **2003**, *218*, 167-168.

19. J.-X. Mi, H. Borrmann, Y.-X. Huang, J.-T. Zhao and R. Kniep
Crystal structure of the 1M-modification of caesium gallium(III) monohydrogen triphosphate, 1M-$CsGaHP_3O_{10}$
Z. Kristallogr. NCS, **2003**, *218*, 169-1670.

20. J.-X. Mi, H. Borrmann, Y.-X. Huang, S.-Y. Mao, J.-T. Zhao, and R. Kniep
Crystal structure of caesium gallium *catena*-[monohydrogen-monoborate-bis(mono-phosphate)], $CsGa[BP_2O_8(OH)]$
Z. Kristallogr. NCS, **2003**, *218*, 171-172.

21. M.-H. Ge, J.-X. Mi, Y.-X. Huang, J.-T. Zhao, and R. Kniep
Crystal structure of lithium cadmium diaqua *catena*-[monoboro-diphosphate]-monohydrate, $LiCd(H_2O)_2[BP_2O_8] \cdot H_2O$
Z. Kristallogr. NCS, **2003**, *218*, 273-274.

22. Y.-X. Huang, G. Schäfer, H. Borrmann, J.-T. Zhao, and R. Kniep
$(C_2H_{10}N_2)[BPO_4F_2]$–Structural Relations between $[BPO_4F_2]^{2-}$ and $[Si_2O_6]^{4-}$
Z. Anorg. Allg. Chem. **2003**, *629*, 2-3.

23. Y.-X. Huang, G. Schäfer, W. Carrillo-Cabrera, H. Borrmann, R. Cardoso Gil, and R. Kniep
$(C_6H_{14}N_2)\{Zn[ZnB_2P_4O_{15}(OH)_2]\cdot(C_6H_{13}N_2)Cl\}$: A New Templated Zincoborophosphate
Chem. Mater. **2003**, *15*, 4930-4935.

Conference contributions

1. Y.-X. Huang, G. Schäfer, J.-T. Zhao, R. Kniep
   Open framework borophosphates (Poster presentation, P083)
   8th European Conference on Solid State Chemistry, July **2001**, Oslo, Norway.

2. Y.-X. Huang
   Zincoborophosphates (oral presentation)
   4th Baltic Boat Conference on Solid State Chemistry, 24.-26. May **2002**, Stockholm, Sweden.

3. Y.-X. Huang, M.-R. Li, J.-X. Mi, S.-Y. Mao, H. Bormann, Z.-B. Wei, J.-T. Zhao, R. Kniep
   Syntheses and Crystal Structures of In(III) - and Ga(III) - Borophosphates (Poster presentation, P9)
   Fourth International Symposium on Inorganic Phosphate materials, and IMPHOS Workshop on Phosphates: New Uses, New Technologies, 10.-13. July **2002**, Jena.

4. Y.-X. Huang, G. Schäfer, R. Kniep
   $(C_2H_{10}N_2)[BPO_4F_2]$ - a fluorine-substituted borophosphate derivative of the pyroxene-type silicates (Poster presentation, P182)
   Third International Conference on Inorganic Materials, 7.-10. September **2002**, Konstanz.

5. Y.-X. Huang, H. Borrmann, R. Kniep
   $(C_6N_2H_{14})\{Zn[ZnB_2P_4O_{15}(OH)_2]\cdot(C_6N_2H_{13})Cl\}$: A new templated zincoborophosphate (Poster presentation, A32)
   11. Vortragstagung der GDCh-Fachgruppe Festkoeperchmie und Materialforschung, 24.-26. September **2002**, Dresden.

6. Y.-X. Huang, Yu. Prots, H. Zhang, R. Kniep
   Control of Channel Shapes in a Manganese-Borophosphate Framework: The Influence of Size and Shape of Organic Template Cations
   9th European Conference on Solid Sate Chemistry, 3.-6. September **2003**, Stuttgart.

Contents

1 Introduction

1.1 General introduction

The borophosphates are intermediate compounds of system of M_xO_y–B_2O_3–P_2O_5–(H_2O) (M = metal; special case: M replaced by NH_4^+ or diamines). Though the first borophosphate was synthesized by *van Kloosters* [1] in 1911, the systematic investigation on borophosphates only started from 1994. As a relatively young class of compounds, borophosphate has already received much attention due to its scientific and technological importance. Microporous phosphates can be used as catalysts, ion exchangers and molecule sieves. Borates are good optical materials, e.g. nonlinear optical properties and luminescence. One can imagine, borophosphates, with a combination of borate-and-phosphate-characteristics, already may have the properties both of phosphates and of borates. The following applications for borophosphates are already established or considered to be potential candidates:

Catalysts

Molecular sieves

Ion exchangers, especially for Li-ion batteries

Optical materials (non-linear optical properties, luminescence, fluorescence)

Corrosion protector for metal surfaces

The catalytic properties of BPO_4 have been well established for a long time [2–4]. It is widely used in the petroleum industry [5–7], such as for dehydration of 2-methylbutanal to 2-methyl-1,3-butadiene (isoprene). The transition metal (Mn, Fe, Co, Ni, Cu) substitutions on boron sites stabilized the structure to the orthorhombic low-cristobalite type with average volumes per tetrahedral unit 30 % larger than that in BPO_4. This change in volume is expected to exhibit novel catalytic properties [8].

Open-framework materials, in general, have been intensively studied in recent years because of their interesting chemical properties and potential application as molecular sieves, and ion exchangers [9] due to their large cavities or channels [10]. Many zeolites have shown these properties. The common motif of these zeolite building units is based on the corner-sharing [SiO_4] tetrahedra. From a crystal chemistry point of view,

BPO_4 possesses the same dense structures as those of "SiSiO$_4$" and AlPO$_4$. The crystal chemistry of the borophosphate exhibits also over oxygen corners linked tetrahedral borate and phosphate building groups as well as protonated species similarities with that of the silicates. In relation to microporous and zeolite-analogous systems such as alumosilicates [11], aluminium/alumophosphates [12, 13], substituted variants [14, 15], and gallium/gallo- [16, 17] and zincophosphates [18, 19], new open-framework structures based on boro- and zincoborophosphates have been successfully characterized. A new class of compounds, $A[ZnBP_2O_8]$ ($A^+ =$, NH_4^+, Rb^+, Cs^+) with tetrahedral frameworks, has been realized, whose topologies display a close relationship to alumosilicates (feldspar family [20] and gismondine [21, 22]) [23, 24]. A chiral tetrahedral framework related to the CZP topology [25] has been observed in the crystal structures of $NaZn(H_2O)_2[BP_2O_8] \cdot H_2O$.

It is well known that LiB_3O_5 (LBO) and β–BaB_2O_4 (BBO) are two types of important Non-Linear Optical (NLO) materials [26]. KH_2PO_4 (KDP) [26], as a phosphate, is also an important NLO material. Borophosphates, as a combination of the characteristics of borates and phosphates, have also been detected containing nonlinear optical properties, e.g. $SrBPO_5$ [27], β-Zn_3BPO_7 [28], $Mg_xZn_{1-x}BPO_7$ ($x = 1.8$) [29], $Na_5[B_2P_3O_{13}]$ [30, 31] and $Cr_2[BP_3O_{13}]$ [32, 33]. Among these, $SrBPO_5$ [27] and $Mg_xZn_{1-x}BPO_7$ ($x = 1.8$) [29] exhibit an optical SHG effect similar to that of KDP (KH_2PO_4).

Some borophosphates doped with rare earth metals exhibit luminescence or fluorescence effects. The compounds with composition of $M^{II}[BPO_5]$ (M^{II} = Ca, Sr [34], Ba [35], Pb [36]) were widely used to investigate the luminescence properties by doping with rare earth metals. For example, Eu^{2+} doped $SrBPO_5$ shows intense photostimulated luminescence for UV and X-ray radiations [37]; Ce^{3+} doping of $CaBPO_5$ also shows luminescent properties [38]. Another example is given by Ce^{3+}, Tb^{3+} and Gd^{3+} doped rare earth borate-phosphate $Ln(BO_3, PO_4)$ (Ln = La, Y) [39]. It was observed that $La(BO_3, PO_4)$: Ce, Tb, Gd phosphors absorb ultraviolet radiation and emit green light with high purity and intensity under 254 nm excitation.

There are also some reports on the application of borophosphates as corrosion protecting materials [40, 41]. These studies show that borophosphates can be used as coatings on metal surfaces, consequently acting as corrosion protectors [40].

Hydrothermal methods and high temperature solid state reactions are commonly

used for the syntheses of borophosphates. Only small amount of known borophosphates were prepared from high temperature solid state reactions because of a number of disadvantages: such as hard to get pure and single phase materials as well as single crystal, B_2O_3 readily vapor at high temperature and form glass, and so on. Thus, people have to search for new synthesis methods for borophosphates. The introduction of hydrothermal syntheses on borophosphate preparation in 1996 made a breakthrough in the development of this class of compounds and led to the syntheses of a large number of new borophosphates with a wide variety of structural building units.

Hydrothermal synthesis utilizes water as a solvent in a closed system. By this pressures and temperatures higher than 1 atm and 100 °C are reached. In nature, many minerals are formed under hydrothermal conditions. Using such methods, it is often possible to obtain larger crystals in shorter periods of time, to grow pure crystals of sufficient size for the measurement and utilization of their physical properties, and even to prepare compounds with elements in oxidation states that are difficult to attain using other techniques [42]. In addition, hydrothermal synthesis also employs relatively mild temperature conditions which also means easy handling. Hydrothermal synthesis is carried out in closed system under autogenous pressure. Temperature and degree of fill are the variables influencing the pressure. Increasing temperature leads to rise in pressure. pH values is an additional important factor affecting on the reaction products. Acid conditions, in general, lead to borophosphates, while basic conditions lead to phosphates as products.

1.2 Overview on borophosphates

In nature, two borophosphate-minerals are known: $Mg_3(H_2O)_6[B_2(OH)_6(PO_4)_2]$ (Lüneburgite) [43] comprising $\{[B(OH)_3(PO_4)]^{3-}\}$ dimers as borophosphate anions; $Mn_3(OH)_2$-$[B(OH)_4][PO_4]$ (Seamanite) [44] consisting of isolated $B(OH)_4$- and PO_4-tetrahedra. Both of them were formed under hydrothermal conditions. Though the systematic investigations on borophosphates started not before 1994, during this short time to now, a broad spectrum of new compounds has already been observed. The development of borophosphates have been discussed in detailed in the dissertations of *Hauf* [31], *Boy* [45], *Engelhardt* [46], and *Schäfer* [47]. Here I will discuss mainly on the structural chemistry of borophosphates.

1.2.1 Systematic principle of a structural chemistry of borophosphates

Borophosphates contain complex anions built from BO_4, BO_3, and PO_4 groups and their partially protonated species. A first approach [48] to the development of a structural chemistry of borophosphates is based on water content (anhydrous and hydrated), molar B : P ratio, and dimentionality of the borophosphate anions (linking principles of the primary building units following the general line of silicate crystal chemistry). The structural chemistry of borophosphate anions extends from isolated species, oligomers, rings, and chains to layers and frameworks. In the known borophosphates, B : P ratios of anhydrous borophosphates are in the range of 0.25–1; while B : P ratios of hydrated borophosphates range from 0.25 to 6, boron are in both trigonal planar and tetrahedral coordination when B : P $\geq$ 3. The anhydrous borophosphate anions consist of isolated species, oligomers, and chains. The hydrated borophosphates, including metallo- and templated-borophosphates, have rich borophosphate anions, which extend from isolated species, oligomers, rings, and chains to layers and frameworks. For further details of the borophosphate anions please see *Table 1.1*.

Some characteristic principles in the crystal structural chemistry of borophosphates can be emphasized:

1. No P–O–P linkages were observed in borophosphates known up to now.

2. The alkali metal and ammonium borophosphates containing boron in both trigonal planar and tetrahedral coordinations have the molar ratio of B : P $\geq$ 3.

3. Additional characteristics are integration of planar BO_3 groups, preferred formation of 3-membered rings, and unusual branching of tetrahedral chains.

4. Templated vanadium and molybdenum borophosphates only consist of oligomers as anionic borophosphates partial structures. Since vanadium and molybdenum have a tending to form clusters built by vanadium- or molybdenum-polyhedra and borophosphate groups.

5. Zinco- and beryllo-borophosphates have a molar ratio of Zn(Be) : B : P = 1 : 1 : 2.

Table 1.1: The borophosphates have been characterized so far.

Compound	Anions complex
Isolated	
α-$M^{II}[BPO_7]$ (M^{II} = Mg, Zn) [49,50] $Co_3[BPO_7]$ [51]	isolated BO_3-triangle and PO_4-tetrahedra
$Ln_7O_6[BO_3][PO_4]_2$ (Ln = Pr, Nd [52], La, Nd, Gd, Dy [53,54])	isolated BO_3-triangle and PO_4-tetrahedra
$Mn_3(OH)_2[B(OH)_4][PO_4]$ [44] (Seamanite)	isolated $B(OH)_4$- and PO_4-tetrahedra
Oligomer	
$Co_5[BP_3O_{14}]$ [55]	dimer $\{[O_2BO_{2/2}PO_3]^{4-}\}$ and isolated PO_4-tetrahedra
$Cr_2[BP_3O_{12}]$ [32]	tetramer $\{[B(O_{2/2}PO_3)_3]^{6-}\}$
$Pb_6[PO_4][B(PO_4)_4]$ [56]	pentamer $\{[B(O_{2/2}PO_3)_4]^{9-}\}$ and isolated PO_4-tetrahedra
$Mg_3(H_2O)_6[B_2(OH)_6(PO_4)_2]$ (Lüneburgite) [43]	dimer $\{[O_3PO_{2/2}B(OH)_3]^{3-}\}$
$NaM^{III}[BP_2O_7(OH)_3]$ (M^{III} = Al, V, Fe, Ga, In) [57–61] $KGa[BP_2O_7(OH)_3]$ [62] $Mg_2[BP_2O_7(OH)_3]$ [49]	trimer $\{[(HO)O_2PO_{2/2}B(OH)_2O_{2/2}PO_3]^{4-}\}$
$CsV_3(H_2O)_2[B_2P_4O_{16}(OH)_4]$ [63]	trimer $\{[O_3PO_{2/2}B(OH)_2O_{2/2}PO_3]^{5-}\}$
$(C_2H_{10}N_2)_2[Na(VO)_{10}\{BP_2O_8(OH)_2\}_5]\cdot 22.5H_2O$ [64]	trimer $\{[(HO)O_2PO_{2/2}B(O)_2O_{2/2}PO_2(OH)]^{5-}\}$
$(C_2H_{10}N_2)_2[(VO)_5(H_2O)\{BP_2O_{10}\}]\cdot 1.5H_2O$ [65]	trimer $\{[O_3PO_{2/2}B(O)_2O_{2/2}PO_3]^{7-}\}$
$(C_4H_{12}N_2)_6[(VO)_2BP_2O_{10}]\cdot nH_2O$ (n = 2, 6, 14) [66]	
$Na_{14}[Na\{(VO)_2BP_2O_{10}\}_5]\cdot nH_2O$ [66]	
$A_{17}[A\{(VO)_2BP_2O_{10}\}_6]\cdot nH_2O$ (A = NH_4^+, K^+, Rb^+, Cs^+) [66]	
$(C_6H_{22}N_3)_4H[M\{(VO)_2BP_2O_{10}\}_6]\cdot nH_2O$ (M = NH_4^+, K^+) [67,68]	
$(NH_4)_2(C_3H_{12}N_3)_8[V_2BP_2O_{12}]_6\cdot 15H_2O$ [69]	
$(NH_4)_2(C_2H_{10}N_2)_6$-$(Sr(H_2O)_5)_2[V_2BP_2O_{12}]_6\cdot 10H_2O$ [70]	
$(NH_4)_2(C_3H_{12}N_2)_6$-$(Sr(H_2O)_4)_2[V_2BP_2O_{12}]_6\cdot 17H_2O$ [70]	
$(NH_4)_3(C_4H_{14}N_2)_{4.5}(Sr(H_2O)_5)_2(Sr(H_2O)_4)$-$[V_2BP_2O_{12}]_6\cdot 10H_2O$ [70]	
$(NH_4)_5[V_3BP_3O_{19}]\cdot H_2O$ [71] $(Co(en)_3)(enH_2)\{V_3BP_3O_{19}\}\cdot 4.5H_2O$ [72]	tetramer $\{[BO_4(PO_3)_3]^{8-}\}$

Table 1.1 Continued

Compound	Anions complex
Oligomer	
$(C_3H_6N_2)_{3.8}(H_3O)_{1.2}[(VO)_4(PO_4)_5(BO)_2] \cdot 0.3H_2O$ [73]	heptamer $\{[B_2P_5O_{21}]^{11-}\}$
$(C_6H_{14}N_2)_2[VO(PO_3OH)_4(B_3O_3OH)] \cdot 4H_2O$ [74]	heptamer $\{[(PO_3OH)_4(B_3O_3OH)]^{6-}\}$
$(C_6H_{14}N_2)_2[VO(HPO_4)_5B_2O] \cdot H_2O \cdot H_3PO_4$ [75]	heptamer $\{[B_2O(HPO_4)_5]^{6-}\}$ and isolate H_3PO_4–tetrahedra
$(C_3H_5N_2)_8[Mo^V{}_5Mo^{VI}{}_7O_{22}(BPO_4)_2(PO_4)_3\text{-}(HPO_4)_3] \cdot nH_2O$ ($n \approx 4$) [76]	pentamer $\{[B(O_{2/2}PO_3)_4]^{9-}\}$ and $\{[O_3PO_{2/2}B(O_{2/2}PO_2(OH))_3]^{6-}\}$
$(C_3H_5N_2)_5[Mo^V{}_5Mo^{VI}{}_7O_{30}(BPO_4)_2(O_3P\text{-}Ph)_6] \cdot H_2O$ [77]	pentamer $\{[O_3PO_{2/2}B(O_{2/2}PO_2\text{-}Ph)_3]^{12-}\}$
Ring	
$A^IM^{III}[BP_2O_8(OH)]$ (A^I = Na, K, NH$_4$, Rb; M^{III} = Fe, In) [57, 78–80]	4-membered ring $\{[BP_2O_8(OH)]^{4-}\}$ open-branched by two PO_4-tetrahedra
$Na_4Cu_3[B_2P_4O_{16}(OH)_2] \cdot 2HPO_4$ [81]	4-membered ring $\{[B_2P_4O_{15}(OH)_2]^{6-}\}$ open-branched by two PO_4-tetrahedra and isolate HPO_4-tetrahedron
$(Ni_{3-x}Mg_x)[B_3P_3O_{12}(OH)_6] \cdot 6H_2O$ (x $\approx$ 1.5) [82] $Mg[BPO_4(OH)_2] \cdot 2H_2O$ [83]	unbranched 6-membered ring $\{[B_3P_3O_{12}(OH)_6]^{6-}\}$
$K_6Cu_2[B_4P_8O_{28}(OH)_6]$ [84]	6-membered ring $\{[B_4P_8O_{28}(OH)_6]^{10-}\}$ open-branched by four HPO_4-tetrahedra
Chain	
$M^{II}[BPO_5]$ (M^{II} = Ca, Sr [27, 34], Ba [85], Pb [36])	loop-branched $\frac{1}{\infty}\{[BPO_5]^{2-}\}$
$M^{II}{}_3[BP_3O_{12}]$ (M^{II} = Ba [34], Pb [36])	open-branched $\frac{1}{\infty}\{[BP_3O_{12}]^{6-}\}$
$Na_5[B_2P_3O_{13}]$ [30]	loop-branched $\frac{1}{\infty}\{[B_2P_3O_{13}]^{5-}\}$
$Li[B_3PO_6(OH)_3]$ [86]	open loop-branched $\frac{1}{\infty}\{[B_3PO_6(OH)_3]^{-}\}^\dagger$
$(NH_4)_2[B_3PO_7(OH)_2]$ [87]	open loop-branched $\frac{1}{\infty}\{[B_3PO_7(OH)_2]^{2-}\}^\dagger$
$K_3[B_5PO_{10}(OH)_3]$ [88]	loop-branched $\frac{1}{\infty}\{[B_5PO_{10}(OH)_3]^{3-}\}^\dagger$
$K[B_6PO_{10}(OH)_4]$ [89]	$\frac{1}{\infty}\{[B_6PO_{10}(OH)_4]^{-}\}^\dagger$
$Fe[B_2P_2O_7(OH)_5]$ [90] $Al[B_2P_2O_7(OH)_5] \circ H_2O$ [91]	unbranched $\frac{1}{\infty}\{[B_2P_2O_7(OH)_5]^{3-}\}$
$A^IM^{III}[BP_2O_8(OH)]$(A^I = NH$_4$, Rb, Cs; M^{III} = V, Fe, Ga, In) [92–102] $Pb_2[BP_2O_8(OH)]$ [56]	open-branched $\frac{1}{\infty}\{[BP_2O_8(OH)]^{4-}\}$

†The anionic borophosphate partial structures consist of boron both in trigonal-planar and tetrahedral coordination.

Table 1.1 Continued

Compound	Anions complex
Chain	
$M^{II}(C_4H_{12}N_2)[B_2P_3O_{12}(OH)]$ (M^{II} = Co, Zn) [103,104]	loop-branch $\frac{1}{\infty}\{[B_2P_3O_{12}(OH)]^{4-}\}$
$(Co(en)_3)[B_2P_3O_{11}(OH)_2]$ [105]	loop-branch $\frac{1}{\infty}\{[B_2P_3O_{11}(OH)_2]^{3-}\}$
$\{Zn_3(C_6H_{14}N_2)_3[B_6P_{12}O_{39}(OH)_{12})]\}$ $\cdot (C_6H_{14}N_2)[HPO_4]$ [106]	helical chain $\frac{1}{\infty}\{[B_6P_{12}O_{39}(OH)_{12})]^{12-}\}$ and isolated HPO_4–tetrahedra
$A^I_x M^{II}_y(H_2O)_2[BP_2O_8]\cdot zH_2O$ (A^I = Li, Na, K, NH_4, Rb, Cs; M^{II} = Mg, Mn, Fe, Co, Ni, Cu, Zn, Cd; x = 0.35–1, y = 1–1.3, z = 0.2–1) [45,46,107–115]	helical chain $\frac{1}{\infty}\{[BP_2O_8]^{3-}\}$
Layer	
$Na_{1-x}Ag_x[BP_2O_7(OH)]$ (x = 0 and 0.11) [116]	$\frac{2}{\infty}\{[BP_2O_7(OH)]^{2-}\}$
$Rb_2Co_3(H_2O)_2[B_4P_6O_{24}(OH)_2]$ [117]	$\frac{2}{\infty}\{[B_4P_6O_{24}(OH)_2]^{8-}\}$
$M^{II}(C_2H_{10}N_2)[B_2P_3O_{12}(OH)]$ (M^{II} = Mg, Mn, Co, Ni, Cu, Zn) [118,119]	$\frac{2}{\infty}\{[B_2P_3O_{12}(OH)]^{4-}\}$
Framework	
$M^I[B_2P_2O_8(OH)]$ (M^I = Rb, Cs) [120]	$\frac{3}{\infty}\{[B_2P_2O_8(OH)]^-\}$ framework
$Na[ZnBP_2O_8]\cdot H_2O$ [108]	$\frac{3}{\infty}\{[ZnBP_2O_8]^-\}$ framework[‡]
$M^I[ZnBP_2O_8]$ (M^I = K, NH_4) [23,24,45]	$\frac{3}{\infty}\{[ZnBP_2O_8]^-\}$ framework[‡]
$M^I[ZnBP_2O_8]$ (M^I = NH_4, Rb, Cs) [23,46] $NH_4[(Zn_{1-x}Co_x)BP_2O_8]$ ($0 \le x \le 0.14$) [121]	$\frac{3}{\infty}\{[ZnBP_2O_8]^-\}$ framework[‡]
$M^I[BeBP_2O_8]\cdot H_2O$ (M^I = Na, K, NH_4) [122]	$\frac{3}{\infty}\{[BeBP_2O_8]^-\}$ framework[‡]

[‡] Anionic partial structures include zinc-/beryllo-, boron- and phosphorus tetrahedra.

1.2.2 Oligomers and chains

About 80 % borophosphates contain oligomers and single chains as their anionic borophosphate partial structures. Oligomers are presented in almost all the templated vanadium borophosphates and molybdenum borophosphates which include dimer, trimer, tetramer, pentamer, hexamer to heptamer. $\{[BP_2O_{10}H_x]^{(7-x)-}\}$ trimers are the most popular oligomers presented in the vanadium(IV) borophosphates as well as M^{III}–borophosphates. Vanadium(V) borophosphates [71, 72] and molybdenum borophos-

phates consist of multinuclear of oligomers, such as tetramers, pentamers and hep-
tamers.

Single chains consist of loop-branched, open-branched, and unbranched single chains.
The hydrated borophosphates with a molar ratio B : P $\geq$ 3 contain open loop-branched
single chains in which boron atoms are in 3-fold and tetrahedral coordinations. BO_3
groups are exclusively linked to borate species. Terminal (nonbridging) oxygen posi-
tions of the BO_3 groups are always protonated. All the corners of BO_4 tetrahedra share
common corners with neighboring units within the chains. The isotypic compounds
$A^I_x M^{II}_y (H_2O)_2 [BP_2O_8] \cdot z H_2O$ (A^I = Li, Na, K, NH_4, Rb, Cs; M^{II} = Mg, Mn, Fe, Co,
Ni, Cu, Zn, Cd; x = 0.35–1, y = 1–1.3, z = 0.2–1) [45, 46, 107–115] contain infinite
$6_1/6_5$-helices loop-branched tetrahedral chains. The central chain is built of alternat-
ing borate and phosphate units; linking of two borate tetrahedra by an additional
PO_4 group along the chain leads to the formation of 4-membered tetrahedral rings.
Stretched and puckered loop-branched single chains, $\frac{1}{\infty}\{[B_2P_3O_{13}]^{5-}\}$, are presented in
$Na_5[B_2P_3O_{13}]$ [30] and $M^{II}(C_4H_{12}N_2)[B_2P_3O_{12}(OH)]$ (M^{II} = Co, Zn) [103, 104], respec-
tively. Up to now, only one type of borophosphate consists of an unbranched single
chain, they are $Fe[B_2P_2O_7(OH)_5]$ [90] and $Al[B_2P_2O_7(OH)_5] \circ H_2O$ [91] which contain
unbranched tetrahedral vierer single chains.

1.2.3   Zincoborophosphates

Zincoborophosphate is a special family of borophosphates in which zinc, boron and
phosphorus are all in tetrahedral coordination. Three different types of zincoborophos-
phates are known with three-dimensional tetrahedral frameworks structures. The
topologies of their framework structures exhibit zeolite-type structures (see *Fig. 1.1*):
$K[ZnBP_2O_8]$ [23] and $NH_4[ZnBP_2O_8]$ [24] (feldspar family, e.g. Anorthite $Ca[Al_2Si_2O_8]$
[123]), $A^I[ZnBP_2O_8]$ (A^I = NH_4, Rb, Cs) [23, 46, 47] (GIS-type, $Ca[Al_2Si_2O_8] \cdot 4H_2O$
[21]), and $Na[ZnBP_2O_8] \cdot H_2O$ [108] (CZP-type, $Na[ZnPO_4] \cdot H_2O$ [25]). In the crystal
structure of $NH_4[ZnBP_2O_8]$ [23], Zn was partially replaced by Co, bringing this redox-
active center that could lead to interesting catalytic characteristic. It is clear that
the known zincoborophosphates have a molar ratio of Zn : B : P = 1 : 1 : 2 accord-
ing to their formula. The known zincoborophosphates contain only inorganic cations
like alkaline metal and ammonium. Thus it is interesting to investigate the templated
zincoborophosphates with large cations.
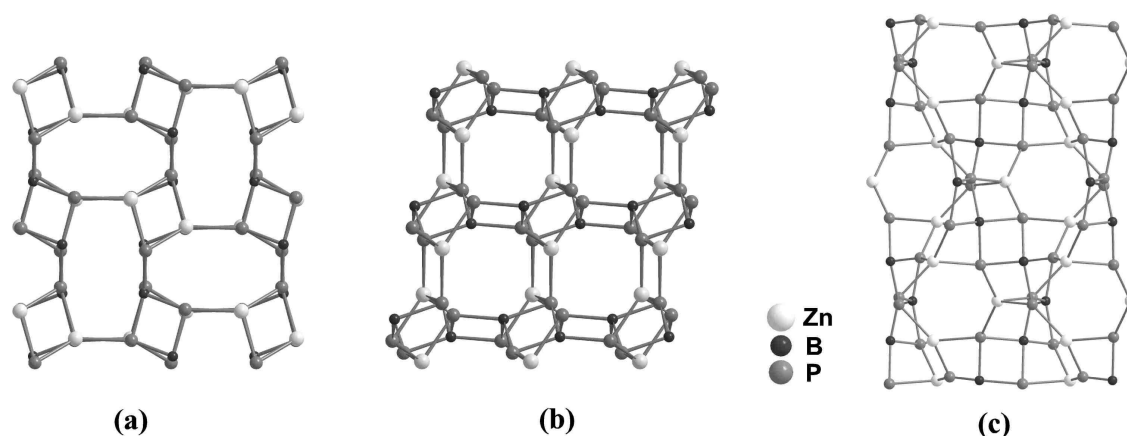
Figure 1.1: Topologies of three different types of zincoborophosphates: (a) K[ZnBP$_2$O$_8$] [23, 45] (feldspar family), (b) NH$_4$[ZnBP$_2$O$_8$] [23] (GIS-type), (c) Na[ZnBP$_2$O$_8$] · H$_2$O [108] (CZP-type).

1.2.4 Templated borophosphates

After the first organic templated borophosphate, Co(C$_2$H$_{10}$N$_2$)[B$_2$P$_3$O$_{12}$(OH)] [118], was reported by Sevov *et al.* in 1996, several templated vanadium(IV/V) borophosphates [64–71,73,74,124] were reported mainly by the groups of Jacobson and Haushalter in USA. Two molybdenum borophosphates [76,77] were also reported by Sevov's group. Some other transition metal (e.g. Zn, Co) templated borophosphates [103,106, 119] were reported by Kniep's group.

The known templated vanadium borophosphates only contain vanadium in the valence state of +4 and +5 in which vanadium atoms are either in square pyramidal (VO$_5$) or distorted octahedral (5+1) and octahedral (VO$_6$) coordinations. It is common that vanadium polyhedra together with borophosphate oligomers form into oxovanadium-borophosphate clusters. *Fig. 1.2* shows three kinds of typical oxo-vanadium borophosphate clusters. Two isotypic molybdenum borophosphates are with the same oxomolybdenum-borophosphate clusters (Wells-dawson) which are built up by twelve MoO$_6$ octahedra and two borophosphate pentamers. Other transition metals (e.g. Zn, Co) are either in perfect octahedral coordination or in distorted octahedral (5+1) coordination which are isolated by anionic borophosphate partial structures.
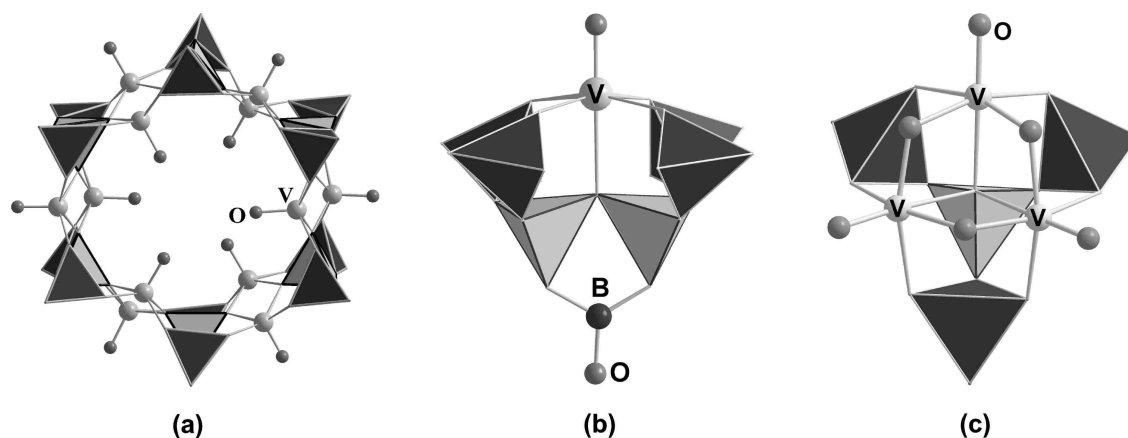
Figure 1.2:   Three types of oxovandium borophosphate clusters are observed in the templated vanadium borophosphates: (a) $\{\{[(V_2O_2)(BP_2O_{10})]_6\}^{18-}\}$ cluster, (b) $[VO(PO_3OH)_4(B_3O_3OH)]^{4-}$ cluster, (c) $[V_3BP_3O_{19}]^{5-}$ cluster.

Organic amines are often used as templates, which are bound to the main structure or act as independent space-needing species (molecular or ionic) to direct the structural arrangement of the framework. In the known templated borophosphates, all the organic templates are diprotonated cations which either reside in the channels and cages or around the clusters. Since the organic template is present as diprotonated cation to balance the charge of framework, it is absolutely necessary for the crystal structure building, it can not be removed by pyrolysis without breaking down the framework.

1.3   Motivation and objective for the present investigations

The goal of the present work was to synthesize and characterize new organo-templated borophosphate with open framework structures.

As mention above, many organo-templated vanadium borophosphates with pure 4+ or 5+ were reported. There is still no report on mix-valence vanadium borophosphate. One of our works is to synthesize and characterize the mix-valency vanadium borophosphates. As a result, we obtained a new compound with new structure motif. Its crystal structure can be considered as "intergrowth" of puckered vanadium(III) borophosphate layers and planar vandium(IV) phosphate layers.

The term template means "form-giving pattern" or "molding matrix". This term is also used for chemical compounds, which affect the structural building of crystalline

solids during crystal growth. So depending upon the shape and size of the templates, organic templates may be able to control the shape and size of cavities, channels or layers in the framework structure. But there are still no good example to prove this. For this reason, our aim is to study the role of template in the borophosphates. It is our chance to obtain two manganese borophosphates with identical framework conformation but difference in the shape and size of channels which are influenced by the shape and size of templates (linear $(H_2DAP)^{2+}$ and cyclic $(H_2PIP)^{2+}$).

The known zincoborophosphates contain only inorganic cations like alkaline metal and ammonium in their crystal structures. To study zincoborophosphate with large size of organo cations become an interesting object. Here we obtain one organo-templated zincoborophosphate. In this crystal structure, the organic template diaza-bicyclo[2.2.2]-octane (DABCO) plays two roles in this structure: the diprotonated one acts as pure template directing the ribbons, the mono-protonated one bonded to Zn positions at the border of zincoborophosphate ribbons. In addition, the thermal behavior of $(C_6H_{14}N_2)\{Zn[ZnB_2P_4O_{15}(OH)_2] \cdot (C_6H_{13}N_2)Cl\}$ has been studied by temperature-dependent X-ray powder diffraction and thermal analysis. The new phase occurring during the decomposition has been identified as $HT\text{-}NH_4[ZnBP_2O_8]$.

Fluorine substituted borophosphates were the first time to be studied. Here we obtained one fluorine substituted borophosphate whose crystal structure is closely related to the pyroxene type structure.

To synthesize the templated borophosphates and metallo-borophosphates, hydrothermal method was employed. The products were characterized by powder X-ray diffraction and single crystal X-ray diffraction. High temperature powder X-ray diffraction (HT-XRD) was applied to identify the intermediate phase during the decomposition. Rietveld refinement was employed to refine the structure where single crystals could not be obtained. ICP-AES, C-/N-/H-analysis and EDX were used to determine the chemical composition of products. Thermal analyses (DTA-TG, DSC) were used to investigate the thermal stability and decomposition process. IR-spectroscopy was performed to confirm the functional groups (O–H, C–H and N–H) in the compounds. The temperature dependent magnetic susceptibilities were measured for the compounds containing transition elements. ^{19}F MAS NMR was applied to check the number of fluorine positions in the crystal structure.

2 Experimental

2.1 Preparation methods and chemicals

Hydrothermal syntheses [42,125] have been employed for preparation of new borophosphates presented in this work. The reactions were carried out in either Teflon autoclaves (ROTH BOLA, reaction volume: 10 ml or 20 ml) (*Fig. 2.1*) or Teflon-lined stainless steel autoclaves (BERGHOF, reaction volume: 25 ml) (*Fig. 2.2*) under autogenous pressure. The reaction temperatures range from 140 °C to 220 °C. At reaction temperatures equal or lower than 170 °C, Teflon autoclaves were used; at higher temperatures (> 170 °C), Teflon-lined stainless steel autoclaves were taken.
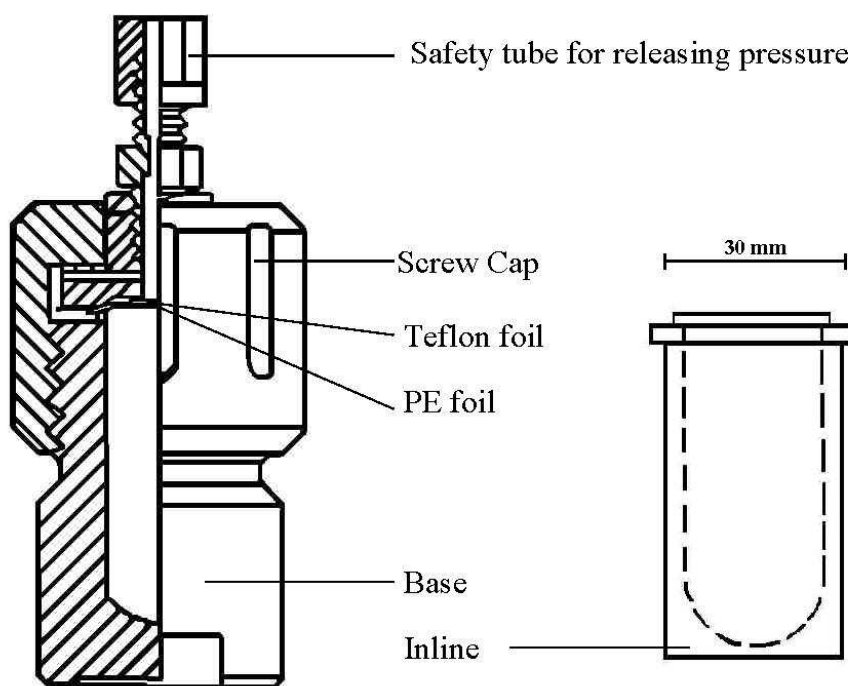
Figure 2.1: Teflon autoclave for hydrothermal syntheses below 170 °C (ROTH BOLA).

The general process of preparation was as follows: A mixture of the reagents was added to water, stirred at room temperature or higher temperature for several hours. 37% HCl was added to adjust the pH value to acid conditions (pH = 1.0−3.0). The mixtures were transferred into autoclaves with different filling degree (30−80%) and

kept in an oven (140 − 220 °C) for 3−30 days. The solid products were filtrated and washed with deionized water, and finally dried at 60 °C. Most of the products contained crystals which were large enough for single crystal measurements and structure determinations. Only few compounds were obtained as fine powders.

The pH value is an important factor to control the reactions, in most of cases, acid conditions lead to borophosphates and basic condition lead to phosphates only.
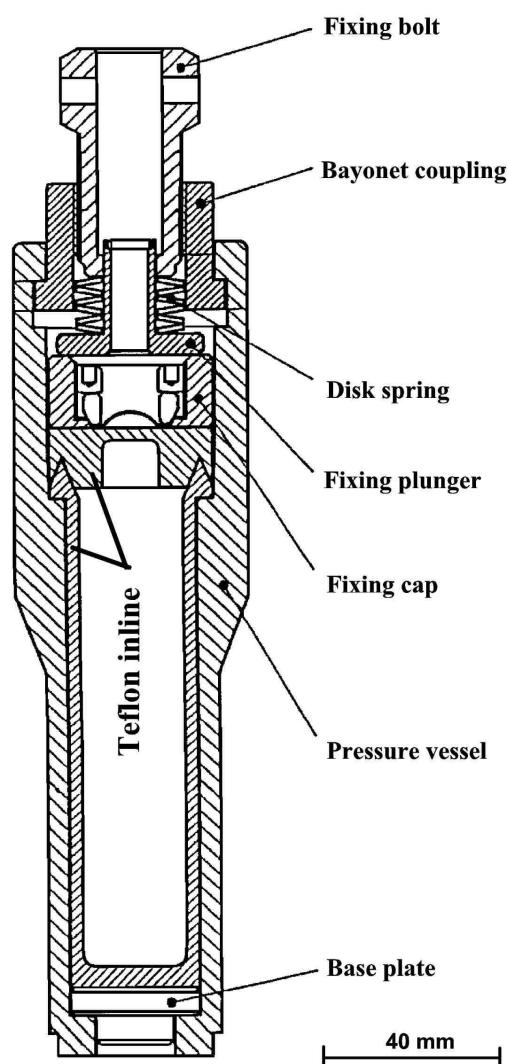
Figure 2.2: Teflon-lined stainless steel autoclave for reaction temperatures up to 220 °C.

The chemicals used for the reactions are listed in *Table 2.1*. As metal sources the respective halides, as boron sources, H_3BO_3, B_2O_3, $BF_3 \cdot C_2H_5NH_2$ and other borates

were used. The phosphorus sources were 85% H_3PO_4 or other phosphates. Aliphatic
diamines were used as organic templates.

Table 2.1: Chemicals used for the hydrathermal synthesis of borophosphates.

Formula	Company	Purity
$ZnCl_2$	MERCK	99.99%
$MnCl_2$	MERCK	96%
VCl_3	ALFA	99%
$FeCl_3 \cdot 6H_2O$	MERCK	99.0%
B_2O_3	ALFA	99.9%
H_3BO_3	ROTH	99.9%
$BF_3 \cdot C_2H_5NH_2$	ALDRICH	99.9%
$K_2B_4O_7 \cdot 4H_2O$	MERCK	99 %
K_2HPO_4	MERCK	99 %
H_3PO_4 (85 %)	MERCK	99.9%
HCl (37 %)	MERCK	99.9%
$C_2H_8N_2$	ALDRICH	99%
$C_3H_{10}N_2$	ALDRICH	99%
$C_4H_{10}N_2$	ALDRICH	99%
$C_6H_{12}N_2$	ALDRICH	99%

2.2   Characterization

2.2.1   Powder X-ray diffraction

Powder X-ray diffraction was primarily used to identify the reaction products by com-
paring with powder patterns from databases (as PDF format) or with powder patterns
simulated from single crystal data. X-ray powder patterns were also used for the precise
determination of cell parameters. The measurements were carried out on the X-ray-
powder-diffractometer of HUBER Image Foil Guinier Camera G670 (Cu $K_{\alpha 1}$-radiation,
Germanium (111) monochromator; Cr $K_{\alpha 1}$-radiation, Germanium (111) monochroma-
tor; and Co $K_{\alpha 1}$-radiation, Quartz ($10\bar{1}\bar{1}$) monochromator). X-ray powder investiga-
tions were prepared by using glass capillaries or flat foils on aluminum rings. In general,
data were collected in the range of $3° \leq 2\theta \leq 100°$ with 0.005 degree per step. The
data were handed by using the STOE Winxpow software package (version 1.09) [P1].

High temperature powder X-ray diffraction (HT-XRD) was carried out on a STOE-diffractometer (STOE STADI MP, Cu$K_{\alpha 1}$-radiation, Ge monochromator, STOE-high temperature attachment 0.65.3). Powder samples were filled in quartz capillaries of 0.5 mm diameter. The capillaries was kept open during the measurements. The heating rate between two steps was 5 K/min and the scanning time was one hour per step.

2.2.2   Single crystal X-ray diffraction

Single crystal X-ray diffraction techniques were used to collect single crystal data for determining the crystal structure. Suitable crystals were fixed on the tip of a capillary by using two-component glue, and mounted on a four-circle-diffractometer equipped with a Mercury-CCD detector (RIGAKU AFC 7 CCD, Mo K_α-radiation, Graphite monochromator) and a RIGAKU AFC 8 diffractometer, equipped with curved R-axis Rapid imagining plate detector (Mo K_α-radiation, Graphite monochromator), respectively. In some cases, the Laue method or a polarization microscope were used in order to check for possible twining of crystals and to check the quality of single crystals. The collected data were corrected for Lorenz, polarization corrections and absorption effects. Initial model of crystal structures were obtained by using direct method and refined by least-square method applying SHELXS-97 [P2] and SHELEXL-97 [P3] programs, respectively. The position of the light atoms were taken from difference Fourier maps. The intensity were corrected by using multi-scan methods, in some cases, additional numerical correction based on the crystal shape was performed. To evaluate the quality of structure model gives the R-value, which indicate the agreement of observed (F_o) and calculated (F_c) F-values. $R1$ is defined by:

$$R1 = \frac{\sum\limits_{hkl} ||F_o| - |F_c||}{\sum\limits_{hkl} |F_o|} \tag{2.1}$$

The weighted R-factor $wR2$ base on F^2.

$$wR2 = \sqrt{\frac{\sum\limits_{hkl} w(F_o^2 - F_c^2)^2}{\sum\limits_{hkl} w(F_o^2)^2}} \tag{2.2}$$

where the w-value is coming from

$$w = \frac{1}{\sigma^2(F_o^2) + (aP)^2 + bP} \tag{2.3}$$

and

$$P = \frac{2F_c^2 + max(F_o^2, 0)}{3} \tag{2.4}$$

Another important factor for evaluating the quality of crystal structure refinement is Goodness-of-fit (GooF):

$$GooF = S = \sqrt{\frac{\sum\limits_{hkl} w(F_o^2 - F_c^2)^2}{n - p}} \tag{2.5}$$

where n is the number of reflections and p is the total number of parameters refined. A right structure model normally require the S value near to 1.

2.2.3   Inductively coupled plasma-optical atomic emission spectroscopy (ICP-AES) and combustion technique

The inductively coupled plasma-optical atomic emission spectroscopy (ICP-AES) [126] was applied to analyze metals, boron, and phosphorus in the reaction products. The analysis is carried out in the spectrometer VARIAN Vista (excited by Ar Plasma, radial observation). Samples of arround $10-20$ mg were dissolved (by 37% HCl, HNO_3 or their mixture) and diluted with water. The solution was injected into the Plasma. The optical emission was detected by an optic spectrometer.

Organic carbon, nitrogen and hydrogen contents were analyzed in a LECO CHNS-932, which applies the hot extraction method [126]. About $10-15$ mg of a sample was encapsulated in tin foil, then exposed to high temperature combustion in an enriched oxygen environment in the presence of WO_3 in which C, H and N were oxidized to CO_2, H_2O and NO_x. The gases pass through heated copper metal where NO_x is reduced and excess O_2 is removed. H_2O and CO_2 are measured using independent NDIR (non-dispersive Infrared Spectroscopy) detectors, N_2 is determined via TC (thermal conductivity) detection. The contents of C, H and N were determined quantitatively.

2.2.4 Scanning electron microscopy (SEM) and energy dispersive X-ray analysis (EDX)

SEM (PHILLIPS XL 30 or Jeol JSM-6400 equipped with energy dispersive spectroscopy EDX) was applied for examining texture, morphology and surface details of crystals. EDX (PHILLIPS XL 30 with software package EDAX, sample sputtered with carbon) was applied to half-quantitatively identify the elements present on the crystal surface by detecting the energy of the emitted X-rays. The samples were placed on a substrate (sample holder), sputtered with Au for SEM and with carbon for EDX to increase their surface conductivity. In general, EDX allows elemental analysis for atomic numbers (Z) greater than 10, therefore boron can not be detected in EDX.

2.2.5 Differential thermal analysis (DTA), thermogravimetry (TG) and differential scanning calorimetry (DSC)

Thermal analysis (DTA/TG) were carried out under static air atmosphere (NETZSCH STA 409 EP). About $30-50$ mg of a sample was put into a corundum-crucible (empty corundum-crucible as reference). The temperature ranges from 30 °C to 1000 °C with the heating and cooling rate of 5 °C/min. The measurements were analyzed by applying the program from NETZSCH (Proteus 4.0 beta, NETZSCH-Gerätebau 1999). Weight changes in TG curves and temperature difference in DTA curves give information on reactions, decompositions, phase transitions, recrystallizations, and so on.

Differential scanning calorimetry (DSC) was carried out in a DSC-equipment (NETZSCH DSC 204, Pt-Pt/Rh-thermoelement). The sample was encapsulated in an aluminum corundum. This method is used to determine thermodynamic parameters such as enthalpy and specific heat.

2.2.6 Infrared spectroscopy (IR)

Infrared spectra were recorded using a spectrometer from BRUKER (IFS 66v/S; Globar (MIR), KBr, DTGS-Detector; Program Opus/IR 3.0.3). The tablets for IR measurements consist of mixtures of 1.5 mg sample together with 150 mg KBr (MERCK, *Uvasol* for IR-Spectroscopy). The investigated wavenumber range was 4000–400 cm^{-1}. The IR spectra were used to obtain either structure information or "finger prints". The coming

out spectra were compared with the literature data from the known borophosphates.

2.2.7   Magnetic susceptibility

The magnetic susceptibilities of $(C_3H_{12}N_2)Fe^{III}_6(H_2O)_4[B_4P_8O_{32}(OH)_8]$, $(C_3H_{12}N_2)$-$\{Mn[B_2P_3O_{12}(OH)]\}$, $(C_4H_{12}N_2)\{Mn[B_2P_3O_{12}(OH)]\}$ and $(C_3H_{12}N_2)_2\{V^{III}_2V^{IV}_3B_2P_8O_{38}H_8\}$ were measured using a SQUID-Magnetometer (Quantum Design, MPMS XL–7). The powders or crystals (about 30 mg) were put in an quartz-glass tube (inner diameter: 4 mm; wall thickness: 1 mm). The magnetic susceptibilities were measured in the temperature range of 1.8–400 K and by applying external magnetic fields from 100 Øe to 70 kØe.

2.2.8 ^{19}F MAS NMR Spectroscopy

The ^{19}F MAS NMR experiment of $(C_2H_{10}N_2)[BPO_4F_2]$ was performed with a BRUKER AV 400WB spectrometer to identify fluorine sites. The ^{19}F MAS NMR spectrum was acquired at a spinning rate of 35 kHz (2.5 mm rotor) under the following conditions: no decoupling referenced to trifluoroacetic acid (-78.5 ppm); a simple one pulse acquisition was used with a ^{19}F $\pi/2$ pulse of 3 ms, an acquisition time of 16 ms, a dead time delay of 4.5 ms, and a recycle delay of 10 s; resonance frequency of 376.5 MHz. A total of 64 scans was accumulated.

3 Results and discussion

3.1 $(C_2H_{10}N_2)[BPO_4F_2]$

3.1.1 Synthesis

$(C_2H_{10}N_2)[BPO_4F_2]$ was prepared under mild hydrothermal conditions from a mixture of 0.81 g (13.5 mmol) ethylenediamine ($C_2H_8N_2$, **en**), 1.12 g (18.1 mmol) H_3BO_3, 2.04 g (18.1 mmol) $BF_3 \cdot C_2H_5NH_2$ and 2.08 g (18.1 mmol) 85 % H_3PO_4 (molar ratio of en : H_3BO_3 : $BF_3 \cdot C_2H_5NH_2$: $H_3PO_4 = 0.75 : 1 : 1 : 1$) by adding 10 ml of deionized water and stirring at 100 °C. Meanwhile, 0.7 ml of 37 % HCl was slowly added leading to a highly viscous red-orange gel with a pH-value of 3. The gel was kept at 220 °C for three days under autogenous pressure in a Teflon-lined stainless steel autoclave ($V = 25$ ml, degree of filling ≈ 30 %). The solid reaction product was filtered, washed with deionized water and dried at 60 °C. Only few colorless crystals of good quality were observed. *Fig. 3.1* shows the SEM micrograph of a single crystal. $(C_2H_{10}N_2)[BPO_4F_2]$ can also be prepared in the absence of H_3BO_3 (molar ratio of **en** : $BF_3 \cdot C_2H_5NH_2$: $H_3PO_4 = 0.75 : 2 : 1$) at 170 °C within three to five days of reaction time. This result indicates that the boron content in $(C_2H_{10}N_2)[BPO_4F_2]$ is originating from $BF_3 \cdot C_2H_5NH_2$.
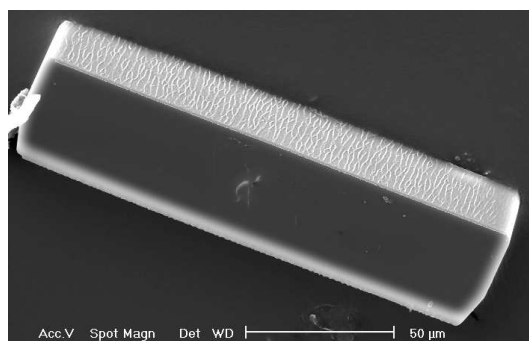
Figure 3.1: SEM micrograph of an elongated prismatic single crystal of $(C_2H_{10}N_2)[BPO_4F_2]$.

Phase purity for the reaction products was initially checked using powder X-ray diffraction (HUBER Image Foil Guinier Camera G670, Cu $K_{\alpha 1}$-radiation, germanium monochromator). *Fig. 3.2* shows the observed and the calculated powder pattern from the structure determination. The good fit indicates a high purity of the sample.
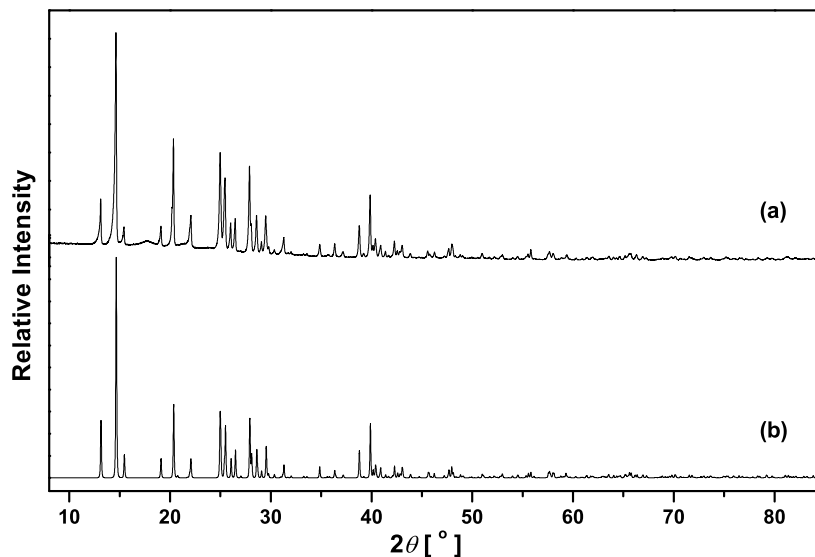
Figure 3.2: Powder X-ray diffraction patterns of $(C_2H_{10}N_2)[BPO_4F_2]$, (a) observed, (b) calculated from structure data (see chapter 2.2.1); Cu $K_{\alpha 1}$-radiation.

Boron and phosphorus were analyzed using ICP-AES, while a hot extraction method was applied for carbon and nitrogen. The fluoride content was determined semi-quantitatively using a fluoride sensitive electrode (Microprocessor-Hochleistungs-pH-Ionen-Meter, pMX 3000/ION, Wissenschaftlich-Technische Werkstätten GmbH). Results of the chemical analyses are given in *Table 3.1*. The presence of the elements, except for boron and hydrogen, were also confirmed by EDX measurements (Philips XL 30 with software package EDAX, sample sputtered with gold).

Table 3.1: Results of the chemical analyses of $(C_2H_{10}N_2)[BPO_4F_2]$.

Element	Obs.(e.s.d.)/mass-%	Calc. /mass-%
B	5.24(2)	5.25
P	14.43(4)	15.04
C	11.68(9)	11.67
N	13.82(9)	13.61
H	4.87(2)	4.89
F	16.9(2)	18.3

3.1.2 Crystal structure determination

The crystal structure of $(C_2H_{10}N_2)[BPO_4F_2]$ was determined by using a colorless prismatic crystal ($0.12 \times 0.03 \times 0.02$ mm^3). Single crystal data were collected on a RIGAKU AFC7 four-circle diffractometer, equipped with a Mercury-CCD detector (Mo K_α-radiation, graphite monochromator) in the angular range $3.38°{\leq}2\theta \leq 56.14°$ ($300°$-ϕ-scan, $60°$-ω-scan at $\chi = 90°$, $0.6°$ steps with 150 s exposure time per step, detector distance: 40 mm; 2θ-offset: $-10.00°$). The data were corrected for Lorentz and polarization effects. A multi-scan absorption correction was applied. The structure was solved in the space group $P\bar{1}$ (No. 2) by direct methods using the program SHELXS-97-2 [P2]. Fourier calculations and subsequent full-matrix least-square refinements were carried out using SHELXL-97-2 [P3] applying neutral-atom scattering factors. The crystallographic results are summarized in *Table 3.2*. After anisotropic displacement parameters had been included in the refinement, all hydrogen atoms were located from the difference Fourier map and refined without applying any restraints. Fluorine positions were deduced according to rather short distance to boron and higher R-values when replaced with oxygen. Atomic coordinates and displacement parameters for $(C_2H_{10}N_2)[BPO_4F_2]$ are given in *Tables 3.3* and *Table 6.3*, selected interatomic distances and angles in *Table 3.4* and *Table 3.5*. Displacement parameters and bond lengths are consistent with an ordered distribution of O and F.

Table 3.2: Crystallographic data and refinement details for $(C_2H_{10}N_2)[BPO_4F_2]$.

Compound		$(C_2H_{10}N_2)[BPO_4F_2]$
Space group	:	$P\bar{1}$ (No. 2)
Cell parameters [pm/°]	:	$a = 451.85(5)/\alpha = 86.08(1)$
		$b = 710.20(8)/\beta = 88.52(2)$
		$c = 1210.2(2)/\gamma = 71.74(1)$
V [$10^6 \cdot$pm^3]$/Z$	:	$367.93(8)/2$
Calc. density ρ [g $\cdot$ cm^{-3}]	:	1.859
Diffractometer	:	RIGAKU AFC7 CCD
		Mo K_α-radiation
		Graphite monochromator
$\mu_{MoK\alpha}$ [mm^{-1}]	:	0.39
Scan type	:	ϕ/ω
2θ range [°]	:	3.38–56.14
Miller-index range	:	$-4 \leq h \leq 5$
		$-8 \leq k \leq 8$
		$-14 \leq l \leq 14$

Table 3.2 Continued

Total data collected	:	3422
Unique data	:	1386
Observed data $I > 2\sigma(I)$	:	1121
R_{int}/R_σ	:	0.035/0.048
Number of refined parameters	:	150
$R1$ $(F_\circ > 4\sigma(F_\circ))/R1$ (all data)	:	0.059/0.082
w$R2$ $(F_\circ > 4\sigma(F_\circ))/wR2$ (all data)	:	0.105/0.113
Goodness-of-Fit (on F^2)	:	1.144
Residual electron density	:	0.294/$-$0.393
(max./min.) [e$\cdot 10^{-6}$pm^{-3}]		
Programs	:	DIAMOND [P4]
		SHELXS–97/2 [P2]
		SHELXL–97/2 [P3]

<u>Table 3.3</u>: $(C_2H_{10}N_2)[BPO_4F_2]$: Atomic coordinates and equivalent/isotropic displacement parameters (10^{-4}pm^2), e.s.d.'s are given in parentheses.

Atom	Site	x	y	z	$U_{\text{eq}}/ U_{\text{iso}}$
P1	$2i$	0.3076(2)	0.29327(15)	0.73839(9)	0.0220(3)
B1	$2i$	0.6952(10)	0.5095(7)	0.7758(4)	0.0268(10)
O1	$2i$	0.9579(6)	0.3291(4)	0.7712(2)	0.0238(6)
O2	$2i$	0.3329(6)	0.3221(4)	0.6137(2)	0.0292(7)
O3	$2i$	0.4038(6)	0.4592(4)	0.7929(2)	0.0270(7)
O4	$2i$	0.4836(6)	0.0890(4)	0.7850(2)	0.0303(7)
F1	$2i$	0.7194(6)	0.6195(4)	0.8634(2)	0.0467(8)
F2	$2i$	0.6765(6)	0.6270(4)	0.6764(2)	0.0476(8)
N1	$2i$	0.0702(8)	0.8874(5)	0.8622(3)	0.0252(8)
H1	$2i$	0.114(10)	0.761(7)	0.841(4)	0.037(13)*
H2	$2i$	-0.117(10)	0.954(6)	0.832(3)	0.021(10)*
H3	$2i$	0.238(13)	0.940(8)	0.838(4)	0.062(16)*
C1	$2i$	0.0478(11)	0.8935(6)	0.9842(3)	0.0290(9)
H4	$2i$	$-$0.104(10)	0.824(7)	1.012(4)	0.040(13)*
H5	$2i$	0.245(12)	0.817(7)	1.014(4)	0.052(15)*
N2	$2i$	0.8598(9)	0.2779(5)	0.4907(3)	0.0266(8)
H6	$2i$	0.667(12)	0.301(7)	0.540(4)	0.052(15)*
H7	$2i$	1.032(12)	0.288(7)	0.532(4)	0.052(15)*
H8	$2i$	0.804 (11)	0.380(8)	0.430(4)	0.057(15)*
C2	$2i$	0.0382(10)	0.9254(6)	0.5497(3)	0.0287(9)
H9	$2i$	$-$0.150(9)	0.945(6)	0.600(3)	0.022(10)*
H10	$2i$	0.206(10)	0.940(6)	0.591(3)	0.031(11)*

*refined with isotropic displacement parameters

3.1.3 Crystal structure description

The crystal structure of $(C_2H_{10}N_2)[BPO_4F_2]$ contains infinite chains $\frac{1}{\infty}\{[BPO_4F_2]^{2-}\}$ which are built from alternating PO_4- and BO_2F_2-tetrahedra sharing common oxygen corners (*Fig. 3.3*(b)). The chains can be classified as unbranched zweier-single chains [20]. They are isoelectronic ($48e^-$ systems) to the zweier-single silicate chains $\frac{1}{\infty}\{[Si_2O_6]^{4-}\}$ (*Fig. 3.3*(a)) which are characteristic for the pyroxene family (e.g. Diopside, $(CaMg)[Si_2O_6]$ [127]). The essential structural difference between the zweier-single chains (*Fig. 3.3*(a) and *Fig. 3.3*(b)) results from the relative orientation (conformation) of adjacent tetrahedra along a chain: In looking along the $Si1\cdots Si1$ ($B1\cdots P1$)-directions, adjacent tetrahedra are in an almost eclipsed (staggered) arrangement, respectively. By this (staggered conformation), the terminal fluorine (F1, F2)- and the terminal oxygen (O2, O4)-positions of adjacent tetrahedra in the borophosphate chain reach $F\cdots O$ distances > 317.3(1) pm ($F1\cdots O2$). Bond angles at the bridging oxygen sites within the chains are $132.5°$ (pyroxene, *Fig. 3.3*(a)), $127.7(3)°$ (B1–O3–P1) and $131.9(2)°$ (P1–O1–B1) for $(C_2H_{10}N_2)[BPO_4F_2]$ (*Fig. 3.3*(b)). Similar values for angles at the bridging oxygen positions are observed in the unbranched vierer-single chain $\frac{1}{\infty}\{[B_2P_2O_7(OH)_5]^{3-}\}$ [90] given in *Fig. 3.3*(c): $135.2(3)°$ (B1–O1–P1) and $130.3(2)°$ (P1–O6–B1).

The arrangement of anionic chains $\frac{1}{\infty}\{[BPO_4F_2]^{2-}\}$ running parallel along [100] in the crystal structure of $(C_2H_{10}N_2)[BPO_4F_2]$ is shown in *Fig. 3.4*. The chains are running along [100] and have a periodicity of 451.85 pm, equal with the crystallographic a-axis. The building units of chains are related by a center of symmetry, leading to alternating sheets along the c axis in the (100) plane. The sheets of $\frac{1}{\infty}[BPO_4F_2]^{2-}$ chains are separated by alternating sheets of either **en1** (built from C1 and N1 with corresponding protons, see *Table 3.3*) or type **en2** (built from C2 and N2). **en1** is located with its center of the C–C bond on the center of inversion in corner of the unit cell, **en2** is arranged with its C–C bond center at the centers of inversion on $(0,0,\frac{1}{2})$, with the same orientation in each case.

$(C_2H_{10}N_2)^{2+}$ ions (denoted as **en1** and **en2**) interconnect the borophosphate chains via N–H$\cdots$O and N–H$\cdots$F hydrogen bridges. The systems of hydrogen bridges which fix the diprotonated **en1**- and **en2**- molecules between neighboring polyhedral chains are shown in *Fig. 3.5*. Concerning the distances of N$\cdots$F and N$\cdots$O (see *Table 3.5*), the hydrogen bridges can be classified as "moderate strong" [128]. The interatomic

distances found for both $(C_2H_{10}N_2)^{2+}$ ions (C1–C1 151.1(8) pm, C1–N1 147.9(5) pm and C2–C2 151.8(8) pm, C2–N2 148.5(5) pm) are comparable with ethylenediammonium ions in other borophosphates $(Mg(C_2H_{10}N_2)[B_2P_3O_{12}(OH)]$ [119]: C–C 151.4(5) pm, C–N 147.2(4) pm and 148.7(4) pm). All angles within the $(C_2H_{10}N_2)^{2+}$ ions are close to tetrahedral angles (see *Table 3.4*).
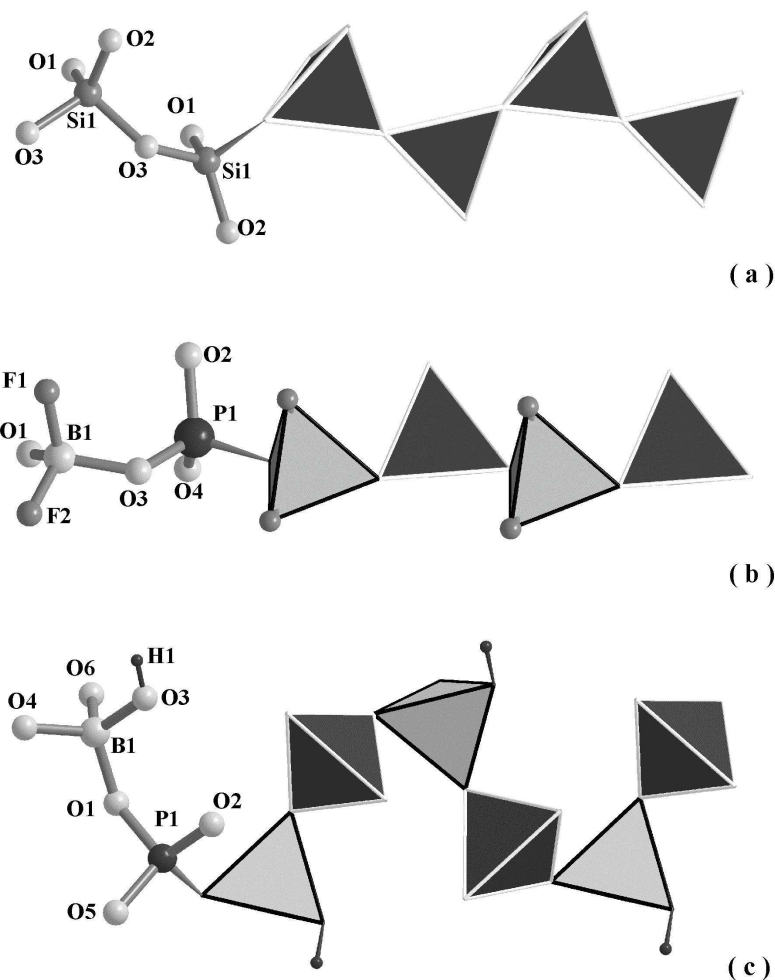
Figure 3.3: (a) Part of an unbranched zweier-single chain $\frac{1}{\infty}\{[Si_2O_6]^{4-}\}$ in the crystal structure of $(CaMg)[Si_2O_6]$ [127]. Ball and stick together with polyhedral presentation. (b) Part of an unbranched zweier-single chain $\frac{1}{\infty}\{[BPO_4F_2]^{2-}\}$ in the crystal structure of $(C_2H_{10}N_2)[BPO_4F_2]$. PO_4 tetrahedra: dark grey, BO_2F_2 tetrahedra: light grey, F atoms: medium grey spheres. (c) Part of the unbranched vierer-single chain $\frac{1}{\infty}\{[B_2P_2O_7(OH)_5]^{3-}\}$ in the crystal structure of $Fe[B_2P_27(OH)_5]$ [90]. PO_4 tetrahedra: dark grey, BO_4 tetrahedra: light grey, hydrogen atoms: black.
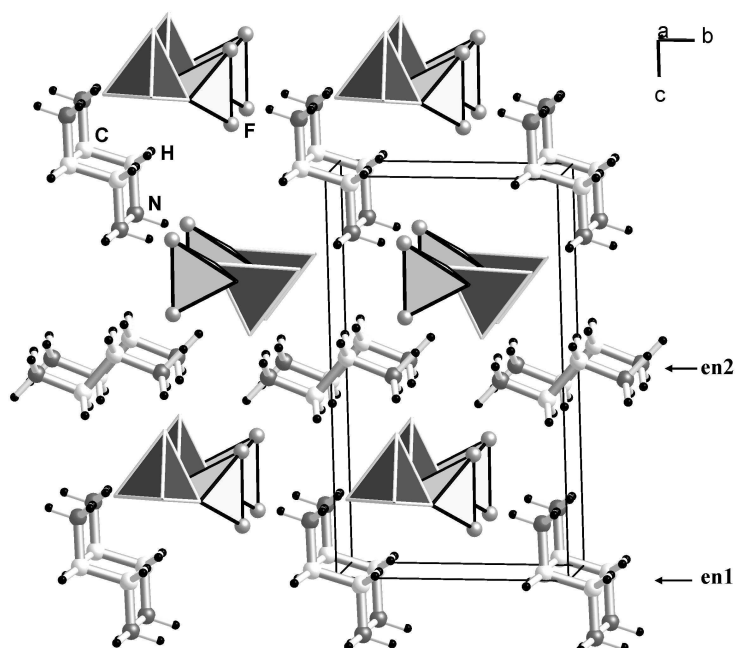
Figure 3.4: Crystal structure of $(C_2H_{10}N_2)[BPO_4F_2]$ viewed approximately along [100]. The two crystallographically inequivalent $(C_2H_{10}N_2)^{2+}$ ions are denoted as **en1** and **en2**, respectively (PO_4 tetrahedra: dark grey, BO_4 tetrahedra: light grey).
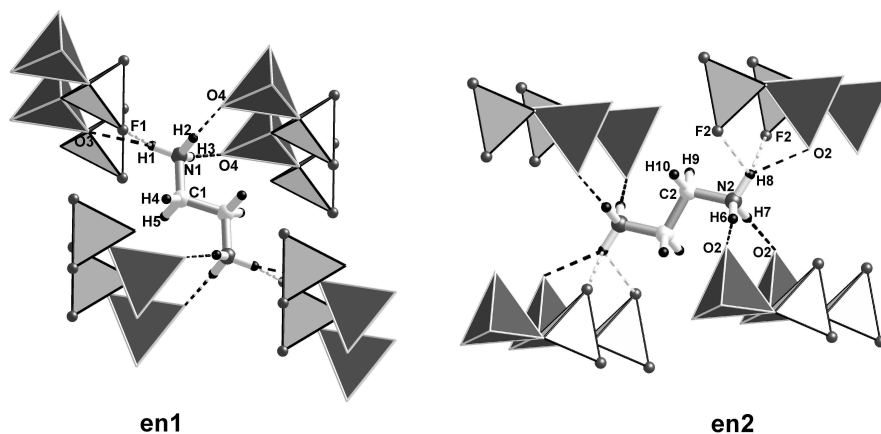
Figure 3.5: Hydrogen bonds N–H$\cdots$O and N–H$\cdots$F between $(C_2H_{10}N_2)^{2+}$ (**en1** and **en2**) and the zweier-single chains $\frac{1}{\infty}\{[BPO_4F_2]^{2-}\}$. N–H$\cdots$O hydrogen bonds are shown as black dotted lines and N–H$\cdots$F hydrogen bonds as grey dotted lines. PO_4 tetrahedra: dark grey, BO_4 tetrahedra: light grey, hydrogen atoms: black. For interatomic distances see *Table 3.5*.

Table 3.4: $(C_2H_{10}N_2)[BPO_4F_2]$: selected interatomic distances and angles, e.s.d.'s are given in parentheses.

		distance [pm]		angle [°]		angle [°]
P–	O4	149.8(3)	O4–P–O2	114.21(17)	O2–P–O3	108.71(16)
	O2	151.5(3)	O4–P–O1	106.47(15)	O1–P–O3	105.46(14)
	O1	156.5(3)	O2–P–O1	109.13(15)		
	O3	156.6(3)	O4–P–O3	112.44(16)		
B–	O1	145.1(5)	O1–B–O3	109.9(3)	O1–B–F1	111.8(3)
	O3	147.5(5)	O1–B–F2	109.9(4)	O3–B–F1	106.7(3)
	F1	138.5(5)	O3–B–F2	109.4(3)		
	F2	140.4(5)	F1–B–F2	109.0(4)		
C1–	C1	151.1(8)	N1–C1–C1	109.8(4)		
	N1	147.9(5)				
C2–	C2	151.8(8)	N2–C2–C2	108.6(4)		
	N2	148.5(5)				

Table 3.5: Hydrogen bonds of $(C_2H_{10}N_2)[BPO_4F_2]$: interatomic distances [pm] and angles [°]

Hydrogen bonds							
N1–H1	91	H1···O3	224	N1···O3	310	N1–H1···O3	158
		H1···F1	231	N1···F1	283	N1–H1···F1	117
N1–H2	90	H2···O4	184	N1···O4	274	N1–H1···O4	174
N1–H3	98	H3···O4	184	N1···O4	280	N1–H1···O4	167
N2–H6	102	H6···O2	171	N2···O2	272	N2–H6···O2	174
N2–H7	96	H7···O2	179	N2···O2	274	N2–H7···O2	175
N2–H8	97	H8···O2	205	N2···O2	291	N2–H8···O2	146
		H8···F2	257	N2···F2	308	N2–H8···F2	112

3.1.4 ^{19}F MAS NMR Spectroscopy

The ^{19}F MAS NMR experiment was performed with a BRUKER AV 400WB spectrometer to identify fluorine sites. The ^{19}F MAS NMR spectrum (*Fig. 3.6*) was acquired at a spinning rate of 35 kHz (2.5 mm rotor) under the following conditions: no decoupling referenced to trifluoroacetic acid (-78.5 ppm); a simple one pulse acquisition was used with a ^{19}F $\pi/2$ pulse of 3 ms, an acquisition time of 16 ms, a dead time delay of

4.5 ms, and a recycle delay of 10 s; resonance frequency of 376.5 MHz. A total of 64 scans was accumulated. The spectrum reveals two resonance peaks at -141.6 ppm and -143.8 ppm with an intensity ratio about 1:1 for the two crystallographically inequivalent fluorine-sites. This observation agrees with the single crystal refinement results of two independent fluorine sites. The resonance peak at -149.5 ppm is coming from impurities which were not identified.
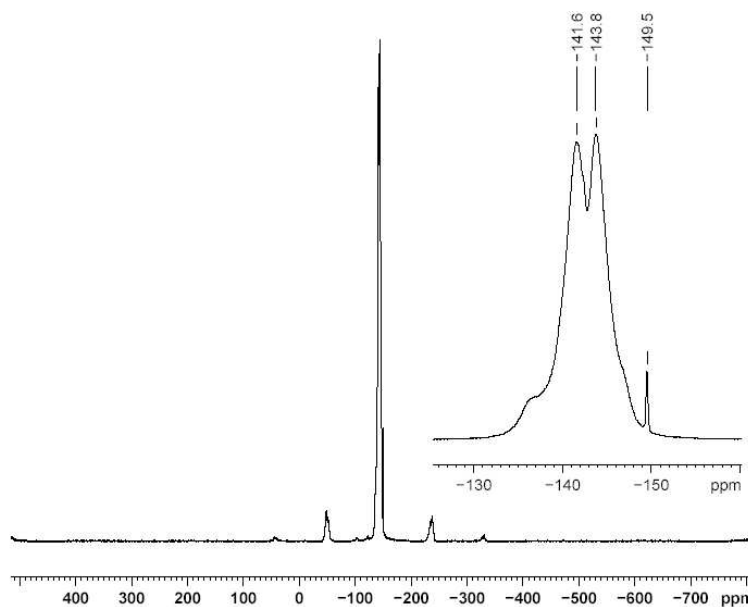
Figure 3.6: ^{19}F MAS NMR spectrum of $(C_2H_{10}N_2)[BPO_4F_2]$.

3.1.5 Thermal analysis

Thermal properties were investigated by DTA/TG methods in a static air atmosphere with heating and cooling rates of 5 °C/min (NETZSCH STA 409)(*Fig. 3.7*). The TG curve of $(C_2H_{10}N_2)[BPO_4F_2]$ shows a three step mass loss with an overall mass loss of 50.7 % (48.6 % calc., according to a hypothetical mass loss of $1 \times C_2H_8N_2$ and $2 \times HF$), consistent with two endothermic peaks in the DTA curve at 329 °C and 424 °C, respectively. Powder X-ray data for the solid product obtained after heating up to 1000 °C appears to contain crystalline α-BPO$_4$ [2] (*Fig. 3.8*).
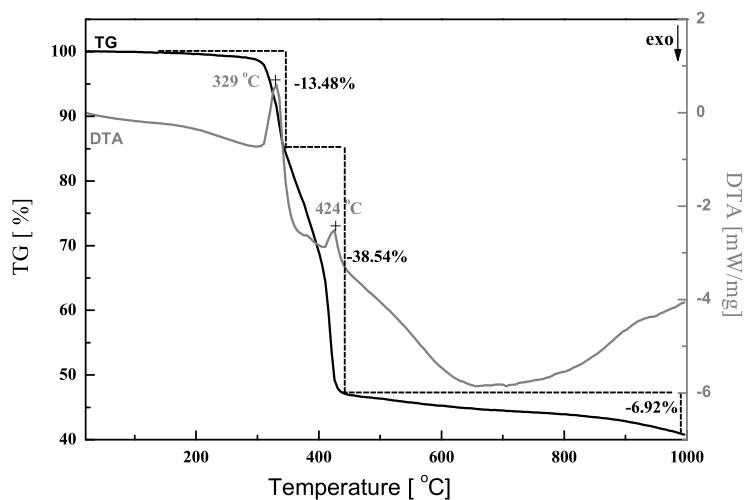
Figure 3.7: DTA-TG curves of $(C_2H_{10}N_2)[BPO_4F_2]$, for details see text.
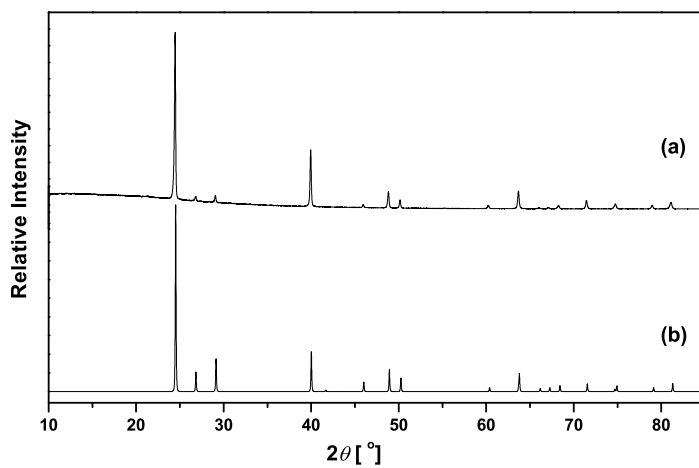
Figure 3.8: Powder X-ray diffraction pattern of $(C_2H_{10}N_2)[BPO_4F_2]$ after heating up to 1000 °C (a), compared with calculated powder diffraction pattern of α-BPO_4(b) [2]; Cu $K_{\alpha 1}$-radiation.

3.1.6 IR-spectroscopy

The IR-spectrum of (C$_2$H$_{10}$N$_2$)[BPO$_4$F$_2$] (1.5 mg sample : 150 mg KBr) in transmittance mode is shown in *Fig. 3.9*. The band positions of N–H and C–H vibrations are summarized in *Table 3.6*. The IR-spectrum confirmed the presence of (C$_2$H$_{10}$N$_2$)$^{2+}$ ions in the structure, as evidenced by the bands observed at 3248, 3018, 2988-2516, 1648, 1559, 1503 and 1336 cm^{-1}.
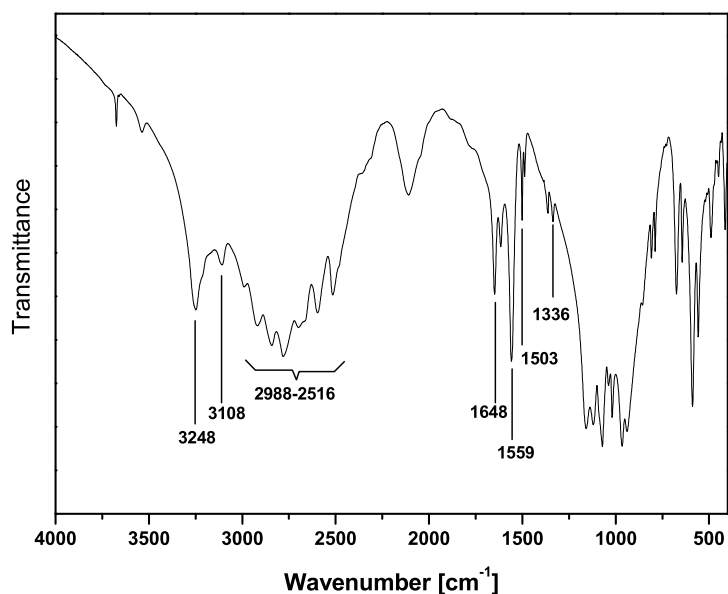
Figure 3.9: IR-spectrum of (C$_2$H$_{10}$N$_2$)[BPO$_4$F$_2$] in the range of 4000–400 cm^{-1}.

Table 3.6: IR-spectroscopy data of (C$_2$H$_{10}$N$_2$)[BPO$_4$F$_2$].

Vibrational frequency $\tilde{\nu}$ [cm^{-1}]	Intensity[†], Band form[‡]	Assignment [129]
3248 and 3108	s,sr	N–H-stretch
2988-2516	m,sr	C–H-stretch
1648-1503	s,sp	N–H-deformation
1336	w,sp	C–H-deformation

[†]vs = very strong, s = strong, m = medium, w = weak
[‡]br = broad, sp = sharp, sr = shoulder

3.1.7   Discussion

The parallel arrangement of $\frac{1}{\infty}\{[BPO_4F_2]^{2-}\}$ single chains along [100] is shown in *Fig. 3.10*. The chains can be simplified as trapezoidal columns which are tilted by approximately 7 ° against the horizontal direction. $(C_2H_{10}N_2)^{2+}$ ions are simplified as elliptical circles. The trapezoidal columns are arranged to layers along [010] with identical orientation, but opposite in neighboring layers along [001]. $(C_2H_{10}N_2)^{2+}$ ions occupy two types of positions: **en1** sites lie between the bases of neighboring trapezoidal layers; while **en2** sites lie between their apices.

The crystal structure of $(C_2H_{10}N_2)[BPO_4F_2]$ is comparable with the typical pyroxene compound $CaMg[Si_2O_6]$ (Diopside) [127] which consists of unbranched single chain, $\frac{1}{\infty}\{[Si_2O_6]^{4-}\}$. The unbranched zweier-single chain of $CaMg[Si_2O_6]$ viewed along [001] can also be simplified as trapezoidal column. The trapezoidal columns are in cross-sectional arrangements within one layer along [010] and are in the same sequence in different layers along [100]. The large size of Ca cations lie on the base of trapezoidal columns in neighboring layers, while small size of Mg cations lie on their apices. Therefore Ca and Mg cations are arranged alternately along [010].

Compared these two structures, it is clear that the arrangement of chains are strongly influenced by the cation sizes. The large size of $(H_2en)^{2+}$ ions ($d_{N\cdots N} = 374$ pm) make the trapezoidal columns tilted and arranged in identical orientation in one layer. While small size of Ca and Mg cations are sufficient with the gap between trapezoidal column layers, so they can have cross-sections arrangement in one layer in the crystal structure of $CaMg[Si_2O_6]$.

Anionic borophosphate chains are known as open-branched, loop- branched, open loop-branched, and unbranched. In the unbrached chains, only vierer-single chain $\frac{1}{\infty}\{[B_2P_2O_7(OH)_5]^{3-}\}$ was found in the crystal structure of $Fe[B_2P_2O_7(OH)_5]$ [90]. The zweier-single chain $\frac{1}{\infty}\{[Si_2O_6]^{4-}\}$ of $(C_2H_{10}N_2)[BPO_4F_2]$ is a new building type in borophosphate anion. Both unbranched single chains have the same ratio of B : P = 1. The unbranched vierer-single chain contains terminal OH-groups bonded to boron with puckered arrangement. The unbranched zweier-single chain contains terminal fluorine instead of OH-group bonded to boron with stretched arrangement. The puckered and stretched arrangement of unbranched single chains may be due to the OH-group prefer to form hydrogen bond and fluorine prefer to be terminal because of its high electroneg-

ativity.

$(C_2H_{10}N_2)[BPO_4F_2]$

$CaMg[Si_2O_6]$ (Diopside)
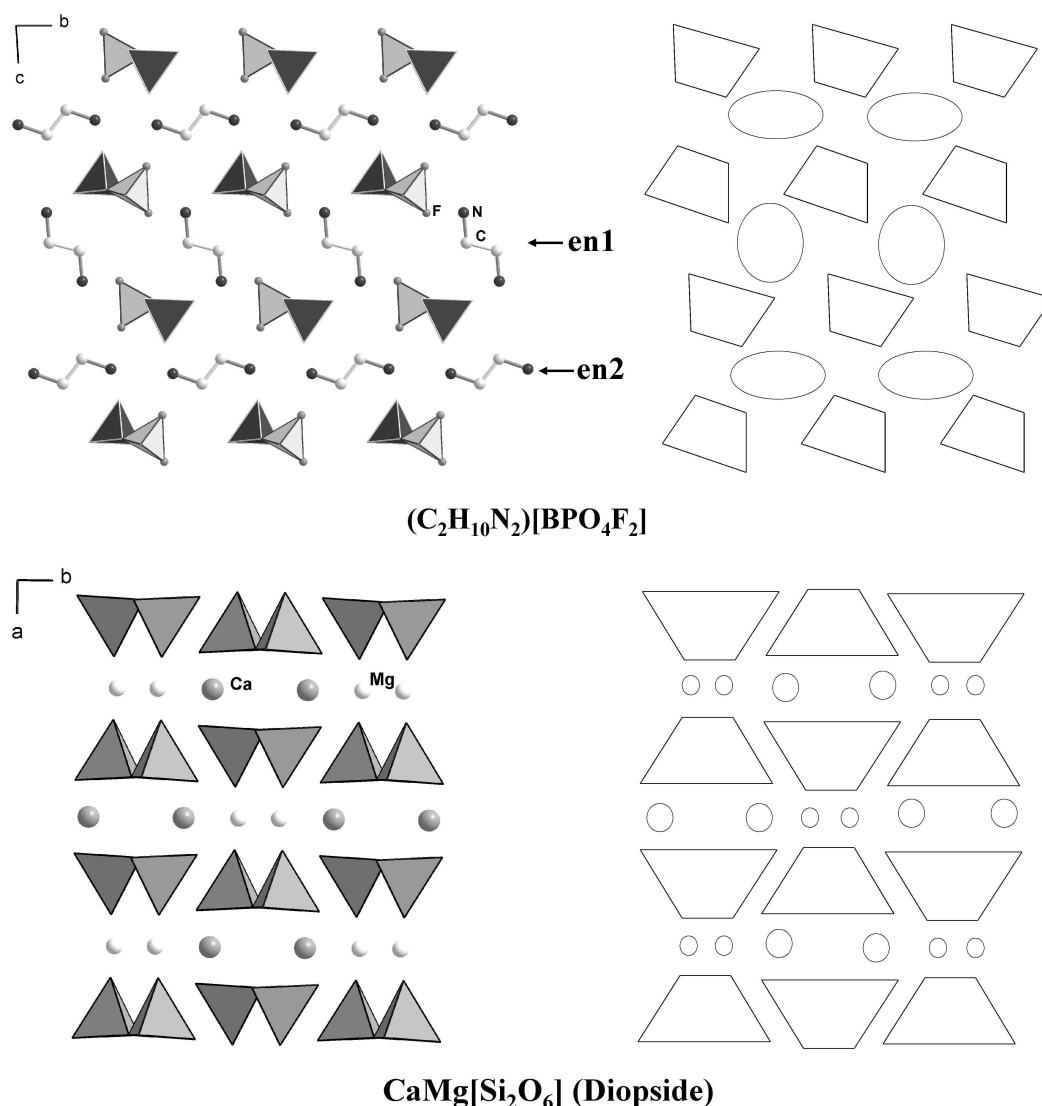
Figure 3.10: *top*: Section of the crystal structure of $C_2H_{10}N_2)[BPO_4F_2]$ viewed along [100]. The two crystallographically different $(C_2H_{10}N_2)^{2+}$ ions are denoted as **en1** (C1/N1) and **en2** (C2/N2), respectively (PO$_4$ tetrahedra: dark grey, BO$_2$F$_2$ tetrahedra: light grey, N atoms: dark grey sphere, C atoms: light grey sphere). The trapezoidal columns and elliptical circles in the right side represent the zweier-single chains $\frac{1}{\infty}\{[BPO_4F_2]^{2-}\}$ and **en** groups. *bottom*: Section of the crystal structure of $CaMg[Si_2O_6]$ viewed along [001] (SiO$_4$ tetrahedra: medium grey, Ca atoms: medium grey spheres, Mg atoms: light grey spheres). The trapezoidal columns in the right side represent the zweier-single chains $\frac{1}{\infty}\{[Si_2O_6]^{4-}\}$. For further details see text.

3.2 $(C_6H_{14}N_2)\{Zn[ZnB_2P_4O_{15}(OH)_2] \cdot (C_6H_{13}N_2)Cl\}$ (zndabcocl)

3.2.1 Synthesis

$(C_6H_{14}N_2)\{Zn[ZnB_2P_4O_{15}(OH)_2] \cdot (C_6H_{13}N_2)Cl\}$ (**zndabcocl**) was prepared under mild hydrothermal conditions from a mixture of 3.894 g (28.6 mmol) of $ZnCl_2$, 0.994 g (14.3 mmol) of B_2O_3, 6.41 g (57.2 mmol) of diaza-bicyclo[2.2.2]-octane $(C_6H_{12}N_2$, DABCO), 7 ml 85 % H_3PO_4, and 10 ml of deionized water stirring at 100 °C. A highly viscous white-colored gel with a pH-value of 1.5–2.0 was filled into a Teflon autoclave ($V = 20$ ml, degree of filling $\approx 60\,\%$) and held at 170 °C for three days under autogenous pressure. Colorless platy crystals (see SEM micrograph of crystals in *Fig. 3.11*) were separated by filtration, washed with deionized water, and dried at 60 °C in air. The Zn^{2+} source, pH value and the degree of filling cause a significant influence on the reaction products formed. When $ZnCl_2$ is replaced by ZnO and the same reaction conditions were applied, the reaction product consists of the compound, $Zn_3(C_6H_{14}N_2)_3[B_6P_{12}O_{39}(OH)_{12}] \cdot (C_6H_{14}N_2)[HPO_4]$ [106], which was already reported only recently. When the degree of filling is lower or equal to 50 % but all other conditions are kept constant, **zndabcocl** and an another "zinc-borophosphate" with a molar ratio of Zn : B : P : C : N = 2 : 2 : 5 : 12 : 4 are obtained. At a pH value of 2.5–3, $(C_6H_{14}N_2)[Zn_2(HPO_4)_3]_{15}$ [130] together with the "zinc-borophosphate" just mentioned are formed as the reaction products.
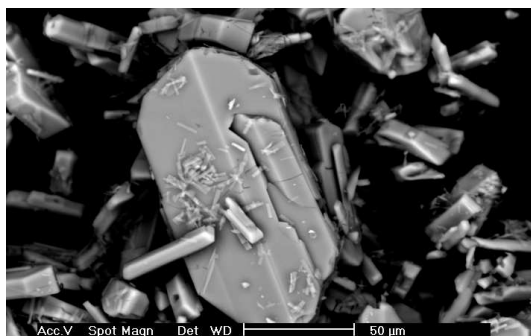
Figure 3.11: SEM micrograph of $(C_6H_{14}N_2)\{Zn[ZnB_2P_4O_{15}(OH)_2] \cdot (C_6H_{13}N_2)Cl\}$ (**zndabcocl**)

Phase purity of the reaction products was checked using powder X-ray diffraction (HUBER Image Foil Guinier Camera G670, Cu $K_{\alpha 1}$-radiation, Ge monochromator).

Fig. 3.12 shows the observed and calculated (from structure data) powder diffraction patterns. The good agreement of observed and calculated powder patterns indicates the purity of the sample.

Zn, B, and P contents were analyzed using ICP-AES, while a hot extraction method was applied for organic carbon and nitrogen. The results are given in *Table 3.7*. The results give a molar ratio of Zn : B : P : C : N = 2.1 : 2 : 2 : 12.3 : 4.1 which is in accordance with the formula of **zndabcocl** obtained by single crystal structure analysis. The presence of chloride was confirmed by EDX measurements (Philips XL 30 with software package EDAX, sample sputtered with carbon).
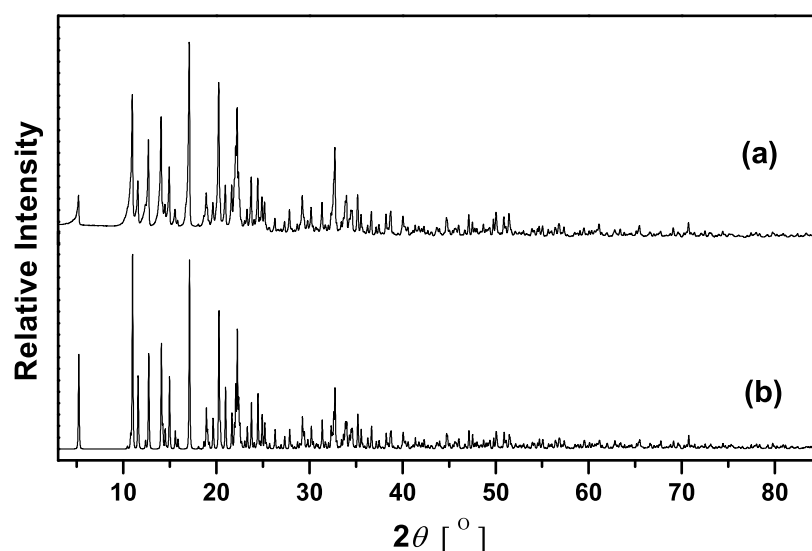
Figure 3.12:   Powder X-ray diffraction patterns of **zndabcocl**, (a)observed, (b)calculated from structure determination; Cu $K_{\alpha 1}$-radiation.

Table 3.7: Chemical analysis results of **zndabcocl**.

Element	Obs.(e.s.d.)/mass-%	Calc. /mass-%
Zn	16.76(6)	16.08
B	2.62(4)	2.66
P	15.0(1)	15.24
C	17.82(2)	17.73
N	6.99(2)	6.89

3.2.2   Crystal structure determination

A suitable but rather small single crystal (platelet, $0.04 \times 0.03 \times 0.02$ mm^3) was fixed on a glass fibre with two-component glue. X-ray data were collected at 295 K using a RIGAKU AFC7 four-circle diffractometer, equipped with a Mercury-CCD detector (Mo K_α-radiation, graphite monochromator). Intensity data were collected in the angular range $4.82° \leq 2\theta \leq 60.8°$ ($240°$-ϕ-scan, $60°$-ω-scan at $\chi = 90°$, $0.5°$ steps with 60 s exposure time per step, detector distance: 40 mm; 2θ-offset: $-15.00°$). The data were corrected for Lorentz and polarization effects. A multi-scan absorption correction was applied. The structure was solved in the space group $P2_1/c$ (No. 14) by direct methods using the program SHELXS-97-2 [P2]. Fourier calculations and subsequent full-matrix least-squares refinements were carried out using SHELXL-97-2 [P3]. The crystallographic results are summarized in *Table 3.8*. After anisotropic displacement parameters had been included in the refinement, all hydrogen atoms could be located from difference Fourier maps. The final residual electron density of $2.04/-0.696$ e$\cdot 10^{-6}$pm^{-3} very close to the O15/B2 and Zn1 (82 pm from O15 and 63 pm from Zn1, respectively). Atomic coordinates for **zndabcocl** are given in *Tables 3.9*, anisotropic displacement parameters in *Table 6.4*, selected interatomic distances and angles in *Table 3.10*.

The high equivalent displacement parameters of O15, O16, O17 and all the carbon atoms of the (DABCO)-units (*Table 3.9*) give a hint for a split model or a lower symmetry of the space group. The split model didn't improve the results: the residual electron density close to O15 and B2 was still present and the atoms still had large displacement parameters, resulting in high R-values. The use of a lower symmetry space group, like $P2_1$, also resulted in high equivalent displacement parameters for O15, O16, and O17. The high displacement parameters for O15, O16, and O17, are probably related to a disorder of the DABCO units coordinating the Zn atoms at the borders of the ribbons. We suppose that there are two very similar structural arrangements with differences in some of the atom positions in the same crystal. So the observed electron density is probably an average value, resulting in high residual electron densities near to O15 and B2.

Table 3.8: Crystallographic data and refinement results of **zndabcocl**, e.s.d.'s are given in parentheses.

Compound		$(C_6H_{14}N_2)\{Zn[ZnB_2P_4O_{15}(OH)_2] \cdot (C_6H_{13}N_2)Cl\}$
Space group	:	$P2_1/c$ (No. 14)
a [pm]	:	1704.3(1)
b [pm]	:	937.03(5)
c [pm]	:	1619.75(8)
β [°]	:	96.894(3)
V [$10^6 \cdot$ pm^3]	:	2567.9(2)
Z	:	2
Calc. density ρ_{calc} [g $\cdot$ cm^{-3}]	:	2.103
Diffractometer	:	RIGAKU AFC7 CCD,
		Mo K_α-radiation,
		graphite monochromator
$\mu_{MoK\alpha}$ [mm^{-1}]	:	2.311
Scan type	:	ϕ / ω
2θ-range [°]	:	4.82–60.8
Miller-index range	:	$-15 \leq h \leq 22$,
		$-9 \leq k \leq 12$
		$-22 \leq l \leq 21$
Total data collected	:	20609
Unique data	:	6484
Observed data ($I > 2\sigma(I)$)	:	5316
R_{int}/R_σ	:	0.0468/0.0597
Number of parameters refined	:	466
$R1$ ($F_o > 4\sigma(F_o)$)	:	0.0640
$R1$ (all data)	:	0.0879
$wR2$ ($F_o > 4\sigma(F_o)$)	:	0.1153
$wR2$ (all data)	:	0.1229
Goodness-of-Fit (for F^2)	:	1.149
$F(000)$	:	1648
Residual electron density	:	2.04/-0.696
(max./min.) [e $\cdot 10^{-6}$pm^{-3}]		
Programs	:	DIAMOND [P4]
		SHELXS–97/2 [P2]
		SHELXL–97/2 [P3]

Table 3.9: Atomic coordinates and equivalent/isotropic displacement parameters $[10^{-4}\mathrm{pm}^2]$ in the crystal structure of **zndabcocl**, e.s.d.'s are given in parentheses.

Atom	Site	x	y	z	$U_{\mathrm{eq}}/U_{\mathrm{iso}}$
Zn1	$4e$	0.39151(3)	0.92506(6)	0.19288(3)	0.01641(13)
Zn2	$4e$	0.09638(3)	0.24598(6)	0.25098(3)	0.01408(12)
Cl1	$4e$	0.06668(9)	0.25843(16)	0.38120(8)	0.0316(3)
P1	$4e$	0.53837(7)	0.15744(13)	0.19843(8)	0.0150(2)
P2	$4e$	0.20015(8)	0.45220(13)	0.16002(8)	0.0161(2)
P3	$4e$	0.20960(7)	0.01202(13)	0.17821(8)	0.0159(2)
P4	$4e$	0.34474(8)	0.72419(14)	0.04696(8)	0.0201(3)
B1	$4e$	0.2299(3)	0.7330(5)	0.1429(3)	0.0133(10)
B2	$4e$	0.3403(4)	0.5797(6)	0.1856(4)	0.0197(11)
O1	$4e$	0.3963(2)	0.8466(4)	0.0801(2)	0.0206(7)
O2	$4e$	0.1830(2)	0.8549(3)	0.1617(2)	0.0205(7)
O3	$4e$	0.2906(2)	0.4525(4)	0.1901(2)	0.0243(8)
O4	$4e$	0.4558(2)	0.1006(4)	0.1890(3)	0.0281(9)
O5	$4e$	0.2561(2)	0.7577(4)	0.0562(2)	0.0214(7)
O6	$4e$	0.2983(2)	0.7092(3)	0.2000(2)	0.0167(7)
O7	$4e$	0.1768(2)	0.6088(3)	0.1338(2)	0.0194(7)
O8	$4e$	0.4545(2)	0.8119(3)	0.2772(2)	0.0194(7)
O9	$4e$	0.2947(2)	0.0199(4)	0.2147(2)	0.0250(8)
O10	$4e$	0.1816(2)	0.3540(4)	0.0875(2)	0.0279(9)
O11	$4e$	0.1966(3)	0.0840(4)	0.0916(3)	0.0298(10)
O12	$4e$	0.3647(2)	0.5853(4)	0.0984(3)	0.0319(9)
O13	$4e$	0.1552(2)	0.0741(4)	0.2354(2)	0.0239(8)
O14	$4e$	0.1575(2)	0.4134(4)	0.2339(2)	0.0249(8)
O15	$4e$	0.5896(3)	0.0571(4)	0.2604(3)	0.0490(14)
O16	$4e$	0.5709(4)	0.1356(5)	0.1137(3)	0.0574(16)
O17	$4e$	0.3516(3)	0.6864(5)	0.9576(2)	0.0416(12)
N1	$4e$	0.6408(3)	0.6165(5)	0.0445(3)	0.0304(11)
N2	$4e$	0.6339(3)	0.8606(5)	0.0992(3)	0.0254(10)
N3	$4e$	0.8678(3)	0.2487(5)	0.0659(3)	0.0240(9)
N4	$4e$	0.9939(2)	0.2459(4)	0.1656(2)	0.0161(8)
C1	$4e$	0.7216(4)	0.6630(7)	0.0786(4)	0.0358(15)
C2	$4e$	0.5997(4)	0.7591(7)	0.1565(4)	0.0369(15)
C3	$4e$	0.7179(4)	0.8248(8)	0.0935(5)	0.0403(16)
C4	$4e$	0.5892(4)	0.6176(7)	0.1136(5)	0.0401(15)
C5	$4e$	0.5873(5)	0.8529(7)	0.0146(4)	0.0402(16)
C6	$4e$	0.6076(5)	0.7113(8)	0.9755(4)	0.0426(17)

Table 3.9 Continued

Atom	Site	x	y	z	$U_{eq}/\,U_{iso}$
C7	$4e$	0.0007(5)	0.1503(11)	0.0951(5)	0.063(3)
C8	$4e$	0.9258(5)	0.1539(11)	0.0322(5)	0.058(2)
C9	$4e$	0.9763(6)	0.3888(9)	0.1327(8)	0.076(4)
C10	$4e$	0.8985(6)	0.3947(9)	0.0767(8)	0.089(4)
C11	$4e$	0.9269(4)	0.1961(14)	0.2056(5)	0.075(4)
C12	$4e$	0.8508(5)	0.1914(16)	0.1460(5)	0.086(4)
H1	$4e$	0.196(5)	0.150(8)	0.094(5)	0.050*
H2	$4e$	0.593(4)	0.219(8)	0.092(4)	0.050*
H3	$4e$	0.638(4)	0.531(8)	0.033(4)	0.050*
H4	$4e$	0.627(4)	0.945(8)	0.121(4)	0.050*
H5	$4e$	0.823(4)	0.253(7)	0.031(4)	0.050*
H6	$4e$	0.754(4)	0.648(8)	0.039(5)	0.050*
H7	$4e$	0.731(4)	0.602(8)	0.126(5)	0.050*
H8	$4e$	0.555(5)	0.796(8)	0.168(5)	0.050*
H9	$4e$	0.638(4)	0.765(7)	0.207(5)	0.050*
H10	$4e$	0.742(4)	0.835(8)	0.143(5)	0.050*
H11	$4e$	0.732(4)	0.871(8)	0.042(5)	0.050*
H12	$4e$	0.537(4)	0.613(8)	0.085(4)	0.050*
H13	$4e$	0.608(4)	0.517(8)	0.151(4)	0.050*
H14	$4e$	0.525(4)	0.859(8)	0.032(4)	0.050*
H15	$4e$	0.604(4)	0.926(8)	-0.022(4)	0.050*
H16	$4e$	0.565(4)	0.662(8)	0.945(4)	0.050*
H17	$4e$	0.645(4)	0.736(8)	0.940(5)	0.050*
H18	$4e$	0.017(4)	0.053(8)	0.121(4)	0.050*
H19	$4e$	0.049(5)	0.199(8)	0.072(4)	0.050*
H20	$4e$	0.896(4)	0.074(8)	0.065(5)	0.050*
H21	$4e$	0.927(4)	0.180(8)	-0.028(5)	0.050*
H22	$4e$	1.023(5)	0.404(9)	0.114(5)	0.050*
H23	$4e$	0.990(5)	0.458(8)	0.151(5)	0.050*
H24	$4e$	0.875(5)	0.459(8)	0.061(5)	0.050*
H25	$4e$	0.924(5)	0.356(8)	0.025(5)	0.050*
H26	$4e$	0.930(5)	0.298(8)	0.227(5)	0.050*
H27	$4e$	0.925(5)	0.173(8)	0.246(5)	0.050*
H28	$4e$	0.813(5)	0.174(9)	0.156(5)	0.050*
H29	$4e$	0.836(5)	0.306(8)	0.150(5)	0.050*

*refined with isotropic displacement parameters

3.2.3   Crystal structure description

The borophosphate partial structure of **zndabcocl** contains loop-branched oligomers, $[B_2P_4O_{15}(OH)_2]^{6-}$ (*Fig. 3.13a*), consisting of two BO_4, two $(OH)PO_3$, and two PO_4 tetrahedra sharing common O-vertices. Neighboring borophosphate oligomers are interconnected by $Zn1O_4$ tetrahedra sharing common O-corners with four adjacent phosphate tetrahedra. This results in tetrahedral zincoborophosphate *zigzag* ribbons, $\frac{1}{\infty}\{[ZnB_2P_4O_{15}(OH)_2]^{4-}\}$ (*Fig. 3.13b*), running along [010]. The terminal phosphate groups at the borders of the zincoborophosphate ribbons are bridged by Zn2-coordination-tetrahedra, ZnO_2NCl, which complete the eight-membered tetrahedral rings within the ribbons (*Fig. 3.13c*).
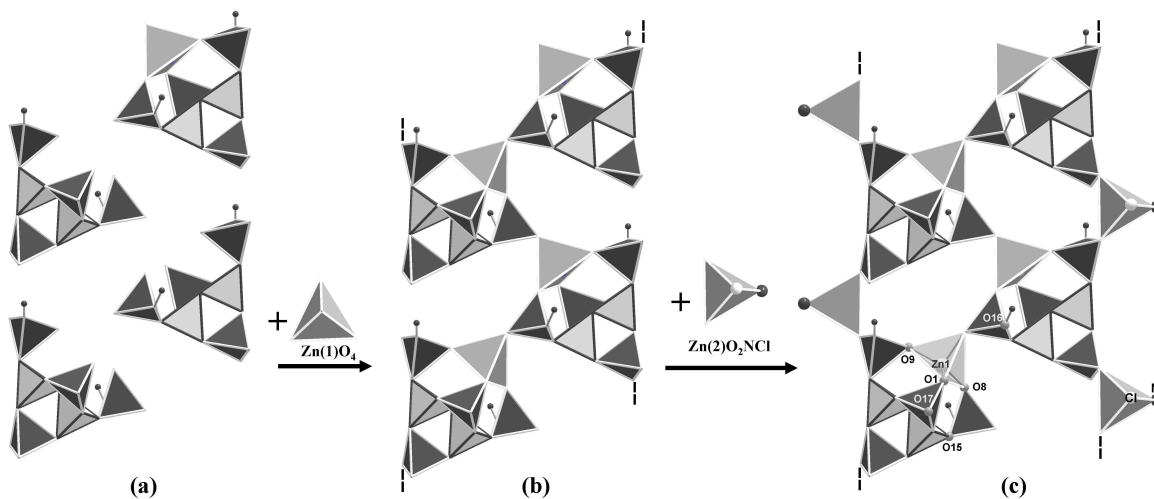
Figure 3.13: Scheme showing (a) loop branched oligomers $[B_2P_4O_{15}(OH)_2]^{6-}$, Together with ZnO_4 tetrahedra (b) zigzag zincoborophosphate ribbons running along [010]; (c) ZnO_2NCl tetrahedra close the zigzag zincoborophosphate ribbons and complete eight-membered tetrahedral rings within the ribbons. PO_4 tetrahedra: dark grey; BO_4 tetrahedra: light grey; ZnO_4 and ZnO_2NCl tetrahedra: medium grey; Cl atoms: light grey spheres; N atoms: dark grey spheres.

Fig. 3.14 shows the crystal structure of **zndabcocl** viewed along [010]. The distance between two neighboring ribbons along [100] (249.5 pm ($d_{O16-O17}$)) is shorter than $d_{N\cdots N} = 252$ pm in the DABCO cations. The diprotonated $(H_2DABCO)^{2+}$ ions, therefore, are located in the cavities between two adjacent eight-membered rings of

neighboring ribbons and interact via hydrogen bonds N–H$\cdots$O with the ribbons(*Fig. 3.16a*).
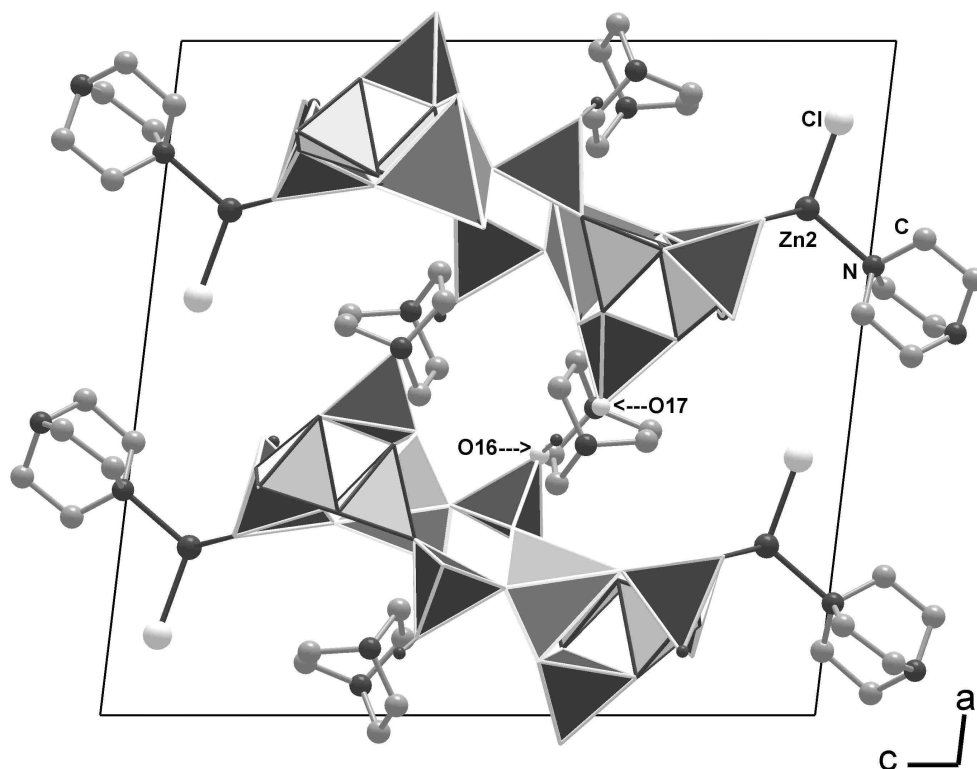
Figure 3.14: The crystal structure of **zndabcocl** (viewed along the *b* axis) shows the zicoborophosphate ribbons in parallel stacking along [010]. The diprotonated $(H_2DABCO)^{2+}$ ions are located between adjacent eight-membered rings of neighboring ribbons. PO_4 tetrahedra: dark grey; BO_4 tetrahedra: light grey; ZnO_4 and ZnO_2NCl tetrahedra: medium grey. Cl atom: light grey spheres; N atom: dark grey spheres. The H atoms in the DABCO cations are no shown for clarity.

Fig. 3.15 shows a part of ribbon running along [010]. The terminal $(HDABCO)^+$ groups connect adjacent ribbons along [001] via N–H$\cdots$O hydrogen bonds (*Fig. 3.16b*). The central part of the ribbons consists of a chain of PO_4- and ZnO_4-tetrahedra sharing common O-corners. This connectivity appears to be rather strong and rigid. The bulky $ZnO_2Cl(HDABCO)^+$ groups take positions at the borders of the ribbons close the eight-membered rings by sharing common oxygen positions with two PO_4 tetrahedra. The rigid connection of the cental tetrahedral chain together with the bulky and flexible $ZnO_2Cl(HDABCO)^+$ groups at the borders of the ribbons, possibly creates the large

displacement parameters for O15.
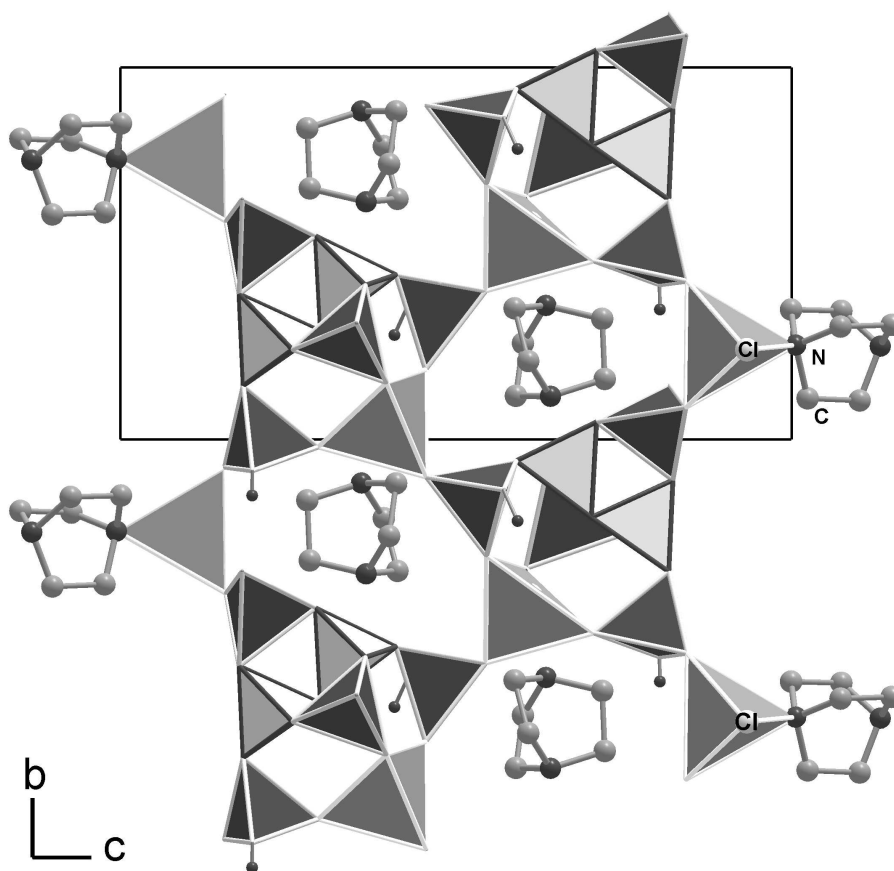
Figure 3.15: Crystal structure of **zndabcocl** viewed along [100] shows a ribbon running along [010]. PO$_4$ tetrahedra: dark grey; BO$_4$ tetrahedra: light grey; ZnO$_4$ and ZnO$_2$NCl tetrahedra: medium grey. Cl atoms: light grey sphere, N atoms: dark grey sphere. The H atoms in DABCO cations are no shown for clarity.

The PO$_4$ and HPO$_4$ groups have an almost ideal tetrahedral geometry: $d_{P-O} = 149.5(4)$ pm $- 156.7(4)$ pm and $\angle$O–P–O $= 104.5(2)°$–$114.6°$ (average bond length and angle: 153.13 pm and 109.4°). Both borate tetrahedra are severely distorted. The distances of B1–O5 (154.1(6) pm) and B2–O5 (152.2(7) pm) are rather large compared with other borophosphates [23], but the average B–O bond lengths (146.88 pm of B1 and 146.08 pm of B2, respectively) have the typical values for boron in tetrahedral coordination. Zn1 has a distorted tetrahedral coordination: $d_{Zn1-O} = 194.4(4)$ pm– 198.2(4) pm, $\angle$O–Zn1–O $= 96.39(16)°$–$122.01(16)°$, respectively, with the central Zn1

position shifted towards the face formed by O1, O8, and O9. Zn2 is tetrahedrally coordinated by two O atoms from the phosphate groups, one non-protonated N atom of (HDABCO)$^+$ and one Cl atom with usual distances and angles: $d_{Zn2-N} = 209.3(4)$ pm, $d_{Zn2-Cl} = 223.04(14)$ pm, $\angle O(N, Cl)-Zn2-O(N, Cl) = 106.36(12)°-111.31(16)°$. Selected bond lengths and bonds angles are given in *Table 3.10*. Ternary zinc tetrahedra in zincophosphates are already known with ZnO$_3$Cl [131, 132] or ZnO$_3$N [130], **zndabcocl** is the first example containing a quaternary Zn tetrahedron, ZnO$_2$NCl, and can formally be described as an adduct of $(C_6H_{14}N_2)Zn[ZnB_2P_4O_{15}(OH)_2]$ with diaza-bicyclo[2.2.2]octane-hydrochloride.

Hydrogen bonds in the crystal structure of **zndabcocl** can be classified by three types of connections. (a) intra-ribbon (within a single ribbon): O11-H11$\cdots$O10; (b) inter-ribbon (linking adjacent ribbons along [100]): O16–H2 $\cdots$ O17, N1–H3$\cdots$O17, N1–H3 $\cdots$ O12, N2–H4 $\cdots$ O15 and N2–H4 $\cdots$ O16; (c) inter-ribbon (linking adjacent ribbons in the (010)-plane): N3–H5 $\cdots$ O5. Hydrogen bond lengths and angles are given in *Table 3.11* and *Fig. 3.16*.
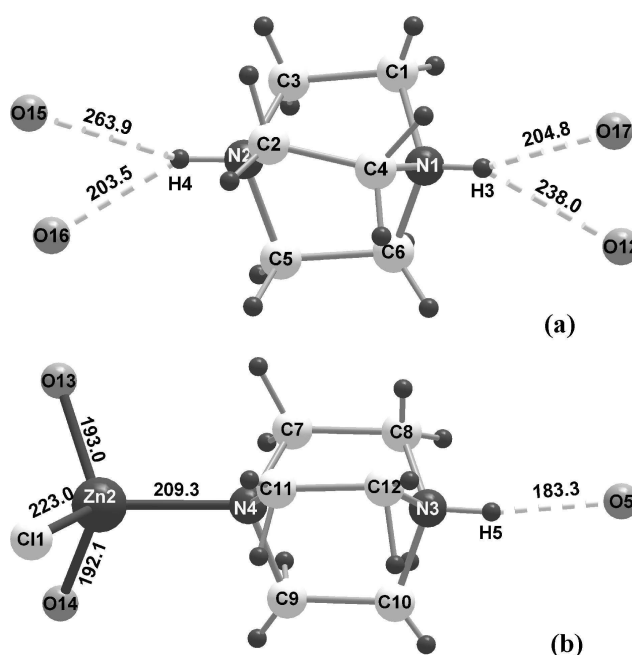
Figure 3.16: Hydrogen bonds N–H$\cdots$O of (a) diprotonated (H$_2$DABCO)$^{2+}$ ions and monoprotonated (HDABCO)$^+$, and the coordination of monoprotonated ZnO$_2$Cl(HDABCO)$^+$ group.

Table 3.10: Crystal structure of **zndabcocl**: selected interatomic distances and angles, e.s.d.'s are given in parentheses.

		distance [pm]		angle [°]		angle [°]
Zn1–	O9	194.4(4)	O9–Zn1–O8	122.01(16)	O8–Zn1–O4	102.36(15)
	O8	194.7(3)	O9–Zn1–O1	117.86(16)	O1–Zn1–O4	101.22(16)
	O1	198.0(3)	O8–Zn1–O1	111.40(15)		
	O4	198.2(4)	O9–Zn1–O4	96.39(16)		
Zn2–	O14	192.1(4)	O14–Zn2–O13	111.31(16)	O13–Zn2–Cl1	110.36(12)
	O13	193.0(3)	O14–Zn2–N4	109.22(16)	N4–Zn2–Cl1	111.02(12)
	N4	209.3(4)	O13–Zn2–N4	108.57(16)		
	Cl1	223.04(13)	O14–Zn2–Cl1	106.36(12)		
P1–	O4	149.5(4)	O4–P1–O8	114.6(2)	O8–P1–O15	112.9(2)
	O8	150.1(3)	O4–P1–O16	107.1(3)	O16–P1–O15	104.9(3)
	O16	155.4(4)	O8–P1–O16	109.4(2)		
	O15	156.3(4)	O4–P1–O15	107.3(2)		
P2–	O10	149.5(4)	O10–P2–O14	113.3(2)	O14–P2–O7	108.0(2)
	O14	151.8(4)	O10–P2–O3	110.7(2)	O3–P2–O7	107.01(19)
	O3	156.0(4)	O14–P2–O3	107.6(2)		
	O7	156.5(3)	O10–P2–O7	110.0(2)		
P3–	O9	150.0(4)	O9–P3–O13	112.1(2)	O13–P3–O2	106.5(2)
	O13	150.4(4)	O9–P3–O11	111.2(3)	O11–P3–O2	104.5(2)
	O11	154.8(4)	O13–P3–O11	111.0(2)		
	O2	155.4(3)	O9–P3–O2	111.2(2)		
P4–	O1	150.4(4)	O1–P4–O17	114.3(2)	O17–P4–O5	109.0(2)
	O17	150.9(4)	O1–P4–O12	111.4(2)	O12–P4–O5	105.5(2)
	O12	156.1(4)	O17–P4–O12	106.2(2)		
	O5	156.7(4)	O1–P4–O5	110.0(2)		
B1–	O6	141.7(6)	O6–B1–O2	114.7(4)	O2–B1–O5	107.5(4)
	O2	144.7(6)	O6–B1–O7	112.9(4)	O7–B1–O5	105.7(4)
	O7	147.0(6)	O2–B1–O7	107.3(4)		
	O5	154.1(6)	O6–B1–O5	108.2(4)		
B2–	O15	141.0(7)	O15-B2–O6	115.2(4)	O6–B2–O12	108.5(4)
	O6	144.2(6)	O15–B2–O3	107.4(4)	O3–B2–O12	107.3(4)
	O3	146.9(6)	O6–B2–O3	112.0(4)		
	O12	152.2(7)	O15–B2–O12	105.9(5)		
N1–	C6	148.4(8)	C6–N1–C1	110.9(6)	C2–C4–N1	107.7(5)
	C1	148.7(8)	C6–N1–C4	110.6(5)	N2–C5–C6	107.3(5)
	C4	150.4(8)	C1–N1–C4	108.6(5)	N1–C6–C5	107.0(5)
N2–	C3	148.3(8)	C3–N2–C2	110.2(5)	N4–C7–C8	111.5(5)
	C2	149.6(8)	C3–N2–C5	110.0(5)	N3–C8–C7	107.9(5)
	C5	150.1(8)	C2–N2–C5	109.4(5)	N4–C9–C10	112.3(6)
N3–	C12	146.5(9)	C12–N3–C10	110.0(8)	N3–C10–C9	108.2(6)
	C10	146.7(9)	C12–N3–C8	108.5(7)	N4–C11–C12	112.4(6)
	C8	148.2(8)	C10–N3–C8	111.0(7)	N3–C12–C11	107.9(6)
N4–	C11	145.5(8)	C11–N4–C7	106.8(7)		
	C7	146.7(8)	C11–N4–C9	108.5(8)		
	C9	146.0(8)	C7–N4–C9	107.9(7)		

Table 3.10 Continued

		distance [pm]		angle [°]	angle [°]
C1–	C3	153.8(10)	C7–N4–Zn2	112.2(3)	
C2–	C4	149.6(9)	C11–N4–Zn2	110.1(4)	
C5–	C7	152.8(9)	C9–N4–Zn2	111.1(4)	
C7–	C8	153.4(9)	N1–C1–C3	107.1(5)	
C9–	C10	155.2(10)	N2–C2–C4	108.0(5)	
C11–	C12	155.2(10)	N2–C3–C1	107.0(5)	

Table 3.11: Hydrogen bonds of **zndabcocl**: interatomic distances [pm] and angles [°].

Hydrogen bonds							
O11–H1	62.1	H1···O10	192.9	O11···O10	254.3	O11–H1···O10	170.41
O16–H2	95.8	H2···O17	157.6	O16···O17	249.5	O16–H2···O17	159.07
N1–H3	82.6	H3···O17	204.7	N1···O17	284.2	N1–H3···O17	161.41
N1–H3	82.6	H3···O12	237.8	N1···O12	298.0	N1–H3···O12	130.37
N2–H4	87.6	H4···O16	202.8	N2···O16	281.2	N1–H4···O16	148.41
N2–H4	87.6	H4···O15	263.8	N2···O15	335.5	N2–H4···O15	139.75
N3–H5	89.7	H5···O15	183.3	N3···O15	271.6	N3–H5···O5	167.66

3.2.4 IR spectroscopy

The IR-spectrum of **zndabcocl** (1.5 mg sample : 150 mg KBr) is shown in *Fig. 3.17*. The band positions of the O–H, N–H and C–H vibrations are summarized in *Table 3.12*. IR-spectrum confirmed the presence of $(C_6H_{14}N_2)^{2+}$ ions in the structure, as evidenced by the bands observed at 3037, 3014, 2811, and 1322 cm^{-1} which belong to N–H and C–H vibrations. Additional absorption band for O–H deformation vibration at 1465 cm^{-1} is also observed.

Table 3.12: IR-spectroscopy data of **zndabcocl**.

Vibration frequency $\tilde{\nu}$ [cm^{-1}]	Intensity[†], Band form[‡]	Assignment [129]
3037–3014	s,sr	N–H-stretch
2811–2611	m,sr	C–H-stretch
1465	s,sp	O–H-deformation
1322	s,sp	N–H-deformation
1138	w,sp	C–H-deformation

[†]vs = very strong, s = strong, m = medium, w = weak
[‡]br = broad, sp = sharp, sr = shoulder
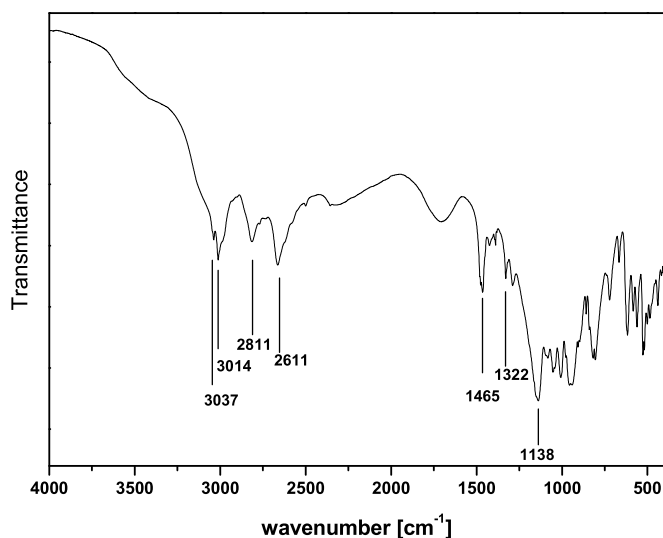
Figure 3.17: IR spectroscopy of **zndabcocl** in the range of 4000–400 cm^{-1}.

3.2.5   Thermal analysis

Thermal investigations (DTA/TG) (*Fig. 3.18*) were carried out in a static air atmosphere with heating and cooling rates of 5 °C/min (NETZSCH STA 409). The TG curve shows the decomposition of **zndabcocl** with a three-step mass loss and an overall mass loss of 35.5 % (36.5 % calc., according to a hypothetical weight loss of 2 × $C_6H_{12}N_2$, 1 × HCl and 2 × H_2O per formula unit), associated with three exothermic peaks in the DTA curve with maximum temperatures at 430, 583, and 654 °C, respectively.

3.2.6   High temperature powder X-ray diffraction

HT-XRD investigations were carried out on a high-temperature powder X-ray diffractometer (STOE STADI MP, Cu $K_{\alpha 1}$ radiation, Ge monochromator, High Temperature Attachment 0.65.3 of Stoe) with a powdered sample of **zndabcocl** filled into an open quartz capillary of 0.5 mm diameter. The powder X-ray diffraction patterns were collected in the temperature range 23 °C – 740 °C with a scanning time of 1 hour per step. The heating rate between the temperature steps was 5 °C/min.
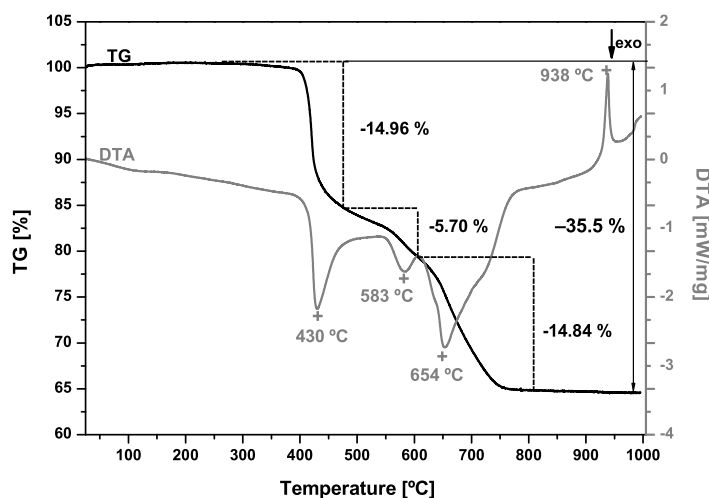
Figure 3.18: DTA-TG curves of **zndabcocl**, for further details see text.

Some selected powder patterns (370 °C − 395 °C) are presented in *Fig. 3.19(top)*. *Fig. 3.19(top)* shows that **zndabcocl** is stable up to 375 °C, although the intensity of reflections continuously decreases. At 380 °C **zndabcocl** decomposes to a polymorph of $NH_4[ZnBP_2O_8]$ (HT-$NH_4[ZnBP_2O_8]$, see Rietveld refinements), and an unidentified intermediate phase stable only between 380 and 390 °C (marked reflections in grey color at low θ-value in *Fig. 3.19(top)*).

Fig. 3.19(bottom) shows the decomposition of **zndabcocl** at higher temperatures (600 °C − 680 °C): HT-$NH_4[ZnBP_2O_8]$ decomposes to a mixture of γ-$Zn_2P_2O_7$ [133] and α-BPO_4 [2] above 620 °C. After the sample is heated to 1000 °C and cooled down to room temperature, the powder X-ray diffraction pattern of the resulting solid product consists of α-$Zn_2P_2O_7$ [134] and α-BPO_4 [2] (see *Fig. 3.20*).

Fig. 3.21 summarizes the results of the thermoanalytical and X-ray investigations. The scheme shows that the large weight loss happening around 375 °C and the remaining weight loss around 620 °C are attributed to the first and the third step in the TG curve (*Fig. 3.18*), respectively. Compared with the DTA/TG results, the higher weight loss of the first step (30.1 %) and the lower weight loss of the third step (6.41 %) are due to the formation of amorphous organic decomposition products remaining in the TG crucible at the first step, followed by complete oxidation pyrolysis at higher

temperatures.
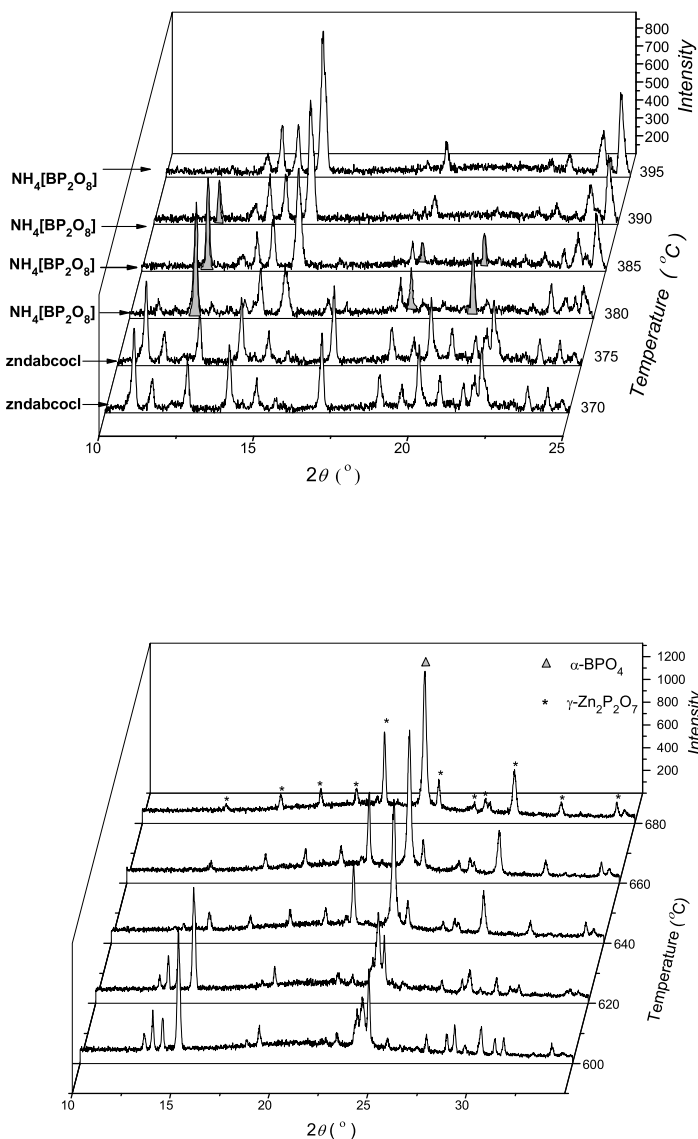
Figure 3.19: Selected high temperature powder X-ray diffraction patterns of **zndab-cocl**: (*top*) temperature range of 370–395 °C shows **zndabcocl** decomposed to a $NH_4[ZnBP_2O_8]$ polymorph at 380 °C, and an unidentified intermediate stable only between 380 °C and 390 °C which were marked in grey; (*bottom*) temperature ranging from 600 to 680 °C shows the polymorph of $NH_4[ZnBP_2O_8]$ decomposes to γ-$Zn_2P_2O_7$ [133] and α-BPO_4 [2] above 620 °C (see also *Fig. 3.18*). Cu $K_{\alpha 1}$ radiation. For further details see text.
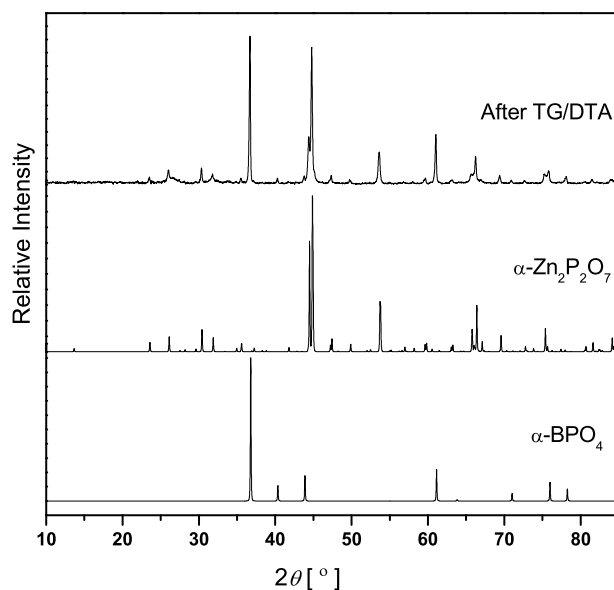
Figure 3.20: Powder X-ray diffraction pattern of the product after TG/DTA investigation compare with the calculated powder diffraction patterns of α-$Zn_2P_2O_7$ [134] and α-BPO_4 [2]; Cr $K_{\alpha 1}$-radiation.
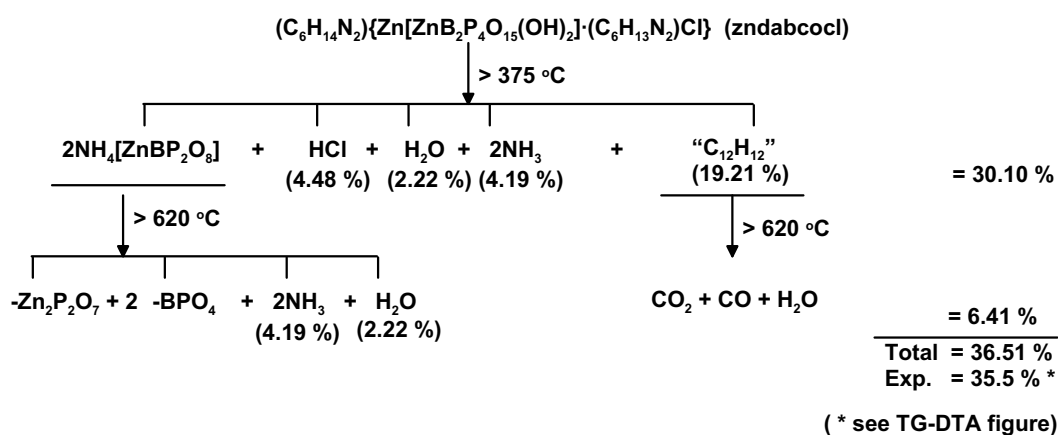
Figure 3.21: Scheme of the decomposition process of **zndabcocl** during heating in air according to high-temperature powder X-ray diffraction. The decomposition species contents are calculated according to the molar mass of **zndabcocl**.

3.2.7   Rietveld refinement

There are two phases of $NH_4[ZnBP_2O_8]$ existing in the known zincoborophosphates. One is with the GIS-type structure (α-$NH_4[ZnBP_2O_8]$) [23], the other is with feldspar structure (β-$NH_4[ZnBP_2O_8]$ [113]).

According to the results of HT-XRD, **zndabcocl** decomposes to a polymorph $NH_4[ZnBP_2O_8]$ at 440 °C (noted as HT-$NH_4[ZnBP_2O_8]$). After cooling this sample from 440 °C to room temperature, the powder X-ray diffraction pattern has the same powder pattern with α-$NH_4[ZnBP_2O_8]$ [23] (see *Fig. 3.22*). So RT-$NH_4[ZnBP_2O_8]$) is the same phase of α-$NH_4[ZnBP_2O_8]$. While the powder X-ray diffraction pattern of HT-$NH_4[ZnBP_2O_8]$ at 440 °C appears to have some additional reflections, which were marked with arrows, compared with the room temperature phase. So it is interesting to know that the two different temperature phases is a phase transition or purely a heating effect.
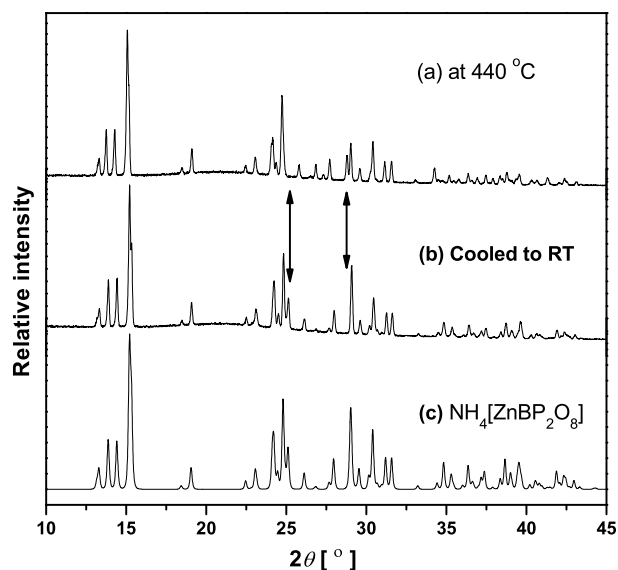
Figure 3.22: Powder X-ray diffraction patterns of (a) **zndabcocl** heated to 440 °C (HT-$NH_4[ZnBP_2O_8]$), (b) cooling from 440 °C to room temperature (RT-$NH_4[ZnBP_2O_8]$), and (c) calculated powder diffraction pattern of α-$NH_4[ZnBP_2O_8]$ [23]; The arrows show the significant different reflections between HT-$NH_4[ZnBP_2O_8]$ and RT-$NH_4[ZnBP_2O_8]$. Cu $K_{\alpha 1}$-radiation.

The DSC result of α-NH$_4$[ZnBP$_2$O$_8$] [23] heated to 400 °C shows a weak endothermic peak with a heat capacity of about 381 J/mol at about 199 °C which is shown in *Fig. 3.23*.
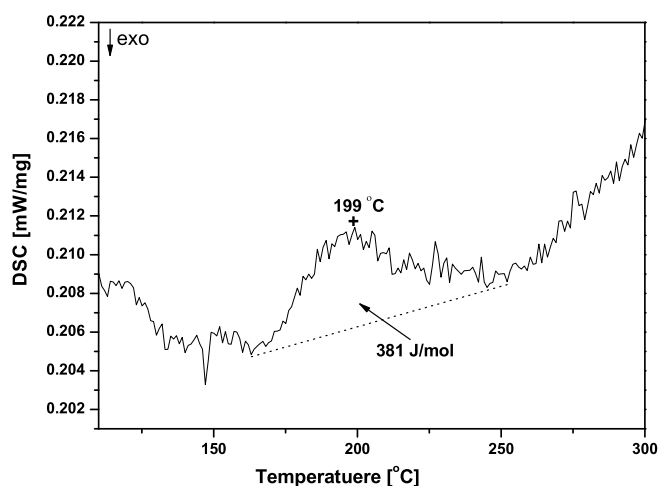
Figure 3.23: The DSC curve of NH$_4$[ZnBP$_2$O$_8$] shows a weak endothermic peak with enthalpy of 381 J/mol.

HT-XRD investigations of α-NH$_4$[ZnBP$_2$O$_8$] were carried out on a high-temperature powder X-ray diffractometer (STOE STADI MP, Cu $K_{\alpha 1}$-radiation, Ge monochromator, High Temperature Attachment 0.65.3 of Stoe) with a powdered sample of α-NH$_4$[ZnBP$_2$O$_8$] [23] filled into an open quartz capillary of 0.5 mm diameter. The powder X-ray diffraction patterns were collected in the temperature range 25 °C − 450 °C with 1 hour scanning time per step. The heating rate between the temperature steps was 5 °C/min. The results (*Fig. 3.24*) show that the peak at about 29 degree (2θ) is split into two peaks at 250 °C, meanwhile the peak at about 24.5 ° (marked with grey) decreases in intensity and moves close to the neighboring peak at 24.4 °. HT-XRD and DSC results together indicate that α-NH$_4$[ZnBP$_2$O$_8$] has a phase transition at about 200 °C.
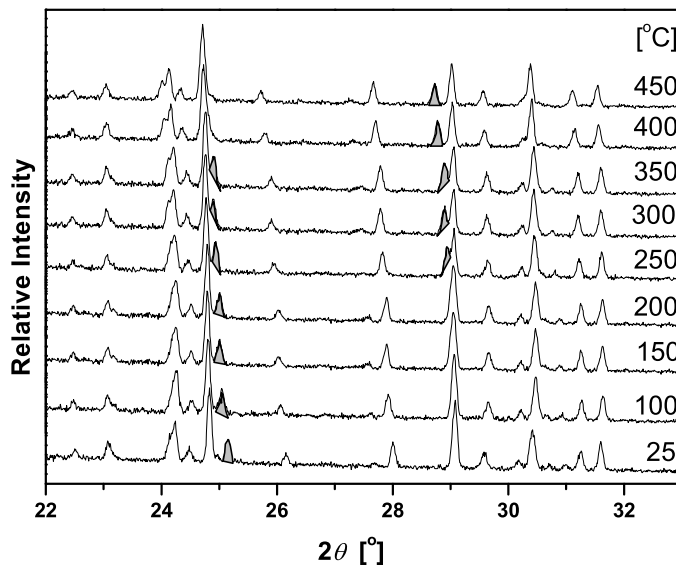
Figure 3.24: Selected high temperature powder X-ray diffraction patterns of α-$NH_4[ZnBP_2O_8]$ in the temperature range of 25–450 °C show RT-$NH_4[ZnBP_2O_8]$ transform to HT-$NH_4[ZnBP_2O_8]$ polymorph at about 250 °C. The significant changes are marked with grey color. Cu $K_{\alpha 1}$-radiation.

The powder X-ray diffraction pattern of HT-$NH_4[ZnBP_2O_8]$, which is obtained by the decomposition of **zndabcocl** at 440 °C, was indexed with the following cell parameters: $P\bar{1}$ (No. 2), $a = 745.64(1)$ pm, $b = 764.560(1)$ pm, $c = 787.725(1)$ pm, $\alpha = 118.096(1)°$, $\beta = 102.061(1)°$, $\gamma = 103.951(1)°$ and $V = 356.15(2)$ 10^6 pm^3. These values are closely related to α-$NH_4[ZnBP_2O_8]$ [23] ($P\bar{1}$ (No. 2), $a = 743.7(1)$ pm, $b = 761.2(1)$ pm, $c = 785.0(1)$ pm, $\alpha = 119.05(2)°$, $\beta = 101.59(1)°$ $\gamma = 103.43(1)°$). We use the atom positions of α-$NH_4[ZnBP_2O_8]$ [23] as a model to refine the crystal structure by use of CSD [P7] program. Positional parameters were refined for all atoms independently (*Table 3.14*), while hydrogen atoms of the ammonium cations were omitted. The difference plot (*Fig. 3.25*), which shows only minor deviations, indicates a successful structure refinement. The U_{iso} value of oxygen atoms might be influenced by the systematic error of the high temperature data (at 440 °C). The crystallographic data are summarized in *Table 3.13*, the atomic position and displacement parameters are given in *Table 3.14*, some selected bond lengths and angles are given in *Table 3.15*.
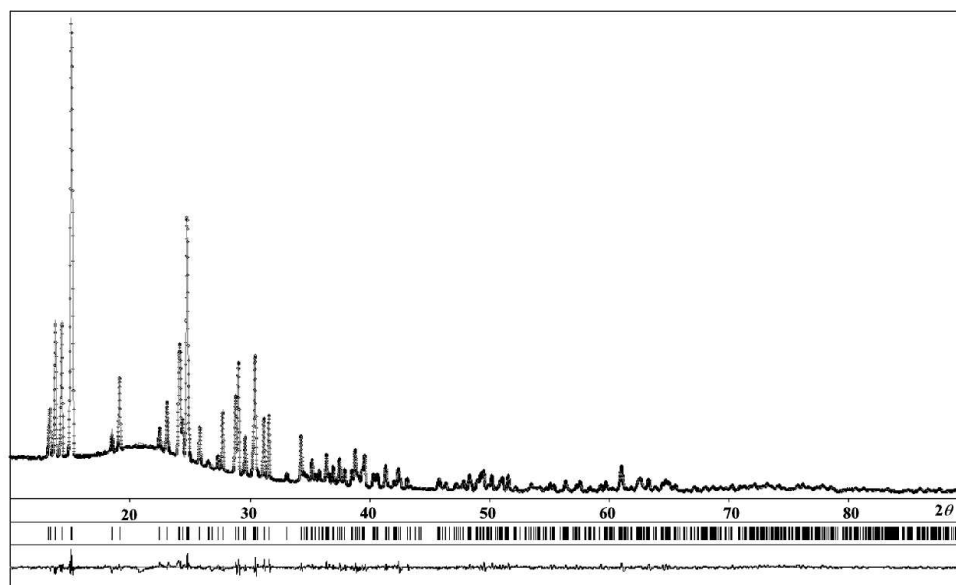
Figure 3.25: Observed (o), calculated (-), and difference powder X-ray diffraction patterns for the Rietveld refinement of HT-$NH_4[ZnBP_2O_8]$ at 440 °C, Cu $K_{\alpha 1}$-radiation.

Table 3.13: Crystallographic data and refinement details for HT-$NH_4[ZnBP_2O_8]$.

Compound		HT-$NH_4[ZnBP_2O_8]$	α-$NH_4[ZnBP_2O_8]$ [23]
Space group	:	$P\bar{1}$ (No. 2)	
Cell parameters [pm/°]	:	$a = 745.64(1)$	$a = 743.7(1)$
		$b = 764.56(1)$	$b = 761.2(1)$
		$c = 787.725(1)$	$c = 785.0(1)$
		$\alpha = 118.096(1)$	$\alpha = 119.05(2)$
		$\beta = 102.061(1)$	$\beta = 101.59(1)$
		$\gamma = 103.951(1)$	$\gamma = 103.43(1)$
V [$10^6 \cdot$ pm^3]$/Z$	:	$356.15(2)/2$	
Temperature [°C]	:	440	
$\rho_{calc.}$ [g $\cdot$ cm^{-3}]	:	$2.6497(1)$	
μ(Cu $K_{\alpha 1}$) [mm^{-1}]	:	9.45	
Diffractometer	:	STOE STADI MP	
	:	Cu $K_{\alpha 1}$-radiation	
	:	Ge monochromator	
2θ-range/step [°]	:	10.0-89.99/0.01	
Number of parameters	:	54	
$R_I/R_p/R_{wp}$	:	0.060/0.1154/0.0839	
F(000)	:	280	
Programs	:	CSD[P7], Diamond[P4]	

Table 3.14: HT-NH$_4$[ZnBP$_2$O$_8$] and α-NH$_4$[ZnBP$_2$O$_8$]: Atomic coordinates and isotropic/equivalent displacement parameters [10^{-4}pm^2], e.s.d.'s are given in parentheses.

Atom	Site	x	y	z	$U_{\text{eq}}/\ U_{\text{iso}}$
			HT-NH$_4$[ZnBP$_2$O$_8$]		
Zn1	$2i$	0.1972(3)	0.2951(3)	0.7396(3)	0.0207(7)
P1	$2i$	0.0394(6)	0.1109(7)	0.2769(6)	0.0151(14)
P2	$2i$	0.4461(7)	0.7740(7)	0.0812(6)	0.0152(13)
B1	$2i$	0.297(3)	0.064(3)	0.082(3)	0.016(6)
O1	$2i$	0.0132(13)	0.8974(15)	0.2573(13)	0.037(4)
O2	$2i$	0.0897(11)	0.2907(12)	0.4931(12)	0.008(3)
O3	$2i$	0.1980(11)	0.1857(12)	0.2049(11)	0.010(3)
O4	$2i$	0.4092(13)	0.1865(13)	0.7259(12)	0.030(3)
O5	$2i$	0.4478(14)	0.2424(14)	0.0713(13)	0.031(3)
O6	$2i$	0.5855(12)	0.0194(13)	0.8396(12)	0.016(3)
O7	$2i$	0.7448(12)	0.4261(12)	0.0386(12)	0.012(3)
O8	$2i$	0.8440(12)	0.0998(12)	0.1434(13)	0.021(3)
N1	$2i$	0.2799(15)	0.666(2)	0.4110(15)	0.032(4)
			α-NH$_4$[ZnBP$_2$O$_8$] [23]		
Zn1	$2i$	0.19425(3)	0.29590(3)	0.74170(3)	0.01644(7)
P1	$2i$	0.03339(7)	0.11359(8)	0.27534(7)	0.01368(10)
P2	$2i$	0.45319(7)	0.78103(7)	0.08724(7)	0.01392(10)
B1	$2i$	0.3003(3)	0.0779(3)	0.0734(3)	0.0144(3)
B1	$2i$	0.3003(3)	0.0779(3)	0.0734(3)	0.0144(3)
O1	$2i$	0.0184(2)	0.9000(2)	0.2476(2)	0.0208(3)
O2	$2i$	0.0783(2)	0.2990(2)	0.4979(2)	0.0198(3)
O3	$2i$	0.2021(2)	0.1931(2)	0.2091(2)	0.0178(3)
O4	$2i$	0.4033(2)	0.1818(2)	0.7199(2)	0.0213(3)
O5	$2i$	0.4471(2)	0.2484(2)	0.0767(2)	0.0176(3)
O6	$2i$	0.5903(2)	0.0088(2)	0.8304(2)	0.0165(3)
O7	$2i$	0.7357(2)	0.4166(2)	0.0160(2)	0.0209(3)
O8	$2i$	0.8378(2)	0.0972(2)	0.1396(2)	0.0181(3)
N1	$2i$	0.2704(4)	0.6598(4)	0.4070(4)	0.0365(5)

Table 3.15: Crystal structures of HT-$NH_4[ZnBP_2O_8]$ and α-$NH_4[ZnBP_2O_8]$: selected interatomic distances [pm] and angles [°], e.s.d.'s are given in parentheses.

		HT-$NH_4[ZnBP_2O_8]$	α-$NH_4[ZnBP_2O_8]$ [23]
Zn1–	O7	187.5(9)	192.56(15)
	O1	188.8(12)	195.23(15)
	O2	192.1(9)	194.86(14)
	O4	195.5(11)	194.68(15)
P1–	O2	148.7(9)	151.94(15)
	O3	151.9(11)	155.75(14)
	O1	152.4(13)	150.50(15)
	O8	156.6(11)	155.90(14)
P2–	O6	150.1(12)	154.97(14)
	O7	151.2(11)	150.68(15)
	O4	151.4(10)	151.83(15)
	O5	154.5(11)	156.09(14)
B1–	O3	146(2)	146.3(2)
	O5	160(3)	157.5(2)
	O6	140(3)	146.8(2)
	O8	152(2)	146.2(2)
O7–Zn1–O1		107.4(4)	106.36(7)
O7–Zn1–O2		105.3(4)	106.42(7)
O7–Zn1–O4		119.0(4)	116.86(6)
O1–Zn1–O2		106.3(4)	106.84(7)
O1–Zn1–O4		107.7(4)	107.25(7)
O2–Zn1–O4		110.5(4)	112.54(7)
O2–P1–O3		106.7(6)	106.11(9)
O2–P1–O1		112.8(6)	115.03(8)
O2–P1–O8		105.3(6)	105.13(8)
O3–P1–O1		114.6(6)	110.60(8)
O3–P1–O8		104.6(6)	106.92(8)
O1–P1–O8		112.1(6)	112.49(8)
O6–P2–O7		114.0(6)	110.97(8)
O6–P2–O4		102.9(6)	104.63(8)
O6–P2–O5		106.9(6)	110.13(8)
O7–P2–O4		116.9(6)	112.30(9)
O7–P2–O5		106.8(6)	108.52(8)
O4–P2–O5		108.8(6)	110.26(8)
O6–B1–O3		120.0(16)	108.77(15)
O6–B1–O8		112.8(15)	110.23(15)
O6–B1–O5		105.6(14)	107.89(15)
O3–B1–O8		111.2(15)	113.14(15)
O3–B1–O5		101.7(14)	104.66(15)
O8–B1–O5		103.2(13)	111.87(15)

The crystal structure of HT-NH$_4$[ZnBP$_2$O$_8$] (at 440 °C) is quite similar to α-NH$_4$[ZnBP$_2$O$_8$] when we consider boron with tetrahedral coordination. The crystal structure is an open-framework structure with Gismondine type topology which is constructed by alternating zincate, borate, and phosphate tetrahedra sharing common O-corners (*Fig. 3.26*). Compared with the crystal structure of α-NH$_4$[ZnBP$_2$O$_8$], boron atoms in HT-NH$_4$[ZnBP$_2$O$_8$] have quite distorted tetrahedral coordinations, B–O bond lengths range from 142 pm to 160 pm and O–B–O angles from 103.2 ° to 120.0 °. The details of the boron coordination environments are shown in *Fig. 3.27*. B1–O5 bond (160 pm) is too long for general B–O distance (about 145 pm). So it may be considered as an intermediate of a BO$_4$ tetrahedron transforming to a trigonal planar BO$_3$ groups.

When B1–O5 bond was not counted as bonding, the boron atoms only have three coordinations. The framework structure of HT-NH$_4$[ZnBP$_2$O$_8$] viewed along [011] is built by 8-membered ring and 4-membered ring which is different from the crystal structure of α-NH$_4$[ZnBP$_2$O$_8$] which only contains 4-membered rings (see *Fig. 3.28*). In this case, the porosities of the framework in HT-NH$_4$[ZnBP$_2$O$_8$] are much larger than that in α-NH$_4$[ZnBP$_2$O$_8$].
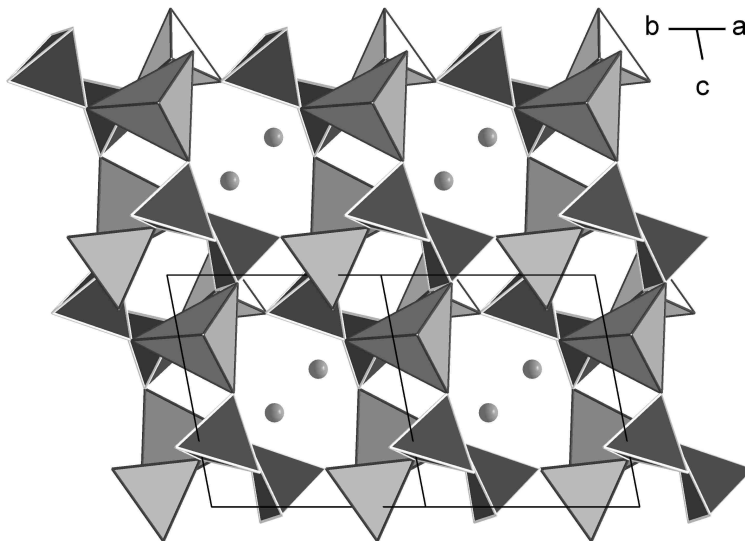
Figure 3.26: Polyhedral representation of the crystal structure of HT-NH$_4$[ZnBP$_2$O$_8$] viewed along [110], PO$_4$ tetrahedra: medium grey; BO$_4$ tetrahedra: light grey; ZnO$_4$ tetrahedra: dark grey. N atoms: dark grey spheres.
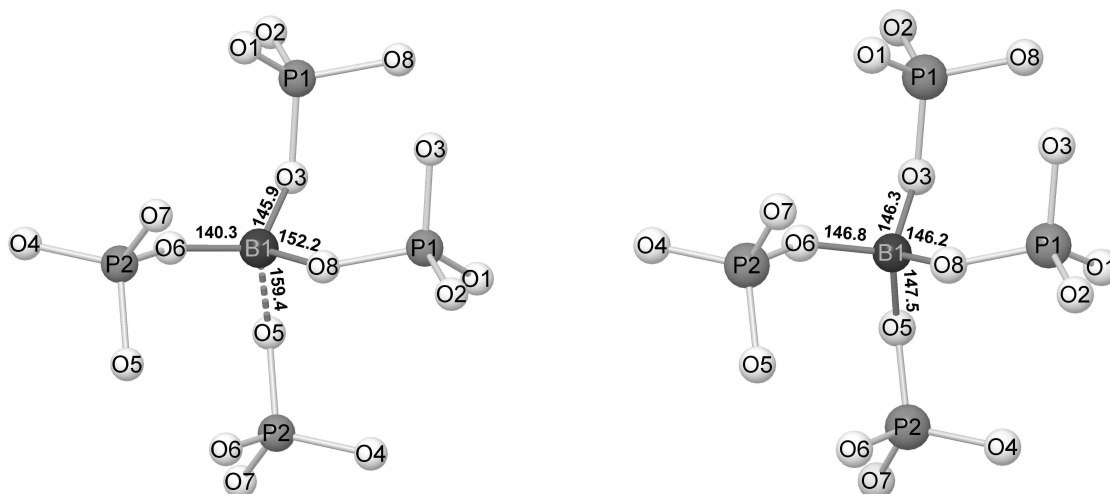
Figure 3.27: The ball and stick presentations of the coordination enviraments around boron in the crystal structures of HT-$NH_4[ZnBP_2O_8]$(left) and α-$NH_4[ZnBP_2O_8]$ (right). P atoms: medium grey spheres, O atoms: light grey spheres; B atoms: dark grey spheres, O atoms: light grey spheres.
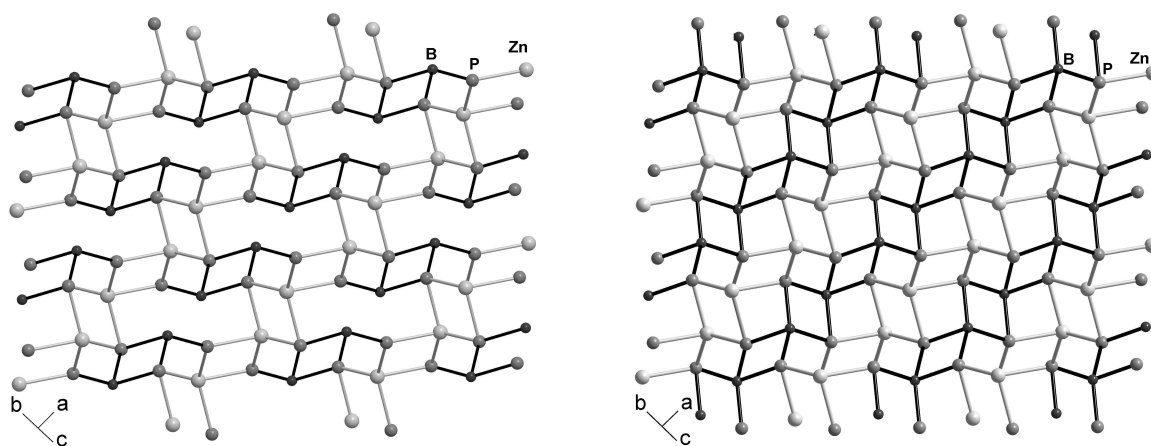
Figure 3.28: The ball and stick presentations of the crystal structures of HT-$NH_4[ZnBP_2O_8]$(left) and α-$NH_4[ZnBP_2O_8]$ (right) viewed along [011] show the significant differences of the frameworks. P atoms: medium grey spheres; Zn atoms: light grey spheres; B atoms: dark grey spheres. B–P bonds: black sticks, Zn–P bonds: light grey sticks.

There are only very few common structural features between HT-$NH_4[ZnBP_2O_8]$ and **zndabcocl**, the presence of condensed four membered rings in both structures

being one of them. All the tetrahedra in HT-NH$_4$[ZnBP$_2$O$_8$] are 4-connected, whereas 2-, 3-, and 4-connected tetrahedra serve as building units in the crystal structure of **zndabcocl**. So it is likely that the formation of HT-NH$_4$[ZnBP$_2$O$_8$] is a reconstructive structure during the decomposition of **zndabcocl**.

3.2.8   Discussion

3.2.8.1   Zn$_3$(C$_6$H$_{14}$N$_2$)$_3$[B$_6$P$_{12}$O$_{39}$(OH)$_{12}$] · (C$_6$H$_{14}$N$_2$)[HPO$_4$] and zndabcocl

Zn$_3$(C$_6$H$_{14}$N$_2$)$_3$[B$_6$P$_{12}$O$_{39}$(OH)$_{12}$] · (C$_6$H$_{14}$N$_2$)[HPO$_4$] [106] is the only borophosphate known up to now containing Zn and protonated DABCO templates. The crystal structure is completely different from **zndabcocl** and contains helical chains constructed from mixed octahedral-tetrahedral secondary building units, $\frac{1}{\infty}${[Zn$_3$B$_6$P$_{12}$O$_{39}$(OH)$_{12}$]$^{6-}$} (zinc in octahedral coordination), which are arranged around 3_1 screw axes. Two types of diprotonated (H$_2$DABCO)$^{2+}$ templates interconnect the helical chains via N-H···O hydrogen bonds. Besides (H$_2$DABCO)$^{2+}$-templates, **zndabcocl** also contains mono-protonated (HDABCO)$^+$ ions which are bound to Zn(2) at the borders of the ribbons via a Zn-N bond. The introduction of the bulky (HDABCO)$^+$ together with Cl$^-$ as co-ordinating ligands to the tetrahedral polymer causes significant structural peculiarities, which favor the formation of a ribbon-like zinccoborophosphate.

Our continuing investigations in the Zn-borophosphate-DABCO system indicate that further templated Zn-borophosphate can be prepared. All of them are obtained via a mild hydrothermal route under acid conditions with minor variations in the synthesis conditions leading to different compositions of the main reaction products. These observations indicate that the system of Zn-B-P-O-DABCO has a very rich structural chemistry compared with the respective ethylene diamine and piperazine templated Zn-borophosphate systems.

It should be noted that the bonding of bulky (HDABCO)$^+$ and Cl$^-$ ions to the tetrahedral coordinated Zn(2) is an important feature in the crystal structure of **zndabcocl**. Monoprotonated (HDABCO)$^+$ ions act as terminal groups as well as Cl$^-$ ions. The short distance between Cl$^-$ and (HDABCO)$^+$ (d$_{Cl\cdots C10}$ = 351.2 pm), precludes these units as linkers for further condensation of tetrahedral groups.

If we consider the "short" distance between HDABCO and chloride from adjacent ribbons, and if we abstract from interlockings within the bc-plane, a Zn–NC$_6$H$_{12}$N–

Zn linkage might be possible [Zn-HDABCO + Zn-Cl $\longrightarrow$ Zn-DABCO-Zn + HCl]. $[Co_2(NH_2(CH_2)_2NH_2)_3][Ge_9O_{18}(OH)_4]$ [135] contains ethylenediamine ligands connecting two structural parts via the Co–N–Co bridges, which confirms our ideas.

3.2.8.2 $(C_6H_{14}N_2)\{Zn[ZnB_2P_4O_{15}(OH)_2] \cdot (C_6H_{13}N_2)Cl\}$ (zndabcocl) and Zincoborophosphates

zndabcocl is the first organo-templated zincoborophosphate. Its crystal structure is quite different from other three types of zincoborophosphates containing alkaline metals known up to now: β-A[ZnBP$_2$O$_8$] (A = K$^+$, NH$_4^+$) [23, 24] with Feldspar-type structure [123], α-A[ZnBP$_2$O$_8$] (A = NH$_4^+$, Rb$^+$, Cs$^+$) [23] with Gismodine-type structure [21], and Na[ZnBP$_2$O$_8$]·H$_2$O [108] with CZP-type [136]. *Fig. 3.29* shows the topologies of all the zincoborophosphates. No Zn–O–B connection is observed in zincoborophosphates according to their topologies. The crystal structures of three types of alkaline zincoborophosphates have three-dimensional tetrahedral frameworks, while **zndabcocl** has a one dimensional structure built by zincoborophosphate ribbons. In the alkaline zincoborophosphates, every tetrahedral center connects to four other tetrahedral centers. While in **zndabcocl**, PO$_4$ tetrahedra only connect to three other tetrahedra and Zn2 only connect to two other tetrahedra. This may be one reason for **zndabcocl** not forming three-dimensional structure.

The low dimensional structure of **zndabcocl** may also be due to the bulky organic templates. The presence of terminal (HDABCO)$^+$ ions together with Cl$^-$ ions coordinated to Zn2 at the borders of ribbons indicates that the zincoborophosphate ribbons along [001] can not be interconnected to form three dimensional structure. In addition, the large size of diprotonated (H$_2$DABCO)$^{2+}$ ions residing between neighboring ribbons along [100] aslo make neighboring ribbons difficult to connect together.

The anionic borophosphate partial structures of all the zincoborophosphates are also quite different, ranging from oligomer, ribbon, chain to layer (*Fig. 3.30*). A hexamer, [B$_2$P$_4$O$_{15}$(OH)$_2$]$^{6-}$ (*Fig. 3.30a*) acts as borophosphate anion in the crystal structure of **zndabcocl**. A helical ribbon, $\frac{1}{\infty}\{[BP_2O_8]^{3-}\}$ (*Fig. 3.30b*), is present in the crystal structure of Na[ZnBP$_2$O$_8$]·H$_2$O [108]. While a loop-branched single chain, $\frac{1}{\infty}\{[BP_2O_8]^{3-}\}$ (*Fig. 3.30c*), is present in the crystal structures of α-A[ZnBP$_2$O$_8$] (A = NH$_4^+$, Rb$^+$, Cs$^+$). A layer structure, $\frac{2}{\infty}\{[BP_2O_8]^{3-}\}$ (*Fig. 3.30d*), is present in the crystal structure of β-A[ZnBP$_2$O$_8$] (A = K$^+$, NH$_4^+$). The helical ribbons and loop-

branched single chains are built from the same 4-ring of alternating BO_4 and PO_4 groups and with the same building sequence. But the loop-branched single chains are in stretched arrangement while the helical ribbons are arranged around 6_1 screw axes.

From the formula of zincoborophosphates, we can obtain one common feature of zincoborophosphates with molar ratio of Zn : B : P = 1 : 1: 2 (see *Table 3.16*).
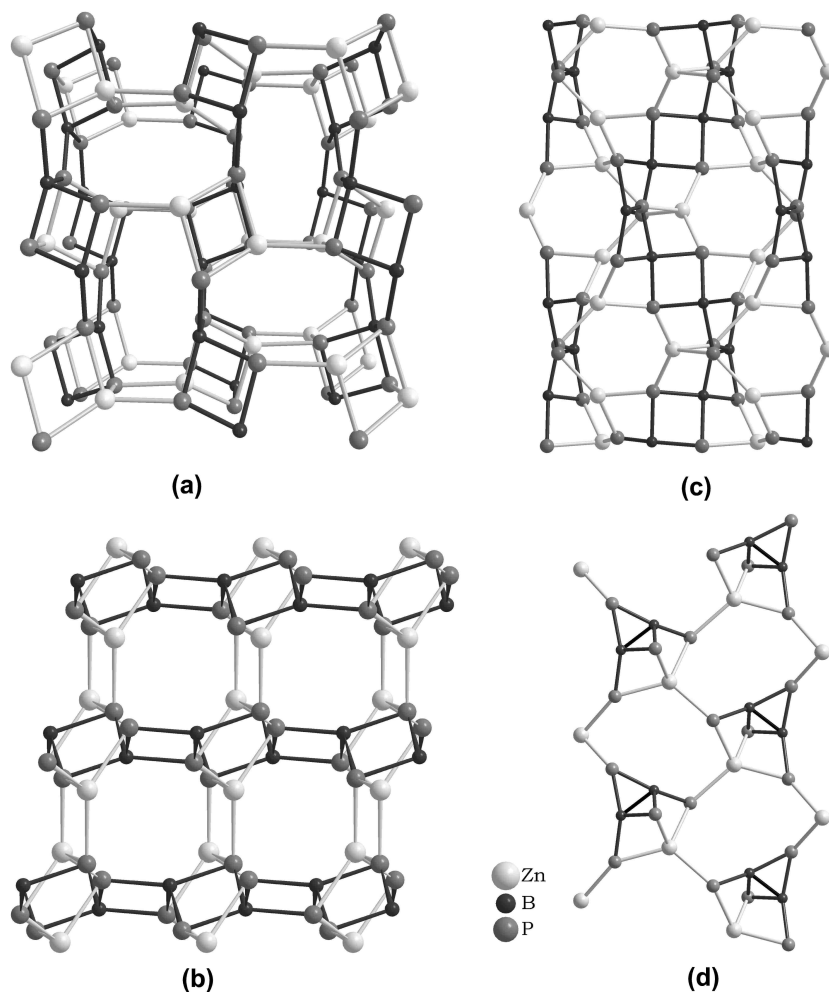
Figure 3.29: (a) Topology of the framework structure of $K[ZnBP_2O_8]$ [23]; (b) Topology of the framework structure of α-$NH_4[ZnBP_2O_8]$ [23]; (c) Topology of the framework structure of $NaZn[BP_2O_8]\cdot H_2O$ [108];(d) Topology of the single ribbon in the crystal structure of **zndabcocl**; Zn atoms: light grey spheres, B atoms: dark grey spheres, P atoms: medium grey spheres; Zn–P bonds: light grey sticks, B–P bonds: dark grey sticks, B–B bonds: black sticks. The oxygen atoms are omitted for clarity.

(a)

(c)

(b)

(d)
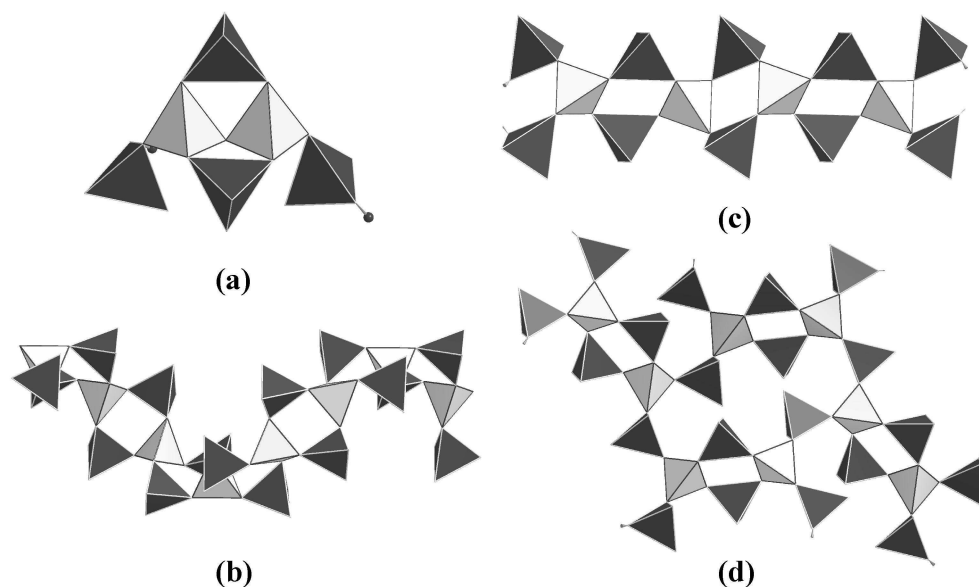
Figure 3.30: Anionic borophosphate partial structures present in the zincoborophosphates: (a) A hexamer $\{[B_2P_4O_{15}(OH)_2]^{6-}\}$ in the crystal structure of **zndabcocl**; (b) A helical ribbon $\frac{1}{\infty}\{[BP_2O_8]^{3-}\}$ in the crystal structure of $NaZn[BP_2O_8] \cdot H_2O$ [108]; (c) A loop-branched single chain $\frac{1}{\infty}\{[BP_2O_8]^{3-}\}$ in the crystal structure of α-$NH_4[ZnBP_2O_8]$ [23]; (d) A layer $\frac{2}{\infty}\{[BP_2O_8]^{3-}\}$ in the crystal structure of $K[ZnBP_2O_8]$ [23]; PO_4 tetrahedra: dark grey, BO_4 tetrahedra: light grey, hydrogen atoms: black spheres.

Table 3.16: The molar ratio of Zn : B : P in the crystal structure of zincoborophosphates

Compound	Zn : B : P
$Na[ZnBP_2O_8] \cdot H_2O$ [108]	1 : 1 : 2
$M^I[ZnBP_2O_8]$ (M^I = K, NH_4) [23, 24, 45]	1 : 1 : 2
$M^I[ZnBP_2O_8]$ (M^I = NH_4, Rb, Cs) [23, 46]	1 : 1 : 2
$(C_6H_{14}N_2)\{Zn[ZnB_2P_4O_{15}(OH)_2] \cdot (C_6H_{13}N_2)Cl\}$	1 : 1 : 2

3.3 $(C_3H_{12}N_2)\{Mn[B_2P_3O_{12}(OH)]\}$ (DAP-Mn) and $(C_4H_{12}N_2)$-$\{Mn[B_2P_3O_{12}(OH)]\}$ (PIP-Mn)

3.3.1 Synthesis

$(C_3H_{12}N_2)\{Mn[B_2P_3O_{12}(OH)]\}$(**DAP-Mn**) was prepared under mild hydrothermal conditions. Mixtures of 0.3775 g (3 mmol) $MnCl_2$, 0.371 g (6 mmol) H_3BO_3, 0.822 g (11 mmol) 1,3-diaminopropane ($C_3H_{10}N_2$, DAP) and 1.26 g (11 mmol) 85 % H_3PO_4, and 7.5 ml of deionized water, was stirred at 60 °C for 2 hours. Meanwhile 0.75 ml HCl (37 %) was added to adjust the pH value to 1.5. The clear light pink solution was filled into a Teflon autoclave (V = 20 ml) with filling degree of about 30 %, and held at 170 °C for one week under autogenous pressure. Colorless prismatic crystals of $(C_3H_{12}N_2)\{Mn[B_2P_3O_{12}(OH)]\}$ (*Fig. 3.31*) were separated by filtration, washed with deionized water and dried at 60 °C in air.

$(C_4H_{12}N_2)\{Mn[B_2P_3O_{12}(OH)]\}$(**PIP-Mn**) was also prepared by hydrothermal synthesis with a similar procedure to **DAP-Mn**. Mixtures of 0.3775 g (3 mmol) $MnCl_2$, 0.371 g (6 mmol) H_3BO_3, 0.2585 g (3 mmol) piperazine ($C_4H_{10}N_2$, PIP) and 1.26 g (11 mmol) 85 % H_3PO_4, and 7.5 ml of deionized water, were stirred at 60 °C for 2 hours. The same products can be found by using the same molar ratio as given for the preparation of **DAP-Mn** (Mn : B : P : PIP = 3 : 6 : 11 : 11). A SEM micrograph of a single crystal of **PIP-Mn** is presented in *Fig. 3.32*.

PIP-Mn is isotypic to $(C_4H_{12}N_2)\{M^{II}[B_2P_3O_{12}(OH)]\}$ (M^{II} = Co, Zn). In case of the DAP-compound, we were not able to obtain isotypes with other transition metals, e.g., Fe, Co, Ni, Cu, Zn. The reason may be due to the variability in condition of Mn^{II}, which is known to be octahedra and square pyramid, while other transition elements, e.g. Co and Zn, prefer octahedra coordination.

Mn, B, and P contents of both compounds were analyzed using ICP-AES, while a hot extraction method was applied for analyzing the organic carbon and nitrogen contents. The results are summarized in *Table 3.17*. Observed and calculated values were found to be in good agreement.

Phase purities of the reaction products for both compounds were checked by powder X-ray diffraction (HUBER Image Foil Guinier Camera G670, Cu $K\alpha_1$-radiation, Ge monochromator). *Fig. 3.33* and *Fig. 3.34* show the observed and calculated powder

patterns for **DAP-Mn** and **PIP-Mn**, respectively. Both figures show that the observed powder patterns match quite well to the calculated patterns. From the close similarities between the powder diffraction patterns of **DAP-Mn** and **PIP-Mn** (shown in *Fig. 3.35*), we concluded that the two structures could be closely related.

Table 3.17: Results of chemical analysis for **DAP-Mn** and **PIP-Mn**; /mass-% (e.s.d.).

Element	**DAP-Mn**(Obs./Calc.)	**PIP-Mn**(Obs./Calc.)
Mn	11.99(5)/12.08	11.98(8)/11.77
B	5.33(2)/4.76	4.54(3)/4.32
P	22.43(5)/20.44	20.1(1)/19.91
C	7.90(4)/7.93	10.27(5)/10.30
N	6.09(3)/6.16	6.13(4)/6.00
H	2.056(4)/2.88	2.81(2)/2.81
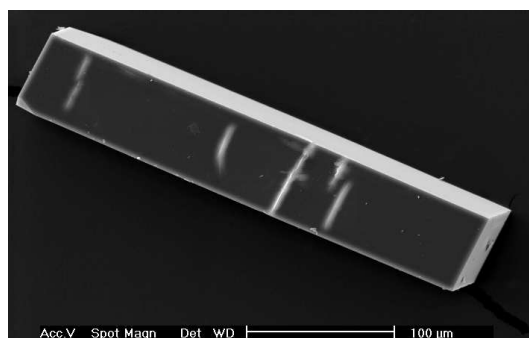
Figure 3.31: SEM micrograph of a prismatic single crystal of **DAP-Mn**
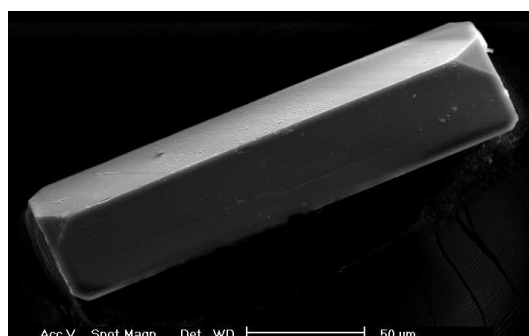
Figure 3.32: SEM micrograph of a prismatic single crystal of **PIP-Mn**.
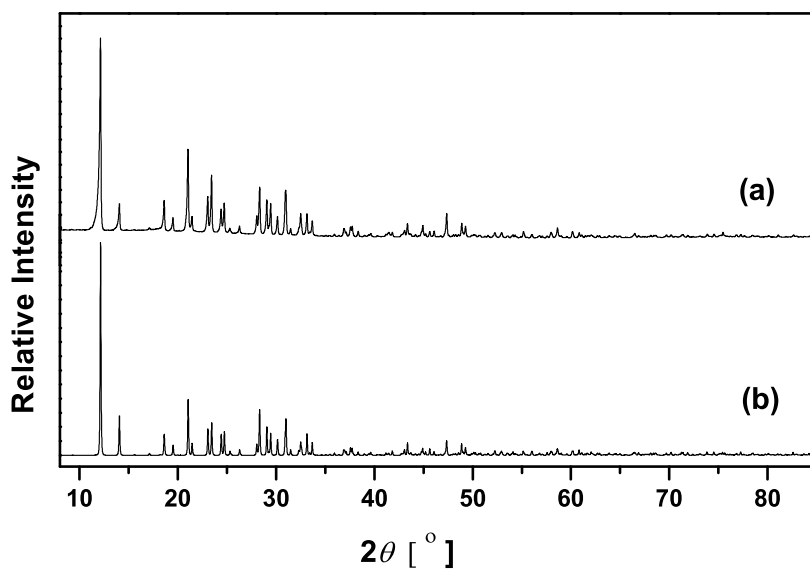
Figure 3.33:   Powder X-ray diffraction patterns of **DAP-Mn**:   (a)observed,
(b)calculated from structure data; Cu $K_{\alpha 1}$-radiation.
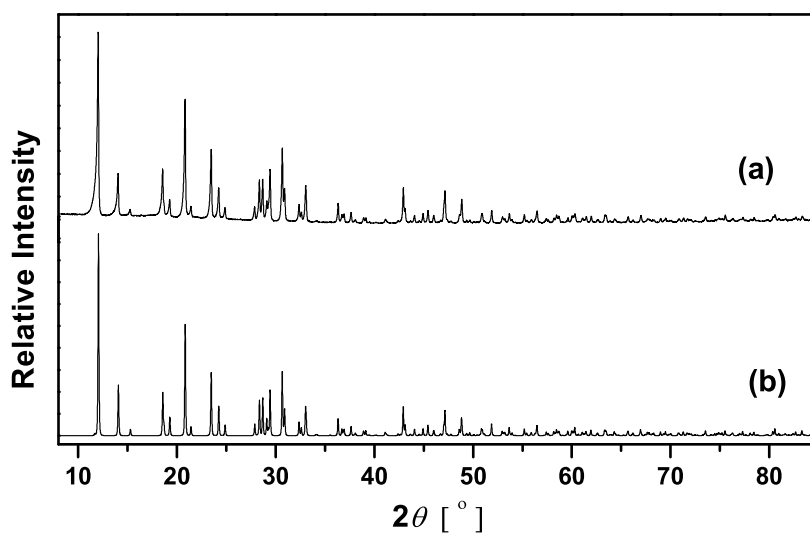
Figure 3.34: Powder X-ray diffraction patterns of **PIP-Mn**: (a)observed, (b)calculated
from structure data; Cu $K_{\alpha 1}$-radiation.
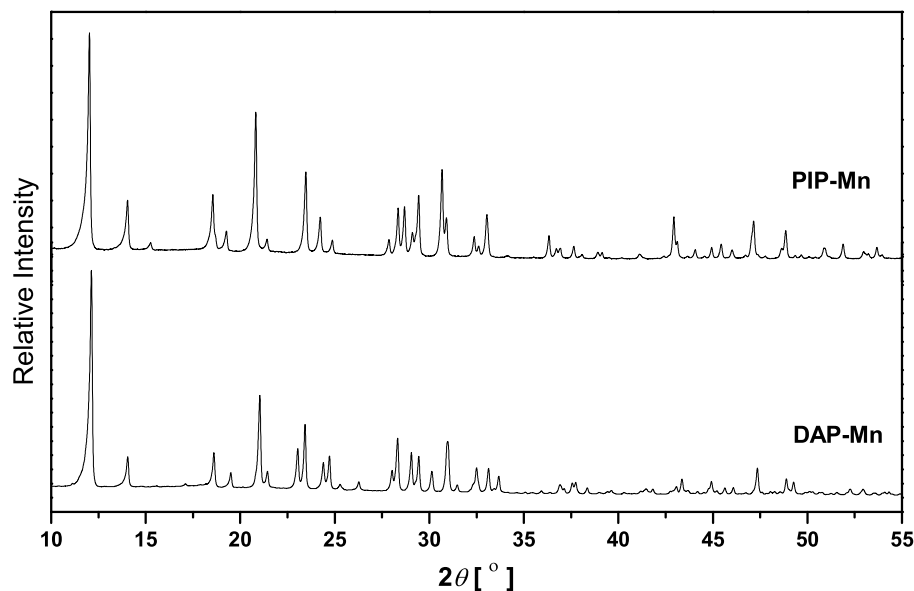
Figure 3.35: Powder X-ray diffraction patterns of $(C_3H_{12}N_2)\{Mn^{II}[B_2P_3O_{12}(OH)]\}$(**PIP-Mn**) and $(C_4H_{12}N_2)\{Mn^{II}[B_2P_3O_{12}(OH)]\}$(**PIP-Mn**); Cu $K_{\alpha 1}$-radiation.

3.3.2 Crystal structure determination

A colorless single crystal of **DAP-Mn** (prismatic, $0.12 \times 0.06 \times 0.04$ mm^3) was fixed on a glass fiber with two-component glue. The crystal quality was first checked with the Laue method. X-ray data were collected at 295 K using a Rigaku AFC7 four-circle diffractometer, equipped with a Mercury-CCD detector (Mo K_α-radiation, graphite monochromator) in the angular range $3.24° \leq 2\theta \leq 68.68°$ ($300°$-ϕ-scan, $60°$-ω-scan at $\chi = 90°$, $0.6°$ steps with 45 s exposure time per step, detector distance: 40 mm; 2θ-offset: $-25.00°$). The data were corrected for Lorentz and polarization effects. A multi-scan absorption correction was applied. The crystal structure was solved in space group $Pmc2_1$ (No. 26) by direct methods using the program SHELXS-97-2 [P2]. Fourier calculations and subsequent full-matrix least-squares refinements were carried out using SHELXL-97-2 [P3]. After anisotropic displacement parameters had been included in the refinement, all hydrogen atoms bond to C and N could be located

from difference Fourier maps and refined without constraints. The only constraint was applied to H1 (bonded to O6, $d_{O6-H1} = 80$ pm) which is at a special position. Final residual electron density of $0.49/-0.49$ e $\cdot 10^{-6}$pm^{-3} was observed close to Mn1 and O16, respectively. Although the Flack parameter [137, 138] of 0.40(1) may give hints to a higher symmetry, no close correlations between atoms and between thermal parameters indicate that it doesn't go to higher symmetry. Therefore the high Flack parameter is due to an inversion twin. When we applied command "TWIN" with an inversion matrix (-1 0 0, 0 -1 0, 0 0 -1) in the structure refinement, the "BASF" value results in the same value (0.40(1)). Moreover, the S (Goodness-of-fit) value was dropped from 1.151 to 1.038, the $R1$ value reduce from 0.0342 to 0.0308, and w$R2$ value reduce from 0.750 to 0.674. Therefore this is an inversion twin. The crystallographic results are summarized in *Table 3.18*. Atomic coordinates and displacement parameters are given in *Table 3.19* and *Table 6.5*, selected interatomic distances and angles are given in *Table 3.21*.

A colorless single crystal of **PIP-Mn** (prismatic, $0.08 \times 0.04 \times 0.04$ mm^3) was measured at 295 K on the same diffractometer with **DAP-Mn**. Intensity data were collected in the angular range $4.78° \leq 2\theta \leq 64.06°$ (240°-ϕ-scan, 60°-ω-scan at $\chi = 90°$, 0.6° steps with 60 s exposure time per step, detector distance: 40 mm; 2θ-offset: $-20.00°$). The data were corrected for Lorentz and polarization effects. A multi-scan absorption correction was applied. The crystal structure was solved in the space group $Ima2$ (No. 46) by direct methods using the program SHELXS-97-2 [P2]. Fourier calculations and subsequent full-matrix least-squares refinements were carried out using SHELXL-97-2 [P3]. After anisotropic displacement parameters had been included in the refinement, all hydrogen atoms could be located from difference Fourier maps and were refined without constraints. The final residual electron density was $0.75/-0.45$ e $\cdot 10^{-6}$pm^{-3}, very close to O9 and P1 respectively. The Flack x-parameter [137, 138] was about 0.01(2). The crystallographic data are summarized in *Table 3.18*. Atomic coordinates and displacement parameters are given in *Table 3.20* and *Table 6.6*, selected interatomic distances and angles are given in *Table 3.22*.

Table 3.18: Crystallographic data and refinement results of $(C_3H_{12}N_2)\{Mn[B_2P_3O_{12}(OH)]\}$(**DAP-Mn**) and $(C_4H_{12}N_2)\{Mn[B_2P_3O_{12}(OH)]\}$(**PIP-Mn**), e.s.d.'s are given in parentheses.

Compound	:	**DAP-Mn**	**PIP-Mn**
Space group	:	$Pmc2_1$ (No. 26)	$Ima2$ (No. 46)
a [pm]	:	1259.43(5)	1257.9(1)
b [pm]	:	949.86(5)	948.69(8)
c [pm]	:	1135.92(5)	1158.19(8)
V [10^6 pm^3]/Z	:	1358.9(1)/2	1382.2(2)/2
$F(000)$	:	916	940
Calc. density ρ [g $\cdot$ cm^{-3}]	:	2.222	2.242
Diffractometer	:	RIGAKU AFC7 CCD	
		Mo K_α-radiation	
		graphite monochromator	
$\mu_{MoK\alpha}$ [mm^{-1}]	:	1.403	1.383
Scan type	:	ϕ /ω	
2θ-range [°]	:	3.24–68.68	5.38–64.38
Miller-index range	:	$-19 \le h \le 19$	$-14 \le h \le 17$
		$-14 \le k \le 14$	$-14 \le k \le 10$
		$-17 \le l \le 17$	$-16 \le l \le 16$
Total data collected	:	15341	5987
Unique data	:	5249	2249
Observed data ($I > 2\sigma(I)$)	:	4917	2077
R_{int}/R_σ	:	0.0297/0.0367	0.0376/0.0531
Number of parameters refined	:	296	154
$R1$ ($F_o > 4\sigma(F_o)$)	:	0.0308	0.0347
$R1$ (all data)	:	0.0359	0.0410
$wR2$ ($F_o > 4\sigma(F_o)$)	:	0.0654	0.0677
$wR2$ (all data)	:	0.0674	0.0698
Goodness-of-Fit (for F^2)	:	1.038	1.042
Residual electron density (max/min) [e $\cdot$ 10^{-6}pm^{-3}]	:	0.49/-0.49	0.75/-0.45
Flack x-parameters	:	0.40(1)*	0.01(2)
Programs	:	DIAMOND [P4]	
		SHELXS–97/2 [P2], SHELXL–97/2 [P3]	

* The Flack x-parameter was reset automatically after every refinement cycle. For this reason, the unrefined value was taken from the SHELXL lst file.

Table 3.19: Atomic coordinates and equivalent/isotropic displacement parameters $[10^{-4}\text{pm}^2]$ in the crystal structure of $(C_3H_{12}N_2)\{Mn[B_2P_3O_{12}(OH)]\}$(**DAP-Mn**), e.s.d.'s are given in parentheses.

Atom	Site	x	y	z	$U_{\text{eq}}/\ U_{\text{iso}}$
Mn1	$2b$	0.5000	0.37292(5)	0.31809(4)	0.01168(8)
Mn2	$2a$	0.0000	0.17919(5)	0.27506(4)	0.01055(8)
P1	$2b$	0.5000	0.35687(8)	0.60698(6)	0.01032(13)
P2	$2a$	0.0000	0.52412(8)	0.19687(7)	0.01195(13)
P3	$2a$	0.0000	0.06878(8)	0.54304(6)	0.01074(13)
P4	$4c$	0.25167(4)	0.25952(5)	0.37404(5)	0.00917(8)
P5	$2b$	0.5000	0.05751(8)	0.14600(7)	0.01218(13)
B1	$4c$	0.09608(16)	0.3165(2)	0.53293(19)	0.0098(3)
B2	$4c$	0.40272(16)	0.1380(2)	0.51371(19)	0.0100(3)
O1	$4c$	0.33272(11)	0.35486(16)	0.31707(15)	0.0143(3)
O2	$4c$	0.19180(11)	0.35254(15)	0.46768(14)	0.0122(2)
O3	$2a$	0.0000	0.3441(2)	0.46455(19)	0.0101(3)
O4	$4c$	0.40113(11)	0.25525(16)	0.60107(13)	0.0128(3)
O5	$4c$	0.40159(11)	0.99976(17)	0.07824(14)	0.0132(3)
O6	$2a$	0.0000	0.5690(3)	0.3290(2)	0.0205(4)
O7	$2b$	0.5000	0.1490(2)	0.44237(17)	0.0093(4)
O8	$4c$	0.17344(12)	0.19228(17)	0.29121(12)	0.0142(3)
O9	$4c$	0.30860(12)	0.13694(16)	0.44115(13)	0.0121(3)
O10	$4c$	0.09865(11)	0.16749(16)	0.56992(14)	0.0133(3)
O11	$2b$	0.5000	0.9808(3)	0.2678(2)	0.0246(5)
O12	$2b$	0.5000	0.2130(2)	0.1593(2)	0.0175(4)
O13	$2b$	0.5000	0.4520(2)	0.4992(2)	0.0151(4)
O14	$4c$	0.09918(11)	0.59401(18)	0.14043(14)	0.0167(3)
O15	$2a$	0.0000	0.0302(2)	0.4148(2)	0.0161(4)
O16	$2a$	0.0000	0.3696(3)	0.1831(2)	0.0205(5)
O17	$2b$	0.5000	0.5619(2)	0.2199(2)	0.0172(4)
O18	$2a$	0.0000	0.0497(3)	0.1282(2)	0.0216(5)
N1	$4c$	0.30207(19)	0.4188(3)	0.0782(2)	0.0216(4)
N2	$4c$	0.23707(19)	0.0889(3)	0.7506(2)	0.0242(4)
C1	$4c$	0.2407(2)	0.3003(3)	0.0294(2)	0.0270(5)
C2	$4c$	0.1974(2)	0.8449(3)	0.3610(3)	0.0287(5)
C3	$4c$	0.2664(3)	0.7237(3)	0.4016(2)	0.0308(6)
H1	$2a$	0.0000	0.496(5)	0.359(8)	0.13(4)*
H2	$2b$	0.5000	1.048(9)	0.334(8)	0.11(3)*
H3	$4c$	0.274(3)	0.497(6)	0.058(4)	0.063(13)*
H4	$4c$	0.296(3)	0.419(4)	0.150(3)	0.032(9)*
H5	$4c$	0.358(3)	0.417(4)	0.058(3)	0.038(11)*
H6	$4c$	0.225(2)	0.001(4)	0.749(3)	0.031(9)*
H7	$4c$	0.196(3)	0.127(5)	0.690(4)	0.066(14)*
H8	$4c$	0.305(4)	0.100(5)	0.757(4)	0.063(14)*

*refined with isotropic displacement parameters

Table 3.19 Continued

Atom	Site	x	y	z	U_{eq}/ U_{iso}
H9	$4c$	0.262(3)	0.218(5)	0.068(4)	0.054(13)*
H10	$4c$	0.170(3)	0.307(4)	0.045(3)	0.045(10)*
H11	$4c$	0.236(5)	0.913(7)	0.426(5)	0.12(2)*
H12	$4c$	0.123(3)	0.819(4)	0.334(3)	0.036(9)*
H13	$4c$	0.258(4)	0.637(6)	0.347(5)	0.10(2)*
H14	$4c$	0.342(4)	0.758(6)	0.389(4)	0.079(16)*

*refined with isotropic displacement parameters

Table 3.20: Atomic coordinates and equivalent/isotropic displacement parameters $[10^{-4}pm^2]$ in the crystal structure of $(C_4H_{12}N_2)\{Mn[B_2P_3O_{12}(OH)]\}$(**PIP-Mn**), e.s.d.'s are given in parentheses.

Atom	Site	x	y	z	U_{eq}/ U_{iso}
Mn1	$4b$	0.7500	0.91166(5)	0.81167(4)	0.00923(12)
P1	$4a$	0.5000	0.0000	0.73191(8)	0.00854(18)
P2	$4b$	0.7500	0.65204(9)	0.03207(8)	0.00953(19)
P3	$4b$	0.7500	0.24022(10)	0.93057(9)	0.01118(19)
B1	$8c$	0.8467(2)	0.4130(3)	0.0826(3)	0.0098(5)
O1	$8c$	0.58081(15)	0.91673(19)	0.79828(17)	0.0134(4)
O2	$8c$	0.94188(15)	0.38937(19)	0.15156(15)	0.0110(4)
O3	$8c$	0.84937(15)	0.55267(19)	0.02646(17)	0.0116(4)
O4	$4b$	0.7500	0.7490(3)	0.9310(3)	0.0183(6)
O5	$4b$	0.7500	0.7728(3)	0.6491(2)	0.0144(6)
O6	$4b$	0.7500	0.3003(3)	0.8048(3)	0.0198(6)
O7	$8c$	0.84939(16)	0.3009(2)	0.99252(17)	0.0154(4)
O8	$4b$	0.7500	0.0840(3)	0.9287(3)	0.0152(6)
O9	$4b$	0.7500	0.4009(3)	0.1530(2)	0.0077(5)
N1	$8c$	0.9455(2)	0.8671(3)	0.1760(3)	0.0196(5)
C1	$8c$	0.9505(3)	0.9549(4)	0.0715(3)	0.0286(8)
C2	$8c$	0.9510(3)	0.9536(4)	0.2832(3)	0.0318(8)
H1	$4b$	0.7500	0.255(9)	0.772(7)	0.09(3)*
H2	$8c$	0.876(4)	0.828(4)	0.183(4)	0.049(13)*
H3	$8c$	1.000(3)	0.804(3)	0.171(3)	0.012(8)*
H4	$8c$	0.947(4)	0.899(4)	0.020(4)	0.047(13)*
H5	$8c$	0.883(4)	1.014(5)	0.068(4)	0.048(14)*
H6	$8c$	0.881(3)	1.005(4)	0.285(3)	0.030(10)*
H7	$8c$	0.948(3)	0.891(4)	0.352(3)	0.025(10)*

*refined with isotropic displacement parameters

3.3.3   Crystal structure description

3.3.3.1   Common Motif

The crystal structures of both compounds contain identical building units related to those in $M^{II}(C_4H_{12}N_2)[B_2P_3O_{13}]$ (M^{II} = Co, Zn) [103]. The anionic borophosphate partial structures consist of infinite loop-branched single chains, $\frac{1}{\infty}\{[B_2P_3O_{12}(OH)]^{4-}\}$, running along [100] (Fig. 3.36a), which are built up from BO_4-, PO_4- and $(HO)PO_3$-tetrahedra. The central chain is built from a sequence of two BO_4-tetrahedra followed by one PO_4-tetrahedron. The terminal corners of adjacent BO_4-tetrahedra are loop-branched by one additional PO_4-group in one side and one $(HO)PO_3$-tetrahedron in another side. This type of chains was already observed in the crystal structures of $M^{II}(C_4H_{12}N_2)[B_2P_3O_{13}]$ (M^{II} = Co, Zn) [103] and is closely related to the stretched loop-branched single chains $\frac{1}{\infty}\{[B_2P_3O_{13}]^{5-}\}$ (Fig. 3.36b) present in the crystal structures of $Na_5[B_2P_3O_{13}]$ [30]. Compared the single chains of $\frac{1}{\infty}\{[B_2P_3O_{12}(OH)]^{4-}\}$ and $\frac{1}{\infty}\{[B_2P_3O_{13}]^{5-}\}$, the periodicity along the chains of $\frac{1}{\infty}\{[B_2P_3O_{12}(OH)]^{4-}\}$ in **DAP-Mn** and **PIP-Mn** is doubled (Fig. 3.36).
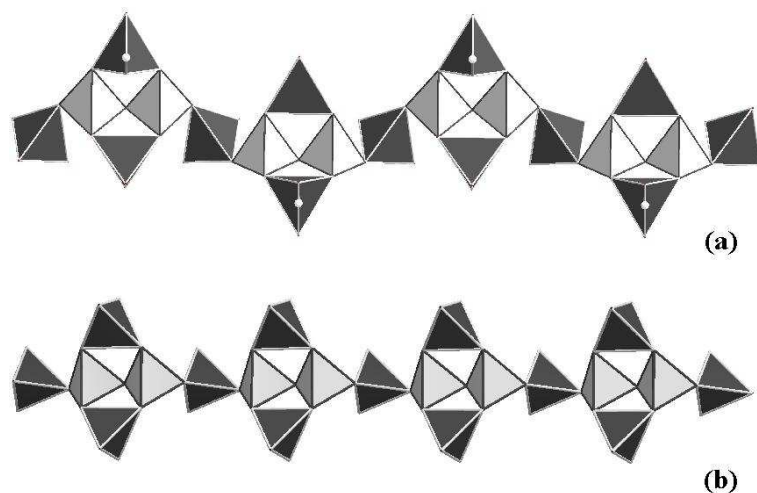
Figure 3.36: (a) Loop-branched single chain $\frac{1}{\infty}\{[B_2P_3O_{12}(OH)]^{4-}\}$ in **DAP-Mn** and **PIP-Mn**, (b) loop-branched single chain $\frac{1}{\infty}\{[B_2P_3O_{13}]^{5-}\}$ in $Na_5[B_2P_3O_{13}]$ [30]; BO_4 tetrahedra: light grey, PO_4 tetrahedra: dark grey. H atoms: white spheres.

The loop-branched single chains also connect to each other through O–H$\cdots$O hydrogen bonds. Fig. 3.37 shows the single chains are interconnected by the hydrogen

bonds forming a three dimensional network.
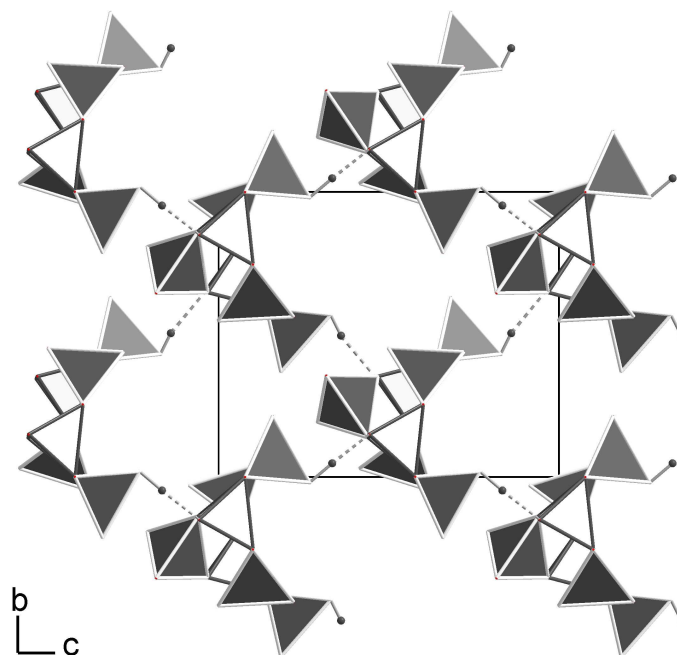
Figure 3.37: Loop-branched single chains $\frac{1}{\infty}\{[B_2P_3O_{12}(OH)]^{4-}\}$ of **DAP-Mn** and **PIP-Mn** are interconnected by hydrogen bonds. BO_4 tetrahedra: light grey, PO_4 tetrahedra: dark grey; H atoms: dark grey spheres; hydrogen bonds: dashed lines.

The BO_4- and PO_4-tetrahedra in both manganese compounds are in an almost regular tetrahedral coordination. Bond lengths and angles are all within normal values and comparable with other borophosphates [103,119]. Detailed bond lengths and angles of B–O and P–O see *Table 3.21* and *Table 3.22*.

The Mn-coordination polyhedra can be described as distorted octahedra when the long Mn–O distances are also taken into consideration. The long Mn–O distances of 255.3 pm and 266.2 pm for **DAP-Mn** and 255.8 pm for **PIP-Mn**, are much longer than the average distance of Mn–O in **DAP-Mn** (210 pm and 222 pm) and in **PIP-Mn** (222 pm) (shown in *Fig. 3.38* and *Table 3.21*), the Mn coordination number therefore is 5+1 for both compounds. In **DAP-Mn**, the bond valence sums [139] for Mn1 and Mn2 under non-consideration of the long bonds are lower ($\sum_s$ Mn1–O = 1.806 for Mn1 and $\sum_s$ Mn2–O = 1.984), but increase to 1.933 for Mn1 and 2.078 for Mn2 after taking the long bonds into account. In **PIP-Mn**, the bond valence sums for Mn1 in the absence of the longer bond distances are lower ($\sum_s$ Mn1–O7 = 1.966), but increase

to 2.092 after taking the longer bond into account. The Mn–O bond lengths range
from 207.3 pm to 266.2 pm for **DAP-Mn** and 207.1 pm to 255.8 pm for **PIP-Mn**.
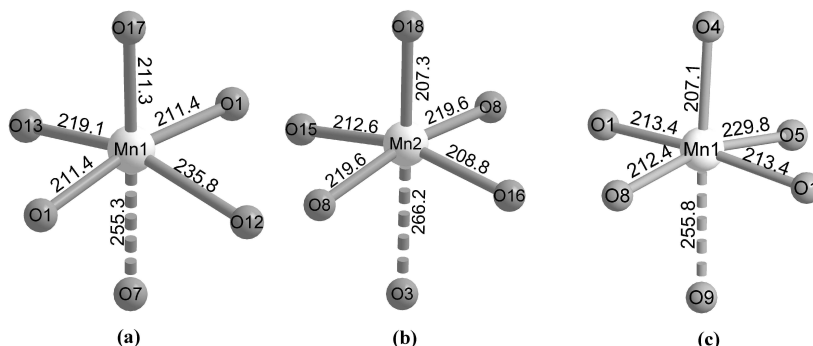
Figure 3.38: Details of MnO_6 octahedral coordination environments: (a) and (b) come
from **DAP-Mn**, and (c) comes from **PIP-Mn**. Bond lengths in pm.

The MnO_6 octahedra connect five PO_4 tetrahedra and two BO_4 tetrahedra via
common oxygen vertices, resulting in secondary building units (SBU), which are shown
in *Fig. 3.39*. It is noteworthy that the MnO_6 octahedra connect two BO_4 tetrahedra via
a μ^3-O corner, which has an additional hydrogen bond to the OH-group of a neighboring
$(OH)PO_3$ tetrahedron. The SBU are connected to each other via O-corners resulting
in a 3D anionic open framework with three-dimensional arrangement of intersecting
channels of different dimensions along [100], [011] and [01$\bar{1}$] directions, respectively
(*Fig. 3.40*).
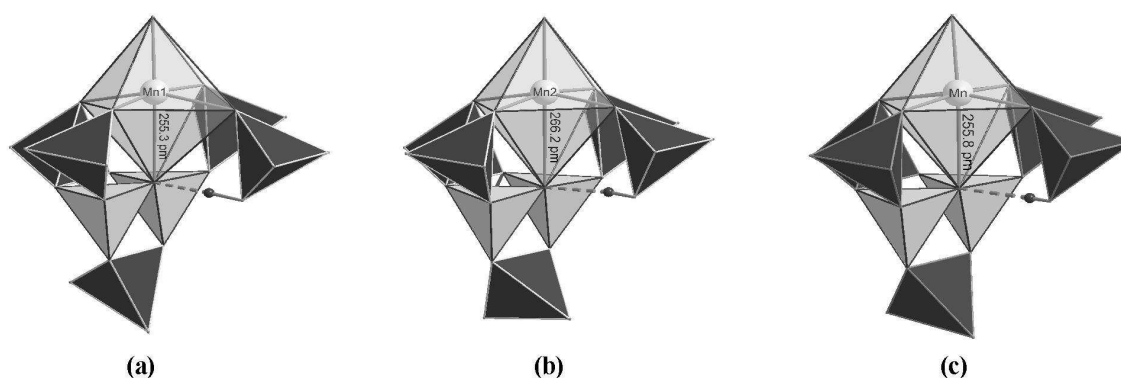
Figure 3.39: Secondary Building Units (SBU) of **DAP-Mn**(a, b) and **PIP-Mn**(c).
MnO_6 octahedra: light grey, BO_4 tetrahedra: light grey, PO_4 tetrahedra: dark grey;
H atoms: dark grey spheres; hydrogen bonds: dashed lines.
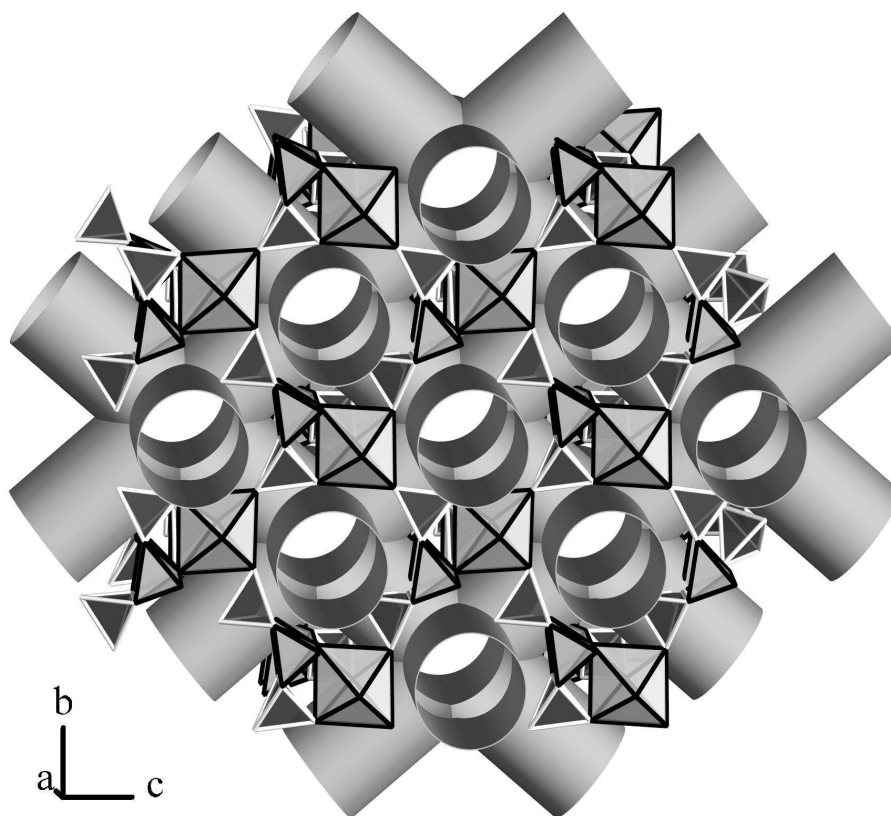
Figure 3.40: Three dimensional intersections channel system running along [100], [011] and [01$\bar{1}$] in the crystal structures of **DAP-Mn** and **PIP-Mn**. MnO_6 octahedra: light grey, BO_4 tetrahedra: light grey, PO_4 tetrahedra: dark grey.

The overall views of the crystal structures of **DAP-Mn** and **PIP-Mn** along [100] are shown in *Fig. 3.41*. Both of structures contain channels running along [100] which are formed by three MnO_6 octahedra, four PO_4 tetrahedra and two BO_4 tetrahedra. The channels are occupied by diprotonated organic molecules stacked along [100] and fixed via N–H$\cdots$O hydrogen bonds to the framework oxygen atoms. Details of the hydrogen bond interactions are given in *Fig. 3.42* and *Fig. 3.43, Table 3.23* and *Table 3.24. Fig. 3.42* shows that the hydrogen bond interactions in **DAP-Mn** connect the neighboring $(C_3H_{12}N_2)^{2+}$ ions to discrete units in the channels running along [100]. *Fig. 3.43* shows hydrogen bond interactions in **DAP-Mn** interconnect the $(C_4H_{12}N_2)^{2+}$ ions to a *zigzag* arrangement running along [100]. All hydrogen atoms coordinated to nitrogen atoms are involved in hydrogen bonds.
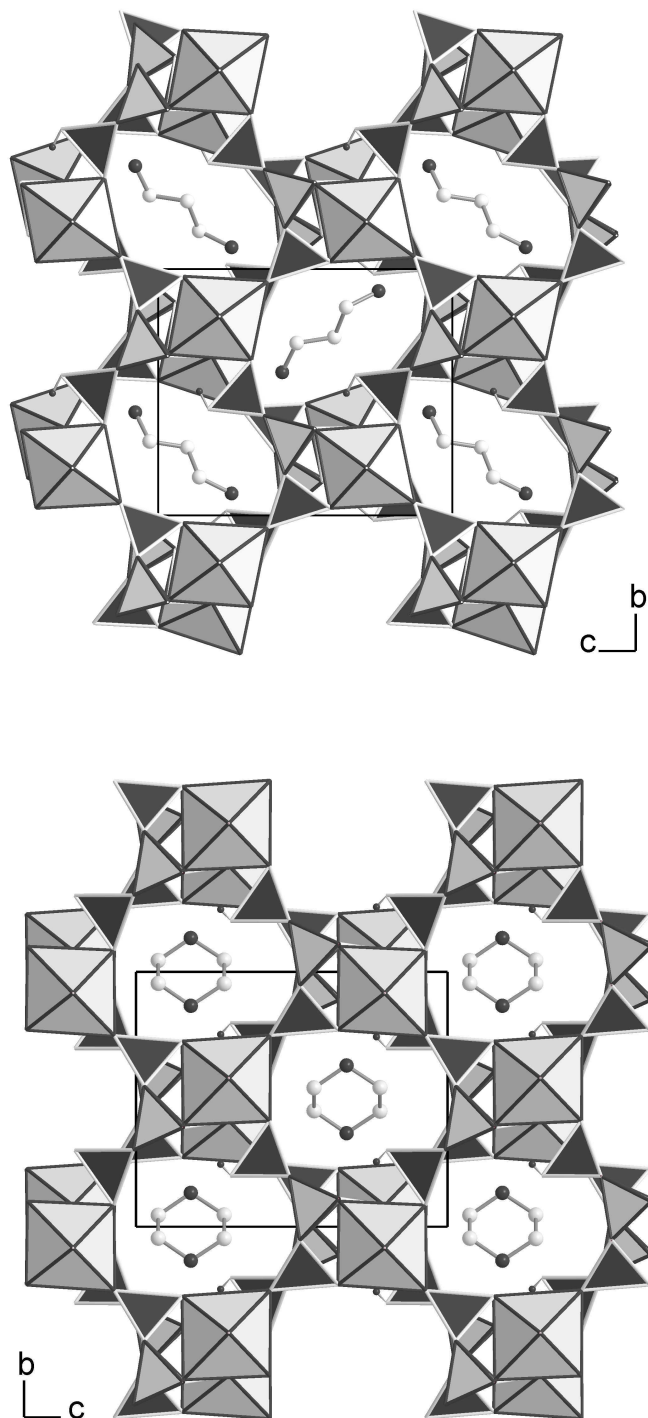
Figure 3.41: *Top*: Crystal structure of **DAP-Mn** viewed along the *a*-axis; *Bottom*: Crystal structure of **PIP-Mn** viewed along the *a*-axis. MnO_6 octahedra: light grey, BO_4 tetrahedra: light grey, PO_4 tetrahedra: dark grey; N atoms: dark grey, C atoms: light grey, H atoms: dark grey (small). Hydrogen atoms of the DAP templates were removed for clarity.
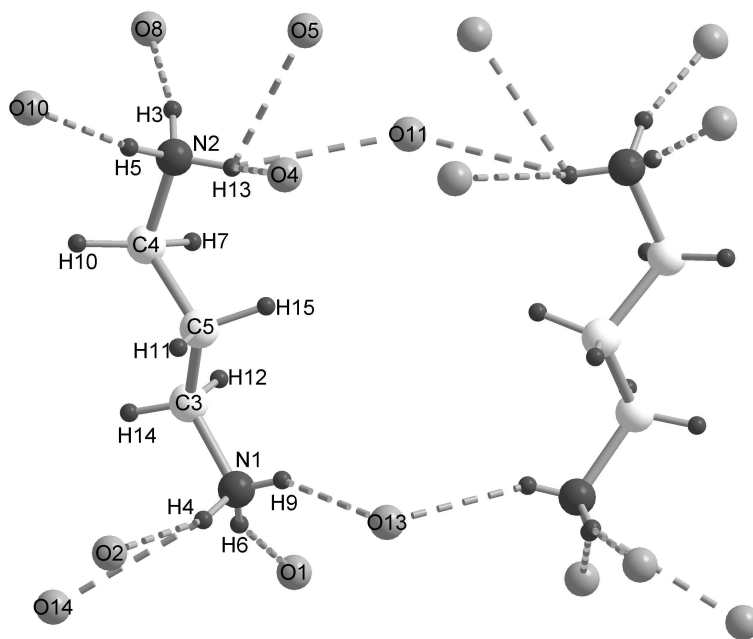
Figure 3.42: Hydrogen bonds in **DAP-Mn** connect neighboring DAP templates to discrete units in the channels running along [100].
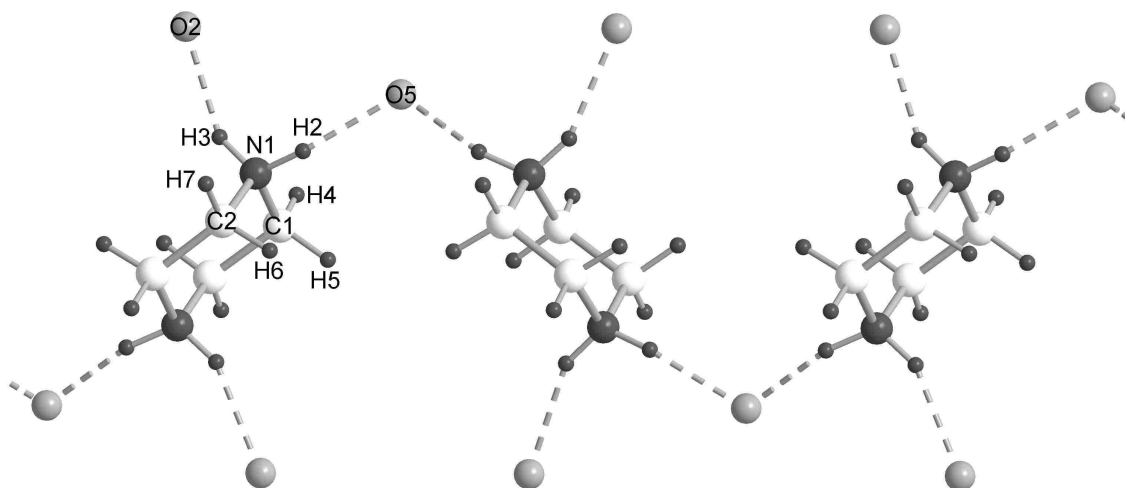
Figure 3.43: Hydrogen bonds in **PIP-Mn** interconnect the templates to a *zigzag* setting running along [100] (direction of the channel).

Table 3.21: Crystal structure of **DAP-Mn**: selected interatomic distances [pm] and angles [°], e.s.d.'s are given in parentheses.

|							
Mn1–	O17	211.3(2)	O17–Mn1–O1 (×2)	93.78(4)	O17–Mn1–O12	98.24(9)	
	O1 (×2)	211.38(14)	O1–Mn1–O1	170.67(9)	O13–Mn1–O12	159.97(8)	
	O13	219.0(2)	O17–Mn1–O13	101.79(9)	O17–Mn1–O7	178.28(8)	
	O12	235.8(2)	O1–Mn1–O13 (×2)	91.89(5)	O12–Mn1–O7	83.48(8)	
	O7	255.3(2)	O1–Mn1–O12 (×2)	86.76(5)	O13–Mn1–O7	76.49(8)	
			O1–Mn1–O7 (×2)	86.30(4)			
Mn2–	O18	207.3(2)	O18–Mn2–O16	96.39(10)	O8–Mn2–O8	168.42(8)	
	O16	208.8(2)	O18–Mn2–O15	101.87(9)	O18–Mn2–O3	179.66(9)	
	O15	212.6(2)	O18–Mn2–O8 (×2)	95.79(4)	O16–Mn2–O3	83.96(8)	
	O8 (×2)	219.56(15)	O16–Mn2–O8 (×2)	89.58(4)	O15–Mn2–O3	77.78(8)	
	O3	266.2(2)	O15–Mn2–O8 (×2)	88.59(4)	O16–Mn2–O15	161.74(9)	
			O8–Mn2–O3 (×2)	84.21(4)			
P1–	O17	149.7(2)	O17–P1–O13	112.53(13)	O4–P1–O4	104.31(12)	
	O13	152.2(2)	O17–P1–O4 (×2)	110.61(8)			
	O4 (×2)	157.69(15)	O13–P1–O4 (×2)	109.23(8)			
P2–	O16	147.6(3)	O16–P2–O14 (×2)	112.41(9)	O16–P2–O6	111.95(14)	
	O14 (×2)	155.31(15)	O14–P2–O14	107.08(12)			
	O6$_{H1}$	156.0(3)	O14–P2–O6 (×2)	106.28(9)			
P3–	O18	148.4(2)	O18–P3–O15	116.55(14)	O10–P3–O10	103.12(12)	
	O15	150.3(2)	O18–P3–O10 (×2)	108.84(9)			
	O10 (×2)	158.62(15)	O15–P3–O10 (×2)	109.32(8)			
P4–	O8	150.46(15)	O8–P4–O1	115.41(10)	O1–P4–O2	106.05(8)	
	O1	151.02(15)	O8–P4–O9	106.78(9)	O9–P4–O2	107.92(9)	
	O9	156.56(15)	O1–P4–O9	110.18(8)			
	O2	157.49(16)	O8–P4–O2	110.31(8)			
P5–	O12	148.5(2)	O12–P4–O5 (×2)	113.59(8)	O12–P4–O11	111.95(14)	
	O5 (×2)	155.87(15)	O5–P4–O5	105.34(12)			
	O11$_{H2}$	156.4(3)	O5–P4–O11 (×2)	105.84(9)			
B1–	O2	145.6(2)	O2–B1–O3	111.87(17)	O3–B1–O14	110.77(17)	
	O3	146.2(2)	O2–B1–O10	110.63(16)	O10–B1–O14	108.27(16)	
	O10	147.6(3)	O3–B1–O10	109.99(16)			
	O14	148.9(3)	O2–B1–O14	105.15(15)			
B2–	O9	144.4(2)	O9–B2–O7	111.68(16)	O7–B2–O5	109.81(16)	
	O7	147.3(2)	O9–B2–O4	111.94(16)	O4–B2–O5	109.03(16)	
	O4	149.2(3)	O7–B2–O4	108.91(16)			
	O5	150.0(3)	O9–B2–O5	105.38(15)			
N1–	C1	147.4(4)	N1–C1–C3	111.4(2)			
N2–	C2	148.9(4)	N2-C2–C3	112.6(2)			
C1–	C3	150.5(4)	C1–C3–C2	106.5(2)			
C2–	C3	151.4(4)					

Table 3.21 Continued

N1–	H3	86(6)	C1–H9	94(4)
N1–	H4	82(4)	C1–H10	91(4)
N1–	H5	74(4)	C2–H11	110(6)
N2–	H6	85(4)	C2–H12	101(4)
N2–	H7	93(5)	C3–H13	104(6)
N2–	H8	86(4)	C3–H14	102(5)

Table 3.22: Crystal structure of **PIP-Mn**: selected interatomic distances [pm] and angles [°], e.s.d.'s are given in parentheses.

Mn1–	O4	207.1(3)	O4–Mn1–O8	98.49(12)	O4–Mn1–O5	96.85(12)
	O8	212.4(3)	O4–Mn1–O1 (×2)	93.74(5)	O4–Mn1–O9	175.89(11)
	O1 (×2)	213.45(19)	O8–Mn1–O1 (×2)	91.66(5)	O8–Mn1–O9	85.62(9)
	O5	229.8(3)	O1–Mn1–O9 (×2)	86.11(5)	O1–Mn1–O1	171.27(11)
	O9	255.8(3)	O1–Mn1–O5 (×2)	87.33(6)	O5–Mn1–O9	79.03(9)
			O8–Mn1–O5	164.65(10)		
P1–	O1 (×2)	149.94(19)	O1–P1–O2 (×2)	109.74(10)	O1–P1–O1	118.32(17)
	O2 (×2)	158.18(19)	O1–P1–O2 (×2)	105.39(10)	O2–P1–O2	107.92(14)
P2–	O4	148.9(3)	O4–P2–O5	114.10(18)	O3–P2–O3	105.82(15)
	O5	153.2(3)	O4–P2–O3 (×2)	109.82(11)		
	O3 (×2)	156.70(19)	O5–P2–O3 (×2)	108.47(10)		
P3–	O8	148.2(3)	O8–P3–O7 (×2)	112.19(10)	O8–P3–O6	110.54(18)
	O7 (×2)	155.2(2)	O7–P3–O7	107.29(15)		
	O6$_{H1}$	156.4(3)	O7–P3–O6 (×2)	107.17(11)		
B1–	O2	145.6(4)	O2–B1–O9	111.4(2)	O9–B1–O7	110.6(2)
	O9	146.9(3)	O2–B1–O3	111.2(2)	O3–B1–O7	109.3(2)
	O3	147.7(3)	O9–B1–O3	109.4(2)		
	O7	149.0(3)	O2–B1–O7	104.8(2)		
N1–	C1	147.1(4)	C1–N1–C2	111.8(3)		
N1–	C2	148.9(5)	N1–C1–C2	110.8(3)		
C1–	C1	151.1(8)	N1–C2–C2	111.0(3)		
C2–	C2	151.6(8)				
N1–	H2	96(5)				
N1–	H3	91(3)				
C1–	H4	80(5)				
C1–	H5	102(5)				
C2–	H6	100(4)				
C2–	H7	100(4)				

Table 3.23: Hydrogen bonds in the crystal structure of **DAP-Mn**: interatomic distances [pm] and angles [°]

Hydrogen bonds							
O6–H1	77.9	H1$\cdots$O3	186.9	O6$\cdots$O3	263.3	O6–H1$\cdots$O3	166.60
O11–H2	98.1	H2$\cdots$O7	156.6	O6$\cdots$O7	254.7	O6–H2$\cdots$O7	177.68
N1–H3	85.8	H3$\cdots$O2	203.7	N1$\cdots$O2	286.8	N1–H3$\cdots$O2	162.60
		H3$\cdots$O14	256.3	N1$\cdots$O14	313.0	N1–H3$\cdots$O14	124.57
N1–H4	82.0	H4$\cdots$O1	204.3	N1$\cdots$O1	280.7	N1–H4$\cdots$O1	154.92
N1–H5	73.9	H5$\cdots$O13	228.1	N1$\cdots$O13	292.0	N1–H5$\cdots$O13	145.29
N2–H6	85.1	H6$\cdots$O8	200.6	N2$\cdots$O8	282.7	N2–H6$\cdots$O8	161.75
N2–H7	93.4	H7$\cdots$O10	187.4	N2$\cdots$O10	279.4	N2–H7$\cdots$O10	168.02
N2–H8	86.2	H8$\cdots$O5	255.3	N2$\cdots$O5	297.3	N2–H8$\cdots$O5	110.95
		H8$\cdots$O11	258.0	N2$\cdots$O11	338.3	N2–H8$\cdots$O11	155.35
		H8$\cdots$O3	260.4	N2$\cdots$O3	310.6	N2–H8$\cdots$O3	118.25

Table 3.24: Hydrogen bonds in the crystal structure of **PIP-Mn**: interatomic distances [pm] and angles [°]

Hydrogen bonds							
O6–H1	57.6	H1$\cdots$O9	201.9	O6$\cdots$O9	259.5	O6–H1$\cdots$O9	178.51
N1–H2	95.6	H2$\cdots$O5	189.0	N1$\cdots$O5	281.2	N1–H2$\cdots$O5	161.39
N1–H3	91.3	H3$\cdots$O2	198.5	N1$\cdots$O2	283.0	N1–H3$\cdots$O2	153.13

3.3.3.2   DAP-Mn and PIP-Mn: differences in channel structure

The obvious structural difference between **DAP-Mn** and **PIP-Mn** is given by the shape of their channels. Especially channels along [100] show dramatic differences in both shape and size (see *Fig. 3.41*). It is likely that the differences in the shape of the channels are due to the shape and the size of the organic templates included. *Fig. 3.44* shows the arrangement of DAP cations and PIP cations in the channels, located between two neighboring 9-membered rings along [100]. The stacking of the two differently orientated 9-membered rings just fit the template shape. The stretched $(H_2DAP)^{2+}$ ions lead to elongated and elliptical channels, the cyclic $(H_2PIP)^{2+}$ ions lead to more isocentric channels. The length of DAP ($d_{N\cdots N} = 493$ pm) is much longer than the diameter of PIP (287 pm). So the stretched $(H_2DAP)^{2+}$ ions probably force the channel shape to elliptic. *Fig. 3.45* shows the different sizes of the 9-membered

rings in **DAP-Mn** and **PIP-Mn**. Two different sizes of 9-membered rings (912 pm × 595 pm) and (852 pm × 661 pm) are present in the crystal structure of **DAP-Mn**; while only one kind of 9-membered ring with an aperture of 788 pm × 739 pm is present in the crystal structure of **PIP-Mn**.
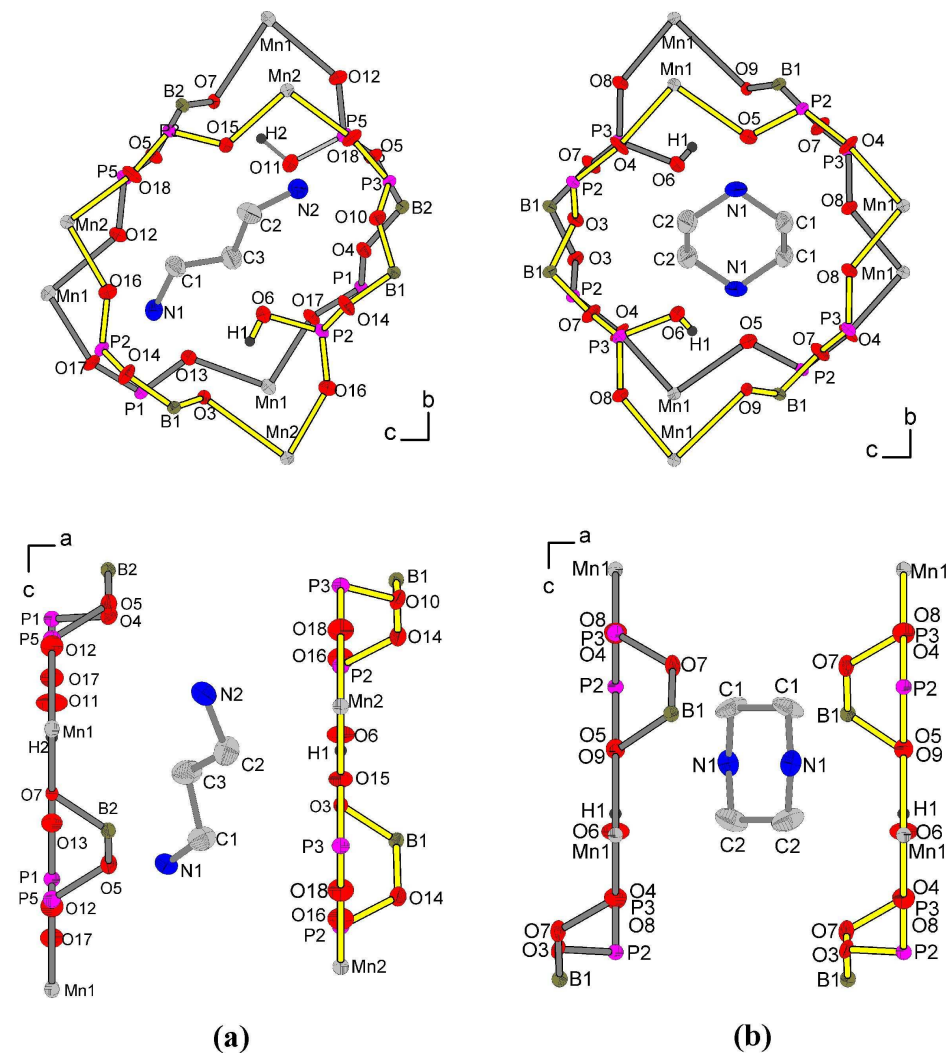

(a) **(b)**

Figure 3.44: (a) The ellipsoid presentation of the arrangement of 9-membered rings and DAP cations, bottom shows that DAP cations locate between two neighboring 9-membered rings along [100]. (b) The ellipsoid presentation of 9-membered rings and PIP cations, bottom shows that PIP cations locate between two neighboring 9-membered rings along [100].
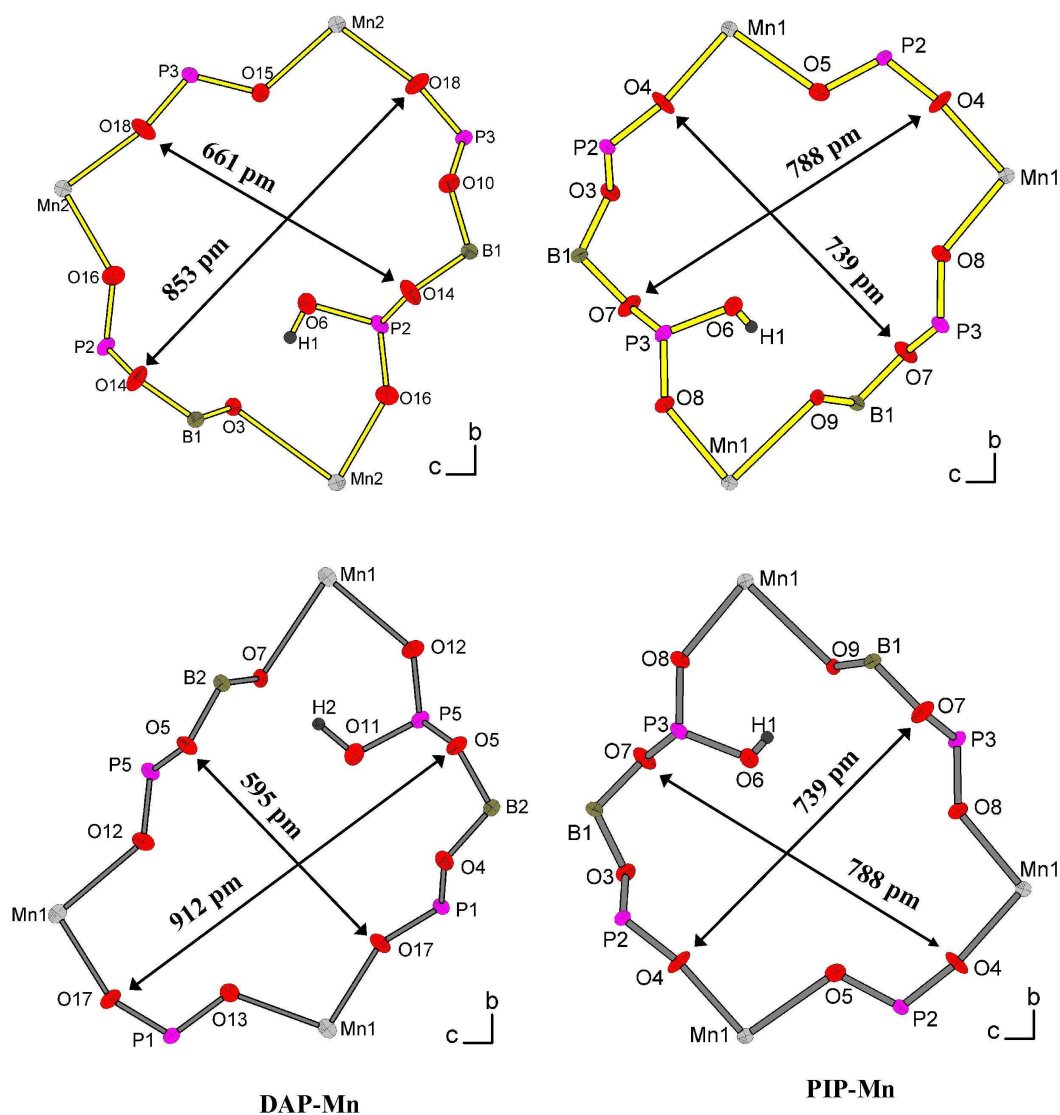
Figure 3.45: The difference sizes of 9-membered rings in **DAP-Mn** and **PIP-Mn** clearly show that **DAP-Mn** consists of elongated and elliptical channels and **PIP-Mn** consists of isocentric channels. Details see text.

$Pmc2_1$ (space group of **DAP-Mn**) is a subgroup of $Ima2$ (space group of **PIP-Mn**). The framework atom positions of **PIP-Mn** can be successfully transformed into those of **DAP-Mn** by using a "Klassengleich" matrix of (1/4, 1/4, 0) [140]. Some transformation principles should be obeyed: $4a \to 4c$, $4b \to 2a + 2b$, and $8c \to 2 \times 4c$ (from space group $Ima2$ to space group $Pmc2_1$). The detailed transformation is shown in *Fig. 3.46*.

PIP-Mn, *Ima*2 (No. 46)

Mn1: 4*b*	P1: 4*a*	P2: 4*b*	P3: 4*b*	O4: 4*b*	O5:4*b*	O6: 4*b*
1/4	0	1/4	1/4	1/4	1/4	1/4
0.91166	0	0.65205	0.24022	0.7490	0.7728	0.3001
0.2347	0.15496	0.45512	0.35361	0.3540	0.0722	0.2278

k2, 1/4, 1/4, 0

Mn1: 2*b*	Mn2: 2*a*	P4: 4*c*	P1:2*b*	P3: 2*a*	P2: 2*b*	P5: 2*a*	O18: 2*a*	O17: 2*b*	O15: 2*a*	O13: 2*b*	O6: 2*b*	O11: 2*a*
1/2	0	0.25169	1/2	0	1/2	0	0	1/2	0	1/2	1/2	0
0.12708	0.3208	0.24046	0.14319	0.43120	0.44253	0.02415	0.4502	0.0620	0.4698	0.0480	0.5193	0.0691
0.72343	0.76647	0.66766	0.43475	0.49866	0.89572	0.34484	0.9136	0.3219	0.6270	0.5424	0.7738	0.2126

DAP-Mn, *Pmc*2$_1$ (No. 26)

PIP-Mn, *Ima*2 (No. 46)

O8: 4*b*	O9: 4*b*	O1: 8*c*	O2: 8*c*	O3: 8*c*	O7: 8*c*	B1: 8*c*
1/4	1/4	0.08080	0.05813	0.15063	0.15060	0.1533
0.0840	0.0991	0.91674	0.11063	0.55267	0.30010	0.0870
0.3518	0.0760	0.22132	0.0746	0.44950	0.41557	0.0057

k2, 1/4, 1/4, 0

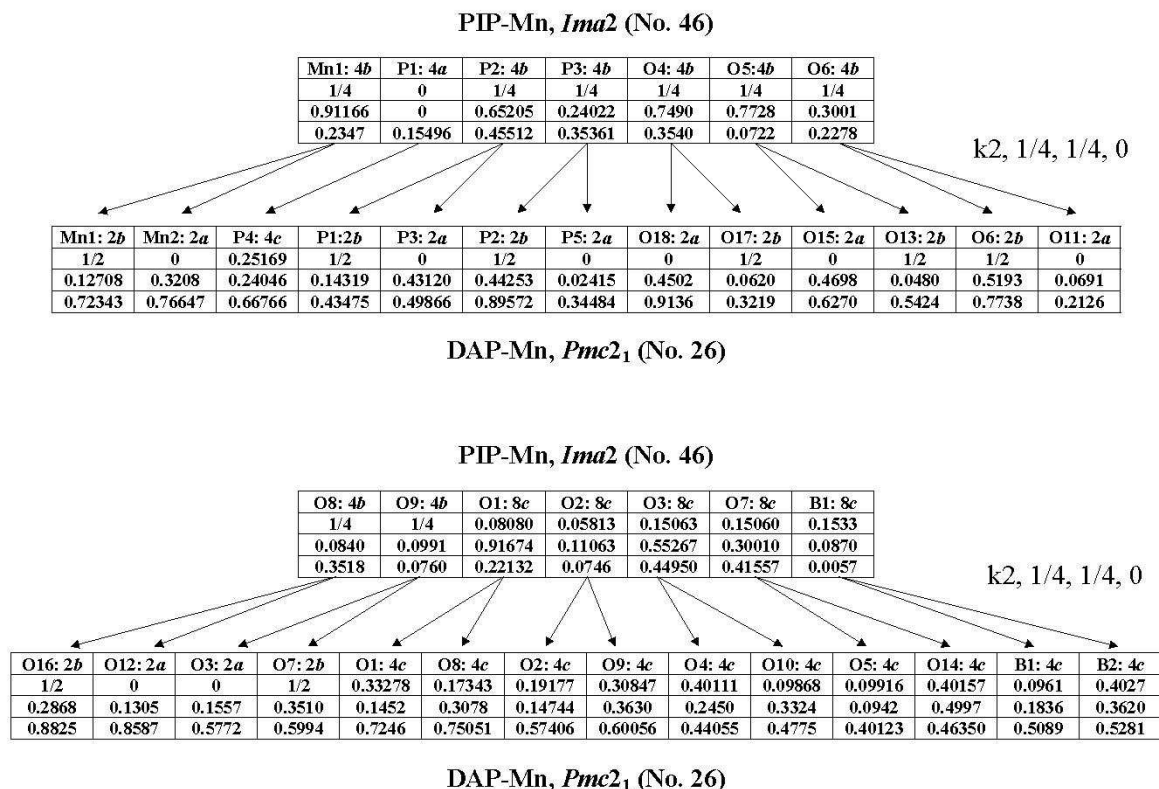| O16: 2*b*	O12: 2*a*	O3: 2*a*	O7: 2*b*	O1: 4*c*	O8: 4*c*	O2: 4*c*	O9: 4*c*	O4: 4*c*	O10: 4*c*	O5: 4*c*	O14: 4*c*	B1: 4*c*	B2: 4*c*
1/2	0	0	1/2	0.33278	0.17343	0.19177	0.30847	0.40111	0.09868	0.09916	0.40157	0.0961	0.4027
0.2868	0.1305	0.1557	0.3510	0.1452	0.3078	0.14744	0.3630	0.2450	0.3324	0.0942	0.4997	0.1836	0.3620
0.8825	0.8587	0.5772	0.5994	0.7246	0.75051	0.57406	0.60056	0.44055	0.4775	0.40123	0.46350	0.5089	0.5281

DAP-Mn, *Pmc*2$_1$ (No. 26)

Figure 3.46: The Bärnighausen system tree shows the structural relationship between **PIP-Mn** and **DAP-Mn**, the atom positions of both compounds are recalculated to an asymmetric cell positions (see appendix I).

3.3.4 IR-spectroscopy

The IR-spectra of **DAP-Mn** and **PIP-Mn** (1.5 mg sample : 150 mg KBr) are shown in *Fig. 3.47*. The band positions of O–H, N–H and C–H vibrations are summarized in *Table 3.25*. IR-spectrum of **DAP-Mn** confirmed the presence of $(C_3H_{12}N_2)^{2+}$ ions in the structure, as evidenced by the bands observed at 3152-2963, 2810-2638, 1514, 1477, and 1426 cm^{-1}, additional absorption bands for O–H stretching and deformation vibrations at 3276 and 1633 cm^{-1} are also observed. IR-spectrum of **PIP-Mn** confirmed the presence of $(C_4H_{12}N_2)^{2+}$ ions and O–H group which is exhibited by the N–H, C–H and O–H stretching vibrations at 3225, 3089-2977, 2840-2645, 1620, and 1482-1428 cm^{-1}.
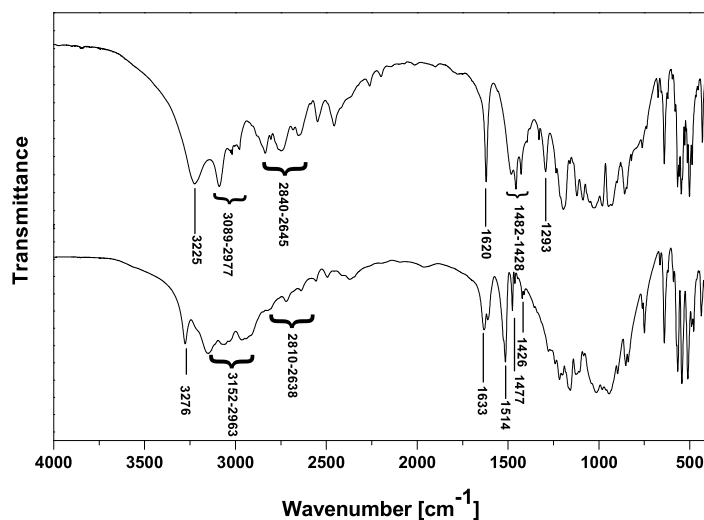
Figure 3.47:   Infrared spectra of **DAP-Mn** and **PIP-Mn** in the range of 4000–400 cm^{-1}.

Table 3.25: IR-spectroscopy data of **DAP-Mn** and **PIP-Mn**.

Vibration frequency $\tilde{\nu}$ [cm^{-1}]	Intensity[†], Band form[‡]	Assignment [129]
DAP-Mn		
3276	s,sp	O–H-stretch
3152–2963	s,sr	N–H-stretch
2810–2638	m,sr	C–H-stretch
1633	s,sp	O–H-deformation
1514, 1477, 1426	s,sp	N–H-deformation
PIP-Mn		
3225	s,sp	O–H-stretch
3089–2977	s,sr	N–H-stretch
2840–2645	m,sr	C–H-stretch
1620	s,sp	O–H-deformation
1482–1428	s,sp	N–H-deformation

[†]vs = very strong, s = strong, m = medium, w = weak
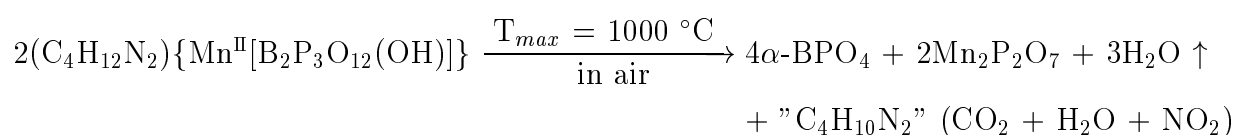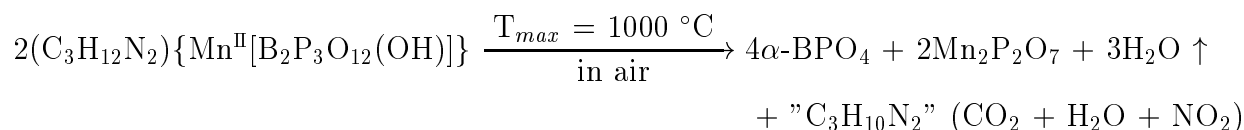[‡]br = broad, sp = sharp, sr = shoulder

3.3.5 Thermal analysis

Thermal investigations (DTA/TG) of **DAP-Mn** (*Fig.3.48*) and **PIP-Mn** (*Fig.3.49*) were carried out under static air with heating and cooling rates of 5 °C/min up to 1000 °C (NETZSCH STA 409).

The TG curve of **DAP-Mn** shows a three-step weight loss with an overall weight loss of 21.59 % (21.25 % calc., according to a hypothetical weight loss of $1 \times C_3H_{10}N_2$ and $1.5 \times H_2O$ per formula unit) with every step weight loss of 11.76 %, 3.04 %, and 6.79 % in the temperature range of 400 – 800 °C. DTA curve shows one sharp endothermic peak with maximum temperatures at 474 °C, one exothermic shoulder and one sharp exothermic peak with maximum temperatures at 598 °C and 633 °C, respectively. These thermal effects are associated with the decomposition of **DAP-Mn**. After DTA/TG investigations, the powder was measured by powder X-ray diffraction and identified as α-BPO$_4$ [2] and $Mn_2P_2O_7$ [141] (*Fig.3.50*).

The TG curve of **PIP-Mn** also shows a three-step weight loss with an overall weight loss of 24.19 % (24.25 % calc., according to a hypothetical weight loss of $1 \times C_4H_{10}N_2$ and $1.5 \times H_2O$ per formula unit) with every step weight loss of 12.42 %, 2.92 %, and 8.85 % in the temperature range of 400 – 800 °C. DTA curve shows one sharp endothermic peak with maximum temperatures at 501 °C, one exothermic shoulder and one sharp exothermic peak with maximum temperatures at 599 °C and 638 °C, respectively. These thermal effects are associated with the decomposition of **DAP-Mn**. The powder X-ray diffraction of the product after DTA/TG investigation was also identified as α-BPO$_4$ [2] and $Mn_2P_2O_7$ [141] (See *Fig. 3.50*).

As shown in the DTA curves of **DAP-Mn** and **PIP-Mn**, **DAP-Mn** and **PIP-Mn** are stable up to 400 °C which are rather high for organo-templated borophosphates. The decomposition process of them can be described as the following equations:

$$2(C_3H_{12}N_2)\{Mn^{II}[B_2P_3O_{12}(OH)]\} \xrightarrow[\text{in air}]{T_{max} = 1000\ °C} 4\alpha\text{-BPO}_4 + 2Mn_2P_2O_7 + 3H_2O \uparrow$$
$$+ "C_3H_{10}N_2"\ (CO_2 + H_2O + NO_2)$$

$$2(C_4H_{12}N_2)\{Mn^{II}[B_2P_3O_{12}(OH)]\} \xrightarrow[\text{in air}]{T_{max} = 1000\ °C} 4\alpha\text{-BPO}_4 + 2Mn_2P_2O_7 + 3H_2O \uparrow$$
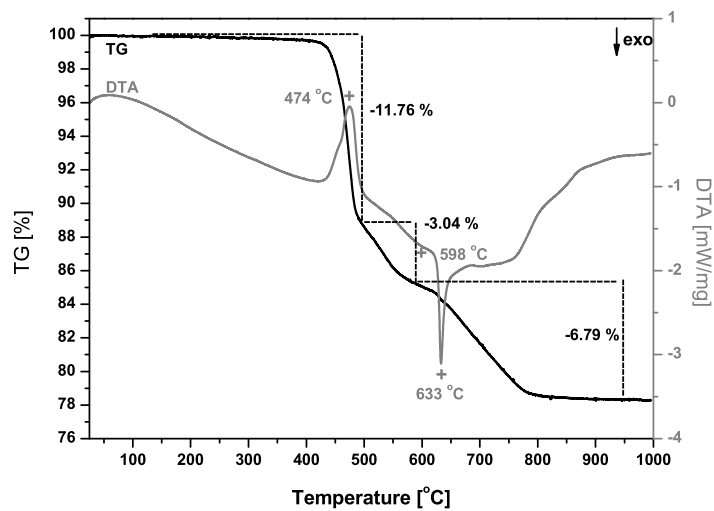$$+ "C_4H_{10}N_2"\ (CO_2 + H_2O + NO_2)$$

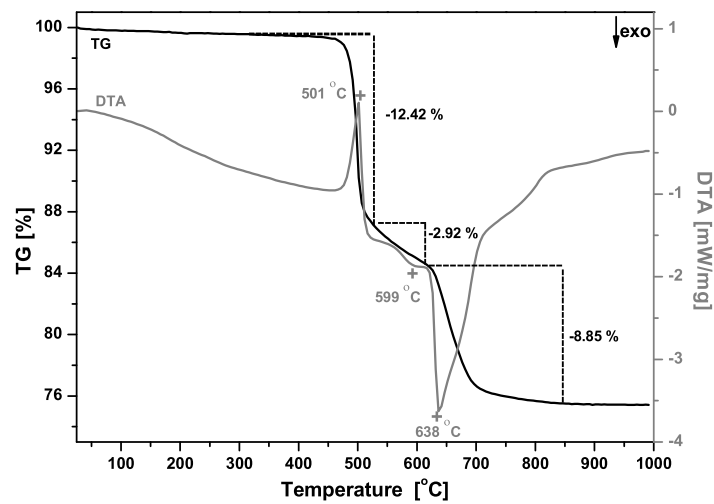Figure 3.48: DTA-TG curves of **DAP-Mn**. For further details see text.

Figure 3.49: DTA-TG curves of **PIP-Mn**. For further details see text.
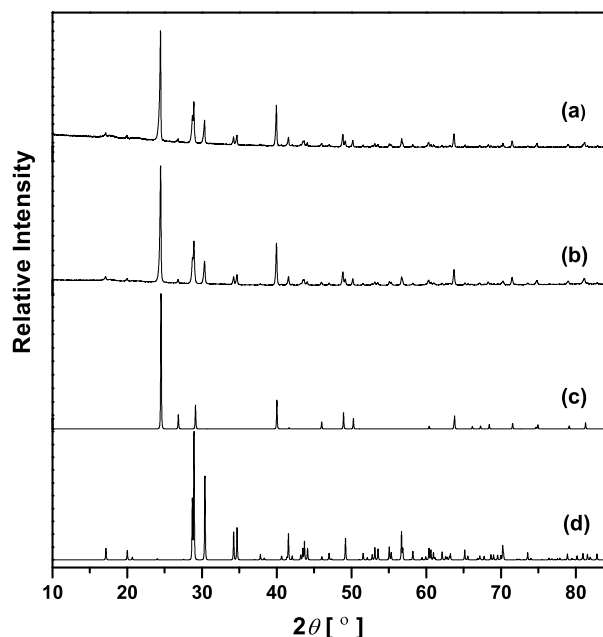
Figure 3.50: Powder X-ray diffraction patterns of **DAP-Mn**(a) and **PIP-Mn** (b) after TG/DTA investigations (up to 1000 °C), compared with calculated powder patterns of α-BPO$_4$ [2](c) and Mn$_2$P$_2$O$_7$ [141](d); Cu $K_{\alpha 1}$-radiation.

3.3.6 Magnetic susceptibility

Magnetic properties of **DAP-Mn** and **PIP-Mn** were investigated on a powdered sample in the temperature range 1.8 K to 400 K using a SQUID-magnetometer (Quantum Design, MPMS XL–7). The data of the magnetic susceptibility for **DAP-Mn** (*Fig. 3.51*) follow the Curie-Weiss law over almost the whole temperature range under investigation (external magnetic field H_{ext} = 1 kØe). The effective magnetic moment μ_{eff} was observed by a nonlinear fit in the temperature range of 20-400 K as 5.86(1) μ_B/Mn-atom (θ = -4.00 K) which is the typical value for Mn^{2+} [142]. Inset of *Fig. 3.51* display antiferromagnetic ordering at $\theta \approx$ 2.3(3) K. The isothermal magnetization at 1.8 K increases with field and reaches a value of 4.43 μ_B at 70 kØe, extrapolates in M(1/H) to approximate 5.0(3) μ_B as expected for Mn^{2+} 3d^5 system (5 μ_B).

The data of the magnetic susceptibility for **PIP-Mn** (*Fig. 3.52*) follow the Curie-Weiss law over almost the whole temperature range under investigation (external mag-

netic field $H_{ext} = 10$ kØe). The effective magnetic moment μ_{eff} was observed by a non-linear fit in the temperature range of 10–400 K as 5.65(1) μ_B/Mn-atom ($\theta = $-3.78 K) which is the typical value for Mn^{2+} [142].
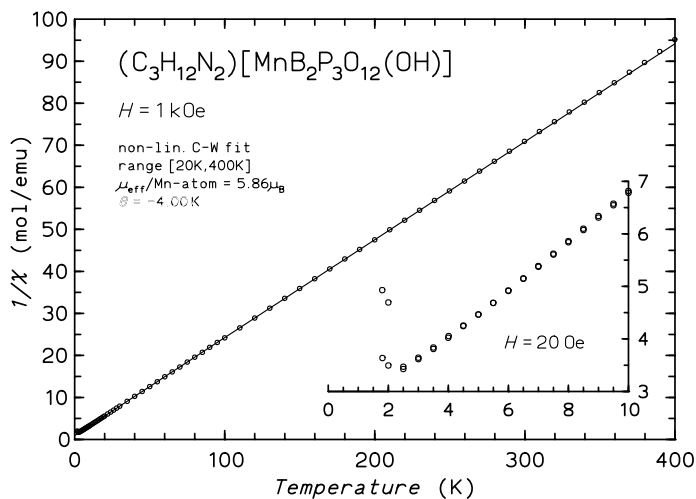

Figure 3.51: Inverse molar magnetic susceptibilities $1/\chi$ of **DAP-Mn** as a function of temperature. Inset shows the antiferromagnetic ordering of **DAP-Mn** at 2.3(3) K in external magnetic field 20 Øe. For further details see text.
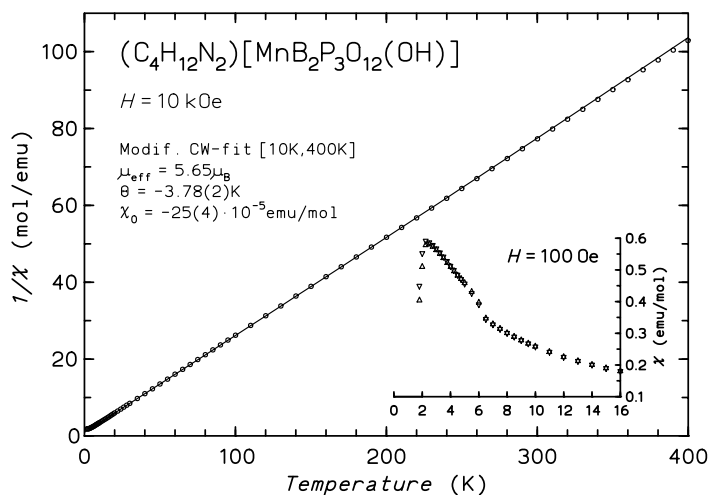

Figure 3.52: Inverse molar magnetic susceptibilities $1/\chi$ of **PIP-Mn** as a function of temperature. Inset shows the antiferromagnetic ordering of **DAP-Mn** at 3.78 K in external magnetic field 100 Øe. For further details see text.

3.3.7 Discussion

3.3.7.1 Flexibility of the frameworks

Both crystal structures of **DAP-Mn** and **PIP-Mn** have identical framework connections with significant distortions being caused by the differences in size and shape of the template molecules. When the cyclic PIP template is replaced by the stretched DAP template, the space group changes from $Ima2$ to $Pmc2_1$. This indicates that the two compounds, probably, have a flexible framework, which may be an important factor for applications in catalysis, and sorption materials. The zeolite RHO [143] contains one of the most flexible frameworks in zeolites. The framework distorts according to dehydration or ion-exchange. The RHO framework represents a tetrahedral framework built up from AlO_4- and SiO_4-tetrahedra. It is well known that tetrahedral frameworks are more rigid compared with frameworks built by a mixture of octahedra and tetrahedra. Therefore, the manganese borophosphate framework is assumed to be more flexible than the RHO zeolite. Thus, it could be a good candidate for catalytic or recycling applications.

It is to be noted that the MnO_6 octahedra are significantly distorted. If the longest distance to oxygen is not considered, the Mn-polyhedra show a square-pyramidal coordination. This indicates that the Mn polyhedra show a significant flexibility in their coordination behaviors. These effects in combination may lead to a high flexibility of the framework.

3.3.7.2 Borophosphate partial structure

$(C_3H_{12}N_2)\{Mn^{II}[B_2P_3O_{12}(OH)]\}$, $(C_4H_{12}N_2)[M^{II}B_2P_3O_{12}(OH)]$ (M^{II} = Co, Zn [103], Mn), $(C_2H_{10}N_2)[M^{II}B_2P_3O_{12}(OH)]$ (M^{II} = Mg, Mn, Fe, Co, Ni, Cu, Zn) [118,119], and $(Co(en)_3)[B_2P_3O_{11}(OH)_2]$ [105] show the same molar ratio of B : P : O/(OH) = 2 : 3 : 13. All these compounds were prepared in the presence of templates. The anionic borophosphate partial structures are built in different ways. *Fig. 3.53* shows the borophosphate partial structures in the borophosphates with M : B :'P : O/(OH) = 1 : 2 : 3 : 13. $(C_3H_{12}N_2)\{Mn^{II}[B_2P_3O_{12}(OH)]\}$ and $(C_4H_{12}N_2)[M^{II}B_2P_3O_{12}(OH)]$ (M^{II} = Co, Zn [103], Mn) contain the same borophosphate structure as infinite loop-branched single chains, $\frac{1}{\infty}\{[B_2P_3O_{12}(OH)]^{4-}\}$ (a), which is closely related to the stretched variant $\frac{1}{\infty}\{[B_2P_3O_{13}]^{5-}\}$ (b) found in $Na_5[B_2P_3O_{13}]$ [30]. In $(C_2H_{10}N_2)[M^{II}B_2P_3O_{12}(OH)]$ (M^{II} = Mg, Mn, Fe,

Co, Ni, Cu, Zn) [118,119], a layer borophosphate partial structure, $_\infty^2\{[B_2P_3O_{12}(OH)]^{4-}\}$
(d), is formed by the condensation of $_\infty^1\{[B_2P_3O_{12}(OH)]^{4-}\}$ (a) by sharing common
O-corners. $(Co(en)_3)[B_2P_3O_{11}(OH)_2]$ [105] also contains infinite loop-branched single
chains (see *Fig. 3.53*(c)) but differences in the connection of rings and the sequence
of rings. Four-membered rings, built of alternating BO_4 and PO_4 groups, interconnect
to each other by sharing the O-corners of BO_4 groups, the rest free O-corners of two
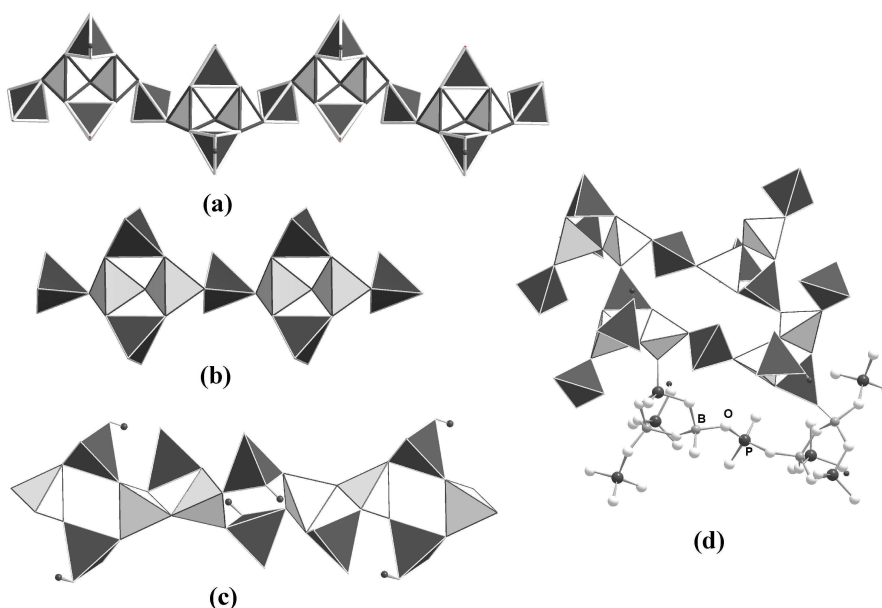neighboring BO_4 groups are loop branched by one PO_4 group.

Figure 3.53:   Borophosphate anionic partial structures of four different types of
borophosphates with $M : B : P : O/(OH) = 1 : 2 : 3 : 13$: (a) $_\infty^1\{[B_2P_3O_{12}(OH)]^{4-}\}$ in the
crystal structure of $(C_3H_{12}N_2)\{Mn^{II}[B_2P_3O_{12}(OH)]\}$ and $(C_4H_{12}N_2)[M^{II}B_2P_3O_{12}(OH)]$
$(M^{II} = Co, Zn$ [103], Mn); (b) $_\infty^1\{[B_2P_3O_{13}]^{5-}\}$ in the crystal structure of $Na_5[B_2P_3O_{13}]$
[30]; (c) $_\infty^1\{[B_2P_3O_{11}(OH)_2]^{3-}\}$ in the crystal structure of $(Co(en)_3)[B_2P_3O_{11}(OH)_2]$
[105]; (d) $_\infty^2\{[B_2P_3O_{12}(OH)]^{4-}\}$ in the crystal structure of $(C_2H_{10}N_2)[M^{II}B_2P_3O_{12}(OH)]$
$(M^{II} = Mg, Mn, Fe, Co, Ni, Cu, Zn)$ [118,119]; PO_4 tetrahedra: dark grey, BO_4 tetra-
hedra: light grey, hydrogen atoms: dark grey spheres.

3.3.7.3   Secondary building units (SBU)

Both $(C_3H_{12}N_2)\{Mn^{II}[B_2P_3O_{12}(OH)]\}$ and $(C_4H_{12}N_2)\{Mn^{II}[B_2P_3O_{12}(OH)]\}$ contain one
type of secondary building units (SBU) which are built from one M^{II} coordination-
octahedron, two BO_4 tetrahedra and five PO_4 tetrahedra.   Similar SUB but with

different polyhedra arrangement also appear in $(C_2H_{10}N_2)[M^{II}B_2P_3O_{12}(OH)]$ (M^{II} = Mg, Mn, Fe, Co, Ni, Cu, Zn) [118, 119], $Zn_3(C_6H_{14}N_2)_3[B_6P_{12}O_{39}(OH)_{12}] \cdot (C_6H_{14}N_2)$-$[HPO_4]$ [106], and $(C_6H_{14}N_2)_2[VO(HPO_4)_5B_2O] \cdot H_2O \cdot H_3PO_4$ [75]. These two types of SUBs are shown in *Fig. 3.54*. In all of these SUBs, the octahedron is connected to two BO_4 tetrahedra via a μ^3-oxygen position. The $M-O^{\mu^3}$ distances of these compounds are much longer than the normal M–O distance. They are listed in *Table 3.26*. The significant long distance $M-O^{\mu^3}$ in the diaminopropane and piperazine compounds may be due to the fact that $O^{\mu 3}$ is involved in an additional hydrogen bond. It is likely that the four-coordinated oxygen causes an elongation of $M^{II}-O^{\mu^3}$.

Table 3.26: $M-O^{\mu^3}$ distances in the templated borophosphates containing μ^3-oxygen positions.

Compound	$M-O^{\mu^3}$ (pm)
$(C_2H_{10}N_2)Mg[B_2P_3O_{12}(OH)]$ [119]	218.6
$Zn_3(C_6H_{14}N_2)_3[B_6P_{12}O_{39}(OH)_{12}] \cdot (C_6H_{14}N_2)[HPO_4]$ [106]	225.1
$(C_6H_{14}N_2)_2[VO(HPO_4)_5B_2O] \cdot H_2O \cdot H_3PO_4$ [75]	235.9
$(C_4H_{12}N_2)Co[B_2P_3O_{12}(OH)]$ [103]	243.9
$(C_4H_{12}N_2)Zn[B_2P_3O_{12}(OH)]$ [103]	259.3
$(C_4H_{12}N_2)\{Mn^{II}[B_2P_3O_{12}(OH)]\}$	255.8
$(C_3H_{12}N_2)\{Mn^{II}[B_2P_3O_{12}(OH)]\}$	255.3 and 266.2
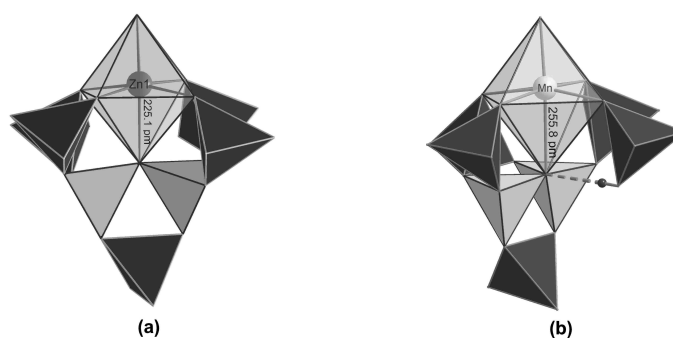
Figure 3.54: Two different types of secondary building units (SBU) with μ^3-oxygen in the templated borophosphates: (a) $\{[ZnO(PO_4)_5B_2O]^{11-}]\}$ in the crystal structure of $Zn_3(C_6H_{14}N_2)_3[B_6P_{12}O_{39}(OH)_{12}] \cdot (C_6H_{14}N_2)[HPO_4]$ [106] and $\{[MnO(PO_4)_4(HPO_4)B_2O]^{11-}]\}$in the crystal structure of (b)$(C_4H_{12}N_2)\{Mn^{II}[B_2P_3O_{12}(OH)]\}$. PO_4 tetrahedra: dark grey, BO_4 tetrahedra: light grey, Hydrogen atoms: dark grey spheres, Hydrogen bonds: dash lines.

3.4 $(C_3H_{12}N_2)Fe^{III}_6(H_2O)_4[B_4P_8O_{32}(OH)_8]$

3.4.1   Synthesis

$(C_3H_{12}N_2)Fe^{III}_6(H_2O)_4[B_4P_8O_{32}(OH)_8]$ was prepared under mild hydrothermal conditions at $170\,°C$. A mixture of $0.811\,g$ ($3\,mmol$) $FeCl_3 \cdot 6H_2O$, $1.484\,g$ ($24\,mmol$) H_3BO_3, $1.26\,mg$ ($11\,mmol$) $85\,\%$ H_3PO_4 and $0.822\,g$ ($11\,mmol$) 1,3-diaminopropane (DAP) (molar ratio of Fe : B : P : DAP = 3 : 24 : 11 : 11), and 7.5 ml of deionized water was stirred at $60\,°C$ for 2 hours. Meanwhile $0.8\,ml$ $37\,\%$ HCl was added to adjust the pH value to 1.0. The clear colorless solution was filled in a Teflon autoclave ($V = 10\,ml$, degree of filling $\approx$ 60-70 %) and held at $170\,°C$ for 8 days under autogenous pressure. Colorless prismatic crystals (*Fig. 3.55*) shows the SEM micrograph of a single crystal) of $(C_3H_{12}N_2)Fe^{III}_6(H_2O)_4[B_4P_8O_{32}(OH)_8]$ were separated by filtration, washed with deionized water and dried at $60\,°C$ in air. When using only the half amount of H_3BO_3 (molar ratio of Fe : B : P : DAP = 3 : 12 : 11 : 12), the products contain only a small amount of $(C_3H_{12}N_2)Fe^{III}_6(H_2O)_4[B_4P_8O_{32}(OH)_8]$ and an additional unidentified phosphate. The more H_3BO_3 was added to the reagents, the larger was the amount of $(C_3H_{12}N_2)Fe^{III}_6(H_2O)_4[B_4P_8O_{32}(OH)_8]$. When the boron content reaches the ratio of Fe : B : P : DAP = 3 : 48 : 11 : 12, large size of crystals were obtained accompany with white fine powder as byproduct which is not identified. The byproduct can be separated by ultrasonic shaking because the two products possessing different density. Therefore, controlling the amount of boron appears to be most important to get the phase in high purity.
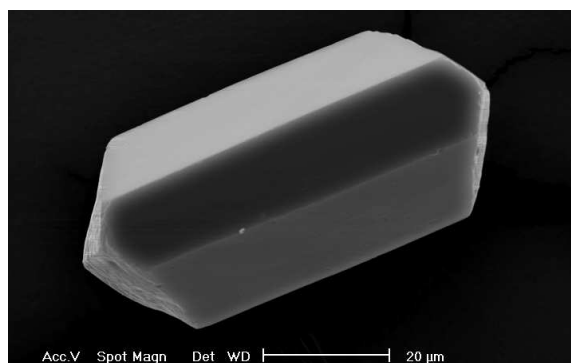

Figure 3.55:   SEM   micrograph   of   a   prismatic   single   crystal   of $(C_3H_{12}N_2)Fe^{III}_6(H_2O)_4[B_4P_8O_{32}(OH)_8]$.

Fe, B, and P contents were analyzed using ICP-AES, while a hot extraction method was applied for analyzing organic carbon, hydrogen and nitrogen. The results give a molar ratio of Fe : B : P : C : N = 6.04 : 4 : 8.12 : 3.00 : 1.91 which is consistent with the formula observed from the single crystal structure refinement (*Table 3.27*). The results of the chemical analyses confirm one $(C_2H_{12}N_2)$ per formula unit.

Table 3.27: $(C_3H_{12}N_2)Fe^{III}_6(H_2O)_4[B_4P_8O_{32}(OH)_8]$: results of the chemical analyses.

Element	Obs.(e.s.d.)/mass-%	Calc. /mass-%
Fe	23.18(7)	23.14
B	2.97(3)	3.04
P	17.28(8)	17.42
C	2.472(5)	2.533
N	1.835(6)	1.970
H	2.056(4)	1.984

The product was identified by using powder X-ray diffraction (HUBER Image Foil Guinier Camera G670, Co $K_{\alpha 1}$-radiation, quartz monochromator). *Fig.3.56* shows the observed and calculated powder patterns of $(C_3H_{12}N_2)Fe^{III}_6(H_2O)_4[B_4P_8O_{32}(OH)_8]$. The good agreement indicates the purity of the sample.
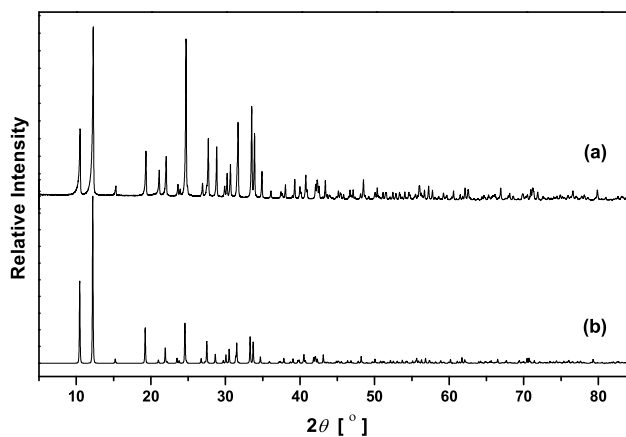
Figure 3.56: Powder X-ray diffraction patterns of $(C_3H_{12}N_2)Fe^{III}_6(H_2O)_4[B_4P_8O_{32}(OH)_8]$: (a)observed and (b)calculated from single crystal structure data (only applying framework atoms); Co $K_{\alpha 1}$-radiation.

3.4.2   Crystal structure determination

A colorless single crystal of $(C_3H_{12}N_2)Fe^{III}_6(H_2O)_4[B_4P_8O_{32}(OH)_8]$ ($0.12 \times 0.06 \times 0.04$ mm^3, platelet) was fixed on a glass fiber with two-component glue. X-ray data were collected at 295 K using a Rigaku AFC 8 diffractometer, equipped with curved R-axis Rapid imagining plate detector (Mo K_α-radiation, graphite monochromator). Intensity data were collected in the angular range $3.24° \leq 2\theta \leq 68.68°$ (60 images, $\omega = 60°-190°$, $\Delta\omega = 3°$, $\chi_1 = 0°$, $\phi_1 = 0°$, $\chi_2 = 45°$, $\phi_2 = 90°$). The data were corrected for Lorentz and polarization effects. A multi-scan absorption correction was applied. The structure was solved in the space group $P2_1/c$ (No. 14) by direct methods using the program SHELXS-97-2 [P2]. Fourier calculations and subsequent full-matrix least-squares refinements were carried out using SHELXL-97-2 [P3], applying neutral atom scattering factors. The framework atom positions were all located and refined. After anisotropic displacement parameters had been included in the refinement, the hydrogen atoms bonded to oxygen could be located from difference Fourier maps and were refined without any restraints. The template atom positions (C and N) could not be located from difference Fourier maps, because only two positions of high electron density were observed (*Fig. 3.57*) after refining all the framework atoms. Their values are 4.81 $e \cdot 10^{-6} pm^{-3}$ and 2.00 $e \cdot 10^{-6} pm^{-3}$. The crystallographic data are summarized in *Table 3.28*. The atom positions and displacement parameters are given in *Table 3.29* and *Table 6.7*. Some selected bond lengths and angles are given in *Table 3.31*.

The electron density of the $(C_3H_{12}N_2)^{2+}$ ions in difference Fourier maps are shown in *Fig. 3.57*. The elliptical shapes of electron densities clearly show that the organic molecules are disordered. The chemical analyses had already shown that there is only one $(C_3H_{12}N_2)^{2+}$ ion per formula unit. This result was applied to constraint the occupancy of C and N positions and to try to fix the possible positions of C and N. The formulated positions of C and N are given in *Table 3.30*. The organic molecule has two different arrangements related by the center of symmetry, which is clearly shown in the electron density maps (see *Fig. 3.57*). The C and N atom positions are only partially occupied. *Fig. 3.58* shows the arrangement of disordering DAP cations which have two different orientations related by center symmetry and represents a continuous arrangement. Due to the overlaping of the DAP molecules, N1 was shared by two different molecules, the DAP cations appear to be arranged continuously along [100] in the channels of the framework structure.
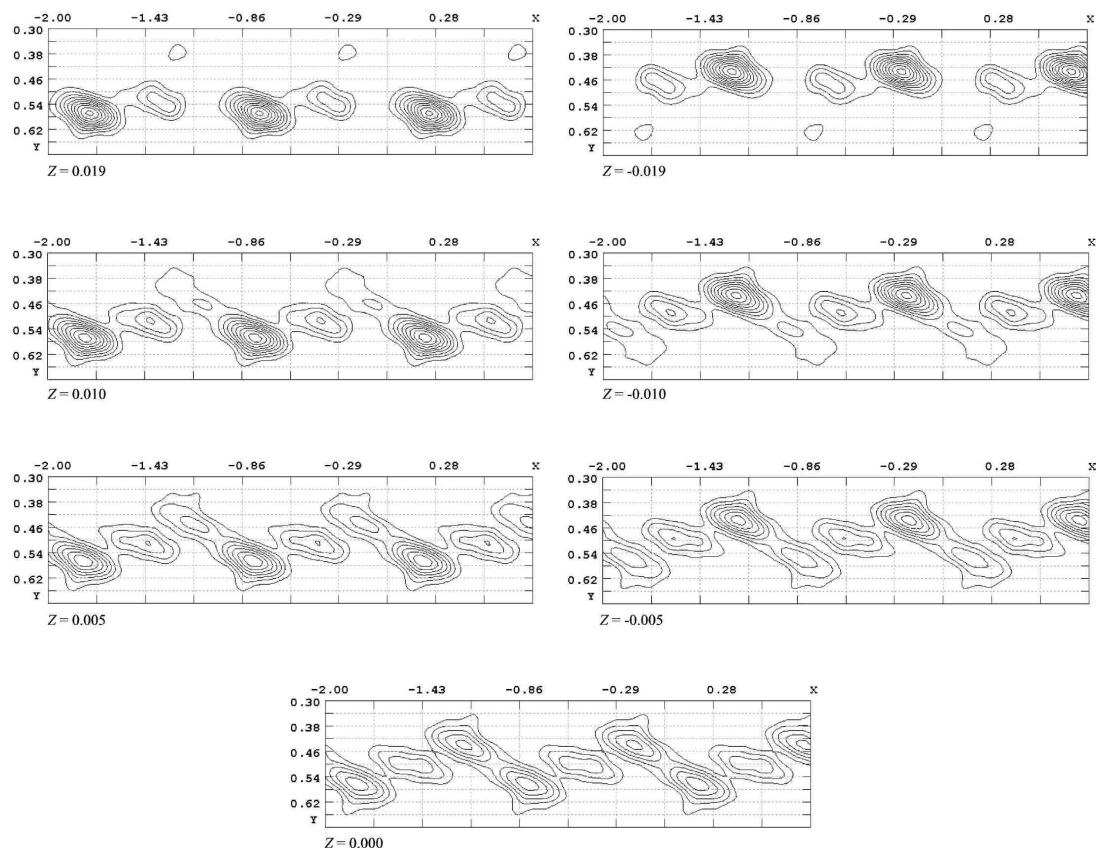
Figure 3.57: $(C_3H_{12}N_2)Fe^{III}_6(H_2O)_4[B_4P_8O_{32}(OH)_8]$: electron densities arround the organic template (C and N atom positions) in the difference Fourier maps. The electron density distribution shows that DAP molecules are related by center symmetry and arranged continuously inside the channels.

Figure 3.58: *Top*: The arrangement of the disordering organic templates, $(C_3H_{12}N_2)$–molecules, in the crystal structure of $(C_3H_{12}N_2)Fe^{III}_6(H_2O)_4[B_4P_8O_{32}(OH)_8]$ which shows two different orientations of $(C_3H_{12}N_2)$–molecules related by center symmetry and represents a continuous arrangement; *Bottom*: two different orientations of DAP-molecules.

Table 3.28:   Crystallographic   data   and   refinement   results   for
$(C_3H_{12}N_2)Fe^{III}{}_6(H_2O)_4[B_4P_8O_{32}(OH)_8]$; e.s.d.'s are given in parentheses.

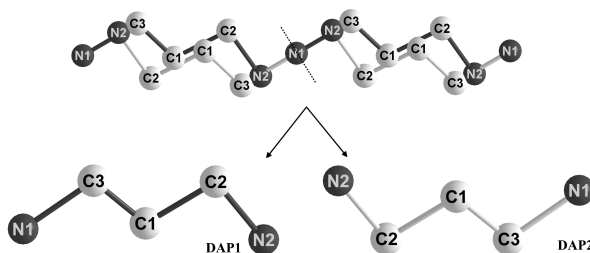| Compound	:	$(C_3H_{12}N_2)Fe^{III}{}_6(H_2O)_4[B_4P_8O_{32}(OH)_8]$
Formula weight (g · mol^{-1})	:	1422.34
Space group	:	$P2_1/c$ (No. 14)
a [pm]	:	501.4(2)
b [pm]	:	930.9(2)
c [pm]	:	2092.3(7)
β [°]	:	110.29(2)
V [$10^6 \cdot pm^3$]	:	915.9(5)
Z	:	1
Calc. density ρ [g · cm^{-3}]	:	2.579
Diffractometer	:	Rigaku R-axis RAPID
		Mo K_α-radiation
		graphite monochromator
$\mu_{MoK\alpha}$ [mm^{-1}]	:	2.813
Scan type	:	ϕ / ω
2θ range [°]	:	6.0–60.0
Miller-index range	:	$-5 \leq h \leq 6$
		$-13 \leq k \leq 13$
		$-29 \leq l \leq 22$
Total data collected	:	5837
Unique data	:	2284
Observed data ($I > 2\sigma(I)$)	:	2234
R_{int}/R_σ	:	0.032/0.046
Number of parameters refined	:	178
$R1(F_o > 4\sigma(F_o))/R1$ (all data)	:	0.0476/0.0490
$wR2$ ($F_o > 4\sigma(F_o))/ wR2$ (all data)	:	0.1068/0.1073
Goodness-of-Fit (for F^2)	:	1.256
Residual electron density (max/min) [e · 10^{-6} pm^{-3}]	:	1.735/$-$1.233
Programs	:	DIAMOND [P4], WinGX [P8]
		SHELXS–97/2 [P2], SHELXL–97/2 [P3]

Table 3.29: Atomic coordinates and equivalent/isotropic displacement parameters [10^{-4}pm^2] in the crystal structure of $(C_3H_{12}N_2)Fe^{III}{}_6(H_2O)_4[B_4P_8O_{32}(OH)_8]$, e.s.d.'s are given in parentheses.

Atom	Site	x	y	z	U_{eq}/U_{iso}
Fe1	$4e$	0.40093(12)	0.68831(5)	0.78393(3)	0.00808(12)
Fe2	$2a$	0.0000	0.0000	0.0000	0.00754(16)
P1	$4e$	0.2184(2)	0.35277(9)	0.78970(5)	0.00746(19)
P2	$4e$	0.3803(2)	0.89334(9)	0.91624(5)	0.00758(19)
B1	$4e$	0.4622(9)	0.6345(4)	0.6378(2)	0.0071(7)
O1	$4e$	0.4604(6)	0.5851(3)	0.70421(14)	0.0122(6)
O2	$4e$	0.4403(6)	0.2857(3)	0.85513(14)	0.0102(5)
O3	$4e$	0.1322(6)	0.8651(3)	0.94073(15)	0.0107(5)
O4	$4e$	0.3400(6)	0.0474(3)	0.88445(14)	0.0111(5)
O5	$4e$	0.2087(6)	0.5144(3)	0.80276(15)	0.0120(6)
O6	$4e$	0.8243(7)	0.1293(3)	0.91461(15)	0.0125(6)
O7	$4e$	0.6600(6)	0.8855(3)	0.97539(15)	0.0110(5)
O8	$4e$	0.6753(6)	0.8302(3)	0.77017(14)	0.0115(5)
O9	$4e$	0.3746(7)	0.7828(3)	0.86235(15)	0.0163(6)
O10	$4e$	0.0687(6)	0.7846(3)	0.72135(15)	0.0145(6)
O11	$4e$	0.7967(7)	0.6042(4)	0.85416(18)	0.0203(7)
H1$_{O6}$	$4e$	0.932(13)	0.140(6)	0.901(3)	0.025(16) *
H2$_{O1}$	$4e$	0.429(14)	0.499(7)	0.707(3)	0.039(18) *
H3$_{O11}$	$4e$	0.895(15)	0.561(8)	0.838(4)	0.05(2) *
H4$_{O11}$	$4e$	0.899(19)	0.670(9)	0.875(5)	0.08(3) *

*refined with isotropic displacement parameters

Table 3.30: Atomic coordinates and isotropic displacement parameters [10^{-4}pm^2] for C and N atoms in the crystal structure of $(C_3H_{12}N_2)Fe^{III}{}_6(H_2O)_4[B_4P_8O_{32}(OH)_8]$, e.s.d.'s are given in parentheses. Details please see text.

Atom	Site	x	y	z	U_{iso}	Occupancy
N1	$2c$	0.0000	0.5000	1.0000	0.0295(9)	0.125
N2	$4e$	0.800(3)	0.4414(13)	0.9838(7)	0.0295(9)	0.375
C1	$4e$	0.580(3)	0.5099(19)	1.0073(11)	0.0295(9)	0.25
C2	$4e$	0.286(3)	0.4425(16)	0.9801(10)	0.0295(9)	0.25
C3	$4e$	0.279(3)	0.5807(17)	1.0165(12)	0.0295(9)	0.25

3.4.3   Crystal structure description

The framework is constructed by connecting Fe1-borophosphate layers through bridging Fe2O$_4$(OH)$_2$ octahedra (*Fig. 3.59*), resulting in 1-D infinite channels running along the *a* axis. *Fig. 3.59* clearly shows that the arrangement of channels exhibits a hexagonal close packing in the *bc* plane. Fe1-borophosphate layer is built up from Fe1O$_4$(OH)(H$_2$O) octahedron interconnecting the borophosphate trimers. It is parallel to the *ab* plane (see *Fig. 3.60*), with five membered ring and three membered ring projected in the *bc* plane (see *Fig. 3.59*). Cross-section of the channels consist of 10-membered rings built up from two Fe1O$_4$(OH)(H$_2$O) octahedra, two Fe2O$_4$(OH)$_2$ octahedra, two BO$_2$(OH)$_2$ tetrahedra and four PO$_4$ tetrahedra with aperture size of 778 pm × 867 pm.
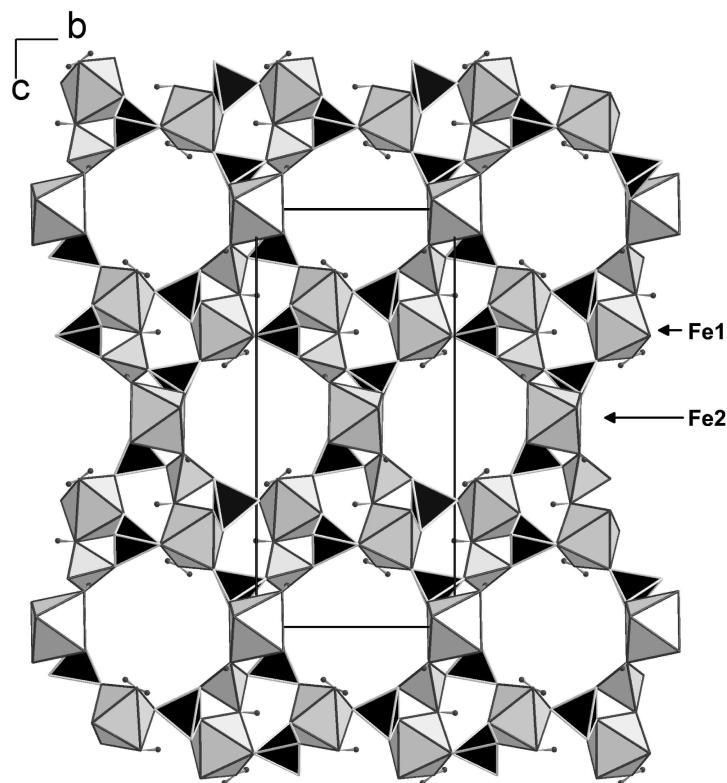
Figure 3.59: Crystal structure of (C$_3$H$_{12}$N$_2$)Fe$^{\text{III}}_6$(H$_2$O)$_4$[B$_4$P$_8$O$_{32}$(OH)$_8$] viewed along [100] shows that the framework is built from Fe1–borophosphate layers interconnected by Fe2–octahedra, the arrangement of channels exhibits hexagonal close packing in the *bc* plane, Fe1 and Fe2 are denoted in the figure. BO$_4$ tetrahedra: light grey, PO$_4$ tetrahedra: dark grey, FeO$_6$ octahedra: light grey, H atoms: dark grey spheres.
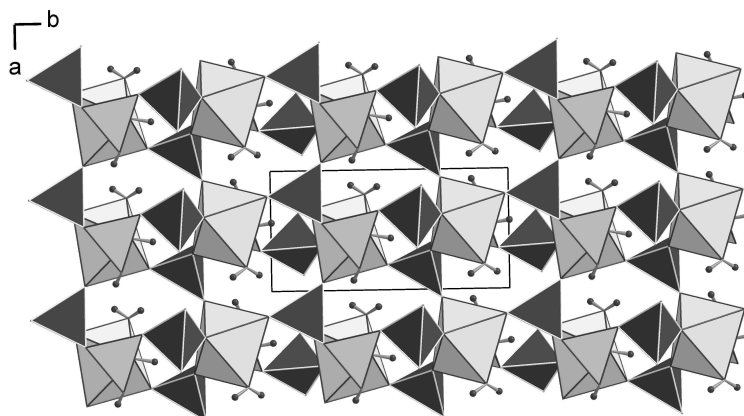
Figure 3.60: $(C_3H_{12}N_2)Fe^{III}_6(H_2O)_4[B_4P_8O_{32}(OH)_8]$: The Fe1–borophosphate layers are built by $Fe1O_4(OH)(H_2O)$ octahedra and $\{[BP_2O_8(OH)]^{5-}\}$ oligomeric trimers viewed along [001]. BO_4 tetrahedra: light grey, PO_4 tetrahedra: dark grey, FeO_6 octahedra: light grey, H atoms: dark grey spheres.
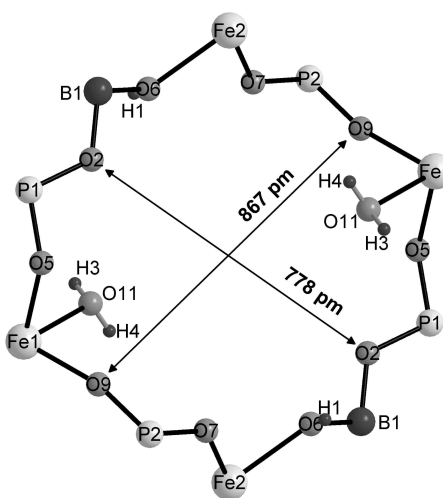
Figure 3.61: Inner-wall of a 10-membered ring (cross-section of a channel) built up from two $Fe1O_4(OH)(H_2O)$ octahedra, two $Fe2O_4(OH)_2$ octahedra, four PO_4 tetrahedra and two $BO_2(OH)_2$ tetrahedra.

The borophosphate anions are the oligomeric trimers, $\{[BP_2O_8(OH)_2]^{5-}\}$, which are built from a central $BO_2(OH)_2$ tetrahedron connected with two PO_4 tetrahedra by sharing common O–corners (*Fig. 3.62*). This building unit has also been observed in the crystal structure of $NaFe[BP_2O_8(OH)]$ [57] and $CsV_3(H_2O)_2[B_2P_4O_{16}(OH)_4]$

[63]. The $BO_2(OH)_2$- and PO_4- tetrahedra are in regular tetrahedral coordination. The B–O and P–O bond lengths (see *Table 3.31*) are comparable with those in the crystal structure of $NaFe[BP_2O_8(OH)]$ [57] (B–O 146.5 pm, B–OH 147.4 pm, P–O 151.8 – 155.9 pm). The O–B–O and O–P–O angles are also comparable with those in $NaFe[BP_2O_8(OH)]$ [57] (O–B–O 104.8 – 112.4°, O–P–O 106.2 – 111.7°).

The two crystallographically inequivalent FeO_6 octahedra have different oxygen environments as shown in *Fig. 3.63*. Fe2 is located at a special position and Fe1 is located at a normal position. Fe2 has a more symmetric octahedral coordination with average bond length 201.1 pm which is the typical value for Fe^{III}–O [57,93]. Fe1 shows a distorted octahedral coordination. The water molecule coordinated to Fe1 makes the Fe1–O11$_{H2O}$ bond (216.5 pm) much longer than the average value of 200.7 pm. Selected interatomic bonds and angles are given in *Table 3.31*.
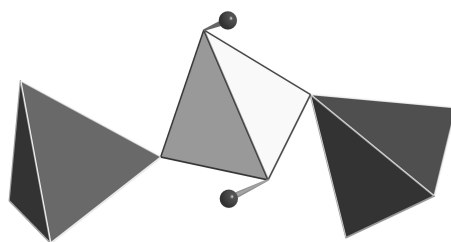
Figure 3.62:   Oligomeric trimer $[BP_2O_8(OH)]^{5-}$ in the crystal structure of $(C_3H_{12}N_2)Fe^{III}_6(H_2O)_4[B_4P_8O_{32}(OH)_8]$. $BO_2(OH)_2$ tetrahedra: light grey, PO_4 tetrahedra: dark grey; Hydrogen atoms: dark grey spheres.
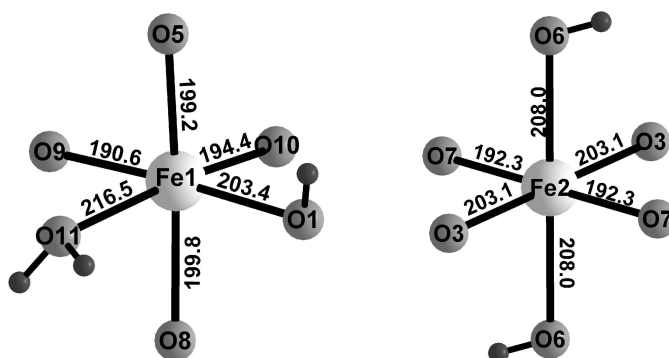
Figure 3.63: Details of the $Fe(1,2)O_6$ octahedral coordination environments in the crystal structure of $(C_3H_{12}N_2)Fe^{III}_6(H_2O)_4[B_4P_8O_{32}(OH)_8]$. Hydrogen atoms: small dark grey spheres. Bond lengths in pm.

The DAP cations are located inside the 10-membered ring channels with aperture sizes of 778 pm and 867 pm ($O2\cdots O2$ and $O9\cdots O9$) (*Fig. 3.61*), which is much larger than the length of the $(H_2DAP)^{2+}$ ions 493 pm ($d_{N\cdots N}$). The large size of channel may be one of the reasons for the disorder of template inside the channel. The weak interactions between the organic cations and the framework also lead to the disorder of the templates. The atom positions of the framework can be refined with a rigid model and are not influenced by the disorder of the template cations. Meanwhile the weak interaction between framework and template cations give an idea for applications related to ion exchange.

<u>Table 3.31</u>: Crystal structure of $(C_3H_{12}N_2)Fe^{III}_6(H_2O)_4[B_4P_8O_{32}(OH)_8]$: selected interatomic distances [pm] and angles [°], e.s.d.'s are given in parentheses.

|		distance [pm]		angle [°]		angle [°]
Fe1–	O9	190.6(3)	O9–Fe1–O10	93.91(13)	O5–Fe1–O1	89.84(11)
	O10	194.4(3)	O9–Fe1–O5	91.25(12)	O8–Fe1–O1	83.68(11)
	O5	199.2(3)	O10–Fe1–O5	98.48(13)	O9–Fe1–O11	84.45(14)
	O8	199.8(3)	O9–Fe1–O8	94.35(12)	O10–Fe1–O11	173.40(13)
	O1	203.4(3)	O10–Fe1–O8	94.02(13)	O5–Fe1–O11	87.95(13)
	O11	216.5(3)	O5–Fe1–O8	165.92(12)	O8–Fe1–O11	79.75(13)
			O9–Fe1–O1	175.72(14)	O1–Fe1–O11	91.44(13)
			O10–Fe1–O1	90.03(12)		
Fe2–	O7	192.3(3)	O7–Fe2–O7	180.0(2)	O3–Fe2–O6	87.93(12)
	O7	192.3(3)	O7–Fe2–O3	93.42(11)	O3–Fe2–O6	92.07(12)
	O3	203.1(3)	O7–Fe2–O3	86.58(11)	O7–Fe2–O6	91.08(12)
	O3	203.1(3)	O7–Fe2–O3	86.58(11)	O7–Fe2–O6	88.92(12)
	O6	208.0(3)	O7–Fe2–O3	93.42(11)	O3–Fe2–O6	92.07(12)
	O6	208.0(3)	O3–Fe2–O3	180.00(14)	O3–Fe2–O6	87.93(12)
			O7–Fe2–O6	88.92(12)	O6–Fe2–O6	180.00(17)
			O7–Fe2–O6	91.08(12)		
P1–	O10	151.6(3)	O10–P1–O5	110.55(16)	O10–P1–O2	108.42(17)
	O5	153.3(3)	O10–P1–O8	113.45(17)	O5–P1–O2	107.01(16)
	O8	153.6(3)	O5–P1–O8	108.74(15)	O8–P1–O2	108.46(16)
	O2	156.4(3)				
P2–	O7	151.7(3)	O7–P2–O9	110.29(17)	O7–P2–O4	109.76(16)
	O9	152.0(3)	O7–P2–O3	110.43(16)	O9–P2–O4	109.83(17)
	O3	152.4(3)	O9–P2–O3	108.98(17)	O3–P2–O4	107.50(15)
	O4	156.4(3)				
B1–	O1	146.7(5)	O1–B1–O6	111.7(3)	O1–B1–O2	108.3(3)
	O6	147.5(6)	O1–B1–O4	110.6(3)	O6–B1–O2	108.0(3)

Table 3.35 Continued

		distance [pm]		angle [°]		angle [°]
B1–	O4	147.6(5)	O6–B1–O4	109.6(3)	O4–B1–O2	108.6(3)
	O2	148.0(4)				
N1–	C3	151.9(9)	N1–C3–C1	124.1(10)		
N2–	C2	147(2)	C3–C1–C2	100.0(12)		
C2–	C1	151.8(10)	C1–C2–N2	77.1(16)		
C1–	C3	130(2)				

Table 3.32: Hydrogen bonds of the framework parts in the crystal structure of $(C_3H_{12}N_2)Fe^{III}_6(H_2O)_4[B_4P_8O_{32}(OH)_8]$: interatomic distances [pm] and angles [°].

Hydrogen bonds							
O6–H1	69.6	H2···O4	235.8	O6···O4	296.6	O6–H1···O4	147.00
O1–H2	82.2	H3···O8	177.6	O1···O8	257.6	O1–H2···O8	163.94
O11–H3	79.0	H4···O5	200.8	O11···O5	276.8	O11–H3···O5	161.26
O11–H4	82.3	H5···O3	233.0	O11···O3	314.6	O11–H4···O3	170.96

3.4.4   IR spectroscopy

The IR-spectrum of $(C_3H_{12}N_2)Fe^{III}_6(H_2O)_4[B_4P_8O_{32}(OH)_8]$ (1.5 mg sample : 150 mg KBr) is shown in *Fig. 3.64*. The band positions of O–H, N–H and C–H vibrations are summarized in *Table 3.33*. The presence of $(C_3H_{12}N_2)^{2+}$ ions and O–H group are confirmed by the N–H, C–H and O–H deformation and stretching vibrations at 3457, 3186–2967, 2580, 1647, 1533-1509, and 1315 cm^{-1}.

Table 3.33: IR-spectroscopy data of $(C_3H_{12}N_2)Fe^{III}_6(H_2O)_4[B_4P_8O_{32}(OH)_8]$.

Vibration frequency $\tilde{\nu}$ [cm^{-1}]	Intensity[†], Band form[‡]	Assignment [129]
3457	s,sp	O–H-hydrogen bond / coordination water
3186–2967	s,br	N–H-stretch
2580	m,sr	C–H-stretch
1647	s,sp	O–H-deformation
1533–1509	s,sp	N–H-deformation
1315	s,sp	C–H-deformation

[†]vs = very strong, s = strong, m = medium, w = weak

[‡]br = broad, sp = sharp, sr = shoulder
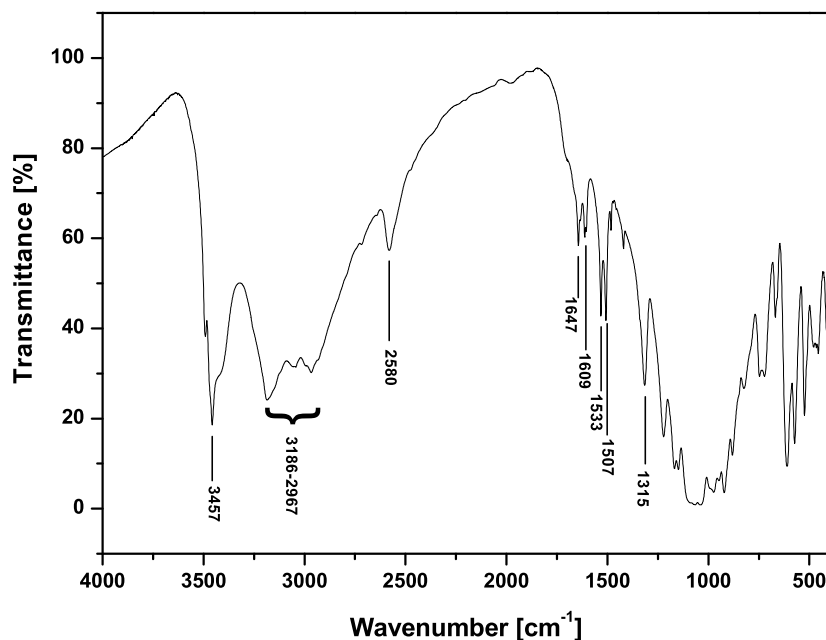
Figure 3.64: Infrared spectrum of $(C_3H_{12}N_2)Fe^{III}_6(H_2O)_4[B_4P_8O_{32}(OH)_8]$ in the range of 4000–400 cm^{-1}.

3.4.5 Thermal analysis

Thermal investigations (DTA/TG) (*Fig. 3.65*) were carried out in a static air atmosphere with heating and cooling rates of 5 °C/min up to 800 °C (NETZSCH STA 409). The TG curve of $(C_3H_{12}N_2)Fe^{III}_6(H_2O)_4[B_4P_8O_{32}(OH)_8]$ shows a four-step mass loss with an overall mass loss of 16.8 % (16.6 % calc., according to a hypothetical weight loss of $1 \times C_3H_{10}N_2$ and $9 \times H_2O$ per formula unit). DTA curve has two endothermic peaks and three exothermal peaks with maximum temperatures at 260, 301, 365, 486, and 569 °C, respectively, accompanying with three exothermal shaoulder at 345, 459, and 539 °C. The thermal effects in the DTA curve are consistent to the decomposition of $(C_3H_{12}N_2)Fe^{III}_6(H_2O)_4[B_4P_8O_{32}(OH)_8]$. After DTA/TG investigation, the white powder was investigated by powder X-ray diffraction (*Fig. 3.66*), and identified as a mixture of $Fe_2(HPO_3)_3$ [144] and $FePO_4$ [145].
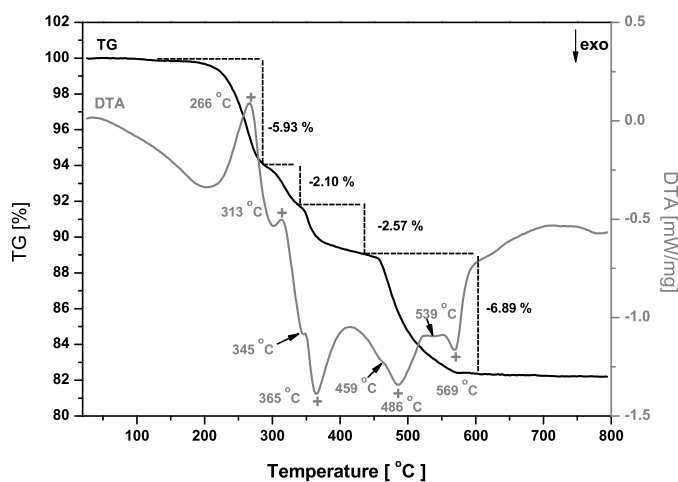
Figure 3.65: DTA-TG curves of $(C_3H_{12}N_2)Fe^{III}_6(H_2O)_4[B_4P_8O_{32}(OH)_8]$.
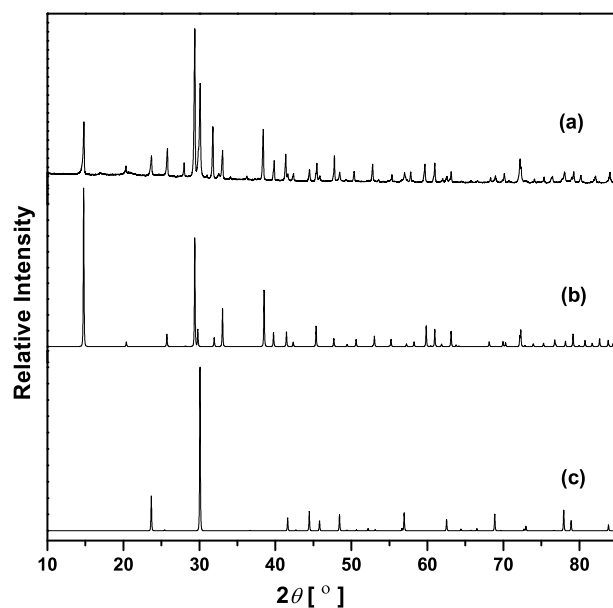
Figure 3.66: Powder X-ray diffraction pattern of $(C_3H_{12}N_2)Fe^{III}_6(H_2O)_4[B_4P_8O_{32}(OH)_8]$ heated up to 800 °C (a), compared with the calculated powder diffraction patterns of $Fe_2(HPO_3)_3$ [144] (b) and $FePO_4$ [145] (c); Co $K_{\alpha1}$-radiation.

3.4.6 Magnetic susceptibility

The magnetization was measured with a SQUID-magnetometer (Quantum Design, MPMS XL–7) in the temperature range 1.8 K to 400 K (*Fig. 3.67*). The room temperature effective magnetic moment value of $\mu_{eff} = 5.92\,\mu_B$/Fe-atom fits with typical values for pure high-spin Fe^{III} compounds (5.8–6.0 μ_B/Fe-atom). The large Weiss constant ($\theta = -55.4(5)$ K) indicates strong antiferromagnetic interactions between the Fe^{III} ions in the 3D structure. At low temperatures deviations from Curie-Weiss behavior are observed. Magnetization data in lower external fields (20 Øe, 100 Øe, 1000 Øe, inset of *Fig. 3.67*) display antiferromagnetic ordering at $T_N \approx 14.0(1)$ K. The isothermal magnetization at 1.8 K increases linearly above 5 kØe and reaches μ/f.u. $= 0.67\,\mu_B$ at 70 kØe.
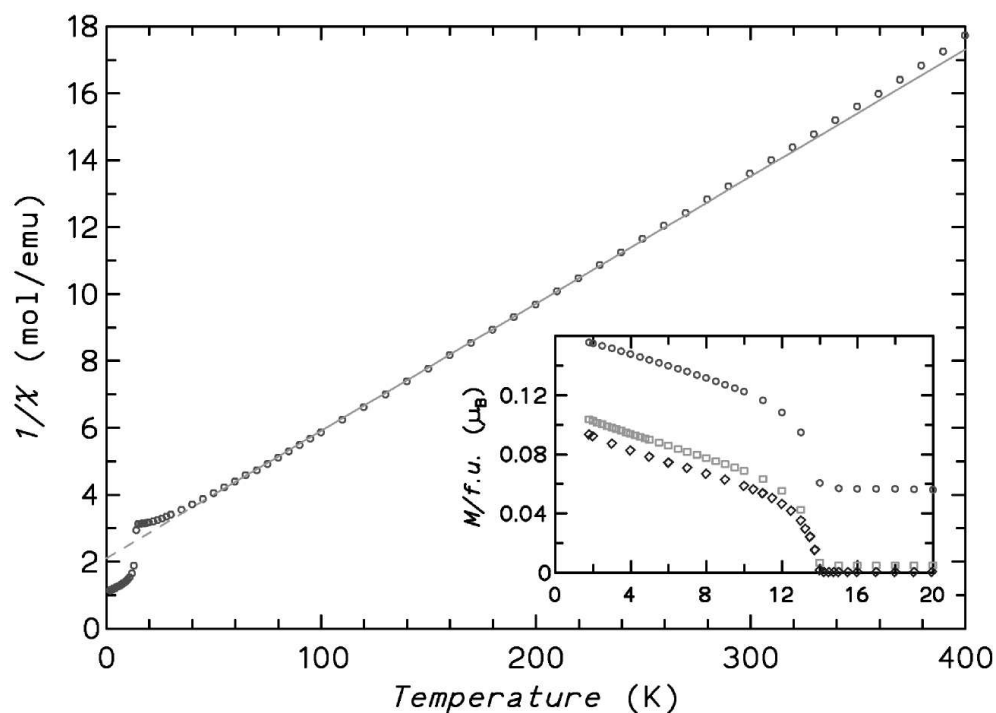
Figure 3.67: Inverse molar magnetic susceptibilities $1/\chi$ for $(C_3H_{12}N_2)Fe^{III}_6(H_2O)_4[B_4P_8O_{32}(OH)_8]$ as a function of temperature (external field 10 kØe) and, in the inset, magnetization in different external fields (from top to bottom: 1000 Øe, 100 Øe, 20 Øe).

3.4.7   Discussion

$(C_3H_{12}N_2)Fe^{III}_6(H_2O)_4[B_4P_8O_{32}(OH)_8]$ and $CsV_3(H_2O)_2[B_2P_4O_{16}(OH)_4]$ [63] have the same ratio of $M^{III} : B : P : O = 3 : 2 : 4 : 22$. Both of them contain the transition metal in oxidation state(III) in octahedral coordination and have the same borophosphate partial structures in form of $[BP_2O_8(OH)_2]^{5-}$ trimer.

Their framework structures, however, show different arrangements (see *Fig. 3.68*): $(C_3H_{12}N_2)Fe^{III}_6(H_2O)_4[B_4P_8O_{32}(OH)_8]$ contains 10-membered ring channels, while CsV_3-$(H_2O)_2[B_2P_4O_{16}(OH)_4]$ [63] only consists of 8-membered ring channels. In the crystal structure of $(C_3H_{12}N_2)Fe^{III}_6(H_2O)_4[B_4P_8O_{32}(OH)_8]$, there are two more Fe-octahedra join the channel formation. For this reason, the octahedral-tetrahedral layers in the crystal structure of $(C_3H_{12}N_2)Fe^{III}_6(H_2O)_4[B_4P_8O_{32}(OH)_8]$ is not as regular as those in the crystal structure of $CsV_3(H_2O)_2[B_2P_4O_{16}(OH)_4]$ [63].

The different sizes of the channels may be due to the differences in the size of the cations; the length of $(H_2DAP)^{2+}$ $(d_{(N\cdots N)} = 493$ pm) is much larger than the radius of Cs^+ (242 pm [146]).

(a)   (b)
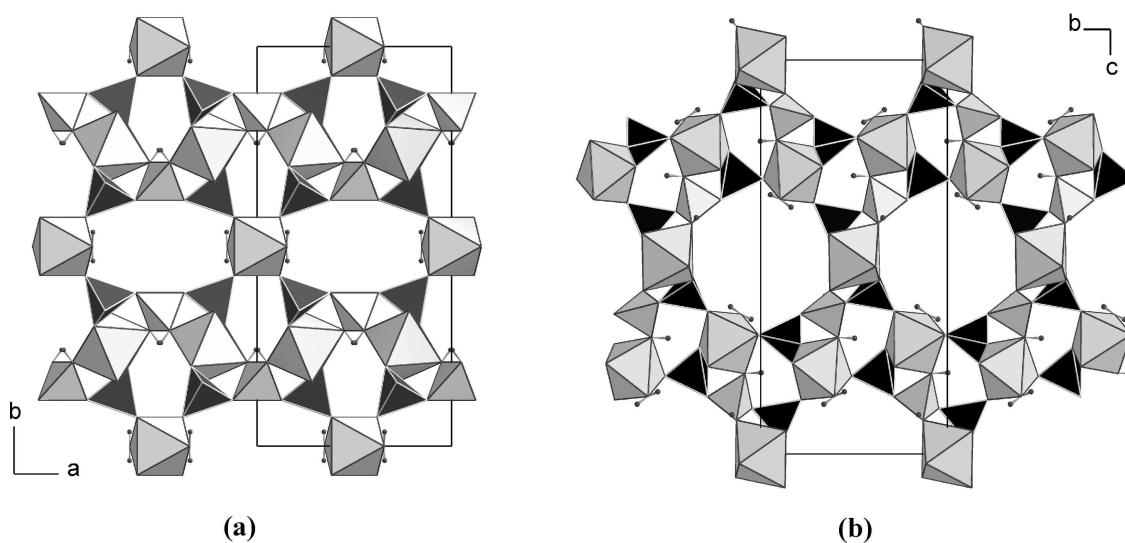
Figure 3.68:   Crystal   structures   of $(C_3H_{12}N_2)Fe^{III}_6(H_2O)_4[B_4P_8O_{32}(OH)_8]$ and $CsV_3(H_2O)_2[B_2P_4O_{16}(OH)_4]$ [63]; FeO_6 and VO_6 tetrahedra: light grey, PO_4 tetrahedra: dark grey, BO_4 tetrahedra: light grey, hydrogen atoms: dark grey spheres.

3.5 $(C_3H_{12}N_2)_2\{V^{III}_2V^{IV}_3B_2P_8O_{38}H_8\}$ (dapvbpo)

3.5.1 Synthesis

$(C_3H_{12}N_2)_2\{V^{III}_2V^{IV}_3B_2P_8O_{38}H_8\}$ (**dapvbpo**) was prepared under mild hydrothermal conditions at 170 °C. A mixture of 0.43 g (2.75 mmol) VCl_3, 0.742 g (12 mmol) H_3BO_3, 0.822 g (11 mmol) 1,3-diaminopropane ($C_3H_{10}N_2$, DAP), 1.26 g (11 mmol) 85 % H_3PO_4, and additional 7.5 ml of deionized water, was stirred at 60 °C for 2 hours. Meanwhile 0.75 ml 37 % HCl was added to adjust the pH value to 1.0. The clear green solution was filled into a Teflon autoclave ($V = 10$ ml, degree of filling $\approx$ 60–80 %) and held at 170 °C for 8 days under autogenous pressure. Yellow-green crystals (*Fig. 3.69*) of **dapvbpo** were filtered, washed with deionized water and dried at 60 °C in air. As crystals prefer to be an intergrowth (formation of sphere), it is hard to find a perfect single crystal for structure investigations.

V, B, and P contents were analyzed using ICP-AES, while a hot extraction method was applied for organic carbon, hydrogen and nitrogen. The results are given in *Table 3.34*.

Table 3.34: **dapvbpo**: results of chemical analyses.

Element	Obs.(e.s.d.)/mass-%	Calc. /mass-%
V	19.49(5)	19.71
B	1.43(1)	1.67
P	18.57(8)	19.17
C	5.14(2)	5.58
N	4.3(1)	4.34
H	2.58(1)	2.50

The new phase was identified by using powder X-ray diffraction (HUBER Image Foil Guinier Camera G670, Cr $K_{\alpha1}$-radiation, germanium monochromator). *Fig. 3.70* shows the observed and calculated (only containing framework part) powder diffraction pattern for **dapvbpo**. The calculated and observed powder patterns have the same reflection positions which shows the reasonable model. While the reflections of calculated and observed patterns are with different intensities which lied in several reasons. First the calculated powder pattern only bases on the framework atoms without templates, second the observed powder pattern may have preferred orientation, third the single crystal data are poor.
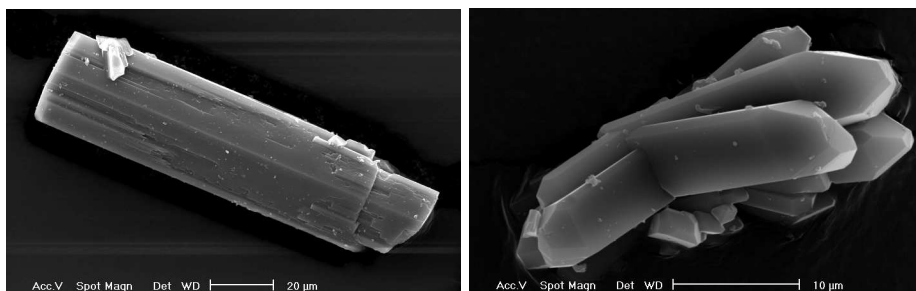
Figure 3.69: SEM micrographs of the crystals of **dapvbpo**.
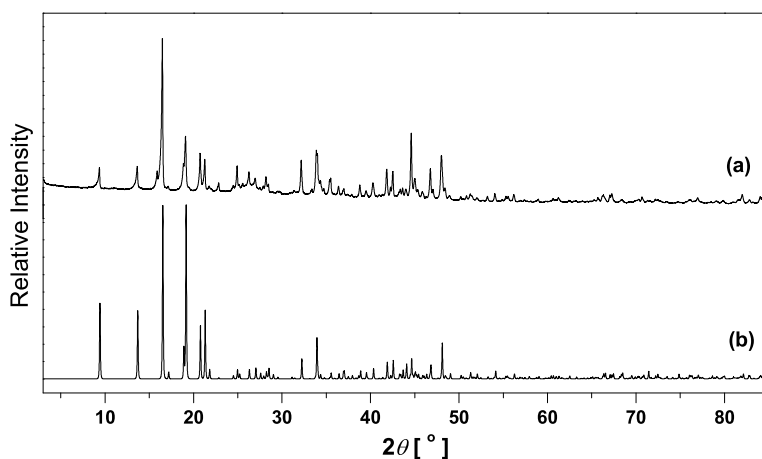
Figure 3.70: Powder X-ray diffraction patterns of **dapvbpo**: (a)observed, (b)calculated from crystal structure data(only containing framework atoms); Cr $K_{\alpha 1}$-radiation.

3.5.2 Crystal structure determination

A small yellow-green crystal of **dapvbpo** (platelet, $0.04 \times 0.02 \times 0.02$ mm^3) was fixed on a glass fiber with two-component glue and mounted on a RIGAKU AFC7 four-circle diffractometer, equipped with a Mercury-CCD detector (MoK_{α}-radiation, graphite monochromator) at 295 K. Intensity data were collected in the angular range $3.52° \leq 2\theta \leq 61.0°$ ($240°$-ϕ-scan, $60°$-ω-scan at $\chi = 90°$, $0.5°$ steps with 90 s exposure

time per step, detector distance: 40 mm; 2θ-offset: $-15.00°$). The data were corrected for Lorentz and polarization effects. A multi-scan absorption correction was applied. The crystal structure of framework part was solved in space group *Pbnm* (No. 62) by direct methods using the program SHELXS-97-2 [P2]. Fourier calculations and subsequent full-matrix least-squares refinements were carried out using SHELXL-97-2 [P3], applying neutral atom scattering factors. The framework atoms (V, B, P and O) were located from the difference Fourier maps. Both V3 and V4 were split into two positions (V3 and V32, V4 and V42) due to high thermal parameters and high residual electron densities close to them, constraints were applied to fix the occupancy of V3 and V32 /(V4 and V42) added up to 1 and the same displacement parameters for each pair. The template atoms (C and N) and hydrogen atoms could not be located from difference Fourier maps because of the poor quality of crystal data. Therefore, this crystal structure of **dapvbpo** determined here is only a preliminary result. The crystallographic results are summarized in *Table 3.35*. The framework atom positions and displacement parameters are given in *Table 3.36* and *Table 6.8*. The bond lengths and angles of framework atoms are given in *Table 3.37*.

The formula was obtained according to the results of crystal structure refinement and chemical analyses. The framework atoms (V, B, P, O) were located reasonably according to the crystal structure refinement, therefore bond valence calculations [139] were performed to appreciate the oxidation number of vanadium (see *Table 3.37*) which gave the ratio of $V^{3+} : V^{4+} = 2 : 3$. The mix-valency vanadium valent state were also supported by the magnetic susceptibilities (details see magnetic measurement part). The amount of $(C_3H_{12}N_2)^{2+}$ ions was obtained according to the results of chemical analyses which gave the ratio of framework atoms and template atoms. Eight hydrogen atoms were added to balance the charge. By this, we got the final formula: $(C_3H_{12}N_2)_2\{V^{III}_2V^{IV}_3B_2P_8O_{38}H_8\}$.

Table 3.35: Crystallographic data and refinement results of **dapvbpo**, e.s.d.'s are given in parentheses.

Compound	:	$(C_3H_{12}N_2)_2\{V^{III}_2V^{IV}_3B_2P_8O_{38}H_8\}$
Formula weight $(g \cdot mol^{-1})$	:	1292.44
Space group	:	$Pbnm$ (No. 62)
a [pm]	:	1024.08(8)
b [pm]	:	1270.0(1)
c [pm]	:	2795.8(2)
V $[10^6 \cdot pm^3]$	:	3636.2(5)
Z	:	4
Calc. density ρ_{calc} $[g \cdot cm^{-3}]$	:	2.363
Diffractometer	:	RIGAKU AFC7 CCD
		Mo K_α-radiation
		graphite monochromator
$\mu_{MoK\alpha}$ $[mm^{-1}]$	:	2.813
Scan type	:	ϕ / ω
2θ-range [°]	:	4.24–60.0
Miller-index range	:	$-13 \leq h \leq 13$
		$-14 \leq k \leq 17$
		$-39 \leq l \leq 38$
Total data collected	:	27487
Unique data	:	5014
Observed data $(I > 2\sigma(I))$	:	3714
R_{int}/R_σ	:	0.1132/0.1091
Number of parameters refined	:	284
$R1(F_\circ > 4\sigma(F_\circ)$	:	0.1499
w$R2$ $(F_\circ > 4\sigma(F_\circ)$	:	0.3533
$R1$ (all data)	:	0.1905
w$R2$ (all data)	:	0.3730
Goodness-of-Fit (for F^2)	:	1.192
Residual electron density	:	3.54/−1.16
(max/min) $[e \cdot 10^{-6}pm^{-3}]$		
Programs	:	DIAMOND [P4]
		SHELXS–97/2 [P2], SHELXL–97/2 [P3]

Table 3.36: Atomic coordinates and equivalent displacement parameters $[10^{-4}\text{pm}^2]$ of the framework atoms in the crystal structure of $(C_3H_{12}N_2)_2\{V^{III}_2V^{IV}_3B_2P_8O_{38}H_8\}$ (**dapvbpo**), e.s.d.'s are given in the parentheses.

Atom	Site	x	y	z	U_{eq}	Occupancy
V1	$8d$	0.78339(19)	0.24002(15)	0.43025(7)	0.0152(5)	
V2	$4c$	0.4868(3)	0.9314(2)	0.2500	0.0217(7)	
V3	$4c$	0.6331(3)	0.1831(3)	0.2500	0.0201(8)	0.823(7)
V32	$4c$	0.6224(16)	0.2549(15)	0.2500	0.0201(8)	0.177(7)
V4	$4c$	0.1240(6)	0.1551(10)	0.2500	0.0224(18)	0.74(3)
V42	$4c$	0.1313(19)	0.197(2)	0.2500	0.0224(18)	0.26(3)
P1	$8d$	0.8853(3)	0.2519(2)	0.31797(10)	0.0155(6)	
P2	$8d$	0.3900(3)	0.1319(2)	0.31681(11)	0.0180(6)	
P3	$8d$	0.5357(3)	0.1947(2)	0.49889(11)	0.0191(7)	
P4	$8d$	0.7897(3)	0.4998(2)	0.40740(11)	0.0190(7)	
B1	$8d$	0.5102(14)	0.1411(12)	0.4038(5)	0.025(3)	
O1	$8d$	0.8893(8)	0.2536(7)	0.3727(3)	0.0212(18)	
O2	$8d$	0.7766(10)	0.3970(6)	0.4338(3)	0.027(2)	
O3	$8d$	0.6126(8)	0.2186(7)	0.3899(3)	0.0228(18)	
O4	$8d$	0.2565(9)	0.1723(8)	0.3034(3)	0.029(2)	
O5	$8d$	0.6662(8)	0.2446(7)	0.4878(3)	0.0208(17)	
O6	$8d$	0.4070(10)	0.0185(7)	0.3010(3)	0.029(2)	
O7	$8d$	0.7939(8)	0.0831(7)	0.4302(3)	0.0229(18)	
O8	$8d$	0.9948(10)	0.1822(8)	0.2998(4)	0.032(2)	
O9	$8d$	0.5964(8)	0.8664(7)	0.2997(3)	0.0233(18)	
O10	$8d$	0.4567(9)	0.1702(8)	0.4519(4)	0.031(2)	
O11	$8d$	0.3945(9)	0.1395(8)	0.3724(3)	0.027(2)	
O12	$8d$	0.7507(9)	0.2142(7)	0.3018(3)	0.0231(18)	
O13	$8d$	0.6377(14)	0.0540(12)	0.2500	0.032(3)	
O14	$8d$	0.4978(10)	0.2038(8)	0.2988(4)	0.036(2)	
O15	$8d$	0.9540(9)	0.2391(8)	0.4683(3)	0.026(2)	
O16	$8d$	0.5690(11)	0.0867(8)	0.5225(4)	0.038(3)	
O17	$4c$	0.3675(12)	0.8366(11)	0.2500	0.025(3)	
O18	$8d$	0.9350(9)	0.5319(7)	0.4087(4)	0.031(2)	
O19	$8d$	0.7500(11)	0.4896(9)	0.3537(3)	0.037(2)	
O20	$4c$	0.1188(14)	0.0225(11)	0.2500	0.032(3)	
O21	$4c$	0.6184(15)	0.3715(12)	0.2500	0.045(4)	

Table 3.37: Crystal structure of $(C_3H_{12}N_2)_2\{V^{III}_2V^{IV}_3B_2P_8O_{38}H_8\}$ (**dapvbpo**): selected interatomic distances and angles of the framework atoms, e.s.d.'s are given in the parentheses.

		distance [pm]	angle [°]		angle [°]	
V1–	O1	194.8(9)	O1–V1–O7	93.3(4)	O2–V1–O15	90.6(4)
	O7	199.6(9)	O1–V1–O2	88.4(4)	O5–V1–O15	95.4(4)
	O2	199.7(8)	O7–V1–O2	177.0(4)	O1–V1–O3	91.8(3)
	O5	200.8(8)	O1–V1–O5	172.7(4)	O7–V1–O3	85.1(4)
	O15	204.5(9)	O7–V1–O5	93.6(4)	O2–V1–O3	97.3(4)
	O3	209.9(8)	O2–V1–O5	84.9(4)	O5–V1–O3	86.3(3)
$\sum(V-O) = 2.896$			O1–V1–O15	87.4(4)	O15–V1–O3	172.1(4)
			O7–V1–O15	87.1(4)		
V2–	O17	171.5(13)	O17–V2–O9	95.4(4)	O9–V2–O6	167.9(4)
	O9	196.8(8)	O17–V2–O9	91.8(3)	O6–V2–O6	92.1(6)
	O9	196.8(8)	O9–V2–O9	85.1(4)	O17–V2–O13	179.4(6)
	O6	198.1(9)	O17–V2–O6	95.8(3)	O9–V2–O13	84.0(4)
	O6	198.1(9)	O9–V2–O6	87.7(3)	O9–V2–O13	84.0(4)
	O13	219.3(16)	O9–V2–O6	168.2(3)	O6–V2–O13	83.9(4)
$\sum(V-O) = 3.926$			O17–V2–O6	95.8(3)	O6–V2–O13	83.9(4)
			O9–V2–O6	168.2(3)		
V3–	O13	164.1(15)	O13–V3–O12	100.8(5)	O12–V3–O14	159.7(5)
	O12	192.3(9)	O13–V3–O12	100.8(5)	O14–V3–O14	88.1(7)
	O12	192.3(9)	O12–V3–O12	97.6(5)	O13–V3–O21	178.0(7)
	O14	196.2(10)	O13–V3–O14	98.9(5)	O12–V3–O21	80.5(4)
	O14	196.2(10)	O12–V3–O14	159.7(5)	O12–V3–O21	80.5(4)
	O21	239.7(16)	O12–V3–O14	83.8(4)	O14–V3–O21	79.8(4)
$\sum(V-O) = 4.273$			O13–V3–O14	98.9(5)	O14–V3–O21	79.8(4)
			O12–V3–O14	83.8(4)		
V32–	O21	148(2)	O21–V32–O14	108.1(9)	O14–V32–O12	80.9(5)
	O14	197.7(16)	O21–V32–O14	108.1(9)	O21–V32–O12	105.9(9)
	O14	197.7(16)	O14–V32–O14	87.2(9)	O14–V32–O12	80.9(5)
	O12	202.2(15)	O21–V32–O12	105.9(9)	O14–V32–O12	146.0(11)
	O12	202.2(15)	O14–V32–O12	146.0(11)	O12–V32–O12	91.4(8)
	O13	255.7(15)				
$\sum(V-O) = 4.513$						
V4–	O20	168.5(19)	O20–V4–O8	98.9(6)	O8–V4–O4	163.6(8)
	O8	195.2(10)	O20–V4–O8	98.9(6)	O4–V4–O4	94.7(6)
	O8	195.2(10)	O8–V4–O8	91.1(7)	O20–V4–O17	179.7(6)
	O4	202.8(10)	O20–V4–O4	97.4(6)	O8–V4–O17	81.3(5)
	O4	202.8(10)	O8–V4–O4	163.6(8)	O8–V4–O17	81.3(5)
	O17	230.7(19)	O8–V4–O4	84.8(4)	O4–V4–O17	82.4(5)
			O20–V4–O4	97.4(6)	O4–V4–O17	82.4(5)
$\sum(V-O) = 3.854$			O8–V4–O4	84.8(4)		

Table 3.37 Continued

		distance [pm]		angle [°]		angle [°]
V42–	O17	177(3)	O17–V42–O8	95.8(10)	O8–V42–O4	164.7(17)
	O8	198.2(17)	O17–V42–O8	95.8(10)	O4–V42–O4	97.0(10)
	O8	198.2(17)	O8–V42–O8	89.3(10)	O17–V42–O20	177.1(13)
	O4	199.2(15)	O17–V42–O4	98.9(11)	O8–V42–O20	82.1(10)
	O4	199.2(15)	O8–V42–O4	164.7(17)	O8–V42–O20	82.1(10)
	O20	222(3)	O8–V42–O4	85.0(5)	O4–V42–O20	83.0(9)
$\sum(V-O) = 3.929$			O17–V42–O4	98.9(11)	O4–V42–O20	83.0(9)
			O8–V42–O4	85.0(5)		
P1–	O1	151.6(10)	O1–P1–O12	112.7(6)	O12–P1–O8	107.7(5)
	O12	152.9(9)	O1–P1–O9	108.9(5)	O9–P1–O8	108.2(5)
	O9	153.1(8)	O12–P1–O9	109.0(5)		
	O8	155.3(9)	O1–P1–O8	110.4(5)		
$\sum(P-O) = 4.860$						
P2–	O6	150.8(9)	O6–P2–O4	110.8(6)	O4–P2–O11	110.3(5)
	O4	151.7(9)	O6–P2–O14	111.8(6)	O14–P2–O11	105.8(6)
	O14	151.8(10)	O4–P2–O14	113.0(6)		
	O11	155.9(9)	O6–P2–O11	104.7(5)		
$\sum(P-O) = 4.952$						
P3–	O15	150.0(9)	O15–P3–O5	112.5(5)	O5–P3–O16	111.5(5)
	O5	151.2(9)	O15–P3–O10	110.9(6)	O10–P3–O16	106.9(6)
	O10	156.0(10)	O5–P3–O10	105.2(6)		
	O16	157.3(10)	O15–P3–O16	109.6(5)		
$\sum(P-O) = 4.820$						
P4–	O7	150.2(9)	O7–P4–O2	110.7(5)	O2–P4–O19	112.1(6)
	O2	150.6(8)	O7–P4–O18	110.7(5)	O18–P4–O19	107.2(6)
	O18	154.4(10)	O2–P4–O18	107.6(6)		
	O19	156.1(9)	O7–P4–O19	108.5(5)		
$\sum(P-O) = 4.919$						
B1–	O3	147.4(17)	O3–B1–O11	114.8(10)	O11–B1–O18	111.8(11)
	O11	149.0(16)	O3–B1–O10	104.1(10)	O10–B1–O18	106.4(10)
	O10	150.0(18)	O11–B1–O10	109.1(11)		
	O18	150.2(18)	O3–B1–O18	110.0(11)		
$\sum(B-O) = 2.890$						

3.5.3 Crystal structure description

The new compound **dapvbpo** is the first example of a mixed-valency vanadium borophosphates up to date. This structure can be described as a 3-dimensional nanocomposite built up from two different layers: one planar vanadium(IV) phosphate layers (**V^{IV}PO-layer**) and another puckered vanadium(III) borophosphate layer (**V^{III}BPO-layer**). The two different layers are stacked and interconnected alternately along the c-axis by

sharing the common O-corners. A projection of the whole structure along the b-axis is illustrated in *Fig. 3.71.*
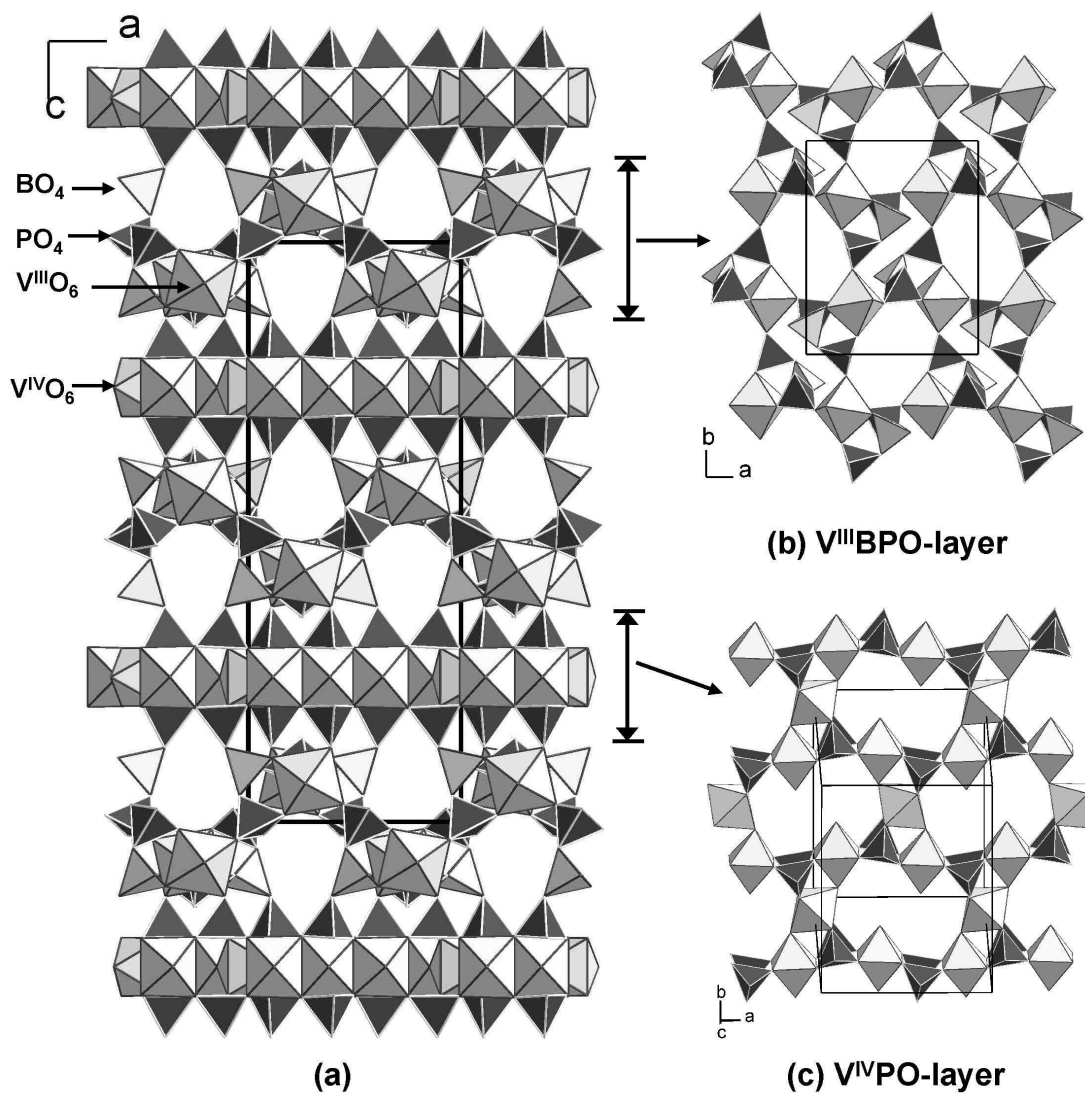
Figure 3.71: (a) A projection of the crystal structure of **dapvbpo** viewed along the b-axis shows **V$^{\text{III}}$BPO-layers** and **V$^{\text{IV}}$PO-layers** are stacked and interconnected alternately along the c-axis. (b) The vanadium (III) borophosphate layer (**V$^{\text{III}}$BPO-layers**) viewed along the c-axis. (c) The vanadium(IV) phosphate layer (**V$^{\text{IV}}$PO-layers**) viewed approximately along the c-axis. BO$_4$ tetrahedra: light grey, PO$_4$ tetrahedra: dark grey, VO$_x$ polyhedra: light grey.

The **V$^{\text{IV}}$PO-layer** (*Fig. 3.72*) is constructed by distorted octahedral vanadium

trimers (V_3O_{16}) interconnected by tetrahedral PO_4 groups, resulting in 3- and 10-membered rings within the layer parallel to the *ab*-plane. The octahedral vanadium timer V_3O_{16} (*Fig. 3.73*) is built up from three distorted $V^{IV}O_6$ octahedra connected to each other by sharing the common O-corners. Every VO_6 octahedron has one short vanadyl V=O bond (V2–O17, 171.5 pm; V3–O13, 164.1 pm; V32–O21, 148.1 pm; V4–O20, 168.5 pm; V42–O17, 177.1pm) *trans* to one long V–O bond (V2–O13, 219.3 pm; V3–O21, ; V32–O13, 255.7 pm;V4–O17, 230.7 pm; V42–O20, 222.2 pm) and four other V–O bonds intermediate in length (detailed bond lengths and angles see *Fig. 3.73* and *Table 3.37*). So the very long V–O bond lengths indicate that V2, V3 and V4 have 5+1 coordination number [147]. Every vanadium trimer shares two PO_4 groups with four neighboring vanadium trimers, resulting in stacks, which are reminiscent of ladders with center distorted octahedra $V2O_6$ as the rungs, that run parallel to [100] as show in *Fig. 3.72*. The PO_4 tetrahedra ($P1O_4$ and $P2O_4$) in the **V^{IV}PO-layer** have regular tetrahedral coordination with bond lengths and angles within the typical ranges for PO_4 tetrahedra [67].
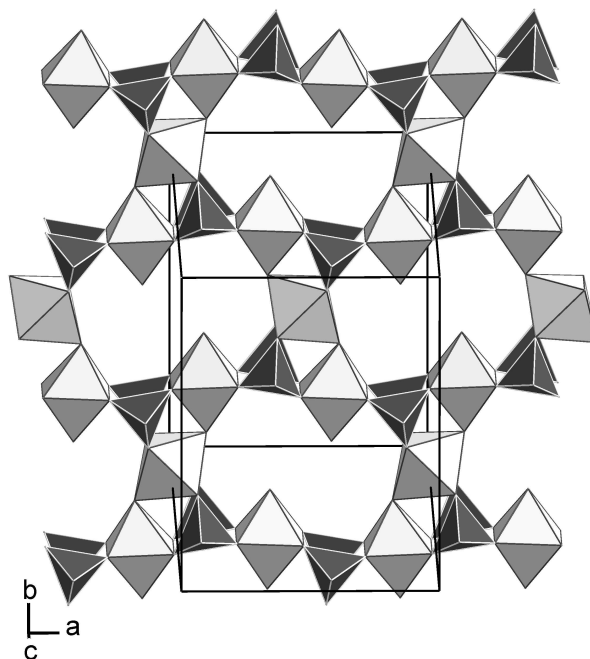

Figure 3.72: The vanadium(IV) phosphate layer (**V^{IV}PO-layer**) views approximately along [001]; BO_4 tetrahedra: light grey, PO_4 tetrahedra: dark grey, VO_6 octahedra: light grey.
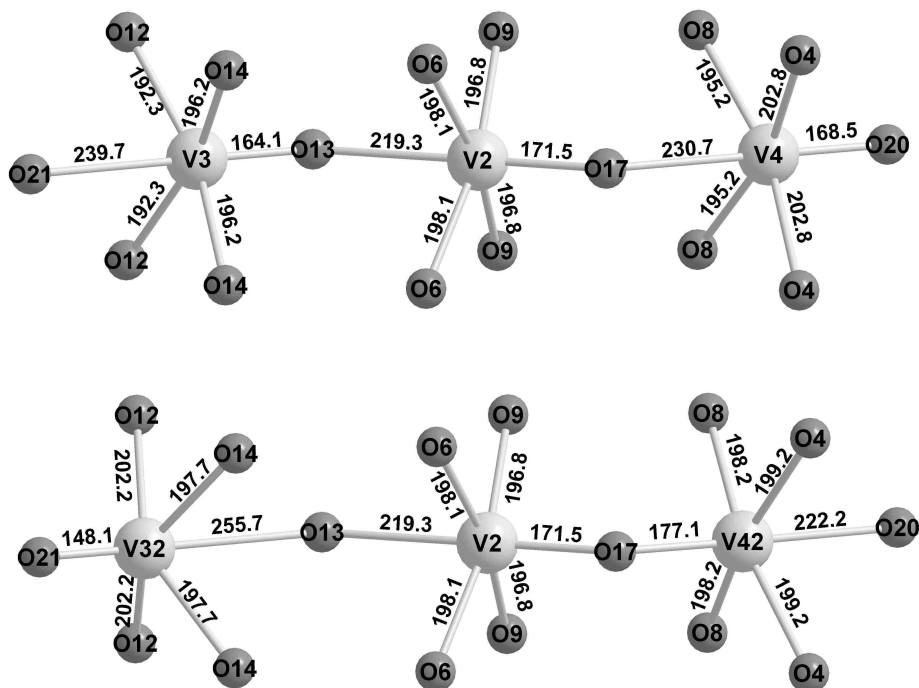
Figure 3.73: Details of the vanadium octahedral trimer coordination environments in the crystal structure of **dapvbpo**. Bond lengths in pm.

Fig. 3.74 shows the vanadium(III) borophosphate layer (**V^{III}BPO-layer**) built from a Secondary Building Units (SBU) [VBP$_2$O$_{13}$]$^{10-}$ (*Fig. 3.75 left*) in which one vanadium octahedron connects with two PO$_4$ tetrahedra and one BO$_4$ tetrahedron. The SBUs connect to each other via the O-corners of VO$_6$ octahedra and PO$_4$ tetrahedra in a zigzag orientation along the *a*- and *b*-axis, respectively, forming a wavy layer parallel to *ab*-plane with 8-membered rings within the layer. V1O$_6$ is in a fairly regular octahedral configuration consisting of five phosphate oxygen atoms and one borate oxygen atom with V–O distance in the range of 194.8(9) − 209.9(8) pm. Such a regular octahedral coordination is usually preferred by V(III) and is consistent with the valence sum calculation [139].

The anionic borophosphate partial structure–tetramer, {[BP$_3$O$_{13}$]$^{8-}$}, is built up from one BO$_4$ tetrahedron connected with three PO$_4$ tetrahedra by sharing the common O-corners(*Fig. 3.75 right*), which has been observed in the crystal structure of (NH$_4$)$_5$[V$_3$BP$_3$O$_{19}$]·H$_2$O [71]. P3O$_4$ and P4O$_4$ tetrahedra are in regular tetrahedral coordinations, the P–O bond lengths and O–P–O angles are in the range 149.3 pm

to 157.4 pm, and 105.5° to 112.1°, respectively. These values are in the typical range for PO_4 tetrahedra in borophosphates [67]. The coordination environments of boron are also regular with the typical B–O bond lengths (146.0 pm – 150.1 pm) and angles (103.9 – 114.1°) in templated vanadium borophosphates [69, 71, 73].
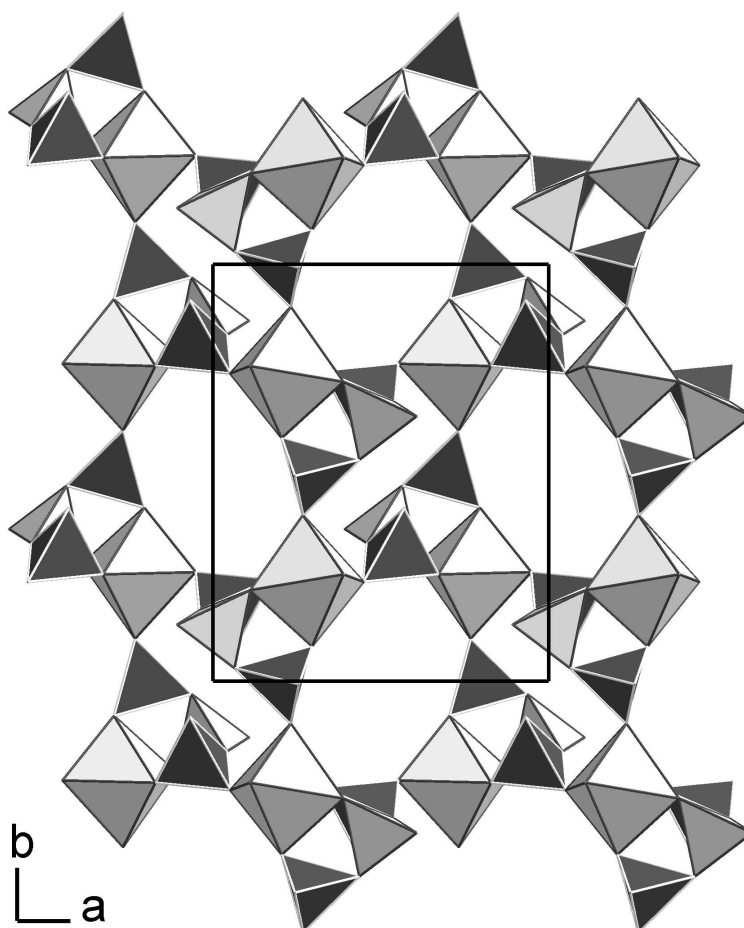
Figure 3.74: The vanadium borophosphate layer (**V^{III}BPO-layer**) views along [001]; BO_4 tetrahedra: light grey, PO_4 tetrahedra: dark grey, VO_6 octahedra: light grey.

The planar **V^{IV}PO-layers** and wavy **V^{III}BPO-layers** are connected by sharing the O-corners of $V^{III}O_6$ octahedra and BO_4 tetrahedra in **V^{III}BPO-layers** with the O-corners of PO_4 tetrahedra in **V^{IV}PO-layers**, resulting in a 3-D framework with channels running along [010] and [001], respectively. The $(H_2DAP)^{2+}$ ions are located inside the channels running along [010]. The C and N positions could not be located reliably from difference Fourier map.

Figure 3.75: *Left*: The secondary building units (SBU), $[VBP_2O_{13}]^{10-}$, is present in the **V^{III}BPO-layer** of the crystal structure of **dapvbpo**. *Right*: Oligomeric tetramer $\{[BP_3O_{13}]^{8-}\}$ is present in the crystal structure of **dapvbpo**; VO_6 tetrahedra: light grey, BO_4 tetrahedra: light grey, PO_4 tetrahedra: dark grey.
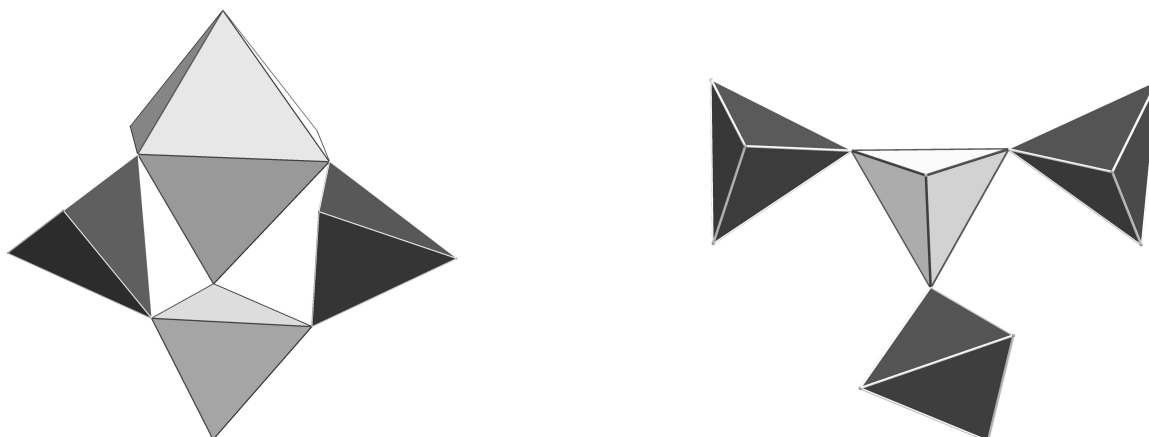
3.5.4   IR spectroscopy

IR-spectrum of $(C_3H_{12}N_2)_2\{V^{III}_2V^{IV}_3B_2P_8O_{38}H_8\}$ (1.5 mg sample : 150 mg KBr) is shown in *Fig. 3.76*. The band positions of O–H, N–H and C–H vibrations are summarized in *Table 3.38*. The presence of $(C_4H_{12}N_2)^{2+}$ ions and O–H group are confirmed by the N–H, C–H and O–H deformation and stretching vibrations at 3247, 2966, 1612, 1472, and 1414 cm^{-1}.

Table 3.38: IR-spectroscopy data of **dapvbpo** in the range of 4000–400 cm^{-1}.

Vibration frequency $\tilde{\nu}$ [cm^{-1}]	Intensity[†], Band form[‡]	Assignment [129]
3247	m,sp	N–H-stretch
2966	w,sr	C–H-stretch
1612	s,sp	O–H-deformation
1472	s,sp	N–H-deformation
1414	s,sp	C–H-deformation

[†]vs = very strong, s = strong, m = medium, w = weak
[‡]br = broad, sp = sharp, sr = shoulder
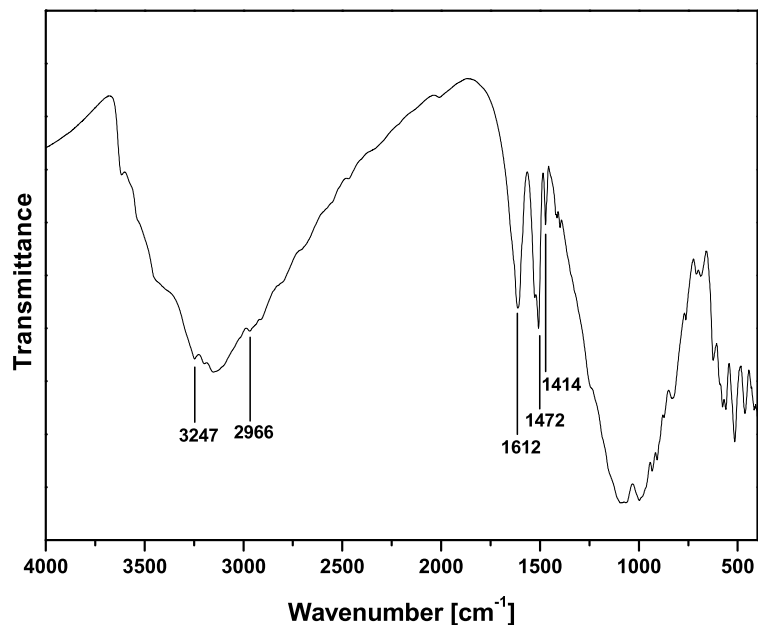
Figure 3.76: Infrared spectrum of **dapvbpo**.

3.5.5 Thermal analysis

Thermal investigations (DTA/TG) (*Fig. 3.77*) were carried out in a static air atmosphere with heating and cooling rates of 5 °C/min up to 1000 °C (NETZSCH STA 409). The TG curve of **dapvbpo** shows a three-step mass loss with an overall mass loss of 20.55 % (19.83 % calc., according to a hypothetical weight loss of $2 \times C_3H_{10}N_2$ and $6 \times H_2O$ per formula unit). DTA curve has three exothermal peaks with maximum temperatures at 372 °C, 527 °C and 759 °C which are correspond to the weight loss. The exothermal peak at 834 °C and one endothermal peak at 892 °C are correspond to the oxidation of V^{3+} and V^{4+} to V^{5+} which are associated to the weight gain (1.5 %) in the TG curve. After DTA/TG investigation, the residue stick strongly to the corundum-crucible so that the final composition of the residue could not be identified.
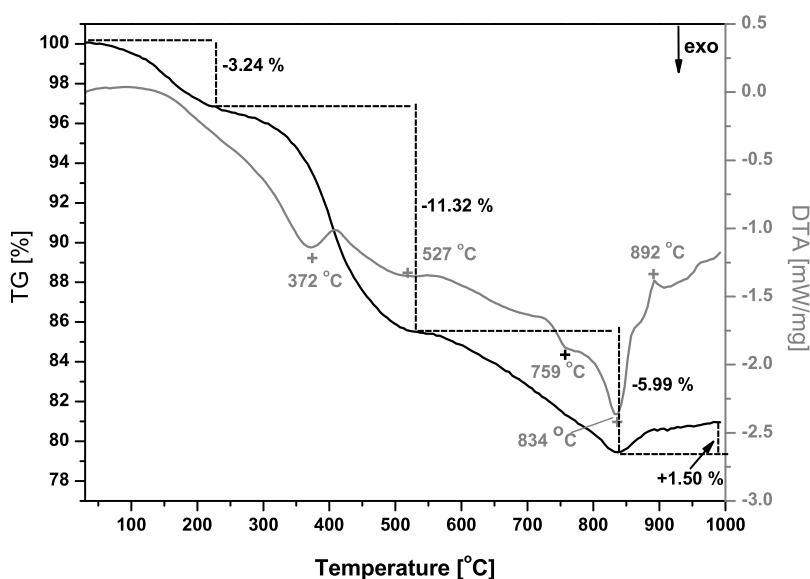
Figure 3.77: DTA-TG curves of **dapvbpo**, For further details see text.

3.5.6   Magnetic susceptibility

The magnetization was measured with a SQUID-magnetometer (Quantum Design, MPMS XL–7) in the temperature range 1.8 K to 400 K (*Fig. 3.78*). The data of the magnetic susceptibility follow the Curie-Weiss law over almost the whole measured temperature range (external magnetic field $H_{\text{ext}} = 1$ kØe). The experimental effective magnetic moment per formula unit is 5.47 μ_{B} (θ = -4.2(1) K) which is between the magnetic moment of V^{3+} (6.32 μ_{B}) and the magnetic moment of V^{4+} (3.87 μ_{B}) per formula unit. Thus the mix-valency situation of vanadium(III/IV) was confirmed. The small θ value indicates no strong (antiferromagnetic) exchange interactions existing in **dapvbpo**. No magnetic ordering is observed above 1.8 K, but increase of $\chi(T)$ below 5.0 K in a field of 20 Øe (no splitting between zfc and fc) has been observed. Isothermal magnetization per f.u. at 1.8K increases in a downwards curved manner up to 4.12 μ_{B} at 70 Øe.

Figure 3.78: Inverse molar magnetic susceptibilities $1/\chi$ for **dapvbpo** as a function of temperature.

3.5.7 Discussion

$(C_3H_{12}N_2)_2\{V^{III}_2V^{IV}_3B_2P_8O_{38}H_8\}$ (**dapvbpo**) is the first mixed-valency vanadium(III/IV) borophosphate. The known temp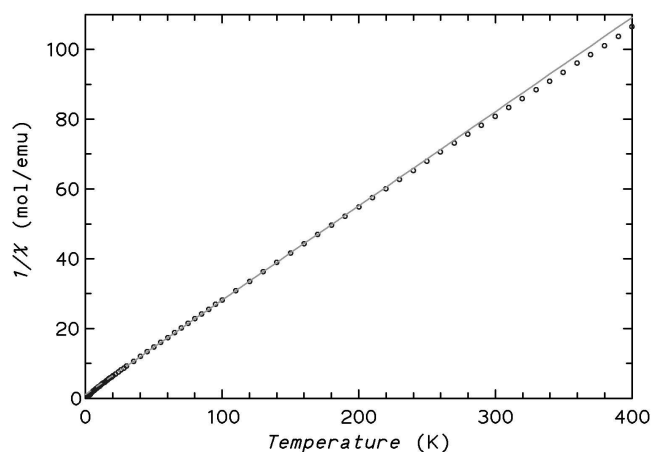lated vanadium borophosphates contain vanadium in either pure 4+ or 5+ valence states [64–71, 73, 74, 124]. The reason for getting a mixed-valency vanadium(III/IV) borophosphate may be due to the acidic conditions employed in the synthesis. Most of the templated vanadium borophosphates reported so far are synthesized under basic conditions [64, 66–72, 74, 75, 124].

dapvbpo also contains oligomeric borophosphate partial structure, $\{[BP_3O_{13}]^{8-}\}$, which has been observed also in other organo-templated vanadium borophosphates. The structure can also be considered as an "intergrowth" of planar **V^{IV}PO–layers** connected with puckered **V^{III}BPO–layers** stacking along the c-axis, which results in a new and unusual building motif. While most of other templated vanadium borophosphates are built from vanadium borophosphate clusters [64, 66–72, 74, 75, 124].

One possible reason for the formation of the intergrowth structure could be due to the mixed-valency states of vanadium. Polyhedra around V^{3+} are normally observed as octahedra, while V^{4+}-polyhedra are normally observed as distorted octahedra, square pyramid or trigonal bipyramid [147]. The combination of different V-polyhedra with B- and P-tetrahedra leads to the different building motif.

dapvbpo can be considered as *pseudo* intercalated or pillared layer compound.

The $\mathbf{V^{IV}PO}$-layer serves as host, and $\mathbf{V^{III}BPO}$-layer serves as pillar (see *Fig. 3.79*). $NH_4[(V_2O_3)_2(4,4'\text{-bpy})_2(HPO_4)(PO_4)_2] \cdot 0.5H_2O$ [148] is a typical vanadium phosphate with a pillared layer structure. In this structure, the host is vanadium phosphate layer, constructed from edge-sharing vanadium(IV,V) octahedra dimers connected by corner-sharing phosphate tetrahedra in the *ab*-plane, the pillar is 4,4'-bipyridine (see *Fig. 3.79*). Compared these two crystal structures, The vanadium phosphate layer serves as host in both of the compounds; while the wavy $\mathbf{V^{III}BPO}$-layer serves as pillar in the crystal structure of **dapvbpo**, 4,4'-bipyridine serves as pillar in the crystal structure of $NH_4[(V_2O_3)_2(4,4'\text{-bpy})_2(HPO_4)(PO_4)_2] \cdot 0.5H_2O$ [148]. Therefore, not only organic species and alkaline cations can act as pillars, but also layers can act as pillar.

(a)   (b)
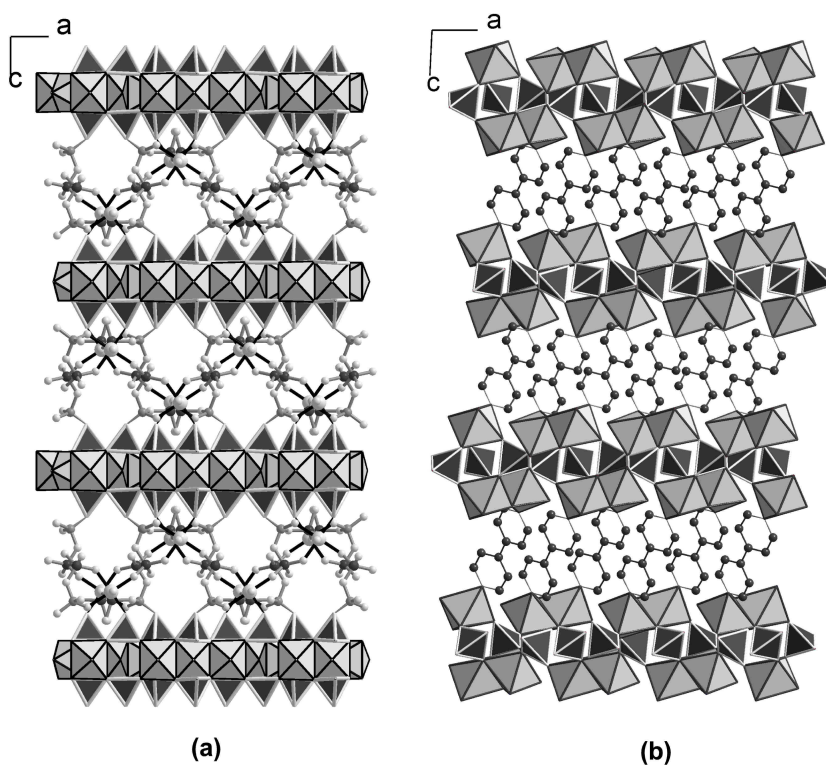
Figure 3.79: (a): Projection of the crystal structure of **dapvbpo** viewed along the *b*-axis, the $\mathbf{V^{IV}PO}$-layer is shown in polyhedra; (b): Projection of the crystal structure of $NH_4[(V_2O_3)_2(4,4'\text{-bpy})_2(HPO_4)(PO_4)_2] \cdot 0.5H_2O$ [148] viewed along the *b*-axis. PO_4 tetrahedra: dark grey, VO_6 octahedra: light grey; B atoms: medium grey spheres, P atoms: dark grey spheres, V atoms: light grey spheres, O atoms: small light grey spheres, C atoms: dark grey spheres.

3.6   K$_3$[B$_5$PO$_{10}$(OH)$_3$]

3.6.1   Synthesis

K$_3$[B$_5$PO$_{10}$(OH)$_3$] was obtained as a byproduct during the preparation of rare earth borophosphates (220 °C). The potassium compound was prepared under mild hydrothermal conditions from a mixture of 3.160 g (12.0 mmol) GdCl$_3$ ·x H$_2$O, 3.6664 g (12.0 mmol) K$_2$B$_4$O$_7$ · 7H$_2$O, and 7.3169 g (42 mmol) K$_2$HPO$_4$ (molar ratio of 2 : 2 : 7) by adding 10 ml of deionized water and stirring at 100 °C. Meanwhile, 0.7 ml of 37 % HCl was slowly added, leading to a white gel with a pH-value of 6. The solution was held at 220 °C for 37 days under autogenous pressure in a Teflon-lined stainless steel autoclave (V = 25 ml, degree of filling $\approx$ 40 %). The solid reaction product was filtered, washed with deionized water and dried at 60 °C. The product contains two phases: K$_3$[B$_5$PO$_{10}$(OH)$_3$] with large size of crystals and an unidentified phase.

Large size of crystals (see SEM micrograph in *Fig. 3.80*) of K$_3$[B$_5$PO$_{10}$(OH)$_3$], were separated from the mixture and were used for powder X-ray diffraction for identifying the phase. The powder data were collected with a X-ray powder diffractometer (HUBER Image Foil Guinier Camera G670, Cu $K_{\alpha 1}$-radiation, germanium monochromator), and are shown in *Fig. 3.81*. The observed powder pattern fits quite well with the calculated powder pattern, but it has some weak reflections which do not appear in the calculated powder pattern of K$_3$[B$_5$PO$_{10}$(OH)$_3$] [88] which could be solved from a twin crystal.

Potassium, boron and phosphorus were analyzed using ICP-AES. Hydrogen was analyzed by using the hot extraction methods. The results are given in *Table 3.39*. No Gd was observed though GdCl$_3$ · xH$_2$O was used as reagent.

Table 3.39: Chemical analysis results of K$_3$[B$_5$PO$_{10}$(OH)$_3$].

Element	Obs.(e.s.d.)/mass-%	Calc. /mass-%
K	27.4(2)	28.38
B	12.0(1)	13.08
P	7.70(6)	7.49
H	0.77(2)	0.73
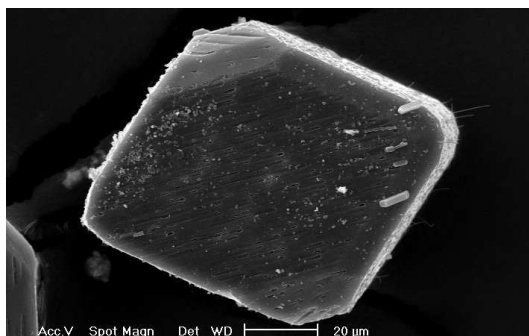
Figure 3.80: SEM micrograph of a single crystal of $K_3[B_5PO_{10}(OH)_3]$.
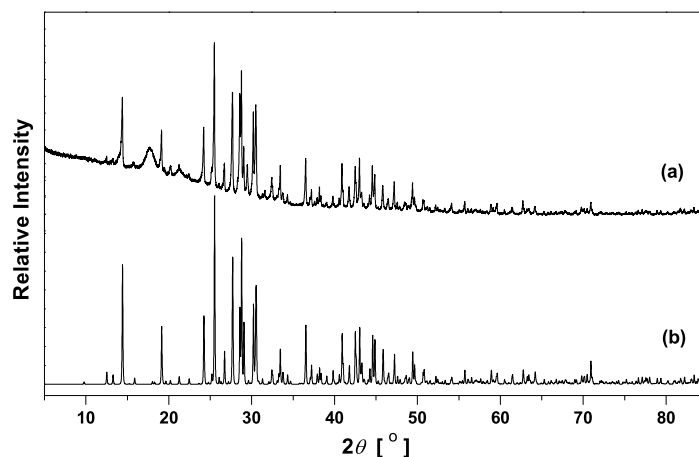
Figure 3.81: Powder X-ray diffraction patterns of $K_3[B_5PO_{10}(OH)_3]$: (a)observed and (b)calculated from structure data; Cu $K_{\alpha 1}$-radiation.

3.6.2   Crystal structure determination

The crystal structure of $K_3[B_5PO_{10}(OH)_3]$ was determined using a colorless prismatic crystal ($0.2 \times 0.2 \times 0.1$ mm^3). Single crystal data were collected at 295 K using a RIGAKU AFC7 four-circle diffractometer, equipped with a Mercury-CCD detector (Mo K_α-radiation, graphite monochromator). Intensity data were collected in the angular range $3.32° \leq 2\theta \leq 65.15°$ ($270°$-ϕ-scan, $60°$-ω-scan at $\chi = 90°$, $0.6°$ steps with 50 s exposure time per step, detector distance: 40 mm; 2θ-offset: $-20.00°$). After application

of Lorenz, polarization and absorption correction, the data were used to determine the space group as $P2_1/c$ (No. 14) with cell parameters: $a = 710.77(5)$ pm, $b = 1332.78(8)$ pm, $c = 1235.28(9)$ pm, $\beta = 96.455(4)°$. A compound with the same chemical formula, K$_3$[B$_5$PO$_{10}$(OH)$_3$], was reported by Hauf [88] (with cell parameters: $P2/c$ (No. 13), $a = 710.8(3)$ pm, $b = 668.7(3)$ pm, $c = 1232.4(5)$ pm, $\beta = 95.68(1)°$). A significant difference is given in the b axes. Weak reflections between the main reflections (*Fig 3.82*) clearly indicate that b has to be doubled. The small b axis in the crystal structure reported by Hauf may be due to a twin crystal. The crystal structure was solved by direct methods and refined with full-matrix least-squares methods [P2,P3]. After anisotropic displacement parameters had been included in the refinement, all hydrogen atoms were obtained from difference Fourier maps and refined without any constraints. The crystallographic data are summarized in *Table 3.40*. Atomic coordinates and equivalent/isotropic displacement parameters are given in *Table 3.41* and *Table 6.9*. Bond lengths and angles are given in *Table 3.42*.
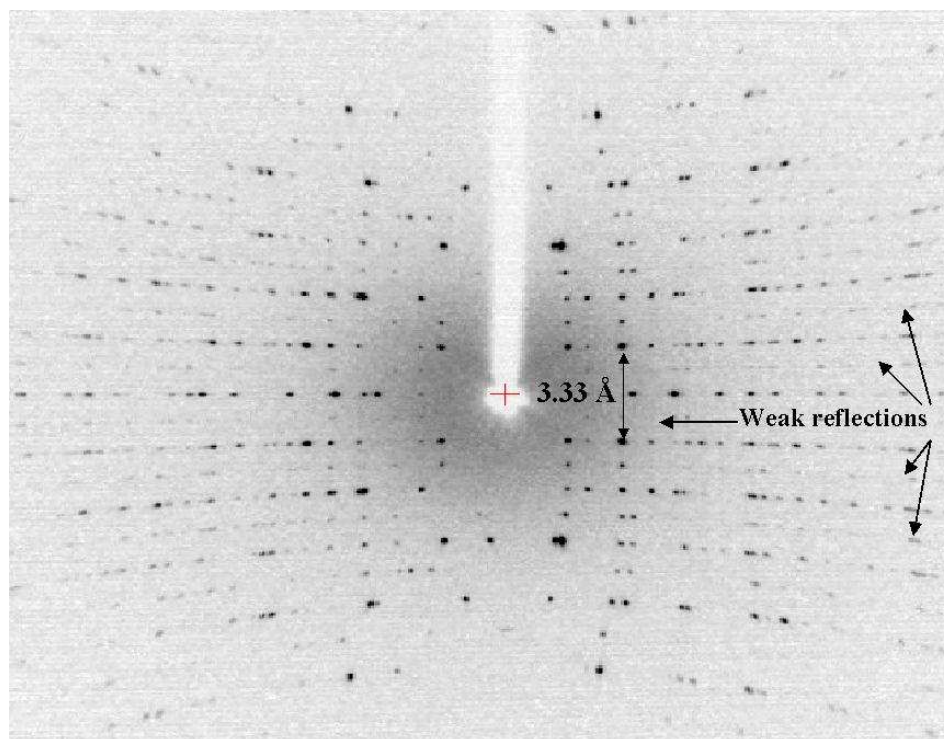
Figure 3.82: b axial photo of K$_3$[B$_5$PO$_{10}$(OH)$_3$] with weak reflections between the main reflections indicate that b has to be doubled. Mo K_α-radiation.

Table 3.40: Crystallographic data and refinement details for $K_3[B_5PO_{10}(OH)_3]$.

Compound		$K_3[B_5PO_{10}(OH)_3]$
Space group	:	$P2_1/c$ (No. 14)
a [pm]	:	710.77(5)
b [pm]	:	1332.78(8)
c [pm]	:	1235.28(9)
β [°]	:	96.455(4)
V [$10^6 \cdot$ pm^3]	:	1162.76(14)
Z	:	4
Crystal size [mm^3]	:	0.2×0.2×0.1
Calc. density ρ [g $\cdot$ cm^{-3}]	:	2.361
Diffractometer	:	RIGAKU AFC7 CCD
		Mo K_α-radiation
		Graphite monochromator
$\mu_{MoK\alpha}$ [mm^{-1}]	:	1.382
Scan type	:	ϕ/ω
2θ range [°]	:	4.52–65.16
Miller-index range	:	$-10 \leq h \leq 10$
		$-19 \leq k \leq 19$
		$-18 \leq l \leq 17$
Total data collected	:	11289
Unique data	:	3704
Observed data $I > 2\sigma(I)$	:	3088
R_{int}/R_σ	:	0.0302/0.0357
Number of refined parameters	:	211
$R1$ ($F_o > 4\sigma(F_o)$)	:	0.0352
$wR2$ ($F_o > 4\sigma(F_o)$)	:	0.0722
$R1$ (all data)	:	0.0505
$wR2$ (all data)	:	0.0769
Goodness-of-Fit (on F^2)	:	1.08
Residual electron density	:	0.42/−0.42
(max./min.) [e $\cdot 10^{-6}$pm^{-3}]		
Programs	:	DIAMOND [P4]
		SHELXS–97/2 [P2], SHELXL–97/2 [P3]

Table 3.41: $K_3[B_5PO_{10}(OH)_3]$: Atomic coordinates and isotropic/equivalent displacement parameters $[10^{-4}pm^2]$, e.s.d.'s are given in parentheses.

Atom	Site	x	y	z	$U_{eq}/\ U_{iso}$
K1	$4e$	0.47093(6)	0.18217(3)	0.73502(4)	0.01950(10)
K2	$4e$	0.84970(6)	0.11218(3)	0.45128(3)	0.01996(10)
K3	$4e$	0.14841(6)	0.12173(3)	0.04192(3)	0.02138(10)
P1	$4e$	0.98000(6)	0.18071(3)	0.76866(3)	0.00992(9)
B1	$4e$	0.1843(3)	0.00381(14)	0.79987(15)	0.0103(3)
B2	$4e$	0.5000(3)	0.06472(14)	0.24997(16)	0.0104(3)
B3	$4e$	0.8088(3)	0.00832(14)	0.69893(15)	0.0107(3)
B4	$4e$	0.6294(3)	0.11109(14)	0.07741(16)	0.0127(3)
B5	$4e$	0.3553(3)	0.11784(14)	0.41584(16)	0.0119(3)
O1	$4e$	0.50516(17)	0.12838(9)	0.15107(10)	0.0136(2)
O2	$4e$	0.48286(17)	0.13356(9)	0.34342(10)	0.0130(2)
O3	$4e$	0.66381(17)	0.00080(9)	0.76674(10)	0.0131(2)
O4	$4e$	0.22833(18)	0.04070(10)	0.40718(10)	0.0145(2)
O5	$4e$	0.6040(2)	0.16742(12)	0.98440(12)	0.0260(3)
O6	$4e$	0.86377(17)	0.11426(9)	0.67934(10)	0.0125(2)
O7	$4e$	0.14821(18)	0.11239(9)	0.81738(10)	0.0139(2)
O8	$4e$	0.77314(17)	0.04284(10)	0.09264(10)	0.0134(2)
O9	$4e$	0.67727(16)	0.00988(9)	0.07171(10)	0.0120(2)
O10	$4e$	0.3521(2)	0.18246(11)	0.50249(11)	0.0234(3)
O11	$4e$	0.05682(19)	0.26975(9)	0.71333(11)	0.0177(3)
O12	$4e$	0.86541(19)	0.20776(10)	0.85935(11)	0.0198(3)
O13	$4e$	0.00620(17)	0.04111(10)	0.24736(11)	0.0140(2)
H1	$4e$	0.011(4)	0.093(2)	0.239(2)	0.038(9)*
H2	$4e$	0.432(5)	0.226(2)	0.495(2)	0.044(8)*
H3	$4e$	0.693(5)	0.166(3)	0.946(3)	0.071(12)*

*refined with isotropic displacement parameters

<u>Table 3.42</u>: Crystal structure of $K_3[B_5PO_{10}(OH)_3]$: selected interatomic distances and angles, e.s.d.'s are given in parentheses.

		distance [pm]		angle [°]		angle [°]
P1–	O12	150.12(13)	O12–P1–O11	113.90(8)	O11–P1–O6	108.32(7)
	O11	150.26(13)	O12–P1–O7	107.90(8)	O7–P1–O6	105.05(7)
	O7	156.81(13)	O11–P1–O7	109.44(8)		
	O6	157.46(13)	O12–P1–O6	111.84(8)		
B1–	O9	140.7(2)	O9–B1–O8	115.23(14)	O8–B1–O13	105.21(13)
	O8	146.7(2)	O9–B1–O7	111.18(14)	O7–B1–O13	105.98(13)
	O7	149.0(2)	O8–B1–O7	107.56(14)		
	O13$_{H1}$	153.4(2)	O9–B1–O13	111.11(14)		
B2–	O3	145.2(2)	O3–B2–O9	112.84(14)	O9–B2–O1	109.67(13)
	O9	145.5(2)	O3–B2–O2	110.26(13)	O2–B2–O1	107.22(14)
	O2	149.0(2)	O9–B2–O2	108.12(14)		
	O1	149.1(2)	O3–B2–O1	108.59(15)		
B3–	O3	140.3(2)	O3–B5–O4	115.64(14)	O4–B5–O13	104.63(13)
	O4	146.2(2)	O3–B5–O6	112.82(14)	O6–B5–O13	104.27(13)
	O6	149.2(2)	O4–B5–O6	107.56(13)		
	O13$_{H1}$	155.1(2)	O3–B5–O13	111.01(14)		
B4–	O1	135.7(2)	O1–B3–O8	123.65(16)		
	O8	136.5(2)	O1–B3–O5	115.82(16)		
	O5$_{H3}$	136.7(2)	O8–B3–O5	120.53(16)		
B5–	O2	135.9(2)	O2–B4–O4	123.28(16)		
	O4	136.4(2)	O2–B4–O10	119.09(16)		
	O10$_{H2}$	137.6(2)	O4–B4–O10	117.63(15)		
		distance [pm]		distance [pm]		distance [pm]
K1–	O1	275.08(13)	K2–O12	266.26(14)	K3–O11	270.35(13)
	O9	276.55(13)	K2–O9	276.95(13)	K3–O1	273.62(13)
	O7	277.24(13)	K2–O4	278.12(13)	K3–O7	277.63(13)
	O3	278.48(13)	K2–O2	280.60(13)	K3–O8	284.48(13)
	O2	279.40(13)	K2–O6	280.78(13)	K3–O8	299.81(13)
	O10	290.15(15)	K2–O4	296.25(13)	K3–O13	303.21(14)
	O12	306.08(15)	K2–O13	301.82(14)	K3–O10	304.99(16)
	O6	308.56(13)			K3–O3	305.38(14)
	O5	312.53(16)			K3–O12	307.02(16)
	O11	314.97(14)				

3.6.3 Crystal structure description

K$_3$[B$_5$PO$_{10}$(OH)$_3$] has the same building units with twin model reported by Hauf [88]. The crystal structure contains 1-D loop-branched single chains, $\frac{1}{\infty}$\{[B$_5$PO$_{10}$(OH)$_3$]$^{3-}$\}, with central tetrahedral borate chain which is loop-branched by planar BO$_2$(OH) and tetrahedral PO$_4$ (*Fig. 3.83*). The BO$_2$OH groups are only linked to borate species. The single chains contain boron in both triangle and tetrahedral coordinations. The BO$_4$ tetrahedra are strongly distorted, with B–O bond lengths (140.3 - 155.1 pm) and bond angles (104.27 - 115.64°). The distances of B1–O13 and B3–O13 are 153.4 pm and 155.1 pm, respectively, which are much longer than the average value for the B-O distance of 147.5 pm. The elongated B–O bond may be due to hydrogen bonded to O13 and the short O$\cdots$O distances of O13$\cdots$O8 (238.4 pm) and O13$\cdots$O4 (238.5 pm) (an extremely short O1$\cdots$O1 distance of 222.2 pm is observed in NbBO$_4$ [149]), but anyway the average bond lengths and angles for the BO4 tetrahedra fall within the usual range [146]. The trigonal planar BO$_2$(OH) groups are in more regular coordination with B–O bond lengths of 135.7 – 137.6 pm and angles of 115.82 – 123.65°. It is clearly shown that the bond lengths in trigonal planar borate units are much shorter than those of tetrahedral arrangement. PO$_4$ tetrahedron presents a regular coordination with P–O distances ranging from 150.12 pm to 157.47 pm and the bond angles ranging from 105.05° to 113.91°. Detailed information on bond lengths and angles are given in *Table 3.42*.
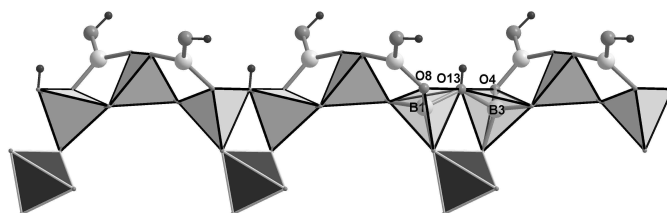
Figure 3.83: Loop-branched single chain $\frac{1}{\infty}$\{[B$_5$PO$_{10}$(OH)$_3$]$^{3-}$\} in the crystal structure of K$_3$[B$_5$PO$_{10}$(OH)$_3$], O13, O8 and O4 are denoted in figure. BO$_4$ tetrahedra: light grey, PO$_4$ tetrahedra: dark grey; B atoms: light grey spheres, O atoms: medium grey spheres, H atoms: small dark grey spheres.

The potassium cations are distributed around the borophosphate single chains (shown in *Fig. 3.85*). They have different polyhedra coordinations. K1 is surrounded

by 9 oxygen atoms with K1–O bond length ranging from 275.8 pm to 314.97 pm. K2 has 7 oxygen atoms surrounding with K2–O bond lengths of 266.26 - 301.82 pm. K3 has 9 oxygen atoms surrounding with K3–O bond lengths of 270.35 - 307.02 pm (*Fig. 3.84*).
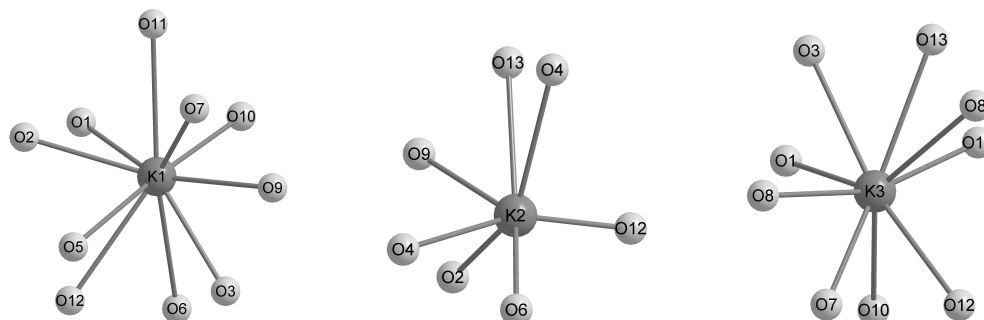

Figure 3.84: Coordination environments of potassium in the crystal structure of $K_3[B_5PO_{10}(OH)_3]$.

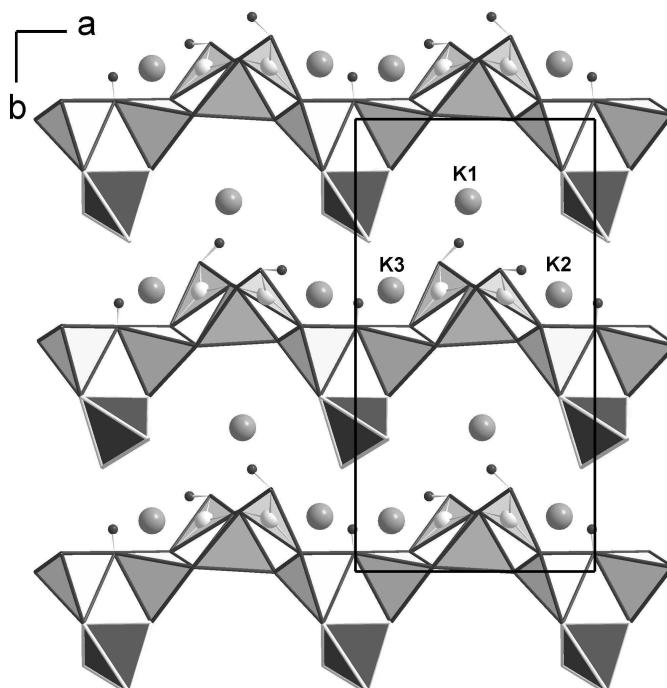Figure 3.85: Crystal structure of $K_3[B_5PO_{10}(OH)_3]$ viewed along the c axis; BO_4 tetrahedra and BO_3 trigonal planar: light grey, PO_4 tetrahedra: dark grey; K atoms: medium grey spheres, H atoms: small dark grey spheres.

The infinite single chains are interconnected by hydrogen bonds O–H$\cdots$O to a three dimensional framework which are shown in *Fig. 3.86*. Lengths and angles of the hydrogen bond systems are given in *Table 3.43*.
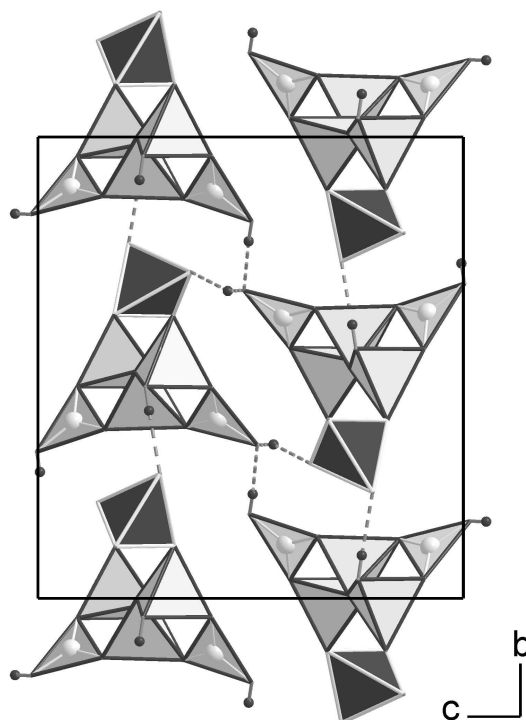
Figure 3.86: Hydrogen bonds connect the single chains to three dimensional framework in K$_3$[B$_5$PO$_{10}$(OH)$_3$]. Hydrogen bonds: dash lines; BO$_4$ tetrahedra and BO$_3$ trigonal planar: light grey, PO$_4$ tetrahedra: dark grey; H atoms: small dark grey spheres.

Table 3.43: Hydrogen bonds in the crystal structure of K$_3$[B$_5$PO$_{10}$(OH)$_3$]: interatomic distances [pm] and angles [°].

Hydrogen bonds							
O13–H1	69.9	H1$\cdots$O11	189.1	O13$\cdots$O11	258.7	O13–H1$\cdots$O11	173.34
O10–H2	82.6	H2$\cdots$O5	188.7	O10$\cdots$O5	271.1	O10–H2$\cdots$O5	175.70
O5–H3	83.4	H3$\cdots$O12	180.2	O5$\cdots$O12	260.3	O5–H3$\cdots$O12	160.47

3.6.4   Thermal analysis

The thermal behavior of $K_3[B_5PO_{10}(OH)_3]$ (*Fig. 3.87*) was analyzed by DTA/TG (NETZSCH STA 409) in the temperature range from 30 °C to 1000° using heating and cooling rates of 5 °C/min in air. The TG curve shows only a one step weight loss of 6.18 %, which is according to a hypothetical weight loss of $1.5 \times H_2O$ per formula unit (6.53 % calc.), consistent to one endothermal peak in DTA curve at 390 °C. This result is consist with the thermal analysis results of $K_3[B_5PO_{10}(OH)_3]$ presented in Hauf's thesis [31]. According to the HT-XRD results shown in Hauf's thesis, the exothermal peak at 534 °C is consistent to the formation of KB_5O_8, the endothermal peaks at 629 °C and 715 °C are consistent to the formation and decomposition of $K_3P_3O_9$. After TG/DTA investigation, the products are glass which are hard to separate from the corundum crucible.
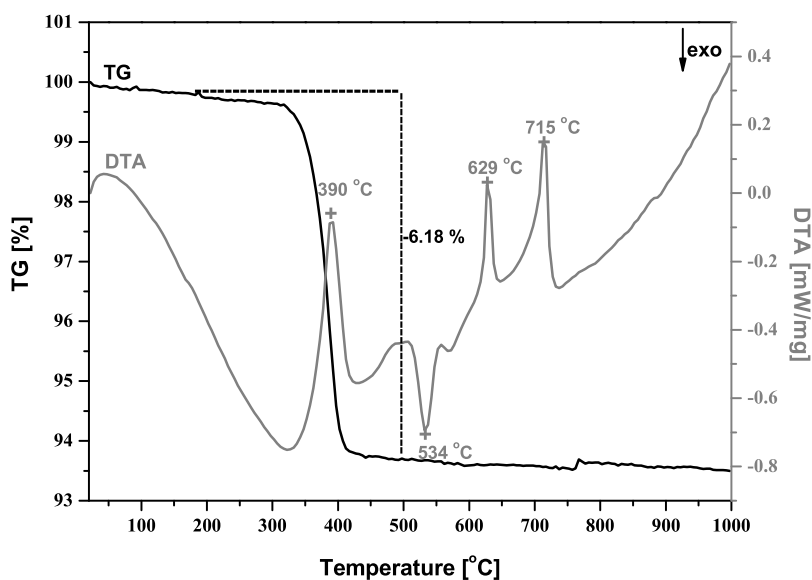
Figure 3.87: DTA-TG curves of $K_3[B_5PO_{10}(OH)_3]$.

3.6.5   IR-spectroscopy

IR-spectrum of $K_3[B_5PO_{10}(OH)_3]$ was investigated in order to confirm the presence of the O–H group in this compound (*Fig. 3.88*). A tablet was prepared from a mixture of 1.5 mg $K_3[B_5PO_{10}(OH)_3]$ and 150 mg KBr, and was measured in the range of 4000–400 cm^{-1}. The band positions at 3237 cm−1, which belongs to O–H hydrogen bond, confirmed the presence of O–H group. Compared with IR-spectrum of $K_3[B_5PO_{10}(OH)_3]$ (Hauf's) [31], they are nearly the same. This is another evidence to show that these two structures are the same compound but different in coming from single crystal and twin crystal.

Figure 3.88: IR-spectrum of $K_3[B_5PO_{10}(OH)_3]$ in the range of 4000–400 cm^{-1}.

3.6.6   Discussion

Fig. 3.89 shows the crystal structures of this work and Hauf [31]. These two crystal structures have the same arrangement of single chains and potassium cations except that the unit cell of this work is double of Hauf's. In the Hauf's model, PO_4 groups

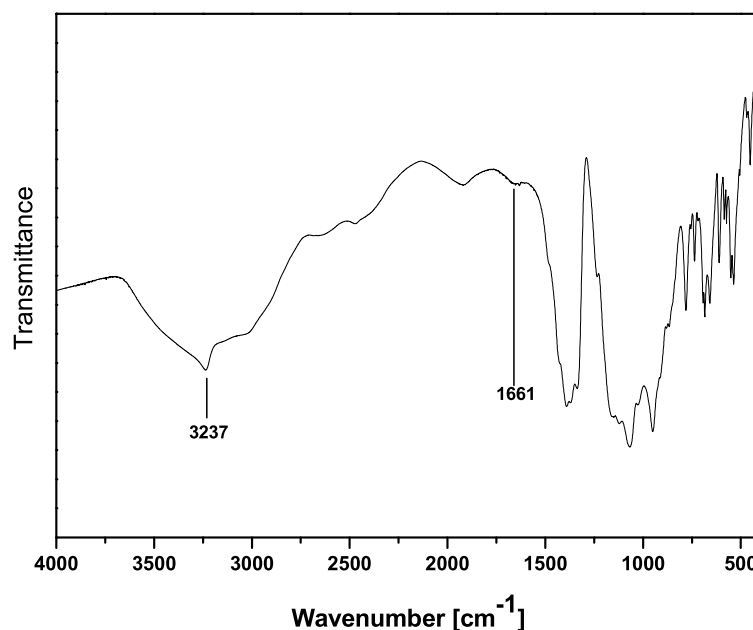have two disordering oxygen positions (O7 and O8) coordinated to the phosphorus. In the single crystal model with double b axis, the PO_4 tetrahedra are all in tetrahedral coordination without any disorder. When we compare these two crystal structures viewed long the c axis, we can see that the overlapping of two different orientations PO_4 groups along b-axis in single crystal model is exactly the case of two sets of disordered PO_4 tetrahedra in the crystal structure of Hauf (it is clearly shown in *Fig. 3.89*). So doubling the b axis just solve the problem of disordering oxygen positions. It is need to note that the disordering oxygen positions could not be ordered even at low temperature (-120 °C) [31]. This gives another hint that the crystal structure of Hauf was determined from a twin crystal. The different domains influence the X-ray data which gave the b-axis with half value. The single crystal X-ray data clearly show that b-axis has to be doubled (details see crystal structure determination part). The double b-axis solved the problem of the disorder and gave a reliable structure.
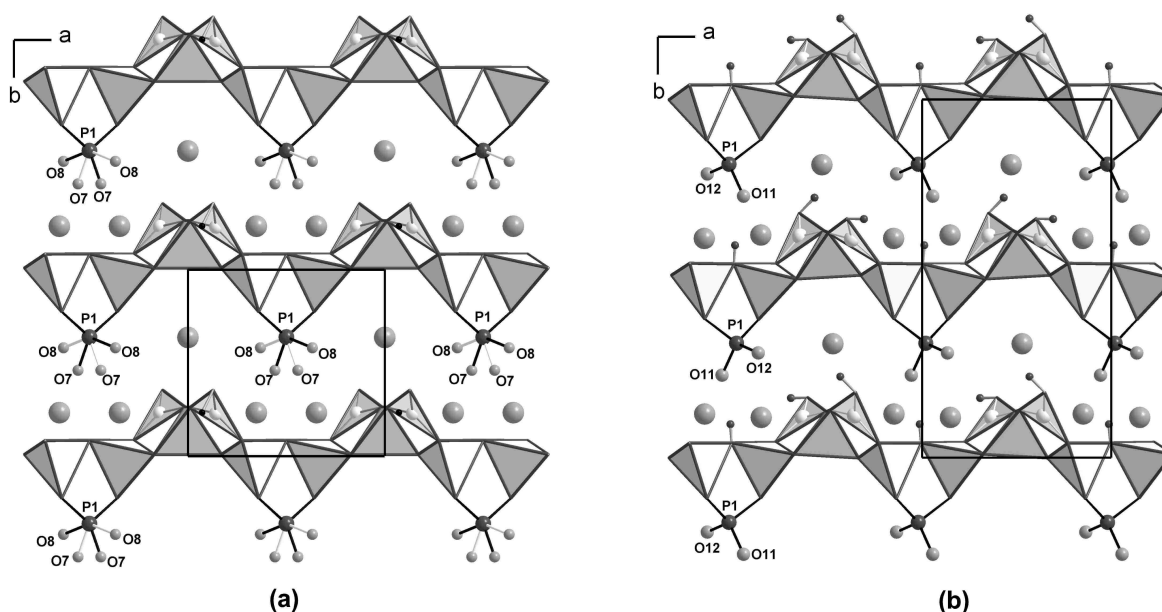
Figure 3.89: (a):Crystal structure of $K_3[B_5PO_{10}(OH)_3]$ [88] (twin) viewed along the c-axis shows the disorder of O7 and O8; (b): Crystal structure of $K_3[B_5PO_{10}(OH)_3]$ (single crystal) viewed along the c-axis shows PO_4 tetrahedra having reasonable tetrahedral coordinations. BO_4 tetrahedra and BO_3 trigonal planar: light grey, PO_4 tetrahedra: dark grey; K atoms: medium grey spheres, H atoms: dark grey spheres (small sphere).

Another proof to show Hauf's model is twin lying in the space group transforation. $P2_1/c$ (this work) is the subgroup of $P2/c$ (Hauf) with the condition of $b' = 2b$ via the Klassengleich. The Bärnighausen [140] tree (*Fig. 3.90*) shows the transformation from $P2/c$ to $P2_1/c$. In principle, one $4g$ position in $P2/c$ spacegroup must be transferred to two $4e$ positions in $P2_1/c$ spacegroup, but the Bärnighausen tree shows that O7 and O8 (position: $4g$) positions in Haufs' only was transferred to one $4e$ position each separately in the single crystal model. This clearly indicates that the crystal structure of this work is from a single crystal, while the crystal structure of Hauf is from a twin crystal.

$K_3[B_5PO_{10}(OH)_3]$, $P2/c$ (No. 13)

K1: $4g$	K2: $2f$	P1: $2e$	B1: $4g$	B2: $4g$	B3: $2f$	O1: $4g$
0.1523	1/2	0	0.1847	0.3582	1/2	0.2251
0.2342	0.6366	0.64	0.9902	0.2306	0.1292	0.0841
0.04574	1/4	1/4	0.3005	0.4208	1/4	0.4072

k2, $b' = 2b$

K2: $4e$	K3: $4e$	K1: $4e$	P1: $4e$	B1: $4e$	B3: $4e$	B4: $4e$	B5: $4e$	B2: $4e$	O4: $4e$	O8: $4e$
0.8497	0.14841	0.47093	0.98	0.1843	0.8088	0.6294	0.3553	0.5000	0.22833	0.77314
0.11218	0.12173	0.18217	0.18071	0.00381	0.00832	0.11109	0.11784	0.06472	0.0407	0.04284
0.45128	0.04192	0.73502	0.76866	0.79987	0.69893	0.07741	0.41584	0.24997	0.40718	0.09264

$K_3[B_5PO_{10}(OH)_3]$, $P2_1/c$ (No. 14)

$K_3[B_5PO_{10}(OH)_3]$, $P2/c$ (No. 13)

O2: $4g$	O3: $4g$	O4: $4g$	O5: $4e$	O6: $4g$	O7: $4g$	O8: $4g$
0.5134	0.1403	0.329	0	0.3725	0.0557	0.1316
0.2629	0.7765	0.0102	0.085	0.6483	0.4629	0.5836
0.1537	0.3188	0.2305	1/4	0.0091	0.2133	0.1395

k2, $b' = 2b$

O1: $4e$	O2: $4e$	O6: $4e$	O7: $4e$	O3: $4e$	O9: $4e$	O13: $4e$	O5: $4e$	O10: $4e$	O11: $4e$	O12: $4e$
0.50516	0.48286	0.86377	0.14821	0.66381	0.67727	0.0062	0.604	0.3521	0.05682	0.86541
0.12838	0.13356	0.11426	0.11239	0.0008	0.00988	0.04111	0.6742	0.18246	0.26975	0.20776
0.15107	0.34342	0.67934	0.81738	0.76674	0.27171	0.24736	0.9844	0.50249	0.71333	0.85935

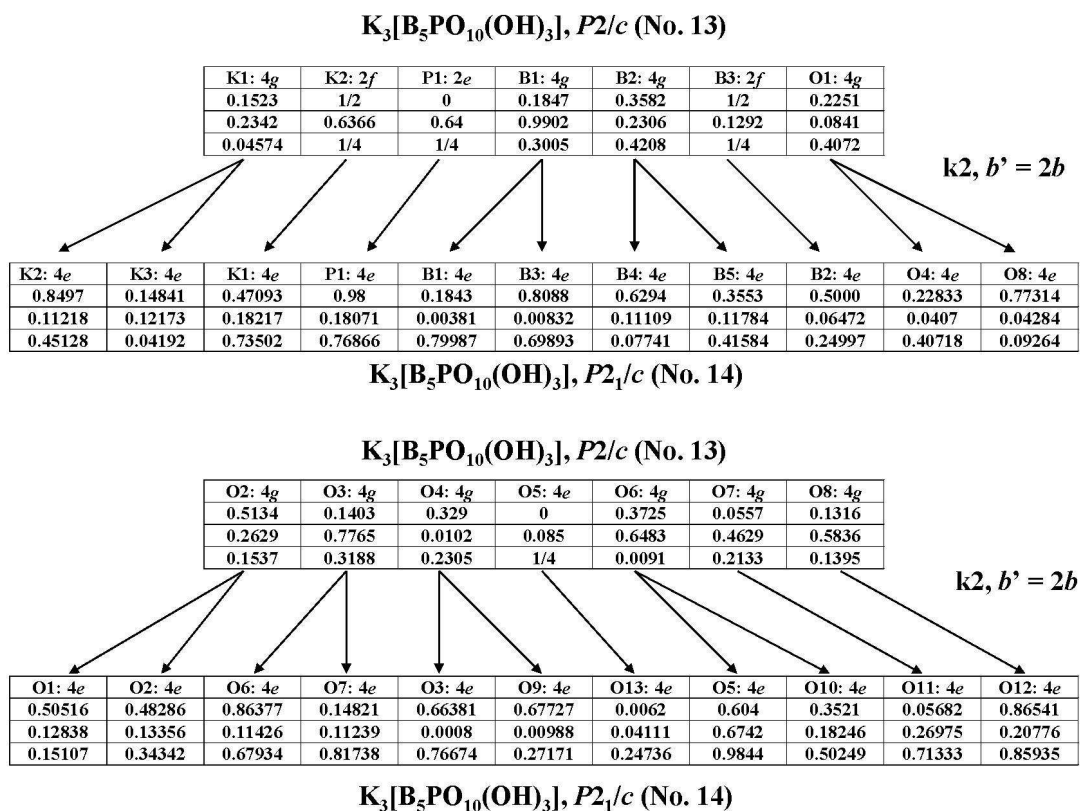**$K_3[B_5PO_{10}(OH)_3]$, $P2_1/c$ (No. 14)**

Figure 3.90: Bärnighausen system tree shows the structure relationship between the single crystal structure ($P2_1/c$) and the twin crystal structure ($P2/c$) [88] of $K_3[B_5PO_{10}(OH)_3]$.

4 Discussion

4.1 Templates

The organo-templated borophosphates, reported in this work, were prepared with aliphatic diamines. The numbers of carbon atoms range from 2 to 6. Differences in their lengths and shapes are shown in *Fig. 4.1*. The length of the template molecule is given by the distances $N \cdots N$ taken from the single crystal structure data. The molecule shapes of 1,2-ethylenediamine (en) and 1,3-diaminopropane (DAP) represent like rectangles, but the length of 1,3-diaminopropane (DAP) (494 pm) is longer than that of 1,2-ethylenediamine (en) (374 pm). The shapes of piperazine (PIP) and diaza-bicyclo[2.2.2]-octane (DABCO) are like flat cylinder and sphere, respectively. In most of the cases, template molecules are protonated to balance the charge of anionic frameworks or ribbons and act as pure templates locating either in the channels or around the anionic part structures. The special case is observed in the crystal structure of **zndabcocl** of which $(HDABCO)^+$ ions act as ligands to anionic part structures. The different shapes and sizes of the template molecules give rise to the differences in the shapes and sizes of the channels which were confirmed by the manganese borophosphates containing DAP and PIP as templates.

4.2 Structural relationships of anionic partial structures in the borophosphates under investigation

Borophosphate partial structures of new compounds described in this work have quite a wide molar ratio ranging from B : P = 1 : 3 to B : P = 5 : 1. They nearly cover the whole region of B : P ratios for known borophosphate partial structures. Boron is in tetrahedral coordination except that boron in the crystal structure of $K_3B_5PO_{10}(OH)_3$ has both 3-coordinated planar and tetrahedral surroundings.

The borophosphate partial structures of the compounds under investigation contain oligomers and single chains. The characterization of the borophosphate partial structures is shown in *Table 4.1* and *Fig. 4.2*.

The relationships among them can be considered based on $\{[BP_2O_8(OH)_2]^{5-}\}$ trimers in the crystal structure of $(C_3H_{12}N_2)(H_2O)_4[Fe^{III}_6B_4P_8O_{32}(OH)_8]$. To add one PO_4 group to one free O-corner of BO_4 group leads to $\{[BP_3O_{13}]^{8-}\}$ tetramers in the

crystal structure of **dapvbpo**. Two $\{[BP_2O_8(OH)_2]^{5-}\}$ trimers were connected together forming $\{[B_2P_4O_{15}(OH)_2]^{6-}\}$ hexamers by sharing two free O-corners of BO_4 group in one trimer to BO_4 and PO_4 groups in the other trimer. $\{[BP_2O_8(OH)_2]^{5-}\}$ trimers connect to each other by sharing PO_4 groups, meanwhile two -OH groups coordinated to boron replaced by fluorine, leading to one dimensional unbranched zweier single chains $\frac{1}{\infty}\{[BPO_4F_2]^{2-}\}$ in the crystal structure of $(C_2H_{10}N_2)[BPO_4F_2]$. $\{[B_2P_4O_{15}(OH)_2]^{6-}\}$ hexamers connect to each other by sharing the branched PO_4 groups resulting in loop-branched single chains $\frac{1}{\infty}\{[B_2P_3O_{12}(OH)]^{4-}\}$ in the crystal structures of **DAP-Mn** and **PIP-Mn**. The detailed relationships of the anionic partial structures in the borophosphates under investigations are shown in *Fig. 4.2*.
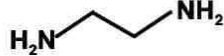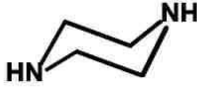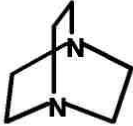
Molecular structure and formula	Space-filling mode	Molecular shape	d (N⋯N) [pm]
1,2-ethylenediamine $H_2NCH_2CH_2NH_2$			374
1,3-diaminopropane $H_2NCH_2CH_2CH_2NH_2$			493
piperazine $C_4H_{10}N_2$			286
1,4-diaza-bicyclo[2.2.2]octane $C_6H_{12}N_2$			252

Figure 4.1: The summary of template molecules (diamine) used in the preparation of templated borophosphates shows their shapes and lengths.

Table 4.1: Classification of borophosphate partial structures investigated in this work.

Compound	B[CN]*	B : P (molar ratio)	Structure of the complex anion
$(C_3H_{12}N_2)_2[V^{III}_2V^{IV}_3B_2P_8O_{38}H_8]$	4	B : P = 1 : 4	tetramer
$(C_3H_{12}N_2)(H_2O)_4[Fe^{III}_6B_4P_8O_{32}(OH)_8]$	4	B : P = 1 : 2	trimer
$(C_6H_{14}N_2)\{Zn[ZnB_2P_4O_{15}(OH)_2]\cdot(C_6H_{13}N_2)Cl\}$	4	B : P = 1 : 2	hexamer
$(C_3H_{12}N_2)[MnB_2P_3O_{12}(OH)]$	4	B : P = 2 : 3	loop-branched
$(C_4H_{12}N_2)[MnB_2P_3O_{12}(OH)]$	4	B : P = 2 : 3	single chain
$(C_2H_{10}N_2)[BPO_4F_2]$	4	B : P = 1 : 1	unbranched single chain
$K_3[B_5PO_{10}(OH)_3]$	3, 4	B : P = 5 : 1	open-branched single chain

*coordination number of boron
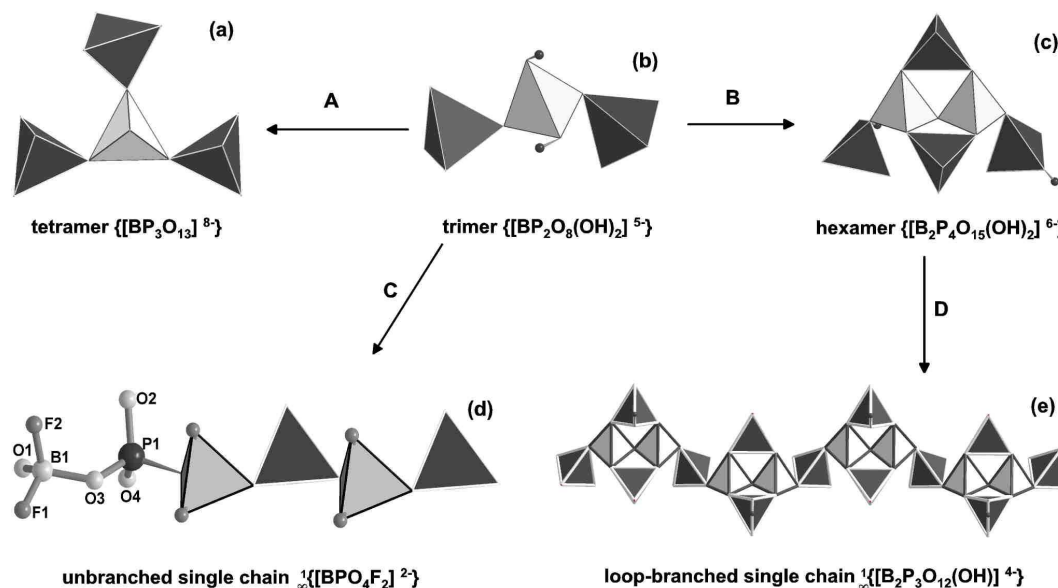
Figure 4.2: Borophosphate partial structures: (a) $\{[BP_3O_{13}]^{8-}\}$ tetramers in the crystal structure of **dapvbpo**; (b) $\{[BP_2O_8(OH)_2]^{5-}\}$ trimers in the crystal structure of $(C_3H_{12}N_2)(H_2O)_4[Fe^{III}_6B_4P_8O_{32}(OH)_8]$; (c) $\{[B_2P_4O_{15}(OH)_2]^{6-}\}$ hexamers in the crystal structure of **zndabcocl**; (d) Unbranched zweier single chain $^1_\infty\{[BPO_4F_2]^{2-}\}$ in the crystal structure of $(C_2H_{10}N_2)[BPO_4F_2]$; (e) Loop-branched single chain $^1_\infty\{[B_2P_3O_{12}(OH)]^{4-}\}$ in the crystal structures of **DAP-Mn** and **PIP-Mn**; PO_4 tetrahedra: dark grey, BO_4 tetrahedra: light grey; Hydrogen atoms: black spheres.

5 Conclusion and outlook

The new borophosphates described here were synthesized under mild hydrothermal conditions (170 °C or 220 °C). Powder X-ray diffraction and single crystal X-ray diffraction were employed to determine and refine the crystal structures. DTA-TG methods were used to analyze the thermal stability of the compounds. High temperature powder X-ray diffraction (HT-XRD) was applied to identify the intermediate phase during the decomposition. Chemical analyses were performed to quantitatively determine the chemical composition of these compounds. Magnetic susceptibility measurement was employed to investigate the magnetic properties of the compounds containing transition metals. ^{19}F MAS NMR was applied to check the number of fluorine positions in the crystal structure. The following compounds were prepared and characterized.

$(C_2H_{10}N_2)[BPO_4F_2]$

$(C_6H_{14}N_2)\{Zn[ZnB_2P_4O_{15}(OH)_2]\cdot(C_6H_{13}N_2)Cl\}$ (**zndabcocl**)

$(C_3H_{12}N_2)\{Mn[B_2P_3O_{12}(OH)]\}$ (**DAP-Mn**) and $(C_4H_{12}N_2)\{Mn[B_2P_3O_{12}(OH)]\}$ (**PIP-Mn**)

$(C_3H_{12}N_2)Fe^{III}_6(H_2O)_4[B_4P_8O_{32}(OH)_8]$

$(C_3H_{12}N_2)_2\{V^{III}_2V^{IV}_3B_2P_8O_{38}H_8\}$ (**dapvbpo**)

$K_3[B_5PO_{10}(OH)_3]$
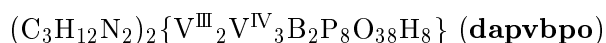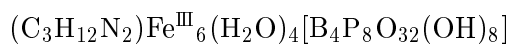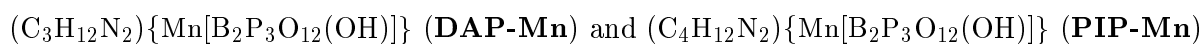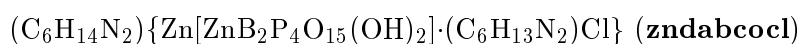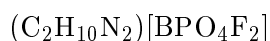
$(C_2H_{10}N_2)[BPO_4F_2]$ is the first fluorine substituted borophosphate and the first borophosphate with crystal structure closely related to the pyroxene type structure. The unbranched zweier single chain $^{1}_{\infty}\{[BPO_4F_2]^{2-}\}$ represents a new type of borophosphate partial structure. The introduction of fluorine coordinating to boron makes the single chain more straight which may be due to its electronegative character.

$(C_6H_{14}N_2)\{Zn[ZnB_2P_4O_{15}(OH)_2]\cdot(C_6H_{13}N_2)Cl\}$ (**zndabcocl**) represents the first organo-templated zincoborophosphate. The crystal structure is built from tetrahedral zigzag ribbons, $^{1}_{\infty}\{[ZnB_2P_4O_{15}(OH)_2]^{4-}\}$, running along [010]. The structure contains diaza-bicyclo[2.2.2]-octane (DABCO) which acts in its diprotonated form $(H_2DABCO)^{2+}$ as a pure template and in its monoprotonated form $(HDABCO)^+$ as a ligand to Zn-positions at the borders of ribbons to complete structural motif. This

compound is also the first example containing a quaternary Zn-tetrahedron (ZnO_2NCl), and can formally be described as an adduct of $(C_6H_{14}N_2)Zn[ZnB_2P_4O_{15}(OH)_2]$ with diaza-bicyclo[2.2.2]octane-hydrochloride. The thermal behavior of **zndabcocl** has been studied by temperature-dependent powder X-ray diffraction and thermal analysis in the temperature range 25–600 °C. The new phase occurring during the decomposition has been identified as HT-$NH_4[ZnBP_2O_8]$.

$(C_3H_{12}N_2)\{Mn[B_2P_3O_{12}(OH)]\}$ (**DAP-Mn**) and $(C_4H_{12}N_2)\{Mn[B_2P_3O_{12}(OH)]\}$ (**PIP-Mn**) contain identical framework interconnections but differences in the shape of resulting channels, which are due to the different shape of organic templates. The crystal structures are built from the same building units: loop-branched infinite single chains are connected via MnO_6-octahedra resulting in a three dimensional structure with intersecting channel systems running along [100], [011] and [01$\bar{1}$], respectively. The different shape of the templates controls the shape of the channels, especially channels running along [100], resulting in dramatic shape-differences. The linear $(H_2DAP)^{2+}$ ions make the channels more elongated, while the cyclic $(H_2PIP)^{2+}$ ions give rise to more regular shaped channels. The different shape of channels influence the symmetry of the crystal structure. Thus, the space group changes from *Ima2* (**PIP-Mn**) to *Pmc2$_1$* (**DAP-Mn**), representing a supergroup/subgroup relation. The flexibility of frameworks may be due to the more flexible coordination of Mn-atoms (octahedron and square pyramid).

$(C_3H_{12}N_2)Fe^{III}_6(H_2O)_4[B_4P_8O_{32}(OH)_8]$ is a new borophosphate with 3-D framework structure with 1D 10-membered ring channel (778 × 867 pm^2) which is occupied by organic templates. The magnetic susceptibility measurements show it to exhibit antiferromagnetic susceptibility at low temperature ($T_N \approx 14$ K).

$(C_3H_{12}N_2)_2\{V^{III}_2V^{IV}_3B_2P_8O_{38}H_8\}$ (**dapvbpo**) is the first mixed-valence vanadium borophosphate with a new structure type. Its structure can be considered as an "intergrowth" of puckered vanadium(III) borophosphate layer (**V^{III}BPO-layer**) and planar vanadium(IV) phosphate layers (**V^{IV}PO-layer**) stacked and interconnected alternately along [001], which results in a new and unusual building motif. The corner sharing trimers of vanadium octahedra are observed for the first time in vanadium borophosphates. This structure can also be treated as a *pseudo* intercalated or pillared structure in which **V^{IV}PO-layer** acts as a solid layer and **V^{III}BPO-layer** acts as a pillar.

$K_3[B_5PO_{10}(OH)_3]$ has a double unit cell of a twin crystal structure having the

same chemical formula. The double b-axis solve the disorder problem of two oxygen positions coordinated to phosphorous. It represents a much more reasonable structure determination. Boron atoms are in both tetrahedral and trigonal-planar coordination.

Further investigation on borophosphates would be desirable on the following directions:

1. Rare earth borophosphates with low-dimensional composite structures.

2. Polyoxoclusters (e.g., V, Mo, W) involved in the crystal structures based on borophosphate matrices.

3. To study building-fragments present in solution which is good for the processes of self-organization and crystallization.

4. Fluorine substitute borophosphates with higher dimensional structure.

Preparations, analyses and characterizations are required in order to obtain these compounds. Meanwhile it is also interesting to study the properties of these compounds, for instance, catalytic properties.

6 Appendix

6.1 Atomic coordinates in asymmetric units of DAP-Mn and PIP-Mn

Table 6.1:   Atomic   coordinates   in   asymmetric   units   and   equivalent/isotropic displacement parameters $(10^{-4}\mathrm{pm}^2)$ in the crystal structure of $(C_3H_{12}N_2)\{Mn[B_2P_3O_{12}(OH)]\}$(**DAP-Mn**), e.s.d.'s are given in parentheses.

Atom	Site	x	y	z	$U_{eq}/\ U_{iso}$
Mn1	2b	0.5000	0.12708(5)	0.72354(4)	0.01168(8)
Mn2	2a	0.0000	0.32081(5)	0.76658(4)	0.01055(8)
P1	2b	0.5000	0.14313(8)	0.43465(6)	0.01032(13)
P2	2b	0.5000	0.44249(8)	0.89564(7)	0.01217(13)
P3	2a	0.0000	0.43122(8)	0.49859(6)	0.01074(13)
P4	4c	0.25167(4)	0.24048(5)	0.66760(5)	0.00917(8)
P5	2a	0.0000	0.02412(8)	0.34476(7)	0.01195(13)
B1	4c	0.09609(16)	0.1836(2)	0.50871(19)	0.0098(3)
B2	4c	0.40273(16)	0.3620(2)	0.52793(19)	0.0100(3)
O1	4c	0.33272(11)	0.14514(16)	0.72457(14)	0.0143(3)
O2	4c	0.19180(11)	0.14745(15)	0.57396(14)	0.0122(2)
O3	2a	0.0000	0.1559(2)	0.57708(19)	0.0101(3)
O4	4c	0.40112(11)	0.24475(16)	0.44057(13)	0.0128(3)
O5	4c	0.09918(11)	0.09401(18)	0.40121(14)	0.0167(3)
O6	2b	0.5000	0.5192(3)	0.7738(2)	0.0246(5)
O7	2b	0.5000	0.3510(2)	0.59927(17)	0.0093(4)
O8	4c	0.17344(12)	0.30772(17)	0.75043(12)	0.0142(3)
O9	4c	0.30860(12)	0.36306(16)	0.60049(13)	0.0121(3)
O10	4c	0.09865(11)	0.33251(16)	0.47171(14)	0.0133(3)
O11	2a	0.0000	0.0690(3)	0.2127(2)	0.0205(4)
O12	2a	0.0000	0.1304(3)	0.8585(2)	0.0205(5)
O13	2b	0.5000	0.0480(2)	0.5424(2)	0.0151(4)
O14	4c	0.40159(11)	0.49976(17)	0.46340(14)	0.0132(3)
O15	2a	0.0000	0.4698(2)	0.6269(2)	0.0161(4)
O16	2b	0.5000	0.2870(2)	0.8824(2)	0.0175(4)
O17	2b	0.5000	0.0619(2)	0.3217(2)	0.0172(4)
O18	2a	0.0000	0.4503(3)	0.9135(2)	0.0216(5)
N1	4c	0.30207(19)	0.0812(3)	0.9634(2)	0.0216(4)
N2	4c	0.23707(19)	0.4111(3)	0.2910(2)	0.0242(4)
C1	4c	0.2407(2)	0.1997(3)	0.0122(2)	0.0270(5)
C2	4c	0.1974(2)	0.3449(3)	0.1806(3)	0.0287(5)
C3	4c	0.2664(3)	0.2236(3)	0.1400(2)	0.0308(6)
H1	2b	0.5000	0.453(8)	0.708(8)	0.11(3)*
H2	2a	0.0000	-0.003(5)	0.180(7)	0.12(3)*
H3	4c	0.274(3)	0.003(6)	0.984(4)	0.063(13)*
H4	4c	0.296(3)	0.081(4)	0.891(3)	0.032(9)*
H5	4c	0.358(3)	0.083(4)	0.983(3)	0.038(11)*
H6	4c	0.225(2)	0.499(4)	0.293(3)	0.031(9)*

Table 6.1 Continued

Atom	Site	x	y	z	$U_{eq}/\ U_{iso}$
H7	$4c$	0.196(4)	0.373(5)	0.352(4)	0.067(14)*
H8	$4c$	0.305(4)	0.399(5)	0.285(4)	0.063(14)*
H9	$4c$	0.262(3)	0.282(5)	-0.027(4)	0.054(13)*
H10	$4c$	0.170(3)	0.193(4)	-0.004(3)	0.045(10)*
H11	$4c$	0.236(5)	0.413(7)	0.116(5)	0.12(2)*
H12	$4c$	0.123(3)	0.319(4)	0.207(3)	0.036(9)*
H13	$4c$	0.258(4)	0.136(6)	0.195(5)	0.10(2)*
H14	$4c$	0.342(4)	0.258(6)	0.153(4)	0.079(16)*

*refined with isotropic displacement parameters

Table 6.2: Atomic coordinates in asymmetric units and equivalent/isotropic displacement parameters $(10^{-4}\mathrm{pm}^2)$ in the crystal structure of $(C_4H_{12}N_2)\{Mn[B_2P_3O_{12}(OH)]\}$(**PIP-Mn**), e.s.d.'s are given in parentheses.

Atom	Site	x	y	z	$U_{eq}/\ U_{iso}$
Mn1	$4b$	0.2500	0.91166(5)	0.23472(4)	0.00924(12)
P1	$4a$	0.0000	0.0000	0.15496(8)	0.00853(18)
P2	$4b$	0.2500	0.65205(9)	0.45512(8)	0.00952(18)
P3	$4b$	0.2500	0.24022(10)	0.35361(9)	0.01118(19)
B1	$8c$	0.1533(2)	0.0870(3)	0.0057(2)	0.0098(5)
O1	$8c$	0.08080(14)	0.91674(19)	0.22132(17)	0.0134(4)
O2	$8c$	0.05813(15)	0.11063(19)	0.07461(15)	0.0110(4)
O3	$8c$	0.15063(14)	0.55267(18)	0.44950(17)	0.0116(4)
O4	$4b$	0.2500	0.7490(3)	0.3540(3)	0.0183(6)
O5	$4b$	0.2500	0.7728(3)	0.0722(2)	0.0145(6)
O6	$4b$	0.2500	0.3001(3)	0.2278(3)	0.0198(6)
O7	$8c$	0.15060(16)	0.3010(2)	0.41557(17)	0.0154(4)
O8	$4b$	0.2500	0.0840(3)	0.3518(3)	0.0152(6)
O9	$4b$	0.2500	0.0991(2)	0.0760(2)	0.0077(5)
N1	$8c$	0.0545(2)	0.6329(3)	0.0991(3)	0.0196(5)
C2	$8c$	0.0495(3)	0.9549(4)	0.4945(3)	0.0286(8)
C3	$8c$	0.0490(3)	0.5464(4)	0.2062(3)	0.0317(8)
H1	$4b$	0.2500	0.260(10)	0.199(9)	0.12(4)*
H2	$8c$	0.053(4)	0.899(4)	0.444(4)	0.047(13)*
H3	$8c$	0.383(4)	0.014(5)	0.491(3)	0.048(14)*
H4	$8c$	0.124(4)	0.672(4)	0.106(4)	0.049(13)*
H5	$8c$	0.000(3)	0.697(3)	0.094(3)	0.012(8)*
H6	$8c$	0.119(3)	0.495(4)	0.208(3)	0.030(10)*
H7	$8c$	0.052(3)	0.609(4)	0.275(3)	0.024(10)*

*refined with isotropic displacement parameters

6.2   Anisotropic displacement parameters

<u>Table 6.3</u>: $(C_2H_{10}N_2)[BPO_4F_2]$: anisotropic displacement parameters U_{ij} $[10^{-4}pm^2]$, e.s.d.'s are given in parentheses.

Atom	U_{11}	U_{22}	U_{33}	U_{23}	U_{13}	U_{12}
P	0.0177(6)	0.0213(5)	0.0273(6)	-0.0007(4)	0.0003(4)	-0.0068(4)
B	0.017(2)	0.027(2)	0.037(3)	-0.002(2)	-0.0012(18)	-0.0079(18)
O1	0.0154(15)	0.0219(14)	0.0346(16)	-0.0001(11)	0.0017(11)	-0.0068(10)
O2	0.0247(16)	0.0397(17)	0.0246(15)	0.0000(12)	0.0015(11)	-0.0124(12)
O3	0.0184(15)	0.0275(15)	0.0377(17)	-0.0088(12)	0.0019(11)	-0.0094(11)
O4	0.0183(15)	0.0241(15)	0.0465(18)	0.0057(13)	-0.0013(12)	-0.0054(11)
F1	0.0315(15)	0.0449(16)	0.070(2)	-0.0303(14)	0.0044(13)	-0.0162(12)
F2	0.0362(16)	0.0418(16)	0.0604(19)	0.0245(13)	-0.0007(12)	-0.0115(12)
N1	0.022(2)	0.0242(19)	0.0293(19)	-0.0028(15)	-0.0004(15)	-0.0074(15)
C1	0.033(3)	0.028(2)	0.023(2)	0.0004(17)	0.0026(17)	-0.0070(18)
N2	0.026(2)	0.0240(18)	0.028(2)	0.0005(15)	0.0002(15)	-0.0066(14)
C2	0.031(3)	0.026(2)	0.029(2)	-0.0028(17)	-0.0005(19)	-0.0085(18)

Table 6.4: $(C_6H_{14}N_2)\{Zn[ZnB_2P_4O_{15}(OH)_2] \cdot (C_6H_{13}N_2)Cl\}$ (**zndabcocl**): anisotropic displacement parameters U_{ij} [$10^{-4}pm^2$], e.s.d.'s are given in parentheses.

Atom	U_{11}	U_{22}	U_{33}	U_{23}	U_{13}	U_{12}
Zn1	0.0146(3)	0.0163(3)	0.0177(3)	-0.0007(2)	-0.0005(2)	0.0011(2)
Zn2	0.0122(3)	0.0139(3)	0.0161(2)	-0.0005(2)	0.0014(2)	0.0005(2)
Cl1	0.0369(8)	0.0405(8)	0.0192(6)	-0.0018(5)	0.0106(5)	0.0010(6)
P1	0.0148(6)	0.0124(6)	0.0179(6)	-0.0019(4)	0.0021(5)	-0.0029(4)
P2	0.0161(6)	0.0128(6)	0.0193(6)	0.0024(4)	0.0022(5)	-0.0017(4)
P3	0.0143(6)	0.0115(6)	0.0223(6)	-0.0030(5)	0.0031(5)	0.0009(4)
P4	0.0216(7)	0.0197(7)	0.0207(6)	-0.0052(5)	0.0093(5)	-0.0064(5)
B1	0.011(2)	0.014(3)	0.015(2)	-0.0013(18)	0.0006(19)	0.0007(18)
B2	0.024(3)	0.008(2)	0.025(3)	0.001(2)	-0.002(2)	-0.001(2)
O1	0.0242(19)	0.0228(19)	0.0154(16)	-0.0029(13)	0.0046(14)	-0.0091(14)
O2	0.0125(17)	0.0120(17)	0.037(2)	-0.0017(14)	0.0044(15)	0.0019(12)
O3	0.0161(18)	0.0119(17)	0.043(2)	0.0088(15)	-0.0026(16)	-0.0006(13)
O4	0.0153(18)	0.021(2)	0.046(2)	0.0013(16)	-0.0045(17)	-0.0054(14)
O5	0.0180(18)	0.033(2)	0.0129(15)	0.0042(14)	0.0003(13)	-0.0028(15)
O6	0.0149(17)	0.0169(17)	0.0168(16)	0.0007(12)	-0.0036(13)	0.0034(13)
O7	0.0127(17)	0.0119(17)	0.0330(19)	0.0021(14)	0.0001(14)	-0.0005(12)
O8	0.0170(18)	0.0123(16)	0.0286(18)	0.0080(14)	0.0019(15)	0.0000(13)
O9	0.0142(18)	0.0201(19)	0.040(2)	-0.0111(16)	0.0002(16)	0.0000(14)
O10	0.042(2)	0.0198(19)	0.0204(18)	-0.0015(14)	-0.0023(17)	0.0011(16)
O11	0.047(3)	0.017(2)	0.0254(19)	0.0019(16)	0.0033(18)	0.0014(19)
O12	0.039(2)	0.0159(19)	0.045(2)	-0.0002(17)	0.023(2)	0.0061(16)
O13	0.0223(19)	0.0185(18)	0.032(2)	-0.0002(15)	0.0079(16)	0.0076(15)
O14	0.027(2)	0.025(2)	0.0236(18)	0.0031(15)	0.0078(16)	-0.0090(16)
O15	0.030(2)	0.0114(19)	0.099(4)	0.011(2)	-0.019(3)	-0.0059(16)
O16	0.106(5)	0.030(3)	0.048(3)	-0.019(2)	0.055(3)	-0.027(3)
O17	0.060(3)	0.041(3)	0.029(2)	-0.0167(18)	0.027(2)	-0.027(2)
N1	0.036(3)	0.019(2)	0.035(3)	-0.009(2)	-0.003(2)	0.004(2)
N2	0.027(3)	0.017(2)	0.033(2)	-0.0094(18)	0.007(2)	0.0013(18)
N3	0.016(2)	0.031(3)	0.024(2)	-0.0025(19)	-0.0045(18)	0.0009(19)
N4	0.0136(19)	0.016(2)	0.0183(19)	0.0002(16)	-0.0021(15)	0.0008(16)
C1	0.028(3)	0.043(4)	0.036(3)	-0.008(3)	-0.001(3)	0.013(3)
C2	0.044(4)	0.037(4)	0.036(3)	-0.005(3)	0.027(3)	0.000(3)
C3	0.025(3)	0.051(4)	0.046(4)	-0.015(3)	0.011(3)	-0.005(3)
C4	0.045(4)	0.027(3)	0.050(4)	0.002(3)	0.014(3)	-0.005(3)
C5	0.056(5)	0.027(3)	0.036(3)	0.008(3)	-0.002(3)	0.009(3)
C6	0.054(5)	0.040(4)	0.031(3)	-0.004(3)	-0.009(3)	0.010(3)
C7	0.036(4)	0.086(6)	0.059(5)	-0.050(5)	-0.027(4)	0.030(4)
C8	0.036(4)	0.092(7)	0.042(4)	-0.033(4)	-0.017(3)	0.024(4)
C9	0.059(5)	0.028(4)	0.123(9)	0.029(4)	-0.067(6)	-0.012(4)
C10	0.080(7)	0.032(5)	0.131(9)	0.021(5)	-0.082(7)	-0.007(4)
C11	0.019(3)	0.175(11)	0.030(4)	0.031(5)	-0.006(3)	-0.025(5)
C12	0.020(4)	0.201(13)	0.036(4)	0.034(6)	-0.002(3)	-0.017(6)

Table 6.5: $(C_3H_{12}N_2)\{Mn[B_2P_3O_{12}(OH)]\}$ (**DAP-Mn**): anisotropic displacement parameters U_{ij} $[10^{-4}pm^2]$, e.s.d.'s are given in parentheses.

Atom	U_{11}	U_{22}	U_{33}	U_{23}	U_{13}	U_{12}
Mn1	0.00874(17)	0.01366(19)	0.01264(18)	0.00286(17)	0.000	0.000
Mn2	0.01045(18)	0.01033(17)	0.01087(17)	-0.00023(15)	0.000	0.000
P1	0.0107(3)	0.0098(3)	0.0105(3)	-0.0018(2)	0.000	0.000
P2	0.0121(3)	0.0120(3)	0.0118(3)	0.0043(3)	0.000	0.000
P3	0.0127(3)	0.0090(3)	0.0105(3)	0.0013(2)	0.000	0.000
P4	0.00617(17)	0.01126(19)	0.01008(17)	-0.00037(18)	-0.00015(17)	-0.00
P5	0.0128(3)	0.0113(3)	0.0124(3)	-0.0032(3)	0.000	0.000
B1	0.0095(8)	0.0095(8)	0.0104(8)	-0.0005(7)	-0.0007(7)	0.0004(7)
B2	0.0088(8)	0.0109(8)	0.0105(8)	0.0017(7)	-0.0004(7)	-0.0004(7)
O1	0.0096(6)	0.0177(7)	0.0155(6)	0.0032(6)	0.0019(6)	-0.0027(5)
O2	0.0091(6)	0.0116(6)	0.0158(6)	-0.0013(5)	0.0026(5)	-0.0009(5)
O3	0.0084(8)	0.0118(9)	0.0101(8)	0.0000(8)	0.000	0.000
O4	0.0113(6)	0.0143(6)	0.0126(6)	-0.0034(5)	0.0017(5)	-0.0019(5)
O5	0.0108(6)	0.0129(6)	0.0159(6)	-0.0057(5)	0.0004(5)	0.0008(5)
O6	0.0318(12)	0.0170(10)	0.0129(10)	0.0016(9)	0.000	0.000
O7	0.0065(8)	0.0128(9)	0.0086(9)	0.0002(7)	0.000	0.000
O8	0.0113(6)	0.0181(7)	0.0131(7)	-0.0009(5)	-0.0037(5)	0.0000(5)
O9	0.0086(6)	0.0115(6)	0.0162(7)	0.0005(5)	-0.0034(5)	-0.0003(5)
O10	0.0102(6)	0.0136(6)	0.0163(6)	0.0025(5)	-0.0036(5)	-0.0005(5)
O11	0.0410(14)	0.0185(11)	0.0144(10)	-0.0031(9)	0.000	0.000
O12	0.0211(11)	0.0124(9)	0.0189(11)	-0.0038(8)	0.000	0.000
O13	0.0179(10)	0.0130(9)	0.0143(9)	0.0010(8)	0.000	0.000
O14	0.0114(6)	0.0230(8)	0.0156(7)	0.0097(6)	-0.0006(5)	-0.0023(5)
O15	0.0238(11)	0.0130(9)	0.0115(9)	-0.0008(8)	0.000	0.000
O16	0.0281(12)	0.0140(10)	0.0194(11)	0.0017(9)	0.000	0.000
O17	0.0222(11)	0.0139(10)	0.0153(10)	0.0067(8)	0.000	0.000
O18	0.0275(12)	0.0164(10)	0.0209(12)	-0.0099(9)	0.000	0.000
N1	0.0212(10)	0.0257(10)	0.0178(9)	0.0007(8)	-0.0031(8)	0.0006(8)
N2	0.0261(11)	0.0232(10)	0.0232(10)	-0.0007(8)	-0.0043(8)	0.0009(8)
C1	0.0320(13)	0.0251(12)	0.0238(12)	-0.0037(10)	0.0025(10)	-0.0069(11)
C2	0.0260(13)	0.0247(11)	0.0353(14)	0.0056(11)	0.0040(11)	0.0015(9)
C3	0.0373(15)	0.0311(14)	0.0239(13)	0.0027(10)	0.0032(10)	0.0104(12)

Table 6.6: $(C_4H_{12}N_2)\{Mn[B_2P_3O_{12}(OH)]\}$ (**PIP-Mn**): anisotropic displacement parameters U_{ij} $[10^{-4}pm^2]$, e.s.d.'s are given in parentheses.

Atom	U_{11}	U_{22}	U_{33}	U_{23}	U_{13}	U_{12}
Mn1	0.0090(3)	0.0087(2)	0.0099(2)	0.0005(2)	0.000	0.000
P1	0.0067(4)	0.0098(4)	0.0091(4)	0.000	0.000	-0.0001(3)
P2	0.0103(5)	0.0085(4)	0.0097(4)	0.0020(3)	0.000	0.000
P3	0.0116(4)	0.0106(4)	0.0114(4)	-0.0037(4)	0.000	0.000
B1	0.0099(14)	0.0085(11)	0.0108(11)	-0.0017(10)	0.0002(10)	-0.0004(10)
O1	0.0088(9)	0.0166(8)	0.0148(10)	0.0025(8)	-0.0011(8)	0.0003(7)
O2	0.0096(9)	0.0095(8)	0.0139(9)	-0.0004(7)	-0.0017(7)	-0.0007(7)
O3	0.0081(9)	0.0126(8)	0.0142(8)	0.0029(7)	0.0033(7)	0.0017(7)
O4	0.0194(14)	0.0172(13)	0.0182(13)	0.0125(12)	0.000	0.000
O5	0.0146(14)	0.0120(13)	0.0167(13)	0.0021(11)	0.000	0.000
O6	0.0324(18)	0.0142(12)	0.0130(12)	-0.0025(13)	0.000	0.000
O7	0.0095(10)	0.0177(9)	0.0190(9)	-0.0096(8)	0.0009(7)	0.0004(7)
O8	0.0208(15)	0.0109(12)	0.0139(13)	-0.0035(11)	0.000	0.000
O9	0.0061(12)	0.0094(12)	0.0076(12)	0.0006(9)	0.000	0.000
N1	0.0177(13)	0.0131(11)	0.0279(12)	0.0010(9)	0.0025(12)	-0.0004(11)
C1	0.040(2)	0.0279(16)	0.0176(14)	-0.0015(13)	-0.0121(14)	-0.0116(16)
C2	0.043(2)	0.0304(17)	0.0224(16)	0.0012(13)	0.0097(15)	-0.0064(17)

Table 6.7: $(C_3H_{12}N_2)(H_2O)_4[Fe^{III}_6B_4P_8O_{32}(OH)_8]$: anisotropic displacement parameters U_{ij} $[10^{-4}pm^2]$, e.s.d.'s are given in parentheses.

Atom	U_{11}	U_{22}	U_{33}	U_{23}	U_{13}	U_{12}
Fe1	0.0092(3)	0.0069(2)	0.0090(2)	-0.00058(17)	0.0043(2)	0.00011(18)
Fe2	0.0064(4)	0.0086(3)	0.0076(3)	-0.0003(2)	0.0025(3)	0.0001(2)
P1	0.0081(5)	0.0062(4)	0.0083(4)	0.0002(3)	0.0032(4)	0.0001(3)
P2	0.0080(5)	0.0081(4)	0.0078(4)	-0.0014(3)	0.0041(4)	-0.0007(3)
B1	0.009(2)	0.0057(15)	0.0068(17)	-0.0024(12)	0.0034(17)	-0.0007(13)
O1	0.0214(16)	0.0064(11)	0.0119(12)	-0.0002(9)	0.0097(12)	-0.0019(10)
O2	0.0123(15)	0.0076(11)	0.0087(12)	0.0003(9)	0.0012(12)	0.0028(9)
O3	0.0093(14)	0.0113(11)	0.0140(13)	-0.0020(10)	0.0071(12)	-0.0020(9)
O4	0.0090(14)	0.0120(11)	0.0136(13)	0.0049(10)	0.0054(12)	0.0021(9)
O5	0.0155(15)	0.0082(11)	0.0159(13)	-0.0009(9)	0.0100(12)	0.0013(10)
O6	0.0096(15)	0.0161(13)	0.0131(13)	0.0050(10)	0.0054(13)	0.0005(10)
O7	0.0077(14)	0.0116(11)	0.0132(13)	0.0011(9)	0.0031(12)	-0.0029(9)
O8	0.0142(15)	0.0115(12)	0.0113(12)	-0.0021(9)	0.0076(12)	-0.0036(10)
O9	0.0201(17)	0.0180(13)	0.0138(13)	-0.0068(10)	0.0096(13)	-0.0010(11)
O10	0.0103(15)	0.0180(13)	0.0156(14)	0.0037(10)	0.0051(13)	0.0052(10)
O11	0.0143(18)	0.0261(16)	0.0211(16)	0.0046(13)	0.0069(15)	0.0058(13)

<u>Table 6.8</u>: $(C_3H_{12}N_2)_2[V^{III}_2V^{IV}_3B_2P_8O_{38}H_8]$ (**dapvbpo**): anisotropic displacement parameters U_{ij} $[10^{-4}pm^2]$ of the framework atoms, e.s.d.'s are given in parentheses.

Atom	U_{11}	U_{22}	U_{33}	U_{23}	U_{13}	U_{12}
V1	0.0155(9)	0.0152(9)	0.0148(9)	-0.0005(7)	-0.0006(7)	-0.0005(7)
V2	0.0287(16)	0.0216(14)	0.0149(13)	0.000	0.000	0.0071(12)
V3	0.0168(16)	0.0269(19)	0.0165(15)	0.000	0.000	-0.0009(14)
V32	0.0168(16)	0.0269(19)	0.0165(15)	0.000	0.000	-0.0009(14)
V4	0.0155(16)	0.037(5)	0.0146(14)	0.000	0.000	0.007(3)
V42	0.0155(16)	0.037(5)	0.0146(14)	0.000	0.000	0.007(3)
P1	0.0165(14)	0.0182(14)	0.0119(12)	0.0000(10)	0.0011(10)	-0.0005(11)
P2	0.0147(14)	0.0230(15)	0.0165(14)	-0.0042(11)	-0.0008(11)	0.0042(11)
P3	0.0173(14)	0.0232(15)	0.0169(13)	-0.0003(12)	0.0031(11)	0.0006(11)
P4	0.0193(14)	0.0166(14)	0.0211(14)	0.0000(11)	0.0016(12)	-0.0003(11)
B1	0.022(7)	0.028(7)	0.026(7)	0.011(6)	0.000(6)	-0.006(5)
O1	0.022(4)	0.027(4)	0.015(4)	0.003(3)	-0.002(3)	-0.003(3)
O2	0.043(6)	0.008(4)	0.029(5)	0.006(3)	0.010(4)	0.001(4)
O3	0.017(4)	0.031(5)	0.021(4)	-0.002(4)	-0.001(3)	-0.005(3)
O4	0.021(4)	0.040(6)	0.027(5)	-0.005(4)	-0.009(4)	0.010(4)
O5	0.018(4)	0.030(5)	0.014(4)	-0.001(3)	0.003(3)	-0.005(3)
O6	0.043(6)	0.018(4)	0.027(5)	-0.005(4)	0.008(4)	0.006(4)
O7	0.022(4)	0.019(4)	0.027(4)	0.005(4)	0.002(4)	-0.004(3)
O8	0.036(5)	0.031(5)	0.029(5)	0.003(4)	0.015(4)	0.003(4)
O9	0.021(4)	0.023(4)	0.025(4)	0.007(4)	-0.009(4)	0.000(3)
O10	0.016(4)	0.041(6)	0.035(5)	-0.005(4)	0.004(4)	-0.002(4)
O11	0.027(5)	0.038(5)	0.016(4)	-0.001(4)	0.001(4)	0.009(4)
O12	0.024(4)	0.030(5)	0.016(4)	0.001(4)	0.003(3)	-0.004(4)
O13	0.036(8)	0.041(8)	0.019(6)	0.000	0.000	0.010(6)
O14	0.030(5)	0.033(5)	0.044(6)	-0.003(5)	0.015(5)	-0.008(4)
O15	0.018(4)	0.039(5)	0.020(4)	-0.008(4)	-0.006(3)	0.004(4)
O16	0.044(6)	0.028(5)	0.044(6)	0.013(5)	0.008(5)	0.009(4)
O17	0.022(6)	0.041(7)	0.013(5)	0.000	0.000	-0.008(6)
O18	0.019(4)	0.026(5)	0.048(6)	0.001(4)	0.004(4)	0.004(4)
O19	0.050(6)	0.046(6)	0.014(4)	-0.008(4)	-0.003(4)	0.014(5)
O20	0.031(7)	0.027(7)	0.037(8)	0.000	0.000	-0.001(6)
O21	0.036(8)	0.029(8)	0.069(12)	0.000	0.000	-0.014(7)

Table 6.9: $K_3[B_5PO_{10}(OH)_3]$: anisotropic displacement parameters U_{ij} $[10^{-4}pm^2]$,
e.s.d.'s are given in parentheses.

Atom	U_{11}	U_{22}	U_{33}	U_{23}	U_{13}	U_{12}
K1	0.02018(19)	0.01280(17)	0.0261(2)	0.00048(15)	0.00510(16)	-0.00136(14)
K2	0.0227(2)	0.0204(2)	0.01674(19)	0.00348(15)	0.00194(15)	-0.00098(15)
K3	0.02041(19)	0.0281(2)	0.01583(19)	-0.00414(16)	0.00281(15)	0.00053(16)
P1	0.00991(18)	0.00756(18)	0.0125(2)	-0.00023(15)	0.00191(15)	0.00027(14)
B1	0.0093(7)	0.0090(8)	0.0126(8)	0.0008(6)	0.0007(6)	0.0011(6)
B2	0.0100(7)	0.0107(8)	0.0111(8)	-0.0004(6)	0.0034(6)	-0.0003(6)
B3	0.0100(7)	0.0091(8)	0.0130(8)	0.0001(6)	0.0014(7)	-0.0013(6)
B4	0.0125(8)	0.0113(8)	0.0146(9)	-0.0022(7)	0.0024(7)	-0.0020(6)
B5	0.0120(8)	0.0115(8)	0.0119(8)	0.0019(7)	0.0006(6)	0.0006(6)
O1	0.0127(5)	0.0135(6)	0.0152(6)	-0.0043(5)	0.0043(5)	-0.0055(5)
O2	0.0123(5)	0.0119(5)	0.0155(6)	0.0037(5)	0.0050(5)	0.0032(4)
O3	0.0103(5)	0.0153(6)	0.0143(6)	-0.0053(5)	0.0037(4)	-0.0039(4)
O4	0.0164(6)	0.0163(6)	0.0112(6)	-0.0024(5)	0.0038(5)	-0.0061(5)
O5	0.0255(7)	0.0335(8)	0.0211(7)	-0.0152(6)	0.0123(6)	-0.0162(6)
O6	0.0138(5)	0.0098(5)	0.0132(5)	0.0014(4)	-0.0011(4)	-0.0015(4)
O7	0.0133(6)	0.0100(5)	0.0174(6)	-0.0023(5)	-0.0029(5)	0.0031(4)
O8	0.0135(6)	0.0164(6)	0.0108(5)	0.0023(5)	0.0031(4)	0.0050(5)
O9	0.0098(5)	0.0153(6)	0.0111(5)	0.0023(5)	0.0023(4)	0.0024(4)
O10	0.0305(8)	0.0227(7)	0.0190(7)	-0.0109(6)	0.0115(6)	-0.0128(6)
O11	0.0217(6)	0.0106(6)	0.0215(6)	0.0016(5)	0.0046(5)	-0.0030(5)
O12	0.0197(6)	0.0189(6)	0.0226(7)	-0.0048(5)	0.0103(5)	-0.0002(5)
O13	0.0088(5)	0.0078(6)	0.0247(7)	0.0026(5)	-0.0014(5)	-0.0005(5)

References

[1] H. S. van Klooster. Über das Verhalten der Metabor- und der Metaphosphorsäure in den Schmelzen ihrer Alkalisalze. *Z. Anorg. Allg. Chem.* **1911**, *69*, 122–134.

[2] G. E. R. Schulze. Die Kristallstruktur von BPO_4 und $BAsO_4$. *Z. Phys. Chem. Abt. B* **1934**, *24*, 215–240.

[3] J. D. Mackenzie, W. L. Roth, R. H. Wentorf. New high pressure modifications of BPO_4 and $BAsO_4$. *Acta Crystallogr.* **1959**, *12*, 79.

[4] F. Dachille, L. S. Dent Glasser. High pressure forms of BPO_4 and $BAsO_4$; quartz analogues. *Acta Crystallogr.* **1959**, *12*, 820–821.

[5] *Gmelin Handbuch der Anorganischen Chemie* Band 19 von *Borverbindungen.* Springer Heidelberg, New York Ergänzungswerk zur 8. Auflage **1975**.

[6] G. J. Hutchings, I. D. Hudson, D. Bethell, D. C. Timms. Dehydration of 2-methylbutanal and methyl isopropyl ketone to isoprene using boron and aluminum phosphate catalysts. *J. Catal.* **1999**, *188*, 291–299.

[7] S. Gao, J. B. Moffat. The Isomerization of 1-Butene on Stoichiometric and Nonstoichiometric Boron Phosphate: The Dependence of the Acidity on Stoichiometry. *J. Catal.* **1998**, *180*, 142–148.

[8] J. X. Mi, S. Y. Mao, Z. H. Chen, Z. L. Huang, J. T. Zhao. Synthesis and Structures of new Borophosphates $(B_{1-x}M_x)PO_4$ (M = Mn, Fe, Co, Ni, Cu) with Orthorhombic Low-Cristobalite Type. *Chin. Chem. Lett.* **1999**, *10*, 707–708.

[9] A. K. Cheetham, G. Férey, T. Loiseau. Open-Framework Inorganic Materials. *Angew. Chem. Int. Ed.* **1999**, *38*, 3268–3292. *Angew. Chem.* **1999**, *111*, 3466–3492.

[10] B. C. Gates. *Catalytic Materials.* Advances in Chemistry Series 245. American Chemical Society Washington, DC **1995**.

[11] D. W. Breck. *Zeolite Molecular Sieves*. John Wiley & Sons New York **1974**.

[12] S. T. Wilson, B. M. Lok, C. A. Messina, T. R. Cannan, E. M. Flanigen. Aluminophosphate Molecular-Sieves - A New Class of Microporous Crystalline Inorganic Solids. *J. Am. Chem. Soc.* **1982**, *104*, 1146–1147.

[13] E. M. Flanigen, B. M. Lok, R. L. Patton, S. T. Wilson. Aluminophosphate Molecular-Sieves and The Periodic-Table. *Pure Appl. Chem.* **1986**, *58*, 1351–1358.

[14] P. Feng, X. Bu, , G. D. Stucky. Hydrothermal syntheses and structural characterization of zeolite analogue compounds based on cobalt phosphate. *Nature* **1997**, *388*, 735–741.

[15] M. Hartmann, L. Kevan. Transition-metal ions in aluminophosphate and silicoaluminophosphate molecular sieves: Location, interaction with adsorbates and catalytic properties. *Chem. Rev.* **1999**, *3*, 636–663.

[16] M. Estermann, L. B. McCusker, C. Baerlocher, A. Merrouche, H. Kessler. A Synthetic Gallophosphate Molecular-Sieve with a 20-Tetrahedral-Atom Pore Opening. *Nature* **1991**, *352*, 320–323.

[17] T. Loiseau, G. Férey. Oxyfluorinated Microporous Compounds VII. Synthesis and Crystal-Structure and ULM-5, A New Fluorinated Gallophosphate $GA_{16}(PO_4)_{14}(HPO_4)_2(OH)_2F_7 \cdot [H_3N(CH_2)_6NH_3]_4 \cdot 6H_2O$ with 16-Membered Rings and Both Bonding and Encapsulated F^-. *J. Solid State Chem.* **1994**, *111*, 403–415.

[18] S. B. Harmon, S. C. Sevov. Synthesis and characterization of a new three-dimensional organically templated zinc phosphate, $Zn_6(PO_4)_4(HPO_4)(H_2O)(H_3NCH_2CH_2NH_3)$, with a chain of corner-linked ZnO_4 tetrahedra. *Chem. Mater.* **1998**, *10*, 3020–3023.

[19] W. T. A. Harrison, L. Hannooman. $N(CH_3)_4 \cdot ZnH_3(PO_4)_2$: A large-pore zincophosphate built up from a 12-ring architecture with a remarkably low tetrahedral-framework-atom density. *Angew. Chem. Int. Ed. Engl.* **1997**, *36*, 640–641. *Angew. Chem.* **1997**, *109*, 663–665.

[20] F. Liebau. *Structural Chemistry of Silicates*. Springer Berlin **1985**.

[21] K. Fischer. The Crystal Structure Determination of the Zeolite Gismondite, $CaAl_2Si_2O_8 \cdot 4H_2O$. *Am. Mineral.* **1963**, *48*, 664–672.

[22] G. Artioli, R. Rinaldi, Å. Kvick, J. V. Smith. Neutron diffraction structure refinement of the zeolite gismondine at 15 K **1986**, *6*, 361–366.

[23] R. Kniep, G. Schäfer, H. Engelhardt, I. Boy. $K[ZnBP_2O_8]$ and $A[ZnBP_2O_8]$ (A = NH_4^+, Rb^+, Cs^+): Zincoborophosphates as a New Class of Compounds with Tetrahedral Framework Structures. *Angew. Chem. Int. Ed.* **1999**, *38*, 3642–3644. *Angew. Chem.* **1999**, *111*, 3858–3861.

[24] R. Kniep, G. Schäfer, H. Borrmann. Crystal structure of ammonium [mono-zinco-monoboro-diphosphate], $NH_4[ZnBP_2O_8]$. *Z. Kristallogr. NCS* **2000**, *215*, 335–336.

[25] W. M. Meier, D. H. Olson, Ch. Baerlocher. *Atlas of Zeolite Structure Types*. Elsevier London, 4th Revised Edition **1996**. update: Ch. Baerlocher, L. B. McCusker. http://www.iza-structure.org/databases.

[26] P. Becker. Borate Materials in Nonlinear Optics. *Adv. Mater.* **1998**, *10*, 979–992.

[27] S. Pan, Y. Wu, P. Fu, G. Zhang, Z. Li, C. Du, C. Chen. Growth, Structure, and Properties of Single Crystals of $SrBPO_5$. *Chem. Mater.* **2003**, *15*, 2218–2221.

[28] Y. Wu, G. Wang, P. Fu, X. Liang, Z. Xu, C. Chen. A new nonlinear optical crystal β-Zn_3BPO_7. *J. Cryst. Growth* **2001**, *229*, 205–207.

[29] G. Wang, Y. Wu, H. Liu, P. Fu, S. Pan, G. Zhang, C. Chen. Crystal growth of magnesium zinc borophosphate. *Chem. Lett.* **2002**, *6*, 620–621.

[30] C. Hauf, T. Friedrich, R. Kniep. Crystal structure of pentasodium *catena*-(diborato-triphosphate), $Na_5[B_2P_3O_{13}]$. *Z. Kristallogr.* **1995**, *210*, 446.

[31] C. Hauf. *Borophosphate der Alkalimetalle: Intermediäre Phasen in den Systemen $M_2O–B_2O_3–P_2O_5–H_2O$*. Dissertation, Technische Hochschule Darmstadt **1997**.

[32] J.-X. Mi, J.-T. Zhao, S.-Y. Mao, Y.-X. Huang, H. Engelhardt, R. Kniep. Crystal structure of dichromium monoborotriphosphate, $Cr_2[BP_3O_{12}]$. *Z. Kristallogr. NCS* **2000**, *215*, 201–202.

[33] J.-T. Zhao. Personal communication.

[34] R. Kniep, G. Gözel, B. Eisenmann, C. Röhr, M. Asbrand, M. Kizilyalli. Borophosphates – A Neglected Class of Compounds: Crystal Structures of $M^{II}[BPO_5]$ (M^{II} = Ca, Sr) and $Ba_3[BP_3O_{12}]$. *Angew. Chem. Int. Ed. Engl.* **1994**, *33*, 749–751. *Angew. Chem.* **1994**, *106*, 791–793.

[35] Y. Shi, J. Liang, H. Zhang, Q. Liu, X. Chen, J. Yang, W. Zhuang, G. Rao. Crystal Structure and Thermal Decomposition Studies of Barium Borophosphate, $BaBPO_5$. *J. Solid State Chem.* **1998**, *135*, 43–51.

[36] P. Tarte, U. de Wispelaere-Schröder. Synthese et caracterisation dún borophos-phate et dún boroarséniate de plomb, $PbBPO_5$ et $PbBAsO_5$. *C. R. Acad. Sc. Paris Série II* **1982**, *t. 295*, 351–354.

[37] H. B. Liang, Q. Su, Y. Tao, T. D. Hu, T. Liu, S. L. E. Shulin. XAFS at Eu-L-3 edge and UV-VUV excited luminescence of europium doped strontium borophos-phate prepared in air. *J. Phys. Chem. Solids* **2002**, *63*, 719–724.

[38] R. Ternane, M. Th. Cohen-Adad, G. Panczer, C. Goutaudier, C. Dujardin, G. Boulon, N. Kbir-Ariguib, M. Trabelsi-Ayedi. Structural and luminescent prop-erties of new Ce^{3+} doped calcium borophosphate with apatite structure. *Solid State Sci.* **2002**, *4*, 53–59.

[39] S. J. Ding, W. Zhang, B. O. Xu, J. T. Wang. Spectra of Ce^{3+}, Tb^{3+} and Gd^{3+} ions in Ln (BO_3, PO_4) [Ln = La, Y]. *Spectrosc. Spect. Anal.* **2001**, *21*, 275–278.

[40] D. Koch. *Untersuchungen zur Darstellung und Strukturchemie von Borophophaten sowie zur Beschichtung von metallischen Substraten in Metallborat-Metallphosphat-Lösungen.* Dissertation, Technische Universität Darmstadt **2002**.

[41] M. Zhou, K. Li, D. Shu, B. D. Sun, J. Wang. Corrosion resistance properties of enamels with high B_2O_3–P_2O_5 content to molten aluminum. *Mater. Sci. Engin.* **2003**, *A346*, 116–121.

[42] A. Rabenau. The Role of Hydrothermal Synthesis in Preparative Chemistry. *Angew. Chem. Int. Ed. Engl* **1985**, *24*, 1026–1040. *Angew. Chem.* **1995**, *97*, 1017–1032.

[43] P. K. S. Gupta, G. H. Swihart, C. B. Slawson. The crystal structure of lünebur-gite, $Mg_3(H_2O)_6[B_2(OH)_6(PO_4)_2]$. *Am. Mineral.* **1991**, *76*, 1400–1407.

[44] P. B. Moore, S. Ghose. A Novel Face-Sharing Octahedral Trimer in the Crystal Structure of Seamanite. *Am. Mineral.* **1971**, *56*, 1527–1538.

[45] I. Boy. *Zur Kristallchemie intermediärer Phasen der Systeme $M_2O/MO/M_2O_3$–B_2O_3–P_2O_5–H_2O.* Dissertation, Technische Universität Darmstadt **1999**.

[46] H. Engelhardt. *Darstellung und Strukturchemie von quarternären Borophosphaten der schweren Alkalimetalle (Rb, Cs)*. Dissertation, Technische Universität Darmstadt **2000**.

[47] G. Schäfer. *Templatgesteuerte Synthesen von Borophosphaten.* Dissertation, Technische Universität Darmstadt **2001**.

[48] R. Kniep, H. Engelhardt, C. Hauf. A First Approach to Borophosphate Structural Chemistry. *Chem. Mater.* **1998**, *10*, 2930–2934.

[49] C. Hauf, I. Boy, R. Kniep. Crystal structure of dimagnesium (monohydrogen-monophosphate-dihydrogenmonoborate-monophosphate), $Mg_2[BP_2O_7(OH)_3]$. *Z. Kristallogr. NCS* **1999**, *214*, 3–4.

[50] K. Bluhm, C. H. Park. Die Synthese und Kristallstruktur des Borat-Phosphats α-$Zn_3(BO_3)(PO_4)$. *Z. Naturforsch.* **1997**, *52b*, 102–106.

[51] A. Yilmaz, X. Bu, M. Kizilyalli, R. Kniep, G. D. Stucky. Cobalt Borate Phosphate, $Co_3[BPO_7]$, Synthesis and Characterization. *J. Solid State Chem.* **2001**, *156*, 281–285.

[52] Y. Shi, J. Liang, Y. Guo, J. Yang, W. Zhuang, G. Rao. Phase relations in the system La_2O_3–B_2O_3–P_2O_5. *J. Alloys Comp.* **1996**, *242*, 118–121.

[53] Y. Shi, J. Liang, H. Zhang, J. Yang, W. Zhuang, G. Rao. X-Ray Powder Diffraction and Vibrational Spectra Studies of Rare Earth Borophosphates, $Ln_7O_6(BO_3)(PO_4)_2$ (Ln = La, Nd, Gd, Dy). *J. Solid State Chem.* **1997**, *129*, 45–52.

[54] K. K. Palkina, S. I. Maksimova, N. T. Chibiskova, B. F. Dzhurinski, L. Z. Gokham. Synthesis and Structure of mixed Rare Earth Borophosphates, $Ln_7O_6(BO_3)(PO_4)_2$ (Ln = La–Dy). *Inorg. Mater.* **1984**, *20*, 919–923.

[55] R. P. Bontchev, S. C. Sevov. $Co_5BP_3O_{13}$: The First Borophosphate with Planar BO_3 Groups Connected to PO_4 Tetrahedra. *Inorg. Chem.* **1996**, *35*, 6910–6911.

[56] E. L. Belokoneva, E. A. Ruchkina, O. V. Dimitrova. Synthesis and crystal structure of the new lead borophosphate $Pb_2[BP_2O_8(OH)]$. *Russ. J. Inorg. Chem.* **2003**, *48*, 157–160.

[57] I. Boy, C. Cordier, B. Eisenmann, R. Kniep. Oligomere Tetraeder-Anionen in Borophosphaten: Darstellung und Kristallstrukturen von $NaFe[BP_2O_7(OH)_3]$ und $K_2Fe_2[B_2P_4O_{16}(OH)_2]$. *Z. Naturforsch.* **1998**, *53b*, 165–170.

[58] D. Koch, R. Kniep. Crystal structure of sodium aluminum (monohydrogenmono-phosphate-dihydrogenmonoborate-monophosphate), $NaAl[BP_2O_7(OH)_3]$. *Z. Kristallogr. NCS* **1999**, *214*, 441–442.

[59] Y.-X. Huang, S.-Y. Mao, J.-X. Mi, Z.-B. Wei, J.-T. Zhao, R. Kniep. Crystal structure of sodium gallium [monohydrogenmonophosphate-dihydrogenmonoborate-monophosphate], $NaGa[BP_2O_7(OH)_3]$. *Z. Kristallogr. NCS* **2001**, *216*, 15–16.

[60] Y.-X. Huang, J.-X. Mi, S.-Y. Mao, Z.-B. Wei, J.-T. Zhao, R. Kniep. Crystal structure of sodium indium (monohydrogenmonophosphate-dihydrogenmonoborate-monophosphate), $NaIn[BP_2O_7(OH)_3]$. *Z. Kristallogr. NCS* **2002**, *217*, 7–8.

[61] L.-R. Zhang, H. Zhang, H. Borrmann, R. Kniep. Crystal structure of sodium vanadium(III) (monohydrogenmonophosphate-dihydrogenmonoborate-monophosphate), $NaV[BP_2O_7(OH)_3]$. *Z. Kristallogr. NCS* **2002**, *217*, 477–478.

[62] J.-X. Mi, Y.-X. Huang, S.-Y. Mao, H. Borrmann, J.-T. Zhao, R. Kniep. Crystal structure of potassium gallium (monophosphate-hydrogenmonoborate-mono-phosphate), $KGa[BP_2O_7(OH)_3]$. *Z. Kristallogr. NCS* **2002**, *217*, 167–168.

[63] H. Engelhardt, H. Borrmann, W. Schnelle, R. Kniep. Das erste Vanadium(III)-Borophosphat: Darstellung und Kristallstruktur von $CsV_3(H_2O)_2[B_2P_4O_{16}(OH)_4]$. *Z. Anorg. Allg. Chem.* **2000**, *626*, 443–444.

[64] C. J. Warren, R. C. Haushalter, D. J. Rose, J. Zubieta. The first oxo-metallate borophosphate polyanion: hydrothermal synthesis and structure of $[H_3NCH_2CH_2NH_3]_2[Na(VO)_{10}\{O_3POB(O)_2OPO_3H\}_5] \cdot 22.5H_2O$. *Inorg. Chem. Commun.* **1998**, *1*, 4–6.

[65] C. J. Warren, R. C. Haushalter, D. J. Rose, J. Zubieta. Three-Dimensional Organic/Inorganic Composite Materials: Hydrothermal Synthesis and Structure Characterization of the Open-Framework Oxovanadium Borophosphate $[H_3NCH_2CH_2NH_3]_2[(VO)_5(H_2O)\{O_3POB(O)_2OPO_3H\}_2] \cdot 1.5H_2O$. *Chem. Mater.* **1997**, *9*, 2694–2696.

[66] R. P. Bontchev, J. Do, A. J. Jacobson. Templated Synthesis of Vanadium Boro-phosphate Cluster Anions. *Angew. Chem. Int. Ed.* **1999**, *38*, 1937–1940. *Angew. Chem.* **1999**, *111*, 2063–2066.

[67] Y. Zhao, G. Zhu, W. Liu, Y. Zou, W. Pang. Synthesis and structures of two new

12-member ring crown-shaped oxovanadium borophosphates. *Chem. Commun.* **1999**, *21*, 2219–2220.

[68] Y. Zhao, Z. Shi, S. Ding, N. Bai, W. Liu, Y. Zou, G. Zhu, P. Zhang, Z. Mai, W. Pang. Synthesis and Structure of 12-Member Ring Crown-Shaped Oxovanadium Borophosphate Polyanions: $[H_3NC_2H_4NH_2C_2H_4NH_2C_2H_4NH_3]_4H[M(VO)_{12}\{O_3POB(O)_2OPO_3\}_6] \cdot nH_2O$ (M = NH_4^+, K^+). *Chem. Mater.* **2000**, *12*, 2550–2556.

[69] J. Do, L.-M. Zheng, R. P. Bontchev, A. J. Jacobson. Synthesis, structure and magnetic properties of $(NH_4)_2(C_3H_{12}N_3)_8[V_2P_2BO_{12}]_6 \cdot 15H_2O$. *Solid State Sci.* **2000**, *2*, 343–351.

[70] J. Do, R. P. Bontchev, A. J. Jacobson. Influence of Hydrogen Bonding on the Assembly of Six-Membered Vanadium Borophosphate Cluster Anions: Synthesis and Structures of $(NH_4)_2(C_2H_{10}N_2)_6[Sr(H_2O)_5]_2[V_2P_2BO_{12}]_6 \cdot 10H_2O$, $(NH_4)_2(C_3H_{12}N_2)_6[Sr(H_2O)_4]_2[V_2P_2BO_{12}]_6 \cdot 17H_2O$, and $(NH_4)_3(C_4H_{14}N_2)_{4.5}[Sr(H_2O)_5]_2[Sr(H_2O)_4][V_2P_2BO_{12}]_6 \cdot 10H_2O$. *Inorg. Chem.* **2000**, *39*, 4305–4310.

[71] R. P. Bontchev, J. Do, A. J. Jacobson. The Vanadium(V) Borophosphate $(NH_4)_5[V_3BP_3O_{19}] \cdot H_2O$. *Inorg. Chem.* **2000**, *39*, 4179–4181.

[72] M. Asnani, A. Ramanan, J. J. Vittal. Hydrothermal synthesis and structural characterisation of a vanadium (V) borophosphate cluster containing solid: $[Co(en)_3][enH_2]V_3BP_3O_{19} \cdot 4.5H_2O$. *Inorg. Chem. Commun.* **2003**, *6*, 589–592.

[73] R. P. Bontchev, J. Do, A. J. Jacobson. Synthesis and Characterization of the Layered Vanadium Borophosphate $(Imidazolium)_{3.8}(H_3O)_{1.2}[(VO)_4(BO)_2(PO_4)_5] \cdot 0.3H_3O$. *Inorg. Chem.* **2000**, *39*, 3320–3324.

[74] R. P. Bontchev, J. Do, A. J. Jacobson. Synthesis and Characterisation of a Borophosphate Anion Containing a Single Vanadium Atom: $[N_2C_6H_{14}]_2$-$VO(PO_3OH)_4(B_3O_3OH) \cdot 4H_2O$. *Inorg. Chem.* **1999**, *38*, 2231–2233.

[75] E. Wikstad, M. Kritikos. $(C_6H_{14}N_2)_2[VO(HPO_4)_5B_2O] \cdot H_2O \cdot H_3PO_4$, a novel borophosphate cluster containing a single vanadium centre and linked by hydrogen bonds into a three-dimensional framework. *Acta Crystallogr.* **2003**, *C59*, 87–89.

[76] E. Dumas, C. Debiemme-Chouvy, S. C. Sevov. A reduced polyoxomolybdenum

borophosphate anion related to the Wells-Dawson clusters. *J. Am. Chem. Soc.* **2002**, *124*, 908–909.

[77] C. Sassoye, K. Norton, S. C. Sevov. $[Mo^V_5M^{VI}_7O_{30}(BPO_4)_2(O_3P\text{-}Ph)_6]^{5-}$: A Phenyl-Substituted Molybdenum(V/VI) Boro-Phosphate Polyoxometalate. *Inorg. Chem.* **2003**, *42*, 1652–1655.

[78] O. A. Gurbanova, E. L. Belokoneva, O. V. Dimitrova. Synthesis and crystal structure of new borophosphate $NaIn[BP_2O_8(OH)]$. *Russ. J. Inorg. Chem.* **2002**, *47*, 56–59.

[79] S.-Y. Mao, M.-R. Li, Y.-X. Huang, J.-X. Mi, Z.-B. Wei, J.-T. Zhao, R. Kniep. Crystal structure of potassium indium (monophosphate-hydrogenmonoborate-monophosphate), $KIn[BP_2O_8(OH)]$. *Z. Kristallogr. NCS* **2002**, *217*, 3–4.

[80] Y.-X. Huang, J.-T. Zhao, J.-X. Mi, H. Borrmann, R. Kniep. Crystal structure of rubidium indium (monophosphate-hydrogenmonoborate-monophosphate), $RbIn[BP_2O_8(OH)]$. *Z. Kristallogr. NCS* **2002**, *217*, 163–164.

[81] I. Boy, C. Cordier, R. Kniep. Crystal structure of tetrasodium tricopper(II) diboro-diphosphate-bis(monohydrogenphosphate) bis(monophosphate), $Na_4Cu_3[B_2P_4O_{15}(OH)_2] \cdot 2HPO_4$. *Z. Kristallogr. NCS* **1998**, *213*, 29–30.

[82] I. Boy, G. Schäfer, R. Kniep. $(Ni_{3-x}Mg_x)[B_3P_3O_{12}(OH)_6] \cdot 6H_2O$ ($x \approx 1.5$): A Novel Borophosphate-Hydrate Containing Isolated Six-Membered Rings of Tetrahedra. *Z. Anorg. Allg. Chem.* **2001**, *627*, 139–143.

[83] H.-Z. Shi, Y.-K. Shan, M.-Y. He, Y.-Y. Liu. Crystal structure of diaquamagnesium (dihydrogenmonoborate-monophosphate), $Mg[BPO_4(OH)_2](H_2O)_2$, containing isolated sixmembered rings of tetrahedra. *Z. Kristallogr. NCS* **2003**, *218*, 21–22.

[84] I. Boy, C. Cordier, R. Kniep. Oligomere Tetraeder-Anionen in Borophosphaten: Sechserringe mit offenen und cyclischen Phosphat-Verzweigungen in der Kristallstruktur von $K_6Cu_2[B_4P_8O_{28}(OH)_6]$. *Z. Naturforsch.* **1998**, *53b*, 1440–1444.

[85] D. Yu. Pushcharovsky, E. R. Gobetchia, M. Pasero, S. Merlino, O. V. Dimitrova. Hydrothermal synthesis and crystal structures of Li,Ba-nanoborate, $LiBaB_9O_{15}$, and Ba-borophosphate, $BaBPO_5$. *J. Alloys. Comp.* **2002**, *339*, 70–75.

[86] C. Hauf, R. Kniep. Crystal structure of lithium *catena*-(monoboro-mono-

dihydrogendiborate-monohydrogenphosphate), $Li[B_3PO_6(OH)_3]$. *Z. Kristallogr. NCS* **1997**, *212*, 313–314.

[87] C. Hauf, R. Kniep. Crystal structure of diammonium *catena*-(monoboro-mono-dihydrogendiborate monophosphate), $(NH_4)_2[B_3PO_7(OH)_3]$. *Z. Kristallogr.* **1996**, *211*, 705–706.

[88] C. Hauf, R. Kniep. Crystal structure of tripotassium *catena*-[triboro-monohydrogenphosphate bis(monohydrogenborate)], $K_3[B_5PO_{10}(OH)_3]$. *Z. Kristallogr.* **1996**, *211*, 707–708.

[89] I. Boy, R. Kniep. $K[B_6PO_{10}(OH)_4]$: Ein Borophosphat mit gestreckten Bändern aus Tetraeder-Vierer-Ringen und offen-zyklischen Verzweigungen über planare $B_2O_3(OH)_2$-Gruppen. *Z. Naturforsch.* **1999**, *54b*, 895–898.

[90] I. Boy, C. Hauf, R. Kniep. $Fe[B_2P_2O_7(OH)_5]$: Ein neues Borophosphat mit unverzweigten Vierer-Einfach Tetraederketten. *Z. Naturforsch.* **1998**, *53b*, 631–633.

[91] R. Kniep, D. Koch, H. Borrmann. Crystal structure of aluminum catena-[mono-hydrogenborate-dihydrogenborate- bis(monohydrogenphosphate)] monohydrate, $Al[B_2P_2O_7(OH)_5]\circ H_2O$. *Z. Kristallogr. NCS* **2002**, *217*, 187–188.

[92] R. Kniep, I. Boy, H. Engelhardt. $RbFe[BP_2O_8(OH)]$: Ein neues Borophosphat mit offen-verzweigten Vierer-Einfach-Tetraderketten. *Z. Anorg. Allg. Chem.* **1999**, *625*, 1512–1516.

[93] H. Engelhardt, R. Kniep. Crystal structure of caesium iron(III) *catena*-[mono-hydrogenmonoborate-bis(monophosphate)], $CsFe[BP_2O_8(OH)]$. *Z. Kristallogr. NCS* **1999**, *214*, 443–444.

[94] H. Engelhardt, H. Borrmann, R. Kniep. Crystal structure of ru-bidium vanadium(III) *catena*-[monohydrogenmonoborate-bis(monophosphate)], $RbV[BP_2O_8(OH)]$. *Z. Kristallogr. NCS* **2000**, *215*, 203–204.

[95] J.-X. Mi, J.-T. Zhao, Y.-X. Huang, J.-F. Deng, H. Borrmann, R. Kniep. Crystal structure of rubidium aluminum *catena*-[monohydrogen-monoborate-bis(monophosphate)], $RbAl[BP_2O_8(OH)]$. *Z. Kristallogr. NCS* **2002**, *217*, 171–172.

[96] M. Kritikos, E. Wikstad, K. Wallden. Hydrothermal synthesis, characteri-zation and magnetic properties of three isostructural chain borophosphates:

$NH_4M^{III}[BP_2O_8(OH)]$ with M = V or Fe and $NH_4(Fe^{III}_{0.53}V^{III}_{0.47})[BP_2O_8(OH)]$. *Solid State Sci.* **2001**, *3*, 649–658.

[97] J.-X. Mi, H. Borrmann, S.-Y. Mao, Y.-X. Huang, H. Zhang, J.-T. Zhao, R. Kniep. Crystal structure of rubidium gallium *catena*-[monohydrogen-mono-borate-bis(monophosphate)], $RbGa[BP_2O_8(OH)]$, from a twinned crystal. *Z. Kristallogr. NCS* **2003**, *218*, 17–18.

[98] J.-X. Mi, Y.-X. Huang, J.-F. Deng, H. Borrmann, J.-T. Zhao, R. Kniep. Crystal structure of caesium aluminum *catena*-[monohydrogen-monoborate-bis(mono-phosphate)], $CsAl[BP_2O_8(OH)]$. *Z. Kristallogr. NCS* **2002**, *217*, 169–170.

[99] J.-X. Mi, H. Borrmann, Y.-X. Huang, S.-Y. Mao, J.-T. Zhao, R. Kniep. Crystal structure of caesium gallium *catena*-[monohydrogen-monoborate-bis(mono-phosphate)], $CsGa[BP_2O_8(OH)]$. *Z. Kristallogr. NCS* **2003**, *218*, 171–172.

[100] Y.-X. Huang, G. Schäfer, W. Carrillo-Cabrera, R. Cardoso, W. Schnelle, R. Kniep. Open-framework borophosphates: $(NH_4)_{0.4}(Fe^{III}_{0.55}Fe^{II}_{0.5})(H_2O)_2[BP_2O_8] \cdot 0.6H_2O$ and $NH_4Fe^{III}[BP_2O_8(OH)]$. *Chem. Mater.* **2001**, *13*, 4348–4354.

[101] M.-R. Li, S.-Y. Mao, Y.-X. Huang, J.-X. Mi, Z.-B. Wei, J.-T. Zhao, R. Kniep. Crystal structure of ammonium gallium (monophosphate-hydrogenmonoborate-monophosphate), $(NH_4)Ga[BP_2O_8(OH)]$. *Z. Kristallogr. NCS* **2002**, *217*, 165–166.

[102] J.-X. Mi, Y.-X. Huang, J.-F. Deng, H. Borrmann, J.-T. Zhao, R. Kniep. Crystal structure of ammonium aluminum *catena*-[monohydrogen-monoborate-bis(mono-phosphate)], $(NH_4)Al[BP_2O_8(OH)]$. *Z. Kristallogr. NCS* **2002**, *217*, 305–306.

[103] G. Schäfer, H. Borrmann, R. Kniep. $M^{II}(C_4H_{12}N_2)[B_2P_3O_{12}(OH)]$ (M^{II} = Co, Zn): Synthesis and crystal structure of novel open framework borophosphates. *Z. Anorg. Allg. Chem.* **2001**, *627*, 61–67.

[104] R. P. Bontchev, A. J. Jacobson. Synthesis and characterization of the open-framework cobalt borophosphate: $(C_4N_2H_{12})Co[B_2P_3O_{12}(OH)]$. *Mater. Res. Bull.* **2002**, *37*, 1997–2002.

[105] G. Y. Yang, S. C. Sevov. $[Co(en)_3][B_2P_3O_{11}(OH)_2]$: A novel borophosphate templated by a transition-metal complex. *Inorg. Chem.* **2001**, *40*, 2214–2216.

[106] G. Schäfer, W. Carrillo-Cabrera, S. Leoni, H. Borrmann, R. Kniep. $Zn_3(C_6H_{14}N_2)_3[B_6P_{12}O_{39}(OH)_{12}] \cdot (C_6H_{14}N_2)[HPO_4]$: A chiral borophosphate – Triethylenediammonium hydrogenphosphate composite. *Z. Anorg. Allg. Chem.* **2002**, *628*, 67–76.

[107] R. Kniep, H. G. Will, I. Boy, C. Röhr. 6_1-Helices from Tetrahedral Ribbons $^1_\infty\{[BP_2O_8]^{3-}\}$: Isostructural Borophosphates $M^I M^{II}(H_2O)_2[BP_2O_8] \cdot 2H_2O$ and Their Dehydration to Microporous Phases $M^I M^{II}(H_2O)[BP_2O_8]$. *Angew. Chem. Int. Ed. Engl.* **1997**, *36*, 1013–1014. *Angew. Chem.* **1997**, *109*, 1052–1054.

[108] I. Boy, F. Stowasser, G. Schäfer, R. Kniep. $NaZn(H_2O)_2[BP_2O_8] \cdot H_2O$: A Novel Open-Framework Borophosphate and its Reversible Dehydration to Microporous Sodium Zincoborophosphate $Na[ZnBP_2O_8] \cdot H_2O$ with CZP Topology. *Chem. Eur. J.* **2001**, *7*, 834–839.

[109] I. Boy, R. Kniep. Crystal structure of lithium copper(II) diaqua *catena*-[monoboro-diphosphate] dihydrate, $LiCu(H_2O)_2[BP_2O_8] \cdot 2H_2O$. *Z. Kristallogr. NCS* **2001**, *216*, 7–8.

[110] I. Boy, R. Kniep. Crystal structure of lithium zinc diaqua *catena*-[monoboro-diphosphate]-monohydrate, $LiZn(H_2O)_2[BP_2O_8] \cdot H_2O$. *Z. Kristallogr. NCS* **2001**, *216*, 9–10.

[111] I. Boy, G. Schäfer, R. Kniep. Crystal structure of sodium nickel diaqua *catena*-[monoboro-diphosphate]-monohydrate, $NaNi(H_2O)_2[BP_2O_8] \cdot H_2O$, at 293 K and 198K. *Z. Kristallogr. NCS* **2001**, *216*, 11–12.

[112] I. Boy, G. Schäfer, R. Kniep. Crystal structure of sodium iron(II) di-aqua *catena*-[monoboro-diphosphate]-monohydrate, $NaFe(H_2O)_2[BP_2O_8] \cdot H_2O$, and of potassium iron(II) diaqua *catena*-[monoboro-diphosphate]-hemihydrate, $KFe(H_2O)_2[BP_2O_8] \cdot 0.5H_2O$. *Z. Kristallogr. NCS* **2001**, *216*, 13–14.

[113] G. Schäfer, W. Carrillo-Cabrera, W. Schnelle, H. Borrmann, R. Kniep. Synthesis and Crystal Structure of $(NH_4)_x Co_{(3-x)/2}(H_2O)_2[BP_2O_8] \cdot (1-x)H_2O$ ($x \approx 0.5$). *Z. Anorg. Allg. Chem.* **2002**, *628*, 289–294.

[114] M.-H. Ge, J.-X. Mi, Y.-X. Huang, J.-T. Zhao, R. Kniep. Crystal structure of sodium cadmium diaqua *catena*-[monoboro-diphosphate]-hydrate, $NaCd(H_2O)_2$-$[BP_2O_8] \cdot 0.8H_2O$. *Z. Kristallogr. NCS* **2003**, *218*, 165–166.

[115] H.-Z. Shi, Y.-K. Shan, M.-Y. He, L.-Y. Dai, Y.-Y. Liu, L.-H. Weng. A New Borophosphate compound with Helix Structure: $(NH_4)_{0.5}(H_3O)_{0.5}Mg(H_2O)BP_2O_8$. *Acta Chimica sinica* **2003**, *61*, 711–714.

[116] R. Kniep, H. Engelhardt. $Na_{1.89}Ag_{0.11}[BP_2O_7(OH)]$ und $Na_2[BP_2O_7(OH)]$ – Isotype Borophosphate mit Tetraeder-Schichtpaketen. *Z. Anorg. Allg. Chem.* **1998**, *624*, 1291–1297.

[117] H. Engelhardt, W. Schnelle, R. Kniep. $Rb_2Co_3(H_2O)_2[B_4P_6O_{24}(OH)_2]$: Ein Borophosphat mit $^2_\infty$-Tetraeder-Anionenteilstruktur und Oktaeder-Trimeren $(Co^{II}_3O_{12}(H_2O)_2)$. *Z. Anorg. Allg. Chem.* **2000**, *626*, 1380–1386.

[118] S. C. Sevov. Synthese and Structure of $CoB_2P_3O_{12}(OH) \cdot C_2H_{10}N_2$. *Angew. Chem. Int. Ed. Engl.* **1996**, *35*, 2630–2632. *Angew. Chem.* **1996**, *108*, 2814–2816.

[119] R. Kniep, G. Schäfer. Isotype Borophosphate $M^{II}(C_2H_{10}N_2)[B_2P_3O_{12}(OH)]$ (M^{II} = Mg, Mn, Fe, Ni, Cu, Zn): Verbindungen mit Tetraeder-Schichtverbänden. *Z. Anorg. Allg. Chem.* **2000**, *626*, 141–147.

[120] C. Hauf, R. Kniep. $Rb[B_2P_2O_8(OH)]$ und $Cs[B_2P_2O_8(OH)]$: Die ersten Borophosphate mit dreidimensional vernetzter Anionenteilstruktur. *Z. Naturforsch.* **1997**, *52b*, 1432–1435.

[121] G. Schäfer, H. Borrmann, R. Kniep. Synthesis and crystal structure of $NH_4[(Zn_{1-x}Co_x)BP_2O_8]$ ($0 \leq x \leq 0.14$), a metallo-borophosphate analogue of the zeolite gismondine. *Micro. Meso. Mater.* **2000**, *41*, 161–167.

[122] H. Y. Zhang, Z. X. Chen, L. H. Weng, Y. M. Zhou, D. Y. Zhao. Hydrothermal synthesis of new berylloborophosphates M^IBeBPO (M^I = K^+, Na^+ and NH_4^+) with zeolite ANA framework topology. *Micro. Meso. Mater.* **2003**, *57*, 309–316.

[123] D. R. Peacor. High-Temperature Single Crystal Study of The Cristobalite Inversion. *Z. Kristallogr.* **1973**, *138*, 274–298.

[124] J. Do, A. J. Jacobson. Mesostructured Lamellar Phases Containing Six-Membered Vanadium Borophosphate Cluster Anions. *Chem. Mater.* **2001**, *13*, 2436–2440.

[125] R. M. Barrer. *Hydrothermal Chemistry of Zeolites*. Academic Press London **1982**.

[126] L. R. Taylor, R. B. Papp, B. D. Pollard. *Instrucmental Methods for Determining Elements*. VCH Publishers, Inc. **1994**.

[127] B. Warren, W. L. Bragg. Zeolite and Molecular Sieve Synthesis. *Z. Kristallogr.* **1928**, *69*, 168.

[128] T. Steiner. The Hydrogen Bond in the Solid State. *Angew. Chem. Int. Ed.* **2002**, *41*, 48–76. *Angew. Chem.* **2002**, *114*, 50–80.

[129] K. Nakamoto. *Infrared and Raman Spectra of Inorganic and Coordination Compounds; Part A: Theory and Applications in Inorganic Chemistry*. John Wiley & Sons New York, 5th edition **1997**.

[130] W. T. A. Harrison, T. E. Martin, T. E. Gier, G. D. Stucky. Tetrahedral-atom Zincophosphate Strucutres: Synthesis and Structural Characterization of Two Novel Anionic Eight-ring Frameworks containing Cationic 1,4-Diazabicyclo[2.2.2]octane Guests. *J. mater. Chem.* **1992**, *2*, 175–181.

[131] S. Neeraj, S. Natarajan. Synthesis and structure of an open-framework chlorophosphate, $[C_6NH_{14}][ZnCl(HPO_4)]$. *J. Mater. Chem.* **2000**, *10*, 1171–1175.

[132] J. Yu, Y. Wang, Z. Shi, R. Xu. Hydrothermal Synthesis and Characterization of Two New Zinc Phosphates Assembled about a Chiral Metal Complex: $[Co^{II}(en)_3]_2[Zn_6P_8O_{32}H_8]$ and $[Co^{III}(en)_3][Zn_8P_6O_{24}Cl] \cdot 2H_2O$. *Chem. Mater.* **2001**, *13*, 2972–2978.

[133] A. Kishioka, K. Itatani, M. Kinoshita. Phase Change during Heating of Ammonium Zinc Phosphate Prepared by Homogenous Precipitation Method. *J. Ceram. Assoc. Jpn.* **1985**, *93*, 606–611.

[134] B. E. Robertson, C. Calvo. The Crystal Structure of α–$Zn_2P_2O_7$. *J. Solid State Chem.* **1970**, *1*, 120–133.

[135] N. N. Julius, A. Choudhury, C.N.R. Rao. An organically templated open-framework cobalt germanate. *J. Solid State Chem.* **2003**, *170*, 124–129.

[136] W. T. A. Harrison, T. E. Gier, G. D. Stucky, R. W. Broach, R. A. Bedard. $NaZnPO_4 \cdot H_2O$, an Open-framework Sodium Zincophosphate with a New Chiral Tetrahedral Framework Topology. *Chem. Mater.* **1996**, *8*, 145–151.

[137] H. D. Flack, G. Bernardinelli. Absolute structure and absolute configuration. *Acta Crystallogr.* **1999**, *A55*, 908–915.

[138] H. D. Flack, G. Bernardinelli. Reporting and evaluating absolute-structure and absolute-configuration determinations. *J. Appl. Cryst.* **2000**, *33*, 1143–1148.

[139] N. E. Brese, M. O'Keeffe. Bond-Valence Parameters for Solids. *Acta Crystallogr.* **1991**, *B47*, 192–197.

[140] H. Bärnighausen. *MATCH, Commun. Math. Chem.* **1980**, *9*, 139–175.

[141] T. Stefanidis, A. G. Nord. Structural Studies of Thortveitite-Like Dimanganese Diphosphate, $Mn_2P_2O_7$. *Acta Crystallogr.* **1984**, *C40*, 1995–1999.

[142] H. Lueken. *Magnetochemie.* Teubner Stuttgart **1999**.

[143] D. R. Corbin, L. Abrams, G. A. Jones, M. M. Eddy, W. T. A. Harrison, G. D. Stucky, D. E. Cox. Flexibility of the Zeolite RHO Framework. In Situ X-ray and Neutron Powder Structural Characterization of Divalent Cation-Exchanged Zeolite RHO. *J. Am. Chem. Soc.* **1990**, *112*, 4821–4830.

[144] M. Sghyar, J. Durand, L. Cot, M. Rafiq. Structure du phosphite de fer: $Fe_2(PO_3H)_3$. *Acta Crystallogr.* **1991**, *C47*, 2515–2517.

[145] G. J. Long, A. K. Cheetham, P. D. Battle. Study of the Iron-Phosphorus-oxygen System by Mossbauer Effect, Neutron Diffraction, Magnetic Susceptibility, and Analytical Electron Microscopy: some Pitfalls and Solutions in the Analysis of a Complex Mixture. *Inorg. Chem.* **1983**, *22*, 3012–3016.

[146] R. D. Shannon. Revised Effective Ionic Radii and Systematic Studies of Interatomic Distances in Halides and Chalcogenides. *Acta Crystallogr.* **1976**, *A32*, 751–767.

[147] P. Y. Zavalij, M. S. Whitingham. Structural Chemistry of Vandium Oxides with Open Frameworks. *Acta Crystallogr.* **1999**, *B55*, 627–663.

[148] L.-I Hung, S.-L. Wang, H.-M. Kao, K.-H. Lii. Synthesis, Crystal Structure, and Solid State NMR Spectroscopy of $NH_4[(V_2O_3)_2(4,4'$-bpy$)_2(H_2PO_4)(PO_4)_2]\cdot 0.5H_2O$, a Mixed-Valence Vanadium(IV,V) Phosphate with a Pillared Layer Structure. *Inorg. Chem.* **2002**, *41*, 3929–3934.

[149] K.-J. Range, M. Wildenauer, A. M. Heyns. Extremely Short Non-bonding Oxygen Oxygen Distances-The Crystal Strctures of $NbBO_4$, $NaNb_3O_8$, and $NaTa_3O_8$. *Angew. Chem. Int. Ed. Engl.* **1988**, *27*, 969–971. *Angew. Chem.* **1988**, *100*, 973-975.

Programs

[P1]   Stoe Win XPOW, Visual XPOW Software Package for STOE Powder Diffraction System, Version 1.2, *Stoe & Cie* GmbH, Darmstadt **2001**.

[P2]   G. M. Sheldrick, SHELXS–97/2, Program for the Solution of Crystal Structures, Universität Göttingen **1997**.

[P3]   G. M. Sheldrick, SHELXL–97/2, Program for Crystal Structure Refinement, Universität Göttingen **1997**.

[P4]   K. Brandenburg, M. Berndt, DIAMOND–Visual Crystal Structure Information System (Version 2.1), Crystal Impact GbR, Bonn **1996–1998**.

[P5]   L. Finger, M. Kröker, DRAWxtl–A program to make ball and stick or polyhedral crystal structure drawings **1997**.

[P6]   C. J. Cason, POV-Ray 3.1 a, Raytracing Tool, **1998**.

[P7]   L. G. Akselrud, P. Yu. Zavalii, Yu. N. Grin, V. K. Pecharski, B. Baumgartner, E. Wölfel, Crystal Structure Determination Program Package WinCSD, Mater. Sci. Forum, 335, 133–136, **1993**.

[P8]   L. J. Farrugia, MAPVIEW–WinGX 1.64.03 System Program, Universität Glasgow **2002**.

Curriculum Vitae

PERSONAL DATA:

Name:	Ya-Xi Huang
Date of Birth:	Nov. 1, 1975
Place of Birth:	Fujian, P. R. China
Marital status:	Married

EDUCATION:

Sept. 1994 – July 1998	Study on material science in Xiamen University, P. R. China; B.S. Degree
Sept. 1998 – Mar. 2001	Study on inorganic chemistry under supervision of Prof. Dr. J.-T. Zhao in Xiamen University, P. R. China; M.S. Degree
May 2001 – present	Study on inorganic chemistry under supervision of Prof. Dr. R. Kniep at the Max-Planck Institute for Chemical Physics of solids, Dresden, Germany; PhD candidate

RESEARCH EXPERIENCE:

Feb. 1998 – July 1998	Research assistant, Department of material science, Xiamen University, P. R. China
Sept. 1998 – Mar. 2001	Research assistant, Department of inorganic chemistry, Xiamen University, P. R. China
Sept. 2000 – April 2001	Visitor, Max-Planck Institute for Chemical Physics of solids, Dresden, Germany
May 2001 – present	Research assistant, Max-Planck Institute for Chemical Physics of solids, Dresden, Germany

Versicherung

Hiermit versichere ich, dass ich die vorliegende Arbeit ohne unzulässige Hilfe Dritter und ohne Benutzung anderer als der angegebenen Hilfsmittel angefertigt habe; die aus fremden Quellen direkt oder indirekt übernommenen Gedanken sind als solche kenntlich gemacht. Die Arbeit wurde bisher weder im Inland noch im Ausland in gleicher oder ähnlicher Form einer anderen Prüfungsbehörde vogelegt.

Die vorliegende Dissertation wurde unter der Betreuung von Herrn Prof. Dr. R. Kniep in der Zeit von Mai 2001 bis Juni 2004 am Max-Planck-Institut für Chemische Physik fester Stoffe in Dresden angefertigt.

Es haben keine frühen erfolglosen Promotionsverfahren stattgefunden.

Ich erkenne die Promotionsordnung der Fakultät Mathematik und Naturwissenschaften der TU Dresden vom 16. April 2003 in vollem Umfang an.

Dresden, den

(Ya-Xi Huang)

HSSS AdminTools (c) 2001, last visited: Mon Feb 21 11:11:07 CET 2005